Sound Absorption Mechanisms in Perforated Plates

Alessia Aulitto

Sound absorption mechanisms in perforated plates

Alessia Aulitto

The work described in this thesis was carried out at the Eindhoven University of Technology.

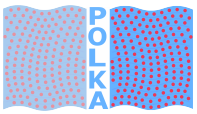

This work is part of the Marie Skłodowska-Curie Initial Training Network Pollution Know-How and Abatement (POLKA). We gratefully acknowledge the financial support from the European Commission under call H2020-MSCA-ITN-2018 (project number: 813367).

A catalogue record is available from the Eindhoven University of Technology Library.
ISBN: 978-90-386-5709-7

Typeset by the author using the pdf LaTeX documentation system.
Cover design: Hellen and Niek Jongeneel based on flow visualization
Reproduction: Ipskamp Printing, Enschede, The Netherlandsl

Sound absorption mechanisms in perforated plates

Proefschrift

ter verkrijging van de graad van doctor aan de
Technische Universiteit Eindhoven, op gezag van de
rector magnificus prof.dr.ir. F.P.T. Baaijens, voor een
commissie aangewezen door het College voor
Promoties, in het openbaar te verdedigen
op vrijdag 31 maart 2023 om 16:00 uur

door

Alessia Aulitto

geboren te Napels, Italië

Dit proefschrift is goedgekeurd door de promotoren en de samenstelling van de promotiecommissie is als volgt:

voorzitter:	prof.dr.ir. P.D. Anderson
1^e promotor:	prof.dr.ir. I. Lopez Arteaga
2^e promotor:	prof.dr. M. Heckl (KU)
co-promotor:	prof.dr.ir. A. Hirschberg
leden:	prof.dr.ir. M.C.J. Hornikx
	prof.dr.ir. J. Westerweel (TUD)
	prof.dr.ir. C.H. Venner (UT)
	prof.dr. S. De Rosa (UniNa)
	dr. H. Bailliet (UP)

Het onderzoek dat in dit proefschrift wordt beschreven is uitgevoerd in overeenstemming met de TU/e Gedragscode Wetenschapsbeoefening.

"Vortices are the voice of the flows",
Mico Hirschberg, citing Müller and Obermeier [1].

Summary

Sound absorption mechanisms in perforated plates

Perforated plates combined with a back cavity are a passive noise-control technology in architectural applications and control of thermo-acoustic instabilities in combustion processes. Circular perforations with sharp edges are traditionally used, showing excellent absorption performances when the dimensions of the perforations are in the sub-millimeter range and viscous effects dominate the sound absorption of the plate. The ratio between the open area and the total plate area is around 1%, implying an extremely high number of perforations to cover small areas. Technical challenges, mainly due to the need for accurate manufacturing of the sharp edges, limit the practical application of micro-perforations.

This work targets non-conventional shapes of perforation, where the focus is on slits. In particular, a slit can replace multiple micro-perforations and can be manufactured in several ways, such as punching and cutting a plate, overcoming production issues and costs of circular perforations. The core of the approach of this thesis is linear theory and numerical simulations combined with systematic experiments on accurately manufactured samples. The real and imaginary parts of the acoustic transfer impedance of the perforated plate (resistance and inertance) provide the input for a lumped-element model to predict the sound absorption properties of the perforated plate backed by a cavity.

In the linear regime, when considering a plate with multiple slits, the sound absorption properties of the plate are predicted by modeling a single slit confined within a channel, accounting for the hydrodynamic interactions with neighboring slits. A systematic study of the influence of details of the slit geometry, such as rounding of the edges, follows. For high acoustic amplitudes, linear theories fail to predict the acoustic properties of micro-perforated plates due to non-linear behavior. A systematic study with medium and high acoustic excitations provides insight into the non-linear sound absorption mechanisms of arrays of slits for the specific slit geometry obtained by punching the plate. The presence of non-linear effects does not decrease the sound absorption of the plate. On the contrary, the

sound absorption increases with the increasing acoustic amplitudes and, although the generation of higher-order harmonics is a drawback of non-linear effects, symmetries in the geometry of the slits can suppress even-order harmonics in the response. In some applications, such as combustion chambers, medical aseptic rooms, or clean rooms, the dimensions of micro-perforations make them vulnerable to dust collection and clogging by particle waste. For these applications, one could combine larger perforations and bias flow to enhance the sound absorption of the plate. A nearly-perfect absorption occurs at low subsonic mean-flow speeds, corresponding to realistic conditions for the applications considered. The bias flow generates a cold wall jet downstream of the plate that protects the wall in several applications, such as combustion chambers. However, the plate exhibits the potential to whistle due to the bias flow.

This work opens the way to develop design rules and optimization tools for perforated plates with slit-shaped perforations and provides insight into the sound absorption mechanism of slit-shaped perforations in several technological applications, ranging from room acoustics to the disruption of thermo-acoustic instabilities in combustion chambers.

Keywords: Sound absorption, micro-slits, bias flow, combustion, non-linear

Samenvatting

Geperforeerde platen gecombineerd met daarachter een holle ruimte (caviteit) bieden een technologische oplossing voor geluidsabsorptie in architecturale toepassingen en voor het beheersen van thermo-akoestische instabiliteiten in verbrandingsprocessen. Traditioneel worden cirkelvormige microperforaties met scherpe randen gebruikt. Die leveren uitstekende absorptieprestaties. Deze microperforaties hebben afmetingen in het submillimeterbereik waarbij viskeuze dissipate de belangrijkste bijdrage levert aan het akoestisch gedrag. De optimale verhouding tussen het open gebied van de perforaties en het totale plaatoppervlak is in de orde van grootte van 1%. Dit impliceert een enorm aantal perforaties. Technische uitdagingen, voornamelijk gerelateerd aan de zeer nauwkeurige toleranties die benodigd zijn, beperken de toepasbaarheid van microperforaties aanzienlijk.
In deze studie wordt de nadruk gelegd op sleuven in plaats van ronde perforaties. De onconventionele vorm van de perforaties is gekozen om verschillende productieproblemen te vermijden. Sleuven kunnen goedkoop vervaardigd wordend door de plaat plaatselijk diep te ponsen zodat een snede ontstaat en een sleuf kan vele microperforaties vervangen. Verder vormen geluidsabsorberende panelen met trillende elementen omringd door sleuven een veelbelovend alternatief voor starre panelen. In dit proefschrift worden lineaire theorie en numerieke simulaties gecombineerd met systematische experimenten op nauwkeurig vervaardigde geperforeerde platen, in aan- of afwezigheid van transversale stationaire doorstroming. De reële en imaginaire delen van de impedantie (respectievelijk de weerstand en traagheid) zijn de invoer van een model dat wordt gebruikt om de absorptie-eigenschappen van een geperforeerde plaat met een achterholte te voorspellen.
In het lineaire regime wordt een enkele sleuf gemodelleerd om de geluidsabsorptie van de volledige plaat met meerdere sleuven te voorspellen. Deze sleuf wordt gemodelleerd in een opgesloten kanaal om rekening te houden met de hydrodynamische interacties met naburige sleuven. Hierna volgt een systematische studie van de invloed van details in de sleufgeometrie, zoals afronding van de randen.
Voor hoge akoestische amplitudes slagen lineaire theorieën er niet in om de akoestische eigenschappen van microgeperforeerde platen te voorspellen vanwege niet-lineair gedrag dat bij hoge akoestische amplitudes optreedt. Een systematische studie met gemiddelde en hoge akoestische excitatie is uitgevoerd en biedt inzicht

in niet-lineaire, geluidsabsorberende mechanismen van een rij met sleuven, waarbij de specifieke geometrie van de sleuven gebaseerd is op de geometrie die ontstaat bij het ponsen van de plaat. De aanwezigheid van niet-lineaire effecten lijkt de absorptie van de plaat niet te verminderen en de absorptie neemt zelfs toe met hogere akoestische amplitudes. Een nadeel van de niet-lineaire effecten is dat er hogere harmonischen ontstaan. Symmetrieën in de geometrie van de sleuven kunnen worden benut om harmonischen van even orde te onderdrukken.
In sommige toepassingen, zoals verbrandingskamers, medische steriele kamers of cleanrooms, zijn microperforaties door hun geringe afmetingen kwetsbaar voor ophoping en verstopping door afvaldeeltjes. Voor deze toepassingen kunnen grotere perforaties worden gebruikt in combinatie met een doorstroming van de plaat om de geluidsabsorberende-eigenschappen te verbeteren. De introductie van doorstroming laat een toename van de geluidsabsorptie van de plaat zien en bij lage subsonische gemiddelde stroomsnelheden, overeenkomend met de omstandigheden van de betreffende toepassing, leidt deze doorstroming zelfs tot bijna perfecte absorptie. Daarnaast genereert de doorstroming, voor de beschouwde geometrie, aan de achterzijde van de plaat een straal die parallel loopt aan de plaat. Bij gebruik in een verbrandingskamer kan deze straal de plaat beschermen tegen warmte. Een nadeel van deze geometrie is echter dat tonaal geluid kan optreden. Dit proefschrift biedt inzicht in de geluidsabsorberende mechanismen van sleufvormige perforaties in verschillende technologische toepassingen, variërend van ruimteakoestiek tot verstoring van thermo-akoestische instabiliteiten in verbrandingskamers. Daarmee maakt dit werk de weg vrij voor de ontwikkeling van optimalisatiemethodes en ontwerpregels voor platen met sleufvormige perforaties.

Societal summary

In recent years, hydrogen combustion has appeared as an emerging technology to replace fossil fuels and provide carbon-neutral energy. When dealing with high-efficiency and low-emission combustion systems, the combination of heat, flow, and acoustic-pressure waves generates instabilities that can lead to severe hardware damage. Noise control techniques based on perforations can provide a solution to disrupt such instabilities, dissipating the energy of acoustic waves in the chambers. However, this is not the only application of perforated plates, which have proven useful in several applications, ranging from room acoustics to acoustic liners in aircraft engines.

For optimal dissipation of the acoustic waves, the dimensions of the perforations are in the sub-millimeter range. Such plates are referred to in the literature as Micro-perforated plates (MPPs). Micro-perforated plates are used as sound absorbers in the low-frequency range when backed by a cavity. Popular solutions use circular perforations, but accurate manufacturing technologies are expensive. Therefore, this work pushes toward alternatives to circular perforations in the shape of slits (micro-slit plates), which display sound absorption mechanisms similar to those of circular perforations. However, a slit can be obtained in different and cheaper ways. The design of slits can be optimized to combine efficient sound absorption with cheaper manufacturing techniques, as in the case of a metallic plate with slits obtained by punching and cutting the plate.

For low acoustic amplitudes, as for room acoustics, a model for slits in an array is proposed. The acoustic dissipation is localized at the sharp edges of the slit. Therefore, attention has to be paid during manufacturing to obtain accurate edges of the slits. For moderate and high acoustic excitations, in the case of combustion chambers, the dissipation is mainly due to unsteady vortex shedding. For low excitations, the vortices remain local at the edges. For higher amplitudes, jets form periodically. Whereas edge geometry remains an important parameter, interactions between slits within and outside the plate become crucial to model the acoustic properties of the micro-slit plate. The geometry of such slits makes them suitable candidates as bias flow liners in hot chambers, using an additional airflow (bias flow) through the slits to enhance the absorption properties and generate a steady cold wall jet flow, which protects the walls of the combustion chamber.

Contents

1
Introduction

1.1 Motivation

"To stop pulsation, drill one hole [...]; if that doesn't work, drill two holes!". In 1971, Putnam reported the advice of a trade journal of 1940 concerning the use of orifices as dampers of acoustic pulsations [2]. Nowadays, passive noise control techniques based on perforated plates are a well-assessed technology for several applications, ranging from room acoustics and aircraft-engine-inlet liners to combustion-chamber liners.

Heavy materials such as absorptive foams or porous materials have been the most common choice for decades. These materials are proven effective for wavelengths up to a quarter of the thickness of the material [3]. For this reason, foams require a large thickness to achieve low-frequency noise reduction. In the architectural sector, the impact of weight and thickness is not always a primary concern [4]. The first real application of perforated plates in a building was in 1993 in the Deutscher Bundestag in Bonn. In transportation, designs are compact, lightweight, and resistant to harsh environments with high temperatures [5]. Perforated plates have the potential to be dissipative mufflers and offer a non-fibrous alternative in heating, ventilation, and air-conditioning (HVAC) systems. The high potential of perforated plates in combination with a bias flow in gas turbines is also well-known [6]. Since the second half of the 20th (twentieth) century, perforated plates appeared as means to suppress instabilities in combustion [7–9]. High efficiency and low emission combustion systems are more sensitive to combustion instabilities [10, 11]. In recent years, hydrogen combustion has appeared as an emerging technology to replace fossil fuels and provide carbon-neutral energy. When dealing with hydrogen, thermo-acoustic instabilities and flashbacks critically limit the possibilities for safe combustion. Thermo-acoustic instabilities are generated by a complex feedback mechanism between heat release fluctuations, flow, and acoustic oscillations. The coupling can generate large-amplitude self-sustained pressure oscillations that can lead to catastrophic damage to the hardware [12]. Perforated plates, backed by cavities, offer an excellent candidate to disrupt the thermo-acoustic coupling that excites the instability. A perforated plate offers an excellent sound absorption ability and provides means to manipulate and re-distribute the acoustic energy loss at the chamber's walls, making the system stable [13–17]. The present thesis focuses on developing physical insight and tools for the optimal design of alternatives to circular perforations for passive noise control techniques in several applications.

1.2 Micro-perforated plates as sound absorbers

Micro-perforated plates (MPPs) are defined here as plates with orifices with a diameter (d_p) in the sub-millimeter range and porosity (open areas) of the order of 1%. In 1975, Maa [18] proposed one of the first studies of plates containing perforations with diameter in the sub-millimeter range (micro-perforations) as sound absorbers in the low-frequency range for industrial applications. Maa [18] proposes MPPs with a few percent porosity, achieving high sound absorption properties, where micro-perforations appear as versatile, suitable candidates for technological applications. MPPs provide a robust alternative to fibrous and porous structures because of their durability in time, the reduction of contamination due to fibers, and their resistance to harsh environments.
In MPPs, the ratio between the radius of the perforations $d_p/2$ and the thickness of the acoustic viscous boundary layer δ_v is of order unity (Figure 1.1c). This ratio is commonly known as the Shear number $Sh = d_p/(2\delta_v)$. When the Shear number is of order unity, the viscous boundary layer occupies the entire perforation cross-section and dissipates the incoming acoustic waves. The acoustic behavior of micro-perforated plates can be described by a complex acoustic impedance which is the sum of a resistive (dissipative, real part) and a reactive (inertial, imaginary part) component. In conventional designs, a shallow cavity is placed behind the micro-perforated plate (Figure 1.1b) leading to a configuration with a thin micro-perforated plate and a back cavity, which is referred to as a single-degree-of-freedom liner [19, 20]. For optimal sound absorption, the acoustic impedance of the combination should match the specific impedance of air $\rho_0 c_0$, with ρ_0 the density of air and c_0 the speed of sound in air. The lumped-element impedance of the absorber is the sum of the inertance of the orifice, the resistance of the orifice, and the compliance of the back cavity. A micro-perforated absorber shows a peak of absorption in a specific frequency range.

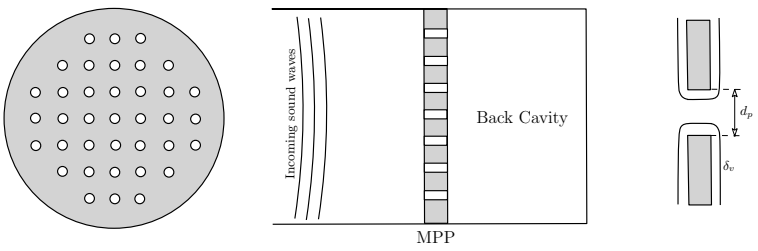

Figure 1.1. A schematic representation of a micro-perforated plate (front view in (a)) mounted with a back cavity as a sound absorber (b). The cross-section for one perforation with a viscous boundary layer is shown in (c).

The frequency associated with the maximum absorption depends on the cavity depth and the effective length of the orifice, while the bandwidth of absorption depends on the resistance.
Maa [18, 21] proposes an analytical model for the impedance of a single perforation in terms of so-called end-corrections, for both resistive and reactive parts of the impedance. These are additions to the perforation length in a parallel-flow model (within the perforation), taking into account the effect of the acoustic flow outside the perforation and the deviations from a parallel flow. Following the example of Maa, several models offer different approaches for the calculations of the end-corrections [22–25]. Most available models and approaches neglect the hydrodynamic interactions between neighboring perforations. Therefore, these models are only valid for low porosities. Tayong *et. al.* [26] and Carbajo *et al.* [27] study the effect of interactions between perforations and consider the effect of a non-uniform distribution of the perforations over the plate.
In literature, sound absorption structures with double back cavities or additional porous materials propose alternatives to single-degree-of-freedom resonators. Several solutions are based on adding degrees of freedom to the resonator structure. A possibility is to sub-divide the cavity in individual cells with different volumes to distribute the sound absorption over a wider frequency range [28–30] or use of complex cavity geometries [20, 31]. So-called zero mass flow liners (ZML) show promising results. In ZML, a single-degree-of-freedom liner is attached to an acoustic actuator emitting a secondary high-amplitude sound field, inducing a periodic bias flow in the orifices [32–34]. Adaptive SDF resonators with tunable cavities [35–40], double-degree-of-freedom (DDOF) with the addition of a porous material in the cavity [41–43] or multi-degree-of-freedom (MDOFs) have been considered [44–46]. Jiménez *et al.* [47] propose a MDOFs using slits combined with a row of Helmholtz resonators.
Interesting results are obtained with so-called zero mass flow liners (ZML) where a single-degree-of-freedom liner is attached to an acoustic actuator emitting a secondary high-amplitude sound field, inducing a periodic bias flow in the orifices [32–34, 48]. The complexity of such sound absorbers represents a drawback in several applications. The acoustic performances of single-degree-of-freedom (SDOF) liners and more complex liners depend on the geometry of the perforated plate [49, 50]. Therefore, accurate modeling of liners starts by gaining an understanding of the acoustic properties of the micro-perforated plates. This is the main focus of the present work.

1.3 From micro-perforations to micro-slits

When referring to micro-perforated plates, one tends to think of a plate with multiple circular-shaped perforations, that require hole sizes in the sub-millimeter range to reach efficient sound absorption in the low-frequency range.

A huge number of holes are necessary to cover even small areas. For instance, a micro-perforated plate with $d = 0.5\,\text{mm}$ and porosity $\Phi = 1\%$, would roughly require 5×10^4 holes per square meter.
Such small holes pose several technical challenges. Assuming the manufacturing issues mentioned above are solved, sub-millimeter holes are in constant danger of clogging due to the presence of dust or combustion materials during their usage. Furthermore, the edges encounter modifications due to aging, and, in some applications, the plates face harsh environments where their properties will degrade in time. In other applications, the plates are mounted on rounded surfaces with the holes losing their original circular shape, as in acoustic liners or airfoil covers. The sum of all these challenges leads to severe limitations of the practical applications of micro-perforations.
One possible solution is to replace circular perforations with slit-shaped perforations, introducing micro-slit plates (MSPs) and absorbers (MSAs). Micro-slit plates have been introduced in 2001 by Maa [51]. Figure 1.2 shows a micro-slit plate on the side of a micro-perforated plate with a similar open area (porosity). A single slit can replace multiple circular perforations maintaining the same porosity, *i.e.* the same open area. If needed, using sub-millimeter slits, one can obtain a relatively large porosity and a higher Helmholtz resonance frequency of the micro-slit absorber. Different techniques allow manufacturing slits. For example, Auriemma [52] investigates the behavior of slits obtained by putting two perforated plates next two each other, while Cobo refers to 3D-machining [53]. Another solution to the manufacturing limitations is punching a metallic sheet without removing material, as used in ventilation grills and air diffusers or to manufacture the Acustimet plates by Sontech [54]. A full metallic plate is well-suited for application with combustion and high temperatures and attracts less dirt. However, developing an accurate model to predict the acoustic behavior of these plates is challenging because of the complex geometry of the slits. It is interesting to note that Maa [51], erroneously assumes that an analytical model for the acoustic properties of slits, equivalent to his model for circular perforations [18] can not be found.

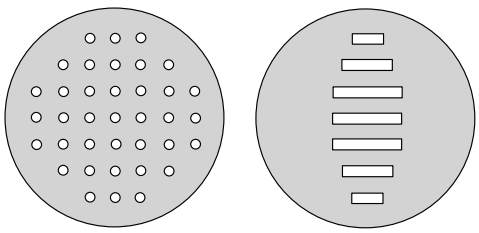

Figure 1.2. A schematic representation of a portion of a micro-perforated plate and a micro-slit plate with approximately the same porosity.

1.4 Flexible micro-slits plates

An emerging application of slits in recent years is the use of flexible micro-slit plates, where the complex interplay between vibrational response and acoustics is yet to be understood. In these plates, slits delimit local-flexible structures embedded in the plates, without necessarily adding mass-spring-damper systems on top, as shown in Figure 1.3 [55–58]. Due to the presence of flexible parts, the acoustic behavior of the plate differs from the one of a rigid, motionless plate. In the linear regime, the sound absorption mechanism of micro-perforations is due to the conversion of the kinetic energy of the fluid particles into heat energy. As the viscous resistance increases quadratically with the relative velocity between the plate and the fluid, the kinetic-energy losses are expected to increase drastically when the excitation frequency approaches the Helmholtz resonance frequency of the combination of the perforated plate with the back cavity. For a rigid MPP, the relative particle velocity of the air is the same for each perforation when excited by a planar acoustic wave. When the plate is flexible, at specific frequencies, the plate vibrates with a given mode shape. Depending on the properties of the plate, the acoustical modes of the medium can couple with the structural modes of the plate, changing the number of absorption peaks, frequency, and amplitude of the acoustic resonance of the system and becomes an extra parameter in the design process. Lee and Swenson [59] observe for the first time the effect of the plate vibration on the acoustic properties of a plate. Since then, several works focus on modeling the impact of the flexibility of the acoustic properties of micro-perforated plates, showing that modifications of the plate structure to include flexible or resonant elements enhance the sound absorption of MPPs and MSPs [60–66]. For example, Bravo *et al.* [64] conclude that if the fundamental frequency of the plate coincides with the peak of absorption of the rigid micro-perforated plate, the sound absorption of the plate increases. On a similar note, Ren *et al.* [66] proposes the addition of mass-spring-damper resonators to one face of the micro-perforated plate to prevent undesired plate vibrations. Due to the periodic structural elastic pattern, a frequency stop-band in the vibrational response appears.

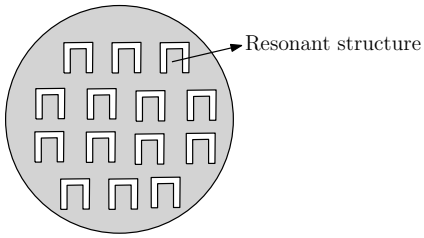

Figure 1.3. A schematic representation of a micro-slit plate with embedded resonant structures.

Since these materials have no natural equivalent, they are referred to as meta-materials. Stop-bands are regions of frequencies where a fano-type interference between incoming and re-radiated waves blocks the free propagation of incoming acoustic waves [67]. Several works focus on viscous-thermal dissipation driven by flexible structures [68–71]. Farooqui and Aurégan [72, 73] propose an innovative liner to reach an optimized coupling between thermo-viscous acoustics and structural mechanics using thin-flexible oscillating structures. Abily *et al.* [58] focus on the non-linear acoustic response of resonators coupled to plates with thin slits. De Priester *et al.* [57] propose an optimized design for the unit cell of a micro-slit plate to maximize the size of the stop-band by changing the shape of the resonator and increasing the ratio between flexible area and total area of the cell (discussed in Appendix A.1).

1.5 Manufacturing challenges of perforations

When considering circular or slit-shaped micro-perforations, the first limitation comes from manufacturing. Accurate and precise holes come with extremely high costs and practical limitations due to the size of the perforations. Several works show that affordable manufacturing techniques, such as laser micro-machining or addictive manufacturing, result in relatively low accuracy. Residues due to thermal treatments, rough surfaces, and significant deviations from the designed dimensions are common problems due to manufacturing inaccuracy [56, 76, 77].In such cases, it is necessary to include systematic corrections in the model to obtain a good prediction of the behavior of the plate. Figure 1.4 shows pictures obtained with a microscope of the edges of the same slit obtained with two different manufacturing processes.

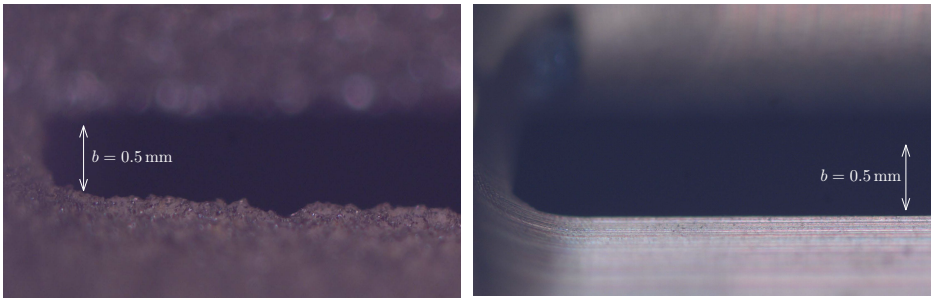

a) b)

Figure 1.4. Pictures obtained by optic microscope. a) Detail of the edge of a slit obtained with electric machine discharging [74]. b) Detail of a sharp edge obtained with milling [75].

The edges of the slits obtained with electric machine discharging (EDM) appear rough due to the micro-burnings on the surface, while the edges of the milled slits appear sharp and clean and the plate parameters respect within micron accuracy of the designed ones. One of the main challenges for manufacturing is obtaining sharp edges, with several works observed that the presence of chamfering or rounded edges heavily impacts the absorption properties of the micro-perforated plate [23, 25]. In some cases, when a steady bias flow is applied, the presence of rounded edges at the orifice can lead to sound production, *i.e.* whistling [78–83]. In conclusion, although micro-perforations provide a perfect candidate for sound absorption in the low-frequency range, several technical challenges appear in practical applications because of the dimensions of the perforations. In this work, the effect of manufacturing inaccuracies, such as asymmetries in the perforations pattern and rounded edges is studied.

1.6 Liners with larger perforations

In combustion chambers, perforated plates with relatively large perforations and high porosity are used to avoid the dangers of clogging but show lower sound absorption than micro-perforations. In these cases, the addition of a grazing flow along the plate or a bias flow through the perforations provides the means to achieve efficient sound absorption. Several models can be found in the literature to account for the effect of flow with extensive research performed on the so-called *bias flow liners* or *grazing flow liners*. Lahiri and Bake [6] present an extensive review of such publications, focusing on the geometry of *slanted perforations* or *grazing effusion holes*, where the micro-jets coalesce downstream of the plate and form a cooling film along the wall that protects the wall surface from hot gasses creating film cooling [84]. A schematic representation is shown in Figure 1.5 inspired by the numerical flow visualization of Eldredge *et al.* [85] and Mendez and Franck [86]. Some works focus on inclined circular holes [87–91], while Moers *et al.* [92] and Tonon *et al.* [93] consider oblique slits showing improved sound absorption compared to orthogonal perforations (with flow direction normal to the plate). Slanted holes and slits are expensive to manufacture in conventional ways. This work proposes a design of slits to obtain an affordable and practical solution for a bias flow liner with film cooling.

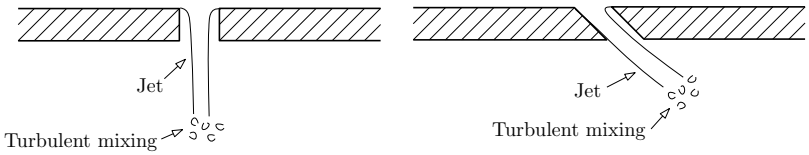

Figure 1.5. Schematic representation of a steady-flow for a straight and a slanted perforation.

1.7 Objectives

The primary objective of this thesis is to investigate the potential of slit-shaped perforations as versatile and affordable passive noise-control solutions. Other objectives of this work are to

- Gain insight into the sound absorption mechanisms of slits in several environmental conditions. The technical applications range from noise reduction in office spaces to disruption of thermo-acoustic instabilities in combustion chambers.
- Promote the use of simple analytical and numerical models in the first phases of the design process.
- Investigate the differences in the acoustic properties of circular perforations and slits.
- Understand the effect of manufacturing issues on the sound absorption of the plate.
- Examine the advantages and limitations of slits obtained by punching and cutting the plate (cheap alternative to circular perforations).
- Provide a systematic study of the acoustic properties of a specific slit geometry.
- Study the effect of high acoustic excitations and mean flow on the acoustic properties of the plate.

1.8 Research approach

Micro-slit plates can be components of single-degree-of-freedom and multiple-degree-of-freedom liners.
The starting point of this work is complementing the existing knowledge on the acoustical properties of slits, in terms of acoustic transfer impedance. In 2001, Maa [51] discussed the limitations of an incompressible model for slits. However, in Maa's work, only infinitely long slits are considered. The present thesis proposes different models for the impedance of micro-slit plates. An array of short slits is considered, where individual slits behave as confined in a channel due to the interaction between neighboring slits. The acoustic behavior of single slits within micro-slit plates (MSPs) is investigated to explore the effect of geometric manufacturing imperfections such as edge geometry or asymmetry of the slits pattern. The study moves toward a specific geometry of the slits, similar to the geometry obtained by cutting and punching a metallic sheet, such as the Acustimet plates [54]. This geometry is a potential candidate for an optimized bias flow liner, also in the presence of medium and high acoustic excitation amplitudes.

In this thesis, analytical models are combined with experiments and numerical simulations to provide knowledge and design tools for the acoustic characteristics of micro-slit plates. The experiments have been carried out with an impedance tube setup, in the absence and presence of a bias flow and complementary measurements are performed on a steady flow setup. For the numerical simulations, the commercial software Comsol [94] is used.

1.9 Contributions

In this Section, the main contributions of this thesis concerning the sound absorption mechanisms of slit-shaped perforations are summarized and discussed. Slits can encounter several environmental conditions, ranging from low acoustic amplitudes in office spaces to high acoustic excitation in the presence of grazing or a bias flow in combustion chambers or aircraft liners.

Contribution I. *This work provides a directly applicable model for the acoustic transfer impedance of a micro-slit plate in the linear regime, accounting for the influence of geometric parameters and manufacturing inaccuracies.*

In office spaces or room acoustic problems, the acoustic excitation amplitude is low and the behavior of the plate is linear. In this case, the absorption is dominated by viscous effects. The acoustic behavior of individual slits within micro-slit absorbers (MSAs) is investigated to explore the influence of porosity, edge geometry, slit position, and plate thickness. The viscous dissipation and the inertia are quantified by the resistive and the inertial end-corrections. These are estimated by using analytical results and numerical solutions of the Linearized Navier-Stokes equations.

Contribution II. *This thesis investigates the effect of the length of the slits on the acoustic properties of the plate and the potential of two-dimensional models.*

In practical applications, a rectangular slit poses similar manufacturing challenges as circular perforations due to the dimensions of the perforations and the edges. This work focuses on a specific micro-slit geometry inspired by cutting and punching the plate. Impedance tube measurements on two accurately manufactured plates are compared to the numerical solution of the Linearized Navier-Stokes equations and to analytical limits.

Conclusions can be generalized to different slit geometries.

Contribution III. *A model for the non-linear acoustic transfer impedance of a micro-slit plate is proposed.*

In the presence of medium and high acoustic excitation amplitudes, the acoustic behavior of the plate becomes amplitude dependent, *i.e.* non-linear. Higher-order harmonics are generated. The model is used to gain insight into the impact of the complex evolution of the vortex shedding as a function of the amplitude and frequency.

Contribution IV. *This thesis investigates a bias flow liner with film cooling obtained with a micro-slit plate in the linear and non-linear regime.*

In aero-engine liners and combustion chambers of gas turbines, perforated liners are used to provide film cooling of the walls. These liners can also mitigate the rising of thermo-acoustic instabilities by damping acoustic energy. A bias flow through the orifices impacts the absorption characteristics of the liner.

Contribution V. *A simple and powerful lumped-element model is proposed to analyze the sound absorption properties of a single-degree-of-freedom liner.*

In practical applications, a micro-slit plate is backed by a cavity forming a single-degree-of-freedom absorber. The sound absorption of the absorber is strongly influenced by the acoustic transfer impedance of the plate.

1.10 Outline of the thesis

The present thesis is organized into separate chapters, schematized in Figure 1.6. **Chapter 2** proposes a model for the acoustic behavior of slits in micro-slit plates. The influence of the geometry of rectangular micro-slits on the acoustic behavior of the plate in the linear regime is discussed. The numerical solution of the Linearized Navier-Stokes equations is compared to analytical results. **Chapter 3** focuses on a micro-slit geometry inspired by cutting and punching the plate. The effect of the length of the slits on the acoustic response in the linear and non-linear regimes is investigated using impedance tube experiments, numerical simulations, and analytical limits.

Chapter 4 extends the study of the acoustic behavior of the plate in the non-linear regime, using numerical simulations to gain physical insight into the findings of the experiments. In **Chapter 5**, the potential of this slit geometry as a bias flow liner is explored at low amplitude (linear response). Numerical simulations are compared to impedance tube experiments in the presence of a bias flow. **Chapter 6** investigated the enhancement of the absorption capability of the plate due to a bias flow in environments with medium and high acoustic-excitation amplitudes. **Chapter 7** brings the findings in this thesis together and proposes a lumped-element model to discuss the sound absorption properties of micro-slit plates in single-degree-of-freedom liners. **Chapter 8** summarizes the general conclusions of this thesis, in combination with recommendations for future work. **Appendix A.1** represents the first step towards shape optimization of a flexible micro-slit plate. The other appendices contain complementary information to the chapters.

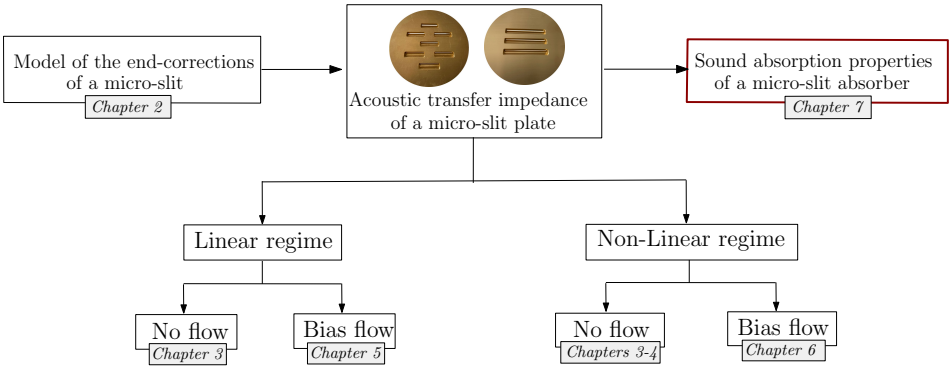

Figure 1.6. Schematic overview of the present thesis.

2

Influence of geometry on acoustic end-corrections of slits in micro-slit plates

Abstract - In this Chapter, the acoustic behavior of individual slits within micro-slit absorbers (MSAs) is investigated to explore the influence of porosity, edge geometry, slit position, and plate thickness. MSAs are plates with arrays of slit-shaped perforations, with the height of the order of the acoustic viscous boundary layer thickness, for optimized viscous dissipation. Due to hydrodynamic interaction, each slit behaves as confined in a rectangular channel. The flow within the slit is assumed to be incompressible. The viscous dissipation and the inertia are quantified by the resistive and the inertial end-corrections. These are estimated by using analytical results and numerical solutions of the Linearized Navier-Stokes equations. Expressions for the end-corrections are provided as functions of the ratio of the slit height to viscous boundary layer thickness (Shear number) and of the porosity. The inertial end-correction is sensitive to the far-field behavior of the flow and low porosities strongly depend on the porosity, unlike circular perforations. The resistive end-correction is dominated by the edge geometry of the perforation. The relative position of the slit with respect to the wall of the channel is important for distances to the wall of the order of the slit height. The plate thickness does not have a significant effect on the end-corrections.

This Chapter is based on:
A. Aulitto, A. Hirschberg, and I. Lopez Arteaga (2021). Influence of geometry on acoustic end-corrections of slits in micro-slit absorbers. The Journal of the Acoustical Society of America, 149(5), 3073-3085.

2.1 Introduction

Microslit absorbers and plates (MSAs, MSPs) have been proposed by Maa as sound absorbers at low frequencies, providing light-weight and compact solutions to substitute conventional materials, such as absorptive foams and porous structures [51]. In simple MSAs, the plate, consisting of an array of slit-like perforations, is mounted with a shallow or sub-partitioned backing cavity. Alternative designs of MSAs have been recently reported in the literature [55, 56, 95, 96]. MSAs have several advantages with respect to micro-perforated plates (MPPs) with circular perforations. Using slits, one can obtain a relatively large porosity, resulting in a higher Helmholtz resonance frequency when needed. For equal porosity, a single slit replaces several circular perforations. Furthermore, a slit can delimit flexible structures whose vibration can contribute to sound absorption [55, 56]. Compared to the literature on circular perforations, fewer publications investigate the acoustic properties of slit-like perforations. Maa [51] states that no theory is available to predict inertial end-correction. The same viscous dissipation as for circular perforations is assumed. In his work, Maa [51], assumes radiation to free space for each slit. The inertial end-correction model fails. This failure is solved when taking the confinement into account as a consequence of the hydrodynamic interaction between slits. Ingard [97] obtains a solution for high Shear numbers, assuming a uniform flow in the slit and matching the resulting rigid piston oscillation model to a modal expansion of the flow in the confinement channel. Correct expressions for the inertial end-corrections, without typos, are presented by Jaouen and Chevillotte [98]. The same model is used by Kristiansen and Vigran [99]. Another model, based on a locally incompressible potential flow with a thin boundary layer, is proposed by Morse and Ingard [100], for an abrupt transition with sharp square edges. This model yields both inertial and resistive end-corrections in the limit of high Shear numbers. For a slit in an infinitely thin plate, the same approach does predict an inertial end-correction. However, the singularity of the potential flow, at the edge of an infinitely thin plate, results in a divergence of the resistive end-correction. Morse and Ingard [100] propose to introduce a finite plate thickness to avoid this problem. The divergence of the resistive end-correction due to the singularity, at the edge of an infinitely thin plate, suggests that the viscous dissipation is a local effect, strongly influenced by the edge geometry. Recent studies on circular perforations confirm the importance of edges on the viscous dissipation [23, 25, 101]. One concludes that there is a lack of a complete model to describe the acoustic behavior of slits. For instance, both Ruiz *et al.* [102] and Cobo [53] state that all the models proposed in the literature do not fit experimental absorption curves of MSPs. Therefore, the goal of the present work is to complement the theoretical knowledge concerning the acoustical properties of micro-slits. In particular two effects appear to be ignored in the literature for slits: the influence of the position of the slit within the confinement channel and the influence of the edge shape. For a circular perforation, Temiz *et al.* [23] observe

that chamfering the edges reduces the effective plate thickness t_{eff} by a length of the order of the total length of the chamfers. A non-symmetric position of the slit within the confinement channel can be found when the periodicity of the array is not perfect or in the case of a sub-partitioned back cavity.
In the present work, a combination of analytical models and numerical solutions of the incompressible Linearized-Navier Stokes equations is proposed. In Section 2.2, two-dimensional analytical models are developed. In Section 2.3, the numerical models and solutions of the incompressible Linearized Navier-Stokes equations (LNSE) using Comsol [94] are described. In Section 2.4, analytical and numerical results are compared. Findings are summarized in Section 2.5.

2.2 Theory

2.2.1 Definition of the problem

Microslit plates (MSPs) are plates with arrays of slit-like perforations with height b in the sub-millimeter range and width $w >> b$. The plate thickness t_p is of the order of magnitude of the slit height. The acoustic properties of MSPs are defined by the porosity $\Phi = b/a$, with a the distance between neighboring slits. The hydrodynamical interaction between neighboring slits in the array can be described by considering a single slit of height b, confined within a channel of height a of rectangular cross-section aw given by the distance a between neighboring slits and the lateral width w of the slit. At the open front side of the MSA, the confinement channel represents the hydrodynamic interaction between neighboring slits. The confinement channel on the cavity side is resulting from physical walls in the case of a sub-partitioned cavity or is due to hydro-dynamical interactions. As illustrated in Figure 2.1, for a periodic array of slits, the confinement channel is placed symmetrically with respect to the slit.

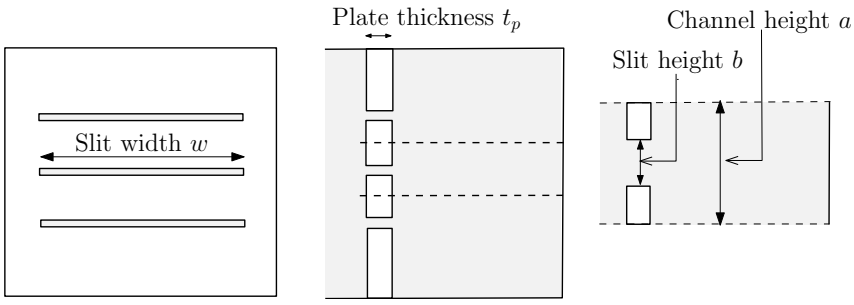

Figure 2.1. On the left, frontal view of the micro-slit plate with slit width w. In the middle, lateral view of the micro-slit plate of thickness t_p with a back cavity. On the right, a single slit of height b with confinement channel of height a.

Assuming a long slit ($w >> b$) implies that one can consider a two-dimensional ($2D$) acoustical flow through the slit. As the slit forms the neck of a Helmholtz resonator with a portion of the back cavity as volume, the flow within the slit can be considered as locally incompressible up to the first resonance frequency of the resonator, $\omega_H = c\sqrt{\Phi/(d_c t_{eff})}$, with c the speed of sound, d_c the back cavity depth and t_{eff} the effective neck length.
In the audio range, the square of the Helmholtz number is small, *i.e.* $He^2 = \left(\frac{\omega b}{c}\right)^2 < 10^{-1}$. Thermal effects in the slit are neglected. In the configuration in Figure 2.1, thermal effects appear on the solid back wall and the front and back sides of the plate. In the confinement channel, the viscous and thermal effects are of the same order of magnitude. The viscous dissipation per unit surface in the perforation increases quadratically with the inverse of the porosity because the velocity increases as the inverse of the porosity and the dissipation are quadratic in the velocity. The temperature fluctuations and thermal dissipation in the perforations are (per unit surface) of the same order of magnitude as that in the confinement channel. Therefore viscous dissipation is in the perforation a factor $(1/\Phi)^2$ larger than thermal dissipation. The thermal boundary layer is described by the classical high Shear number model of Landau and Lifshitz [103]. Thermal effects within the perforations are negligible compared to those on the back wall and the surface of the plate, because of the small porosity [25], in fact, the thermal dissipation on the back wall and the two sides of the perforated plate appears to be negligible compared to the viscous dissipation in the pore (for sufficiently small porosities) as demonstrated by Billard *et al.* [25]. The discussion is limited to the normal incidence of acoustic waves. One can describe the transition between the slit and the confinement channel by assuming over the plate thickness t_p an ideal 2D parallel flow for a long slit of height b extended over a so-called end-correction length. The extrapolation of the linear dependency of the acoustic pressure as a function of the distance from the slit opening in both the slit and the confinement channel is used to define the end-corrections. There is a resistive end-correction δ_{res} and an inertial end-correction δ_{in} corresponding to the pressure components $Re[\hat{p}]$ and $\mathrm{Im}[\hat{p}]$, respectively in phase with the volume flow oscillation $\hat{U}e^{(i\omega t)}$ and in phase with the time derivative of the volume flow oscillation. The inertial end-correction determines the Helmholtz resonance frequency, as shown in Zielinski *et al.* [56]. Assuming the same geometry on the front and backside of the plate, the effective neck length of the perforation is given by $t_{eff} = t_p + 2\delta_{in}$. The resistive end-correction takes into account the viscous dissipation and influences the quality factor of the Helmholtz resonance. To optimize viscous dissipation, the slit height is chosen to be of the order of magnitude of the acoustical viscous boundary layer thickness $\delta_v = \sqrt{2\nu/\omega}$, where ν is the kinematic viscosity of air and $\omega = 2\pi f$, with f the frequency. Hence, for typical applications, the Shear number $Sh_b = b/\delta_v$ is of order unity. The range $0.05 < Sh_b < 20$ is considered. As the plate thickness and end-corrections in MSPs are both of the order of the slit height, it is important to obtain an accurate prediction of end-corrections to design the absorbers.

2.2.2 Parallel flow

An analytical model for the flow in a long slit of height b is used as a reference to define the end-corrections and to define low and high Shear number limits. It is also used to assess the accuracy of the numerical solution of the incompressible Linearized Navier-Stokes equations. At low Helmholtz numbers ($He^2 = (\omega b/c)^2 << 1$), in absence of main flow, the acoustic field is considered incompressible and is described by the equation of continuity

$$\nabla \cdot \boldsymbol{v} = 0 \tag{2.1}$$

and the linearized equation of motion

$$\rho \frac{\partial \boldsymbol{v}}{\partial t} = -\nabla p + \eta \nabla^2 \boldsymbol{v}, \tag{2.2}$$

where $\boldsymbol{v}$ is the velocity vector, p is the pressure fluctuation, ρ density of the air is assumed to be uniform and constant and η is the dynamic viscosity. In a long thin slit of height b, width $w >> b$ and length $t_p >> b$, for $0 < x < t_p$ and $-b/2 < y < b/2$, the flow can be approximated by a 2D parallel flow $\boldsymbol{v} = (u(y,t), 0, 0)$. The continuity equation (Equation 2.1) implies, in a two-dimensional parallel flow, that

$$\frac{\partial u}{\partial x} = 0. \tag{2.3}$$

Hence, the derivative with respect to x of the $x-$component of the equation of motion (Equation 2.2) implies

$$\frac{\partial^2 p}{\partial x^2} = 0, \tag{2.4}$$

i.e. the pressure is given by a linear function of the $x-$coordinate. The $y-$ and $z-$components of the equation of motion reduce to

$$\frac{\partial p}{\partial y} = \frac{\partial p}{\partial z} = 0. \tag{2.5}$$

This results in a uniform pressure in a cross-section of the slit. Consequently one has

$$\frac{\partial p}{\partial x} = \Delta p / t_p, \tag{2.6}$$

with $\Delta p = p(t_p, t) - p(0, t)$. For a harmonic oscillation $\Delta p = \Delta \widehat{p} e^{i\omega t}$ the flow profile satisfying the no-slip boundary condition $(u, v) = (0, 0)$ on the slit walls $y = \pm b/2$ is

$$u(y,t) = \widehat{u} e^{i\omega t} = -\frac{i}{\rho\omega} \frac{\Delta \widehat{p}}{t_p} \left[1 - \frac{\cosh\left(\frac{(1+i)}{\delta_v} y\right)}{\cosh\left(\frac{(1+i)}{2\delta_v} b\right)} \right] e^{i\omega t}. \tag{2.7}$$

The cross-sectional averaged amplitude of the velocity $< \widehat{u} >$ is

$$< \widehat{u} >= \frac{1}{b}\int_{-b/2}^{b/2} \widehat{u} dy = -\frac{i}{\rho\omega}\frac{\Delta\widehat{p}}{t_p}\cdot\left[1 - \frac{2}{(1+i)Sh}\tanh\left(\frac{(1+i)}{2}Sh\right)\right]e^{i\omega t}, \quad (2.8)$$

with $Sh_b = b/\delta_v$, the Shear number. The slit impedance Z_b is defined as by Morse and Ingard [100]:

$$Z_b = \frac{\Delta\widehat{p}}{wb < \widehat{u} >}. \quad (2.9)$$

At low Shear numbers $Sh_b < 1$, one can use the approximation

$$Z_b \approx \frac{12\eta t_p}{(wb)b^2} + i\frac{6}{5}\frac{\rho\omega t_p}{(wb)}. \quad (2.10)$$

One recognizes in the real part of Z_b the resistance corresponding to a parabolic flow (quasi-steady Poiseuille flow approximation). At high Shear numbers $Sh_b >> 1$, one has

$$Z_b \approx \frac{\rho\omega t_p}{(wb)Sh} + i\frac{\rho\omega t_p}{(wb)}\left(1 + \frac{1}{Sh}\right). \quad (2.11)$$

The first addend of the imaginary part corresponds to the inertia of a uniform flow, which is a factor 6/5 lower than that of a parabolic flow (see Equation 2.10). The time-averaged viscous dissipation $\bar{P}_W$ in the slit is given by Morse and Ingard [100]:

$$\bar{P}_W = \frac{1}{2}\mathrm{Re}[Z_b]| < \widehat{u} > |^2(wb)^2. \quad (2.12)$$

For $Sh_b >> 1$ using Equation 2.11 one has

$$\bar{P}_W = \frac{1}{2}\rho\omega\delta_v| < \widehat{u} > |^2 wt_p. \quad (2.13)$$

This thin boundary layer approximation is used in Section 2.2.5 for channels with non-uniform height. In this limit, the flow in the boundary layer is quasi-parallel along the wall. Therefore, one can use the dissipation per unit surface found in Equation 2.13 when replacing $| < \widehat{u} > |$ by the amplitude of the tangential velocity $|\widehat{u}_{tan}|$ prevailing just outside the viscous boundary layer. By integration over the surface, one obtains the total dissipation. This tangential velocity corresponds to that of a frictionless potential flow. This will be referred to as the high Shear number limit or the thin boundary layer limit. Alternative derivations of this thin boundary layer equation are provided in literature [100, 104–106]. As explained by Morse and Ingard [100], this approximation fails for infinitely thin orifice plates. While Morse and Ingard [100] suggest that the approximation is valid for sharp square edges, the numerical integration of the Linearized Navier-Stokes equations will allow us to verify this assumption.

2.2.3 Impedance and end-corrections

A formal definition of impedance and end-corrections is provided. Consider the transition from a slit of height b to a channel of height $a > b$. In an ideal configuration, the transition from the slit to the channel is abrupt: the flow can be described as a piece-wise parallel flow. Hence, the effective thickness of the plate is equal to the actual thickness. In the actual flow, the transition from the slit to the channel is smooth. Hence, the effective thickness of the plate is larger than the physical thickness of the plate, with the effective thickness $t_{eff} = t_p + \delta$, where δ represents the so-called end-corrections. Far from the transition, one can observe a linear change in the amplitude of the pressure as a function of the distance from the slit opening. This corresponds to a parallel flow in a slit of height b and a confinement channel of height a. This far field can be extrapolated at each side of the transition towards the plate surface at $x = 0$ (slit opening). The complex pressure amplitude difference $\Delta\widehat{p}_t$ obtained across the transition by this extrapolation divided by volume flux amplitude $\widehat{U} =< \widehat{u} > bw$ is the transition impedance Z_t. The inertial end-correction δ_{in} and the resistive end-correction δ_{res} are defined by

$$\delta_{in} = \frac{\mathrm{Im}\left[Z_t\right]}{\mathrm{Im}\left[\frac{dZ_b}{dt_p}\right]}, \tag{2.14}$$

$$\delta_{res} = \frac{\mathrm{Re}\left[Z_t\right]}{\mathrm{Re}\left[\frac{dZ_b}{dt_p}\right]}. \tag{2.15}$$

The value of Z_b is calculated by combining Equation 2.8 and Equation 2.9. The resistive end-correction δ_{res} is in principle different from the inertial end-correction δ_{in}. In this work, the inertial and resistance end-correction of Morse and Ingard [100] will be used as a reference. One has

$$\mathrm{Im}[Z_{t,ref}] = \frac{\rho\omega}{\pi w}\left[\frac{(1-\Phi)^2}{2\Phi}\ln\frac{(1+\Phi)}{(1-\Phi)} + \ln\frac{(1+\Phi)^2}{4\Phi}\right], \tag{2.16}$$

$$\mathrm{Re}[Z_{t,ref}] = \frac{\rho\omega}{2aShw}(1-\Phi)\left[1 + \frac{(1-\Phi^2)}{\pi\Phi}\ln\frac{(1+\Phi)}{(1-\Phi)}\right]. \tag{2.17}$$

The reference end-corrections, $\delta_{in,ref}$ and $\delta_{res,ref}$, can be calculated by replacing $\mathrm{Im}[Z_{t,ref}]$ and $\mathrm{Re}[Z_{t,ref}]$ in Equation 2.14 and Equation 2.15. For low porosity, the inertial end-correction becomes $\delta_{in,limit}/b = (1 - \ln(4\Phi))/\pi$. The inertial end-correction becomes infinitely large for vanishing porosity. This divergence can be avoided when taking into account the influence of the flow compressibility as in Lesser and Lewis[107]. The resistive end-correction increases with decreasing porosity but reaches an asymptote $\delta_{res,limit}/b = (\pi + 2)/(2\pi)$ for $\Phi \to 0$. In Figure 2.2 values of the inertial and resistive end-corrections obtained from the literature for perforations with sharp edges are shown as a function of the inverse

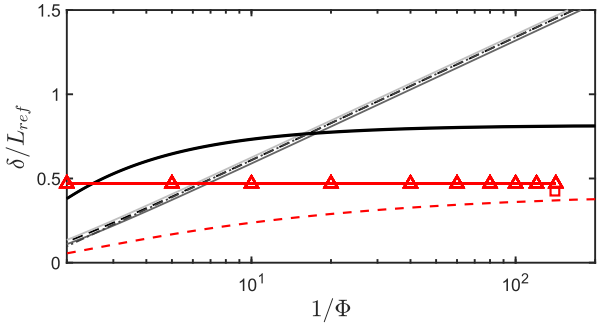

Figure 2.2. Comparison of end-corrections for sharp-edged slit ($L_{ref} = b$) and circular perforation ($L_{ref} = d_p$) from the literature. Inertial end-corrections δ_{in} for slits (MSPs): (- - -) High Sh_b number limit for a slit in an infinitely thin plate [100], (——) Modal expansion [97], (——) Thin boundary layer for square edged transition in channel [100]. (——) Resistive end-correction δ_{res} for square edged transition in channel [100]. (- - -) Inertial end-correction for circular perforations [108]. Resistive end-correction for circular perforations with (□) [23] and (–△) [24].

of the porosity $1/\Phi = a/b$. Results for circular perforations are also displayed. A critical discussion of these data is provided by Kergomand and Garcia [109]. The reference length L_{ref}, in Figure 2.2 refers either to the height b for slits or to the perforation diameter d_p.
It can be noted that the various results at high Sh_b numbers for the inertial end-corrections for slits, including the value for an infinitely thin plate, are in close agreement. This indicates that at high Shear numbers, the plate thickness has a minor effect on the inertial end-correction. For a circular perforation, the finite limit value from Maa [21] $\delta_{in,\Phi\to 0} = 0.41 d_p$ is found. For circular perforation, resistive and inertial end-corrections are of the same order of magnitude. It should be noted that for relevant porosities all end-corrections are of the order of L_{ref} (either b or d_p). For a given plate impedance, the normal incidence absorption of a micro-slit plate backed by a cavity with depth d can be calculated as shown, for example, in Zielinski *et al.* [56].

2.2.4 Modal expansion

In this subsection, the frictionless modal expansion proposed by Ingard [97] is used to derive an expression for the inertial end-correction. Given an arbitrary velocity profile at the end of the slit, it is possible to derive the inertial end-correction by matching this velocity profile with an expansion in modes of the confinement channel. Outgoing plane wave and evanescent transversal modes are considered.

Kergomand and Garcia [109] discuss the convergence of the modal expansion. When using the rigid piston approximation in the slit the number of modes used in the channel should be of the order of the inverse of the porosity [106], $1/\Phi = a/b$. An expression of the inertial end-correction for low the Sh_b number is obtained by assuming a parabolic flow (see Section 2.2.2) at the end of the slit. This is used as input for the frictionless modal expansion of the acoustic pressure in the channel. One finds:

$$\delta_{in} = \frac{5}{6}\sum_{n=1}^{\infty}\frac{3}{2n\pi}\left(\frac{a}{n\pi b}\right)^3\left\{4\cos^2(n\pi)\cdot \left[\cos\left(\frac{n\pi b}{a}\right) - \frac{a}{bn\pi}\sin\left(\frac{n\pi b}{a}\right)\right]\sin\left(\frac{n\pi b}{a}\right)\right\}. \quad (2.18)$$

Several modes of the order of $N_m = 3(a/b)$ are sufficient to reach a reasonable accuracy. For the asymmetric case, the influence of the position of the slit with respect to the wall is investigated. In Figure 2.3, the transition from an asymmetric slit to a channel is displayed. The slit height is $b = b_1 + b_2$, the channel height is $a = a_1 + a_2$. The geometry is chosen such that $(a/b) = (a_1/b_1) = (a_2/b_2)$. In the limit case of a slit sharing the flat wall with the channel, one has $a_2 = 0$ or $a_1 = 0$. The vertical positions of the slit edges (at $x = 0$) are $y_1 = a_1(1 - b/a)$ and $y_2 = a - a_2(1 - b/a)$. Assuming at the end of the slit a uniform acoustic velocity amplitude and expanding the amplitude of the pressure in frictionless modes in the channel one finds:

$$\delta_{in} = \sum_{n=1}^{\infty}\frac{2}{n\pi}\left\{\frac{\left[\sin\left(\frac{n\pi y}{a}\right)\right]_{y_1}^{y_2}}{\frac{n\pi b}{a}}\right\}. \quad (2.19)$$

In the symmetric case, $a_1 = a_2$ one finds the result of Ingard [97], where $n = 2m$. The sum is limited to even values of n. The influence of the position of the slit on the inertial end-correction is discussed in Section 2.4.3

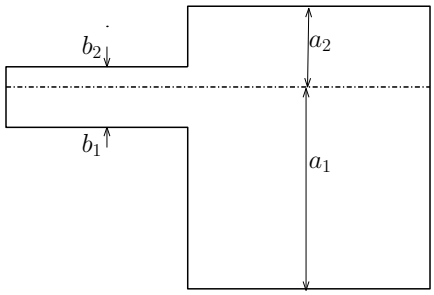

Figure 2.3. Geometry of the asymmetric slit of height $b = b_1 + b_2$ emerging in a channel of height $a = a_1 + a_2$.

2.2.5 Thin boundary layer approximation

For the high Sh_b range, the viscosity effects are concentrated in a thin boundary layer at the wall and do not impact the main, potential flow. The incompressible potential flow theory combined with the thin boundary layer approximation proposed by Morse and Ingard [100] can be used. A generalization of this model is presented by Berggren *et al.* [105]. In the present work, this approximation is used to investigate the end-corrections for smooth edges and asymmetric slit sharing the flat wall with the confinement channel. It is also used to explore the effect of viscous friction along the confinement channel walls (in the case of a partitioned back cavity). The smooth edge geometry is obtained using the conformal transformation introduced by Henrici [110] (Appendix B.1 for details). An analytical solution is proposed in Appendix B.1 for a smooth transition, providing a generalization of the results of Morse and Ingard [100] for sharp edges (Equation 2.16-2.17). In Figure 2.4, a 2D slit of height b in $x < 0$ and a 2D channel of height $a > b$ in $x > 0$ are shown. The end of the uniform slit (point B in Figure 2.4) is at $(x, y) = (-d, a - b)$, with d being the transition length. The uniform confinement channel begins at $x = 0$ (point C in Figure 2.4. The duct can be associated with a region in the complex $z-$plane by $z = x + iy$, with $i^2 = -1$ and spatial coordinates (x, y). Using conformal mapping, the flow region in the duct can be mapped into the upper half-plane in the complex $\zeta-$plane. The mapping of the contraction is a modified Schwarz-Christoffel transformation introduced by Henrici and Hirschberg *et al.* [110, 111]. The differential form of Henrici's transformation is

$$\frac{dz}{d\zeta} = \zeta^{-1}\left[\alpha(\zeta - 1)^{1/2} + \beta(\zeta - G^2)^{1/2}\right] \cdot (\zeta - G^2)^{-1/2}, \tag{2.20}$$

where α, β, and G are parameters of the transformation depending on the slit and channel heights and on the transition length d.

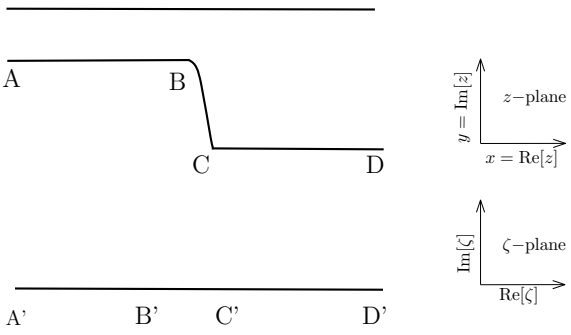

Figure 2.4. Henrici's transformation of half the channel with a smooth transition from the slit to the channel in the physical plane $z = x + iy$ to the $\zeta-$plane. Coordinates of the points: $A(-\infty; (a + b)/2)$, $B(-d; (a + b)/2)$, $C(0, 0)$, $D(\infty; 0)$.

The parameters α and β are functions of the parameter G obtained numerically as the solution of a non-linear equation. Details are discussed in Appendix B-1. The equation for the sharp square edge transition is recovered for $d = 0$. Using the thin boundary layer approximation one can find the real and imaginary part of the impedance of the transition Z_t and the corresponding inertial and resistive end-corrections. Formulas are provided in Appendix B.2.
A similar approach can be followed for a fully asymmetric slit, presented in Figure 2.3. When $a_2 = 0$, the slit and the confinement channel share the flat wall. One has to add the dissipation of the flat wall, shared by the slit and the channel. This will be done by modifying the limits of integration when calculating the total dissipation along the walls (Appendix B.2). When the confinement channel walls are representing the influence of hydrodynamic interaction, the flow at the channel walls is frictionless. This can also be taken into account by simply modifying the integration limit when integrating to calculate the dissipated power. Details are in Appendix B.2. Parameters such as G are obtained numerically by solving a non-linear equation. The analytical solution for sharp edges can be used as an initial guess for small values of the transition length d. Then the parameter d can be increased using the previous value of G as an initial guess in an iteration process. Given G, in the symmetrical case, a fully analytical final solution is obtained. In other cases, a numerical integration remains to be carried out.

2.3 Numerical model

2.3.1 Uniform channel

Consider a uniform channel of height b and length t_p, with $t_p >> b$.
The x-axis goes from $x = 0$ to $x = t_p$. The y-axis extends between the walls at $y = \pm b/2$. As stated in Section 2.2.1, the low He number approximation is made. The incompressible harmonic linearized Navier-Stokes equations for a 2D domain in a dimensionless form are

$$\frac{\partial u^*}{\partial x^*} + \frac{\partial v^*}{\partial y^*} = 0, \tag{2.21}$$

$$iu^* = -\frac{\partial p^*}{\partial x^*} + \frac{1}{2Sh^2}\left(\frac{\partial^2 u^*}{\partial {x^*}^2} + \frac{\partial^2 u^*}{\partial {y^*}^2}\right), \tag{2.22}$$

$$iv^* = -\frac{\partial p^*}{\partial y^*} + \frac{1}{2Sh^2}\left(\frac{\partial^2 v^*}{\partial {x^*}^2} + \frac{\partial^2 v^*}{\partial {y^*}^2}\right), \tag{2.23}$$

with $x^* = x/b$ and $y* = y/b$. The dimensionless velocity (u^*, v^*) is $(u/b\omega, v/b\omega)$ and the dimensionless pressure is $p^* = p/(\rho(b\omega)^2)$. These equations are implemented in *Comsol Multiphysics* as user-defined equations (PDE) and solved. At the inlet ($x^* = 0$) and at the outlet ($x^* = t_p/b$) of the domain the uniform pressure values are imposed: respectively, $p^*_{inlet} = 1$ and $p^*_{outlet} = 0$.

At the walls ($y^* = y/b = \pm 1/2$) no-slip boundary conditions, $(u^*, v^*) = (0, 0)$ prevail. An unstructured mesh of quadratic triangular elements is used, with the finest mesh at the walls. The density of elements at the walls depends on the Sh_b number: the element sizes at the wall are $0.2/Sh$ or less, to accurately capture the viscous boundary layer. Several checks are performed to gain insight into the accuracy of the numerical simulations. Firstly, the computational domain length t_p is increased to exclude an influence of the channel length on the transition impedance. It appears that the quantity $U_L = Ut_p/t_{ref}$, with U being the flux in a cross-section of the channel and $t_{ref} = 6b$, is constant within a relative deviation of 10^{-5} for $0.5 < t_p/t_{ref} < 2$. Secondly, a mesh convergence study is performed and shows convergence to computer accuracy (10^{-13}). For this study, three additional meshes are used: one coarser and two finer meshes respectively with half, two, and four times the basic number of elements at the wall. To compare the results, the cross-sectional average velocity $< \widehat{u^*} >= \int_0^{b^*} \widehat{u^*} dy^*$ is used. Comsol [94] performs the integration element-wise using numeric quadrature of the 4^{th} order. The cross-sectional average velocity in the channel obtained with the numerical simulations shows a deviation of 10^{-4} from the analytical solution for the parallel flow in an infinitely long channel, discussed in Section 2.2.2.

2.3.2 Change in cross-section with sharp square edges

The set of Equations 2.21-2.23 is used to study the channel in Figure 2.5 presenting at $x^* = 0$ a sharp square-edged transition from a uniform height b^* to a uniform height $a^* > b^*$. The channel extends from $x^* = -t_b^*$ to $x^* = t_a^*$, with $t_a^* = 6a/b$ and $t_b^* = t_a^*/2$. The symmetry of the problem allows limiting the numerical domain to half the channel. For the inlet segment AF and outlet segment DE constant pressures are imposed, $p_{AF}^* = 1$ and $p_{DE}^* = 0$. At segments AB and BC, no-slip boundary conditions are applied. At segment EF (symmetry axis) slip boundary conditions are implemented, $\partial u^*/\partial y^* = 0$ and $v^* = 0$. The effect of the boundary condition on the walls is investigated. When considering a confinement channel due to hydrodynamic interaction, the slip boundary condition is used on segment CD. Far from the transition located at $x^* = 0$ the acoustic pressure is uniform in the cross-section and the amplitude of the pressure depends linearly on the

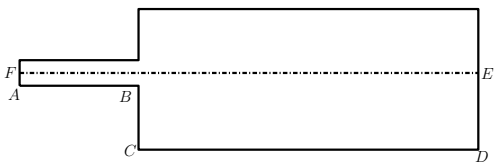

Figure 2.5. Geometry of a channel with the sudden transition from the slit of height b to the channel of height a.

position along the duct (parallel flow behavior). One has

$$\begin{cases} \widehat{p^*}(x) = \widehat{A}x^* + \widehat{B}, & \text{for } -2a^* < x^* < -1a^* \\ \widehat{p^*}(x) = \widehat{C}x^* + \widehat{D}, & \text{for } 3a^* < x^* < 5a^* \end{cases} \tag{2.24}$$

The complex constants can be determined by a linear fit of the pressure data obtained by numerical simulations for these regions far from the discontinuity. The linear fit gives a coefficient of determination $1 - R^2 = 10^{-6}$ [112]. The impedance Z_t of the transition is determined by

$$Z_t = \frac{\widehat{B} - \widehat{D}}{\widehat{U}^*} \tag{2.25}$$

with $\widehat{U}^*$ being the flux calculated in a generic section of the slit far from the discontinuity, defined as $\widehat{U}^* = w < \widehat{u^*} > b$. For a height ratio $a/b = 10$ and $Sh_b = 20$, in the proximity of the edges, the maximum element size is $M_{el}/b = 2 \times 10^{-2}$ and the minimum is $m_{el}/b = 7 \times 10^{-4}$. The original mesh chosen for the standard calculations has a total of 13324 total elements, of which 804 are edge elements (at the walls). For a porosity $\Phi = b/a = 1/10$ at $Sh_b = 20$, numerical simulations show that the effect of the boundary condition at the lower wall of the channel is negligible. This confirms that the dissipation is mainly concentrated inside the slit and around the edges. In the assumption of locally incompressible flow, the volume flux along the duct axis is constant. This is verified numerically with a maximum relative deviation of 10^{-4}. The coefficients $\widehat{A}$ and $\widehat{C}$ of the linear fittings of $\widehat{p^*}$ can be compared to the theoretical values of the $\Delta\widehat{p^*}/t^*$ for the parallel flow in a long channel, respectively of height b and a. The discrepancy is in the order of 10^{-4}. The accuracy in the calculation of the volume flux is the limiting factor for the global accuracy of the numerical model.

2.4 Results

2.4.1 Symmetrical slit with sharp square edges

End-corrections at low and high Sh_b number

In this subsection, the end-corrections for a sharp square-edged transition derived from the numerical simulations are compared with the analytical solutions proposed in Section 2.2. An overview of the behavior of the end-corrections in the range $0.05 < Sh < 20$ is shown in Figure 2.6. In Figure 2.6 the behavior of δ_{in}/b and δ_{res}/b is shown as a function of the Shear number and for several porosity values. The Shear number range is divided into a low Sh_b range ($Sh_b < 0.6$) and a high Sh_b range $0.6 < Sh < 20$ and the two ranges are discussed separately in the next subsections. For low Shear numbers, the inertial end-correction can be calculated using the oscillating parabolic flow approximation. For high Shear numbers,

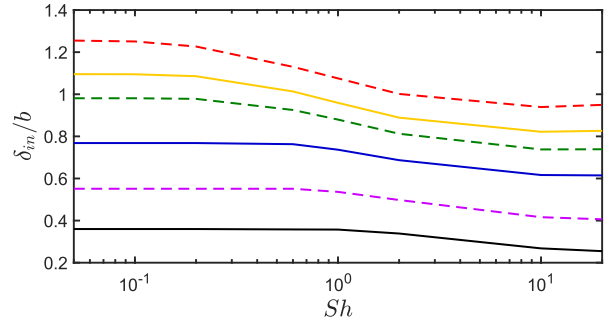

(a)

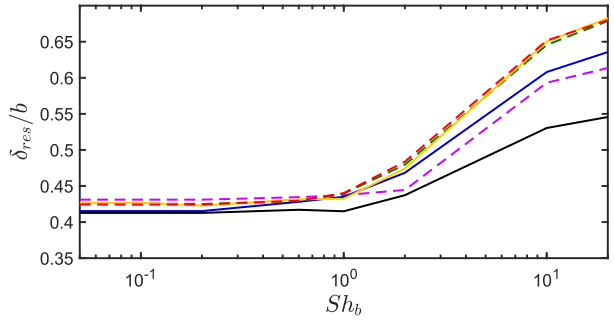

(b)

Figure 2.6. Behavior of a) δ_{in}/b and b) δ_{res}/b from the numerical simulations as function of the Sh_b number for several porosities: (——) $1/\Phi = 3$, (- - -) $1/\Phi = 5$, (——) $1/\Phi = 10$, (- - -) $1/\Phi = 15$, (——) $1/\Phi = 20$,(- - -) $1/\Phi = 30$.

the modal expansion of Ingard [97] and the thin boundary layer approximation of Morse and Ingard [100], (Section 9.1, pages 483-490) are used. The inertial end-correction calculated using modal expansion with the parabolic flow approximation is about twice the value for uniform flow. In Figure 2.7 the comparison between the numerical, the modal expansion, and thin boundary layer approximation, are shown as a function of the inverse of the porosity Φ. The numerical results are obtained for a $Sh_b = 0.05$ and for $Sh_b = 20$. At low Shear numbers, the Poiseuille flow approximation is used. At high Shear numbers, the thin boundary layer approximation and the plane piston model are compared. It appears that the parabolic (Poiseuille) flow approximation captures well the behavior of the inertial end-correction for $Sh_b = 0.05$, while the rigid piston and thin boundary layer models are in good agreement with the result for $Sh_b = 20$.

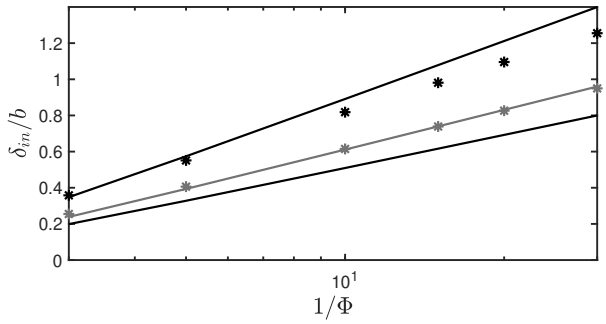

Figure 2.7. Comparison of inertial end-correction δ_{in} as functions of $1/\Phi$: (——) Parabolic flow approximation, (——) Uniform flow approximation [97]. (——) High Sh_b number limit [100]. Stars refer to the results of numerical calculations for $*$ $Sh_b = 0.05$ and $*$ $Sh_b = 20$.

End-corrections at Low Sh_b number

For $Sh_b < 0.6$, the dimensionless inertial end-correction δ_{in}/b and the resistive end-correction δ_{res}/b are functions of the porosity and, to a much lesser degree, of the Sh_b number. The dependency of the end-corrections on Sh_b is therefore neglected for low Shear numbers. The dependency of δ_{res}/b on both porosity and the Sh_b number is negligible. The following fits are proposed:

$$\frac{\delta_{in,fit}}{b} = -2.17 + 2.18\left(\frac{1}{\Phi}\right)^{0.13}, \qquad \frac{\delta_{res,fit}}{b} = 0.425, \tag{2.26}$$

for $Sh_b < 0.6$ and $3 < 1/\Phi < 30$. The coefficient of determination [112] $1 - R^2$, describing the quality of the fit, for δ_{in}/b is 0.997. The choice of the fit for δ_{res}/b results is a maximum underestimation of the actual value of 2.5%. The negligible effect of the porosity on δ_{res}/b indicates again that the dissipation is a local effect at the sharp edges.

End-corrections at high Sh_b number

In the region $0.6 < Sh < 20$ the deviations of δ_{in} and δ_{res} from the high Sh_b limits $\delta_{in,ref}$ and $\delta_{res,ref}$ (described in Section 2.2.3 and calculated for the same Shear number value as the numerical simulation), predicted by Morse and Ingard [100], have been obtained (see Appendix B.2). Proposed fits of the numerical results are:

$$\frac{\delta_{in}}{\delta_{in,ref}} - 1 = \frac{C_1}{C_2 + Sh}, \tag{2.27}$$

$$\frac{\delta_{res}}{\delta_{res,ref}} - 1 = \frac{C_3}{Sh\,(C_4 + Sh)}, \tag{2.28}$$

$$\text{with } C_i = D_{i,1} + D_{i,2} \cdot (\Phi)\,. \tag{2.29}$$

From Equation 2.29, it appears that the coefficients C_i are linear functions of the porosity. Table 2.1 provides the values of the coefficients $D_{i,j}$.

Table 2.1. Values of the coefficients for the fitting in the range $0.6 < Sh < 20$.

	C_1	C_2	C_3	C_4
First coefficient $D_{i,1}$	0.52	1.27	5.19	1.69
Second coefficient $D_{i,2}$	9.34	7.45	28.74	3.97

In Figures 2.6a-2.6b both the inertial and resistive dimensionless end-corrections show a dependency on the porosity that becomes less important for decreasing porosity. This behavior is more noticeable for $\delta_{res}/\delta_{res,ref}$. In Figure 2.8a the linear approximations of the coefficients C_1 and C_2 for the inertial end-correction are

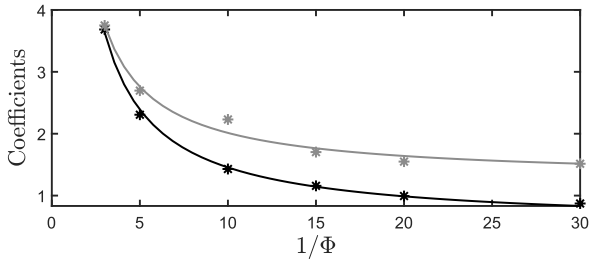

(a)

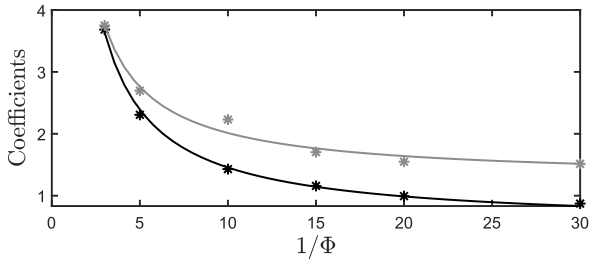

(b)

Figure 2.8. Comparison of the coefficients C_i of the fitting of the inertial and resistive end-corrections as a function of the porosity Φ in the range $0.6 < Sh < 20$. In a) (——) C_1 and (——) C_2. In b) (——) C_3 and (——) C_4. In both, asterisks refer to the numerical data and solid lines are referred to the results of the fitting process.

compared with the actual values. In Figure 2.8b the results for C_3 and C_4 for the resistance are presented. The average adjusted coefficients of determination [112] $1 - R^2$ are 0.987 for the inertial term and 0.998 for the resistive term.
It appears that both $\delta_{in}/\delta_{in,ref}$ and $\delta_{res}/\delta_{res,ref}$ are converging to the unit value for high Sh_b numbers. For higher Sh_b numbers, some additional calculations are carried out for a typical porosity $1/\Phi = 10$. At $Sh_b = 100$, one has $\delta_{in}/\delta_{in,ref} = 1.0116$ and $\delta_{res}/\delta_{res,ref} = 0.9465$. At $Sh_b = 200$, $\delta_{in}/\delta_{in,ref} = 1.0061$ and $\delta_{res}/\delta_{res,ref} = 0.996$. This confirms the validity of the thin boundary layer approximation for sharp square edges.
Furthermore, the effect of the boundary condition (slip or no-slip) on the channel walls is investigated for a typical porosity $1/\Phi = 10$ with $Sh_b = 2$ and $Sh_b = 20$. Numerical simulations for $1/\Phi = 10$ show that the introduction of a no-slip boundary condition at the walls of the confinement channel has a negligible effect on the results. For $Sh_b = 2$, one finds a ratio $\delta_{res,no-slip}/\delta_{res,slip} = 1.032$. For $Sh_b = 20$, $\delta_{res,no-slip}/\delta_{res,slip} = 1.044$. Using the thin boundary layer theory, for high Sh_b one finds $\delta_{res,no-slip}/\delta_{res,slip} = 1.041$, in agreement with numerical results. One expects that this ratio increases with increasing porosity.
For an extremely large porosity $1/\Phi = 3$, one finds a ratio $\delta_{res,no-slip}/\delta_{res,slip} = 1.185$. One can conclude that the inertial end-correction is determined by the porosity. The porosity has a modest effect on the resistive end-correction. The negligible effect of the no-slip boundary condition in the channel suggests that, for $\Phi = 0.1$, dissipation is mainly concentrated around the edges.

2.4.2 Symmetric slit with smooth edges

Consider a slit of height b with rounded edges of radius r placed symmetrically with respect to a channel of height a. The results of incompressible LNS simulations are compared to the high Shear numbers approximation for a smooth transition discussed in Section 2.2.1. The geometry of the smooth transition is determined using the transformation of Henrici [110]. Experimental and numerical data for a circular perforation obtained for a 45° chamfered circular perforation by Temiz *et al.* [23] are also displayed. The reference length L_{ref} is introduced. For the round edges $L_{ref} = r$ is the radius of curvature of the rounded edge. For Henrici's transformation, $L_{ref} = d$ is the transition length. For chamfered, $L_{ref} = c_{ch}$ is the chamfer length. It appears that the transition length d well approximates the radius r of an equivalent rounded edge for $d/b < 1$. In Figure 2.9, $\delta_{in,round}/\delta_{in,sharp}$ and $\delta_{res,round}/\delta_{res,sharp}$ are displayed as function of L_{ref}/b. Numerical results for a slit with a height ratio of $a/b = 10$ are shown for 1) rounded edges at several Sh_b numbers ($Sh_b = 0.2, 2, 20$), 2) chamfered edges for $c_{ch} = 0.5b$ at $Sh_b = 20$, 3) Henrici's geometry for $Sh_b = 20, 200$. The analytical potential solution for smooth edges is validated by the LNSE numerical simulations for Henrici's geometry at high Shear numbers. In Figure 2.9a, for the inertial end-correction the analytical solution well approximates the numerical results for a smooth transition.

The 2D planar result for the 45° chamfered edge is relatively far from the analytical and numerical results for a smooth transition. In Figure 2.9b, for the resistive end-correction the analytical solution provides a good approximation for high Sh_b numbers, both for a round edge and for a chamfered edge. It is interesting to note that the resistive end-correction becomes negative for L_{ref}/b of order unity. Physically, this would mean that the effective plate thickness is smaller than the actual thickness. For comparison, the influence of chamfer on circular perforations from Temiz *et al.* [23] is also displayed in Figure 2.9.

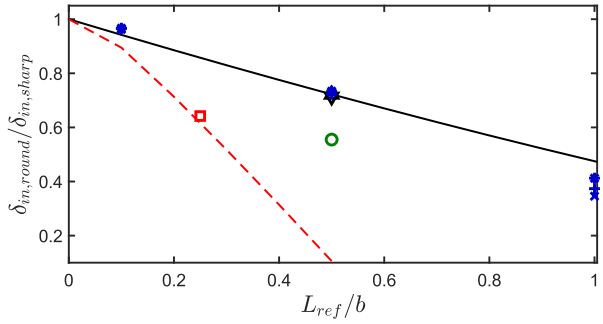

(a)

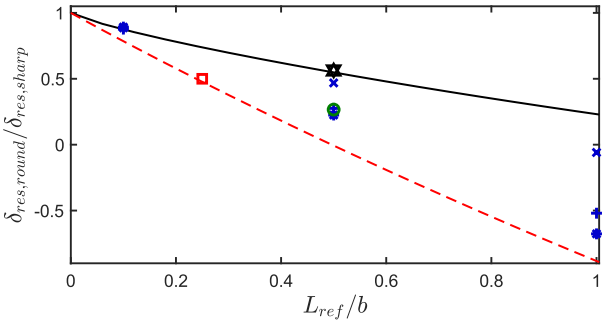

(b)

Figure 2.9. Comparison of the high Sh_b number approximation for a smooth transition with numerical results for several ratios L_{ref}/b for a) $\delta_{in,round}/\delta_{in,sharp}$ and b)$\delta_{res,round}/\delta_{res,sharp}$ for several Sh_b numbers: (——) Slit with smooth transition, ($*$) Slit with rounded edges for $Sh_b = 0.2$, ($+$) Slit with rounded edges for $Sh_b = 2$, ($\times$) Slit with rounded edges for $Sh_b = 20$, ($\triangledown$) Slit with Henrici's transition for $Sh_b = 20$, ($\triangle$) Henrici's transition for $Sh_b = 200$, ($\bigcirc$) Chamfered edge for $Sh_b = 20$, (- - -) Fit of numerical results and ($\square$) Experimental result for circular perforations of Temiz *et al.* [23].

In Figure 2.10a and 2.10b, $\delta_{in,round}/\delta_{in,sharp}$ and $\delta_{res,round}/\delta_{res,sharp}$ are shown for height ratios a/b relevant in MSPs. The inertial end-correction shows a dependency on a/b that increases with the increase of the ratio L_{ref}/b.
The resistive end-correction shows a much more modest dependency on the porosity than the inertial end-correction, as already observed for sharp edges. Rounded edges and chamfered edges have a similar effect on the end-correction, for a small radius of curvature of the edge compared to the slit height b. The effect of rounded edges on a slit is similar to the effect of a chamfered edge for circular perforations. In conclusion, it appears that a fair estimation of the edge geometry is necessary to obtain meaningful estimations of the end-correction for both slits and circular perforations.

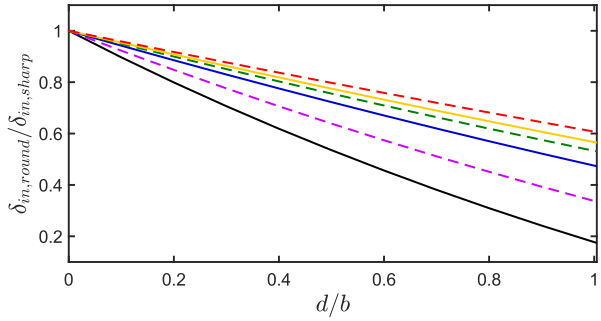

(a)

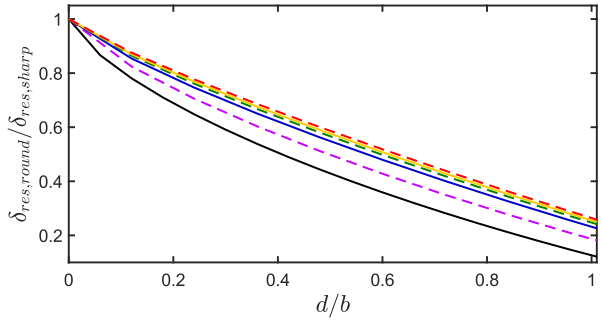

(b)

Figure 2.10. Behavior of a) $\delta_{in,round}/\delta_{in,sharp}$ and b) $\delta_{res,round}/\delta_{res,sharp}$ as function of the edge rounding L_{ref}/b for several $1/\Phi = a/b$: (——) $1/\Phi = 3$, (- - -) $1/\Phi = 5$, (——) $1/\Phi = 10$, (- - -) $1/\Phi = 15$, (——) $1/\Phi = 20$, (- - -) $1/\Phi = 30$.

2.4.3 Asymmetric slit

In this section results for asymmetric slits are discussed. The position of the slit is determined using the distances a_1 and a_2 defined in Figure 2.3. The inertial end-correction is calculated for high Sh_b numbers, using the modal expansion method of Ingard [97] presented in Section 2.2.4. In the extreme case that $a_2 = 0$, the high Sh_b number limit of Morse and Ingard [100] can be used to calculate both the inertial and the resistive end-corrections. In Figure 2.11, the ratio of the inertial end-corrections for the asymmetric case ($\delta_{in,asym}$) and the symmetric case ($\delta_{in,sym}$) is displayed as a function of a_2/a_1 for several height ratios a/b, with $a = a_1 + a_2$. The value of a_2/a_1 where the effect of the position has a significant effect decreases with the increase of a/b. It appears that for a slit positioned at the wall ($a_2 = 0$), the inertial end-correction is, as expected, double the value for the symmetric case, for all the ratios a/b. Numerical calculations are performed for a slit positioned at the wall and compared to the analytical results. In Figure 2.12, for $Sh_b = 20$ the end-corrections for an asymmetric slit ($a_2 = 0$) as a function of the height ratio a/b are plotted using the corresponding values (same Sh_b number) for a symmetric slit as a reference. The inertial end-correction is double the value for the symmetric slit. The resistive end-correction instead increases for decreasing porosity $\Phi = b/a$. It approaches the asymptotic value of $\delta_{res,asym} = 2.3\delta_{res,sym}$. This asymptotic value reduces for increasing Sh_b approaching the analytical value for very high Shear numbers. Considering the common wall as a mirror, the flow corresponds to that in a slit with double width $2b$ placed symmetrically with respect to a channel of width $2a$. This explains the behavior of the inertial end-correction. For the resistive end-correction, the dissipation occurs in a small region around the edge. This region can be addressed as the dissipation region. When keeping the flow velocity in the slit constant, but doubling the slit and channel

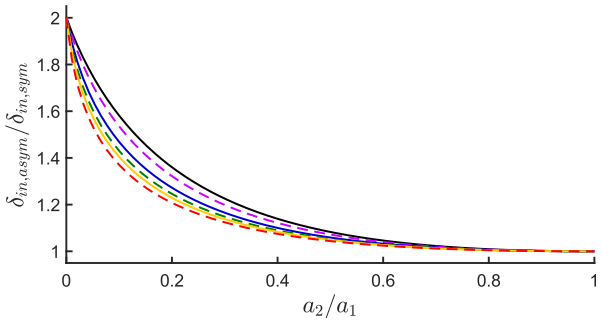

Figure 2.11. Analytical results for the inertial end-correction obtained using modal expansion for an asymmetric slit for several $1/\Phi$: (——) $1/\Phi = 3$, (- - -) $1/\Phi = 5$, (——) $1/\Phi = 10$, (- - -) $1/\Phi = 15$, (——) $1/\Phi = 20$, (- - -) $1/\Phi = 30$.

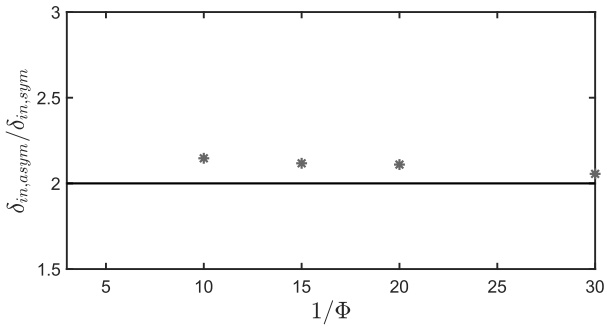

(a)

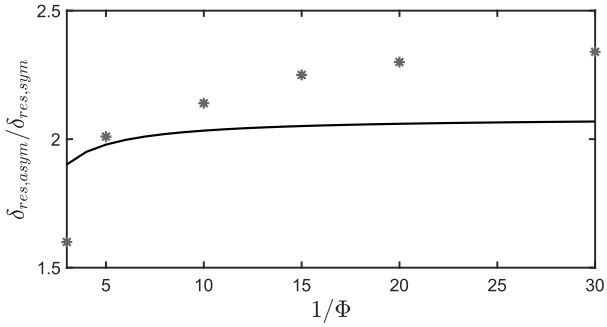

(b)

Figure 2.12. Comparison of the numerical simulations ($*$) for $Sh_b = 20$ and potential flow theory (——) results as function of a/b for a) $\delta_{in,asym}/\delta_{in,sym}$ and b) $\delta_{res,asym}/\delta_{res,sym}$.

height, one increases the dissipation region length by a factor of 2. The resulting resistive end-correction doubles. In practice, the end-correction increase is larger (15%) than the factor 2 because one has to account for an additional dissipation along the flat wall common to the slit and the channel.
The deviation at $a/b = 30$ for the resistive end-correction indicates that the thin boundary layer limit is not yet reached for $Sh_b = 20$. This was also observed for the symmetrical case. In conclusion, it appears that the influence of the position on the end-corrections cannot be neglected for positions of the slit with respect to the channel of the order of magnitude of the slit height.

2.4.4 Finite thickness plate with sharp square edges

In Figure 2.13a and 2.13b the deviations of the inertial and resistive end-correction for a finite thickness are compared with the transition between a very long slit and

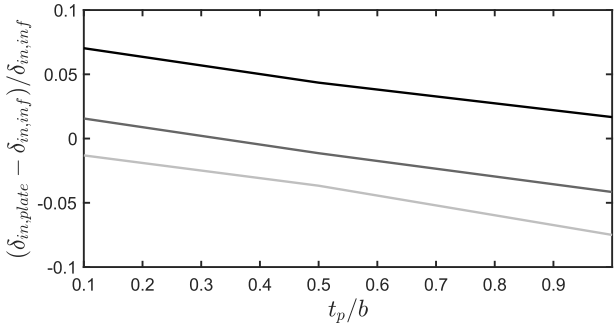

(a)

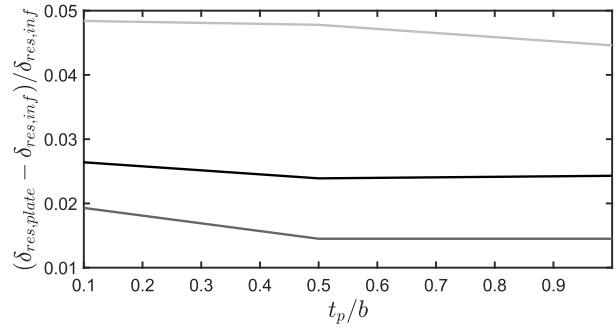

(b)

Figure 2.13. Deviation of a) $\delta_{in,plate}$ and b)$\delta_{res,plate}$ from the semi-infinite slit as function of the ratio t/b for: (——) $Sh_b = 0.2$, —— $Sh_b = 2$ and (——) $Sh_b = 20$.

the confinement channel discussed in the previous sections. In the range of interest, the deviation lies within 10% and 5% accuracy, respectively for the inertial and the resistive end-correction. $\delta_{res,plate}$ shows a negligible dependency on t_p/b with respect to the dependency on the Sh_b number. From this study, one can state that for practical purposes the influence of the thickness of the plate on the end-corrections can be neglected.

2.5 Conclusions

In typical micro-slit plates (MSPs) the acoustic end-corrections and the plate thickness are both of the order of the slit width. Hence an accurate prediction of the end-corrections is needed for the design of MSPs. This study combines two-dimensional analytical and numerical solutions of the incompressible Linearized Navier-Stokes equations to investigate the acoustic behavior of micro-slit absorbers (MSAs and

MSPs). A single slit of height b is studied as confined in a rectangular channel of height a determined by the porosity of the plate $\Phi = b/a$. The flow within the slit is assumed to be locally incompressible (low He numbers). Thermal effects are neglected. Focus is given to the frequency range of application for MSAs and resonant metamaterials. For sharp edges, numerical simulations demonstrate that for low Sh_b numbers a parabolic-flow approximation provides a good approximation of the inertial end-correction, whereas the thin boundary layer approximation predicts both the end-corrections at high Sh_b numbers. The inertial end-correction of slits is strongly dependent on the porosity, showing a very different behavior compared to that of circular perforations. A striking result is that the ratio of the resistive end-correction and the slit height is weakly dependent on the porosity, independently of the Shear number. This indicates that viscous friction is a local phenomenon occurring near the edges. This is confirmed by the negligible influence of the no-slip boundary condition at the walls of the confinement channel, for $\Phi < 0.1$. The final proof is gathered in Section 2.4.2 where the effect of the edge geometry is discussed. The analytical model for a smooth transition provides a reasonable prediction for rounded and chamfered edges at high Sh_b numbers. These results demonstrate that, without information on the edge shape, an accurate prediction of the end-corrections is not possible. In Section 2.4.3 it has been shown that the position of the slit becomes an important effect for distance from the wall in the order of the slit height b. For the limit case of a slit sharing the wall with the channel, the inertial and resistive end-corrections are both approximately twice the values for a symmetrical slit. In Section 2.4.4 it is shown that, for $t_p > 0.1b$, the effect of the plate thickness on the end-corrections is negligible.

3

Effect of slit length on linear and non-linear acoustic transfer impedance of a micro-slit plate

Abstract - This Chapter explores the effect of the slit length on the acoustic transfer impedance of micro-slit plates (MSPs) in the linear and non-linear regimes for a specific slit geometry. This geometry is inspired by slits obtained by cutting and bending the plate. MSPs are plates with arrays of slit-shaped perforations, with the width of the order of the acoustic viscous boundary layer thickness. Impedance tube measurements on two accurately manufactured plates are compared to the numerical solution of the Linearized Navier-Stokes equations and analytical limits. The impedance of the plate is obtained by the impedance of a single slit divided by the plate porosity. The resistance of a slit is independent of the slit length and plate porosity. In the linear regime, the resistance is accurately predicted by a two-dimensional numerical model. In the non-linear regime, the resistance is strongly dependent on the amplitude of the acoustic waves. The inertance of the slit is weakly dependent on the slit length and the plate porosity, for low and moderate amplitudes. For high amplitudes, a complicated amplitude dependency of the inertia of short slits is found. One expects that most of the conclusions obtained can be generalized to other slit geometries.

This Chapter is based on:
A. Aulitto, A. Hirschberg, and I. Lopez Arteaga and E. L. Buijssen (2022). Effect of slit length on linear and non-linear acoustic transfer impedance of a micro-slit plate. Acta Acustica, 6, 6.

3.1 Introduction

Micro-slit absorbers and plates (MSAs, MSPs) have been proposed as sound absorbers at low frequencies, providing lightweight and compact solutions to substitute conventional materials [51]. MSPs are plates with slit widths in the sub-millimeter range and low porosity (order of 1%). In conventional designs, micro-slit plates are backed by a cavity, forming micro-slit absorbers (MSAs). One of the advantages of slits with respect to circular perforations is that, for equal porosity, a single slit replaces a large number of circular perforations. Furthermore, a slit can be used to delimit flexible structures whose vibration can contribute to sound absorption [55, 56]. However, the manufacturing of slits is difficult and can be an obstacle in industrial applications. A possible manufacturing process is to cut the plate, bending the two portions close to the cut, as displayed in Figure 3.1. A slit is created without removing material from the plate and can lead to new designs. One of the advantages of this geometry is that the edges in contact with the slits are protected from external agents in harsh environments. Another advantage is the possibility to reach sub-millimeter slit widths. This manufacturing technique is used to produce ®Acustimet plates by Sontech [54, 113].

In this Chapter, a geometry inspired by the geometry of Figure 3.1 is studied. Impedance tube measurements are used to investigate the effect of the slit length in two accurately manufactured micro-slit plates. The edges of the slits are kept as sharp as possible. Both plates have the same porosity and total slit perforation length. In the linear regime, experimental results are compared to numerical solutions of the Linearized incompressible Navier Stokes equations. Micro-perforated plates and micro-slit plates can be designed to obtain excellent linear acoustic properties but, at high amplitudes, the non-linear effects deteriorate the performance of the absorbers [52, 114, 115]. However, in practical applications, the acoustic particle velocity in the slits can reach high amplitudes. For this reason, the change of resistance and inertance of the slits due to non-linear effects for long and short slits has been studied in this Chapter. In literature, several manufacturing techniques are employed to create slits. In classical applications, a slit can be created by removing material from the plate [53, 55, 56]. Slits can also be generated by mating two slotted layers [52, 116]. Alternative designs of MSAs have been reported in the literature [52, 55, 56, 95, 96].

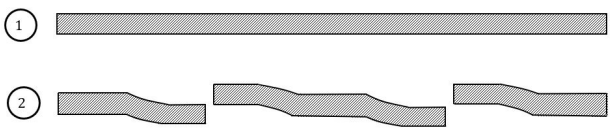

Figure 3.1. Schematic cross-section of a typical geometry obtained with the process of cutting the plate and bending the extremities.

Several publications concern the acoustic impedance of MPPs at high amplitudes in the presence of a bias flow or for sound-excited flows [117–121]. In Section 3.2, the theoretical background is presented for the linear and non-linear regimes. In Section 3.3, the experimental setup and the geometry of the plates are discussed. In Section 3.4, the two-dimensional numerical model is described. In Section 3.5, the comparison between numerical and experimental results is presented in the linear and non-linear regimes. As explained by Cummings and Eversman [122], non-linear losses at very high amplitudes are due to the formation of a quasi-steady jet flow. This jet displays a contraction after flow separation from the edges of the slit: the so-called *vena contracta*. In Appendix C.1, the *vena contracta* factor for a simplified model of the geometry is calculated. In Appendi C.2, the quasi-steady incompressible model is presented. In Appendix C.3, a correction of the quasi-steady model for the viscous boundary layer thickness is discussed.

3.2 Theoretical background

In the linear regime, dissipation of acoustic energy takes place in the oscillating boundary layer of thickness $\delta_v = \sqrt{2\mu/\omega\rho}$, where $\omega = 2\pi f$ is the angular frequency, ρ is the air density ($\rho = 1.18\,kg/m^3$ at 25°C and atmospheric pressure) and μ is the dynamic viscosity of air ($\mu = 1.85 \times 10^{-5}\,kg/ms$ at 25°C). The ratio between the slit width b and the thickness of the viscous boundary layer δ_v is the Shear number

$$Sh_b = \frac{b}{\delta_v}. \tag{3.1}$$

In a micro-slit plate, typical Shear numbers, in the frequency range of interest, are of order unity. In the non-linear regime, for moderate excitation amplitudes, vortices form locally at the edges of the slits. At very high amplitudes, this leads eventually to the formation of jets. Additional dissipation of acoustic energy is involved. The behavior of the plate can be studied as a function of the Strouhal number (St_b), defined as the ratio between the slit width b and the amplitude of the oscillating particle displacement at the slits. In formulas,

$$St_b = \frac{\omega b}{U_p}, \tag{3.2}$$

where U_p is the cross-sectional surface averaged acoustic velocity amplitude at the slit ($u_p(t) = Re[\widehat{u}_p e^{(i\omega t)}] = U_p \cos(\omega t)$, for harmonic oscillations). For $St_b >> 1$ (linear regime) the particle displacement is smaller than the slit width and vortices are not formed. For $St_b << 1$ (strongly non-linear), vortices are formed and they move away from the slit forming a free jet. For $St_b \approx 1$ (moderate non-linear) vortices form at the edges of the slits and they remain local. Alternatively, one can define a Strouhal number St_t based on the plate thickness at the slit ($t = t_p - t_d$ in Figure 3.3) to compare the vortices displacement with the thickness of the plate at the slit [123].

3.2.1 Transfer impedance in linear regime

In the linear regime, the concept of transfer impedance is introduced in the frequency domain (for purely harmonic oscillations) of frequency f. At a distance large compared to the slit width b but small compared to the acoustic wavelength $\lambda = c/f$, the flow can be described in terms of plane acoustic waves. As this region is compact, the corresponding complex amplitude $\widehat{u}$ of the acoustic velocity $u(t) = Re[\widehat{u}e^{(i\omega t)}] = U\cos(\omega t)$ is the same on both sides of the plate. The transfer impedance of the plate is defined as the ratio between the complex acoustic pressure difference $\Delta\widehat{p}$ and the amplitude of the acoustical velocity $\widehat{u}$ in a cross-section upstream of the plate. The pressure is found by the extrapolation of the plane wave solutions (on both sides) to the sample surface (a formal discussion can be found in Section 3.4). The dimensionless transfer impedance of the plate is

$$z_{plate} = \frac{\Delta\widehat{p}}{\rho c\widehat{u}}, \tag{3.3}$$

where ρ is the density of air and c is the speed of sound in air. Note that the plate transfer impedance is a complex quantity. The dimensionless transfer impedance of the plate z_{plate} is

$$z_{plate} = Re[z_{plate}] + \mathrm{i}Im[z_{plate}], \tag{3.4}$$

with $\mathrm{i}^2 = -1$, $Re[z_{plate}]$ the resistive part of the transfer impedance of the plate (or resistance of the plate) and $Im[z_{plate}]$ the reactive part of the transfer impedance of the plate (or inertance of the plate). The transfer impedance of a slit is defined as the ratio between the complex pressure difference $\widehat{p}$ and the amplitude of the cross-sectional acoustical velocity $\widehat{u}_p$ in the slit. In formulas,

$$z_{slit} = \frac{\Delta\widehat{p}}{\rho c\widehat{u}_p} = z_{plate}\Phi, \tag{3.5}$$

where $\widehat{u}_p = \widehat{u}/\Phi$ and Φ the porosity of the plate. Therefore, in the first order of approximation, the transfer impedance of the plate can be obtained by the impedance of a single slit. In practical applications, the micro-slit plate is backed by a cavity. As the slit forms the neck of a Helmholtz resonator with a portion of the back cavity as volume, the flow within the slit will be considered locally incompressible up to the first resonance frequency of the resonator. In the audio range, the square of the Helmholtz number is small,'*i.e.*' $He^2 = \left(\frac{\omega b}{c}\right)^2 < 10^{-1}$. Therefore, one can assume a frictionless flow of the incompressible flow. Thermal effects in the slit are neglected [124].

3.2.2 Transfer impedance in non-linear regime

In the non-linear regime, the resistance due to vortex shedding dominates the absorption mechanism, as shown by Ingard and Ising [125]. Cummings and Eversmann [122] assume a quasi-steady flow behavior to describe the behavior of perforations at high Shear numbers and very high amplitudes of acoustic particle velocity.

The model assumes that the acoustic flow separates at the edges of the slits and forms a free jet with a cross-section smaller than the perforation area. The ratio between the cross-section of the jet and the cross-section of the perforation is called the *vena contracta* factor α. In their model, using the Bernoulli equation one can derive the relationship between pressure change across the plate and particle velocity $\Delta\widehat{p} \approx \frac{1}{2}\rho\widehat{u}_p|\widehat{u}_p|$ and $\widehat{u}_p$, with $u_p(t) = Re[\widehat{u}_p e^{(i\omega t)}] = U_p\cos(\omega t)$. For $St_b << 1$ one can assume a quasi-steady incompressible flow with a free jet of *vena contracta* factor α. Assuming a harmonically oscillating velocity, $u(t) = U\cos(\omega t)$, one can calculate the time-averaged dissipated power and define the (time-averaged) non-linear dimensionless plate resistance $Real[z_{plate,NL}]$ as

$$Real[z_{plate,NL}] - Real[z_{plate,L}] = \frac{4}{3\pi}\frac{U}{\alpha^2\Phi^2 c}, \tag{3.6}$$

where $Real[z_{plate,L}]$ is the dimensionless plate resistance in the linear regime. Derivation of the theoretical limit can be found in Appendix C.2. The *vena contracta* coefficient for the geometry discussed in this study is assumed to be $\alpha = 0.82$. This value is found in the potential flow limit for small porosity using the hodographic method [126, 127]. Derivation of the *vena contracta* factor α can be found in Appendix C.1. The theoretical limit can be corrected for the effect of the quasi-steady viscous boundary layer. This causes a reduction of the effective porosity that leads to an increase in the resistance. The correction for the thickness of the viscous boundary layer is in Appendix C.3. For the inertial part of the transfer impedance $Im[z_{plate}]$, Ingard and Ising assume that in the upstream of the flow separation, the flow remains identical to the potential flow prevailing in the linear case [125]. In the downstream free jet, the inertia is negligible. Hence, the inertia should be reduced by a factor of 2. In other words, $\Delta Im[z_{plate,NL}] = -Im[z_{plate,L}]/2$. The factor one-half is explicitly discussed in Morse and Ingard [100]. This simple limit will be compared to experimental results in Section 3.5.2.

To study non-linear effects, the linear contribution is subtracted from the non-linear resistance and inertance. To analyze the effect on a single slit, the porosity Φ is introduced. The change in resistance $(Real[z_{plate,NL}] - Real[z_{plate,L}])$ is normalized with the non-linear limit proposed by Ingard and Ising [125] and corrected by the *vena contracta* factor as in Temiz *et al.* [115]. The *vena contracta* factor is $\alpha = 0.82$ (see Appendix C.1). The change in inertance is normalized by dividing by the linear contribution $Imag[z_{plate,L}]$. The dimensionless corrected resistance and inertance changes due to non-linear effects are:

$$\Delta R_{NL} = 2\alpha^2\Phi\frac{(Real[z_{plate,NL}] - Real[z_{plate,L}])}{\rho U_p} \tag{3.7}$$

$$\Delta I_{NL} = \Phi\frac{(Imag[z_{plate,NL}] - Imag[z_{plate,L}])}{Imag[z_{plate,L}]}. \tag{3.8}$$

3.3 Experiments

3.3.1 Impedance tube setup

The experimental setup used in this study is an impedance tube with 6 pre-polarized 1/4 in microphones (type BWSA, sensitivity 50 mV/). The tube is made of aluminium with an inner diameter $D_i = 50\,\text{mm}$, a wall thickness $t_w = 10\,\text{mm}$ and length $l_t = 1000\,\text{mm}$. The excitation system is a $25\,W$ loudspeaker. The six microphones are equally placed at a distance of 175 mm. A relative calibration is performed on the microphones using the microphone closest to the end of the tube (sample side) as the reference microphone. The position of this microphone with respect to the end of the impedance tube is $x_{ref} = 47.7\,\text{mm}$. Details on the setup and the calibration system can be found in the works of Temiz *et al.* and Kojourimanesh *et al.* [23, 128].
The micro-slit plates are positioned at the end of the impedance tube through a sample holder. For this study, two sample holders are used to compare the effects of three-dimensional effects for a plate confined by the impedance tube from two sides and from one side ($L_{h_1} = 50\,\text{mm}$ and $L_{h_2} = 9\,\text{mm}$). The impedance tube termination with the sample holders is shown in Figure 3.2. Both the sample holders have a groove for an o-ring to guarantee air-tightness from both sides of the sample. A script built-in $NILabView$ software controls the signal processing and data acquisition during the measurements. For this study, the sampling rate is $20\,k$Hz for the excitation signal and $10\,k$Hz for recording the input signal. The amplitude of the excitation signal is adjusted automatically until it satisfies the pre-determined pressure value for the reference microphone $\widehat{p}(x_{ref})$ within an accuracy of 2%. This amplitude is also used to derive the acoustic velocity at the sample.
The calculation of the reflection coefficient at the sample is based on the plane wave assumption. For the evaluation of the reflection coefficient, the method from Jang and Ih [129] is used.

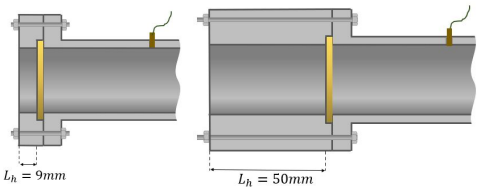

(a) **(b)**

Figure 3.2. Impedance tube termination with *a*) short sample holder of length $L_h = 9\,\text{mm}$ and *b*) long sample holder of length $L_h = 50\,\text{mm}$.

For each frequency, every microphone records the complex pressure amplitude $\widehat{p}(x)$ at position x,

$$\widehat{p}(x) = \widehat{p}_+(x)e^{(-\mathrm{i}kx)} + \widehat{p}_-(x)e^{(\mathrm{i}kx)}, \tag{3.9}$$

with p^+ and p^- respectively the amplitudes of the wave traveling in the positive and in the negative directions $x = 0$ correspond to the end of the impedance tube (sample side), k is the complex wavenumber. Taking visco-thermal effects into account as proposed in Peters *et al.* [130], the complex wavenumber is

$$k = \frac{\omega}{c_0}\left[1 + \frac{1-\mathrm{i}}{\sqrt{2}Sh_D}\left(1 + \frac{\gamma-1}{Pr^{0.5}}\right)\right] - \frac{\omega}{c_0}\left[\frac{\mathrm{i}}{Sh_D^2}\left(1 + \frac{\gamma-1}{Pr^{0.5}} - \frac{1}{2}\gamma\frac{\gamma-1}{Pr}\right)\right], \tag{3.10}$$

where i is the imaginary unit, Pr is the Prandtl number ($Pr = 0.72$), γ is the heat capacity ratio ($\gamma = 1.4$) and Sh_D the Shear number based on the impedance tube diameter D_i defined as the ratio of the tube diameter and the viscous boundary layer thickness in the tube ($Sh_d = D_i/\delta_v$). The reflection coefficient at the end of the tube ($x = 0$) is [129]

$$R = \frac{\widehat{p}_-}{\widehat{p}_+}. \tag{3.11}$$

Experimentally, the closed pipe termination at $x = 0$ is used as a reference for the accuracy of the measurements. For an amplitude $\widehat{p}(x_{ref}) = 2\,\mathrm{Pa}$, the maximum deviation from the theoretical value $R = 1.000$ is less than 0.3%. The closed-end measurements are performed for several excitation amplitudes. It appears that for amplitude $\widehat{p}(x_{ref}) > 23\,\mathrm{Pa}$ the accuracy of the measurements reduces to 1% up to $f = 400\,\mathrm{Hz}$. For $f > 400\,\mathrm{Hz}$ this accuracy reduces to around 3%. Hence, the study of the amplitude dependence of the measurements is restricted to $0.4\,\mathrm{Pa} < \widehat{p}(x_{ref}) < 23\,\mathrm{Pa}$. For low frequencies ($f < 200\mathrm{Hz}$), no significant effects are found in increasing the measurement time (number of samples).
For $f > 700\,\mathrm{Hz}$ the results appear to be less reliable. Therefore, the frequency range of the measurements is restricted to $20\,\mathrm{Hz} < f < 700\,\mathrm{Hz}$ corresponding to $1 < Sh < 6$.

Measuring the transfer impedance of the sample and acoustic velocity

To measure the transfer impedance of the plate the following procedure is followed. At the impedance tube termination, an additional pipe segment of the same length as the sample holder is added. The open pipe termination is located at $x_{open} = x_0 + L_h + t_p$, with $x_0 = 0$ is the right side of the plate in Figure 3.2, L_h the length of the holder and t_p the thickness of the sample. The reflection coefficient R_o for the open pipe termination is measured. The dimensionless radiation impedance is calculated using $Z_{rad} = (1 + R_o)/(1 - R_o)$. The tube is then loaded with the sample with the use of a sample holder. The reflection coefficient of the sample-loaded termination R_s is measured. The sample-loaded impedance can be calculated in the same way as the radiation impedance as $Z_s = (1 + R_s)/(1 - R_s)$.

The samples have relatively low porosity. Therefore, the radiation impedance is expected to be much lower than the impedance of the plate. Nevertheless, the radiation effects are taken into account and the dimensionless transfer impedance of the plate z_{plate} is calculated as the difference between the sample-loaded impedance and the radiation impedance, in formula $z_{plate} = z_s - z_{rad}$. The radiation of the room is close to that of a free field. Deviations due to unwanted changes in room acoustics are taken into account by repeating the open pipe termination experiments before each set of measurements. One does observe some systematic deviation from free-space radiation as a result of room resonances. Assuming the radiation impedance is in series with the plate impedance, the room effect is corrected by measuring the radiation impedance. In this open pipe radiation impedance measurement, the sample is replaced by a ring in the sample holder so that the geometry (pipe length, position in the room) is the same as when measuring with a sample. The analysis for non-linear studies is performed for $f \leq 200\,\text{Hz}$. In this analysis of non-linear effects the amplitude $|\widehat{u}|$ of the flow velocity is a key parameter. The magnitude of the acoustic velocity at the plate is calculated as $|\widehat{u}| = \widehat{p}(x_{ref})/|Z_{plate}|$, with $Z_{plate} = \rho c z_{plate}$. Hence, it is assumed that $\widehat{p}(x = 0) \approx \widehat{p}(x_{ref})$. This is certainly accurate at low frequencies ($f < 340\,\text{Hz}$) given $x_{ref} \approx 50\,\text{mm}$.

3.3.2 Specifications of the samples

The acoustical behavior of short and long slits in micro-slit plates is compared by considering two samples. The geometry of the plates is inspired by the plate in Figure 3.1. The plates are made in brass using a milling process [131]. Sketches of the plates showing the main parameters are shown in Figure 3.3. The plates are shown in Figure 3.4. The external diameter of the plates is $D_p = 70\,\text{mm}$, allowing hosting the plates in the holder. The effective diameter of the portion of the plate where the slits are located is $D_i = 50\,\text{mm}$, with D_i the internal diameter of the impedance tube. The total plate thickness is $t_p = 5\,\text{mm}$ and the nominal slit width is $b = 0.5\,\text{mm}$. The external width of the ditch is $w_{d,e} = 5\,\text{mm}$, the internal

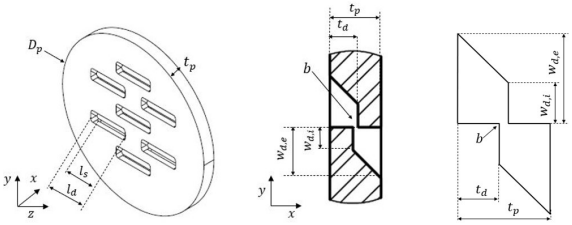

Figure 3.3. Sketches of the plate and the cross-section of a single slit with dimensional parameters.

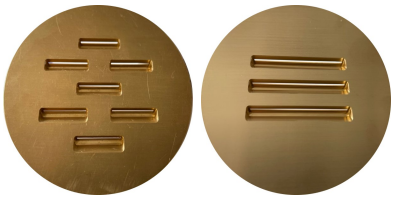

(a) **(b)**

Figure 3.4. Picture of the samples: *a*) plate with short slits and *b*) plate with long slits.

width of the ditch is $w_{d,i} = 2.25\,\text{mm}$. The ditch thickness is $t_d = 2.75\,\text{mm}$.
The thickness of the plate at the slit is $t = t_p - t_d = 2.25\,\text{mm}$. The slit length is $l_{s,short} = 15\,\text{mm}$ for short slits and $l_{s,long} = 35\,\text{mm}$ for long slits. The angle between the internal ditch and the outside ditch is 45°. The plates are realized in such a way that the total length of the slits P is the same. The total slit length is $P = 7 \times l_{s,short} = 3 \times l_{s,long} \approx 105\,\text{mm}$. The porosity (of the portion of the plate in the impedance tube) is $\Phi = 2.7\%$. To provide access to the rotary cutter, the ditch length is longer than the slit length, $l_d = l_s + 2\,\text{mm}$.
The actual widths of the single slits are measured experimentally using a digimatic indicator. Maximum deviations from the prescribed dimensions are of the order of 2% ($\pm 1\,\mu$m) for the plate with short slits and 4% ($\pm 1\,\mu$m) for the plate with long slits. The measured average of b over the slit length has been used $b = 0.505\,\text{mm}$ for short slits and $b = 0.520\,\text{mm}$ for long slits. Therefore, the porosity is $\Phi_{short} = 2.7\%$, for the plate with short slits, and $\Phi_{long} = 2.78\%$, for the plate with long slits. The edges in contact with the slits are kept as sharp as possible to remove effects due to the rounding of the edges. Observations under a microscope (magnification 50x) did not show any significant deviation from sharp edges.

3.4 Numerical model

In this section, a two-dimensional numerical model is proposed, where the solution of the linearized Navier-Stokes equations for an incompressible flow is applied.
A single slit of width b in a confinement channel of width a is considered (Figure 3.3). The confinement channel width is chosen such as the porosity of the two-dimensional model Φ_{2D} is equal to the actual porosity of the plate Φ. The plate of thickness t_p is enclosed between an upstream and a downstream channel of lengths L_u and L_d. The computational domain, shown in Figure 3.5, is divided into three sub-domains for meshing purposes. Continuity of pressure and velocity is assumed at the boundaries between the calculation domains. All the lengths are normalized with the slit width b, where the dimensionless plate thickness is

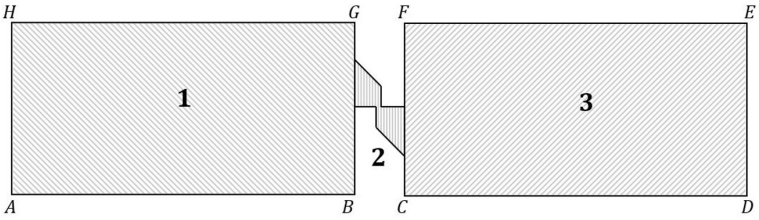

Figure 3.5. Two-dimensional computational domain for the plate of thickness t_p and slit width b enclosed between an upstream and a downstream channel. Three sub-domains (1-2-3) are defined for meshing purposes.

$t_p^* = t_p/b = 5\text{mm}/0.5\text{mm} = 10$ (Distance BC in Figure 3.5) and the confinement channel width is $a^* = a/b = 18\text{mm}/0.5\text{mm} = 36$ (Segment AH in Figure 3.5). The lengths of the channels upstream (Segment AB in Figure 3.5) and downstream the channel (Segment CD in Figure 3.5) are chosen to have $L_u^* = L_d^* = 2a^*$. The upstream face of the plate is located at $x_{BG}^* = -4.5$ and the slit opening at $x^* = 0$. The downstream face of the plate is located at $x_{CF}^* = 5.5$ and the end of the slit at $x^* = 1$. The upstream side of domain AH is located at $x_{AH}^* = -L_u^* - x_{BG}^* = -72 - 4.5 = -76.5$. The downstream side of domain DE is located at $x_{DE}^* = x_{CF}^* + L_d^* = 4.5 + 1 + 72 = 77.5$. Therefore, the domain extends between $x^* = x/b = [x_{AH}^*, x_{DE}^*] = [-76.5, 77.5]$ and $y^* = y/b = [0, 36]$. The low He number approximation is made. The incompressible harmonic linearized Navier-Stokes equations for a 2D domain in a dimensionless form are hereby presented for a radial frequency ω:

$$\frac{\partial \widehat{u}^*}{\partial x^*} + \frac{\partial \widehat{v}^*}{\partial y^*} = 0, \tag{3.12}$$

$$i\widehat{u}^* = -\frac{\partial \widehat{p}^*}{\partial x^*} + \frac{1}{2Sh_b^2}\left(\frac{\partial^2 \widehat{u}^*}{\partial {x^*}^2} + \frac{\partial^2 \widehat{u}^*}{\partial {y^*}^2}\right), \tag{3.13}$$

$$i\widehat{v}^* = -\frac{\partial \widehat{p}^*}{\partial y^*} + \frac{1}{2Sh_b^2}\left(\frac{\partial^2 \widehat{v}^*}{\partial {x^*}^2} + \frac{\partial^2 \widehat{v}^*}{\partial {y^*}^2}\right), \tag{3.14}$$

with $x^* = x/b$ and $y^* = y/b$. The dimensionless velocity $(\widehat{u}^*, \widehat{v}^*)$ is $(\widehat{u}/b\omega, \widehat{v}/b\omega)$ and the dimensionless pressure is $\widehat{p}^* = \widehat{p}/(\rho(b\omega)^2)$. These equations are implemented in *Comsol Multiphysics* as user-defined partial differential equations (PDE) and solved. For the inlet segment AH and outlet segment, DE uniform pressures are imposed, $p_{AH}^* = 1$ and $p_{DE}^* = 0$. At segments BC and FG (walls) no-slip boundary conditions are applied, *i.e.* $(u^*, v^*) = (0, 0)$. At segments $AB, CD, FE,$ andGH, slip boundary conditions are implemented to simulate the hydro-dynamical interaction between neighboring slits in the micro-slit plate with multiple slits.

In the present case, the slits are very thin ($b/a << 1$) therefore a slip boundary condition is used instead of a periodic boundary condition. A slip condition implies an equality of the velocities at the corresponding boundaries. Due to the dimensions of the slits, the deviation from a symmetric case is small. An unstructured mesh of quadratic triangular elements is used, with a finer mesh at the walls with no-slip conditions. The mesh inside the plate domain (Domain 2) is finer with the maximum element size is $M_{el}/b = 5 \times 10^{-2}$ and the minimum is $m_{el}/b = 1 \times 10^{-4}$. A mesh convergence study shows a quadratic convergence of the results using the average velocity in a cross-section (line) calculated at a location $x^* = -1.7a^*$. Far from the slit, the acoustic pressure is uniform in the cross-section and the amplitude of the pressure depends linearly on the position along the duct (parallel flow behavior described in Aulitto *et al.* [124]). For $-1.7a^* < x^* < -1.1a^*$, one has $\widehat{p}^{\,*}(x^*) = \widehat{\alpha}x^* + \widehat{\beta}$. For $1.1a^* < x^* < 1.7a^*$, one has $\widehat{p}^{\,*}(x^*) = \widehat{\gamma}x^* + \widehat{\delta}$. The complex constants can be determined by a linear fit of the pressure data obtained by numerical simulations for these regions far from the discontinuity. For a $Sh_b = 2.5$ (corresponding to $f = 120\,\text{Hz}$ for a slit width $b = 0.5\,\text{mm}$), the linear fit gives a coefficient of determination $1 - R^2 = 10^{-6}$ [112].

The transfer impedance of the slit Z^*_{slit} is determined by $Z^*_{slit} = \frac{\widehat{\beta}-\widehat{\delta}}{\widehat{U}^*}$ with $\widehat{U}^*$ being the flux calculated in a generic section of the channel upstream the slit, defined as $\widehat{U}^* = w^* < \widehat{u}^* > b^*$, with $w^* = 1$. From Z^*_{slit} one can derive the dimensionless transfer impedance of the slit z_{slit} as

$$z_{slit} = \frac{2\nu Sh_b^2}{bc} Z^*_{slit}, \tag{3.15}$$

with Sh_b the Shear number based on the slit width. Tests for several channel widths a are performed. It appears that the resistance of the slit is independent of the porosity of the plate. Reducing the porosity by a factor of 7, the resistance increases by less than 0.7%. The inertia of the plate changes with changing the porosity. For a drastic reduction of the porosity, by a factor of 7, the inertia increases by 30%. For small changes in the porosity around the nominal value, as the difference found between the two samples, the change is negligible. One can conclude that the transfer impedance of the slit appears to be only weakly dependent on the porosity Φ.

3.5 Results

3.5.1 Results in linear regime

In Figure 3.6, the resistive and the reactive part of the impedance are shown for long and short slits in the range $2.5 < Sh_b < 6$ corresponding to $120\,\text{Hz} < f < 700\,\text{Hz}$. The slit impedance of a single slit is displayed, $z_{slit} = z_{plate}\Phi$, calculated using Φ_{short} and Φ_{long} for the short slits and long slits, respectively. The amplitude of the acoustic waves is $\widehat{p}(x_{ref}) = 2$ Pa.

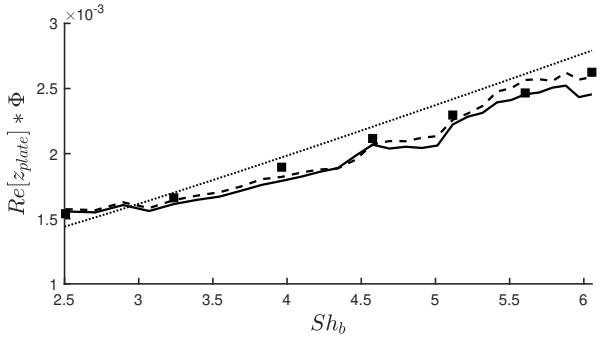

(a)

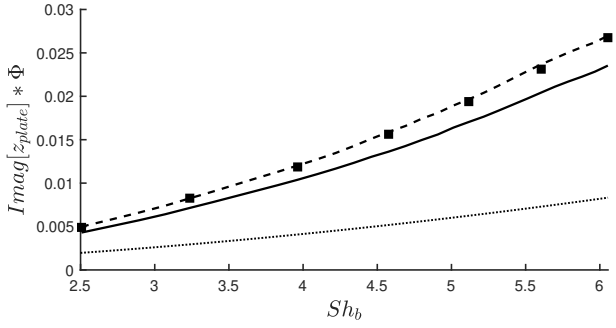

(b)

Figure 3.6. Comparison of the *a*) slit resistance and *b*) slit inertance for short (——) and long (- - -) slits as a function of Shear number in the linear regime. The numerical model (■) and the semi-analytical model for a plate with square sharp edges (·····) are shown [124].

Frequencies below 120 Hz are excluded because of the presence of non-linear effects that will be discussed in Section 3.5.2. Frequencies above 700 Hz are ignored due to uncertainties in the measurements. The results are presented for a sample holder $L_h = 9$ mm. It appears that the maximum deviation between the resistance of long and short slits is of the order of 4%. This deviation is most probably due to the difference in slit width between the two plates and could be due to differences in edge sharpness. At low Sh_b the resistance scales with $1/b^2$. An uncertainty of 2% in b explains a difference of the order of 4%. The influence of the length of the slits is negligible. The difference between the inertance of short and long slits is of the order of 10%. The inertance of short slits is lower than the

inertance of long slits. This is due to three-dimensional effects due to the geometry of the slits. Three-dimensional effects do not change significantly for the plate confined from both sides (holder with $L_h = 50\,\text{mm}$) or for a free plate (holder with $L_h = 9\,\text{mm}$). The effect of the sample holder length is negligible for $f < 500\,\text{Hz}$. At higher frequencies, the data with the long holder show oscillating frequency dependency. This is expected to be connected to the presence of a table in the measurement room. Therefore, the small holder is chosen to display the results. In Figure 3.6, the two-dimensional numerical model for a single slit is compared to the experimental results. It appears that the 2D numerical model of a single slit predicts (within a few percent of accuracy) the impedance (both resistive and reactive parts) of long slits and the resistance of short slits. In the same figure, the semi-analytical model for high Shear numbers of Aulitto *et al.* [124] for a plate with square sharp edges with thickness $t_p = 0.5\,\text{mm}$ is shown. For the semi-analytical model, the plate thickness is assumed to be the same as the slit width. It appears that the model predicts reasonably well the resistance of the plate with the geometry proposed in this Chapter. This confirms that the resistance of the micro-slit plate is a local effect, strongly affected by the geometry of the edge and less sensitive to the global geometry of the plates [124]. The inertance obtained when assuming $b = t_p = 0.5\,\text{mm}$, on the other hand, is much lower than that of the plates used in this study. In conclusion, in the linear regime ($Sh_b > 2.5$), the difference between the resistance (or resistive part of the impedance) for short and long slits is small. The inertance (or reactive part) of short slits is smaller (within 10%) than long slits due to three-dimensional effects. Experiments with two sample holders exclude dependence on the confinement of the plate. It appears that the two-dimensional numerical model well predicts the resistance of long and short slits.

3.5.2 Results in non-linear regime

For Shear numbers ($Sh_b < 2.5$) deviations from the numerical model for both short and long slits appear. These deviations depend on the amplitude of the acoustic waves. This is shown for long slits for several amplitudes in Figure 3.7. These deviations at low frequencies are due to non-linear effects and decrease for increasing Shear numbers. At $Sh_b < 2.5$ for $\widehat{p}(x_{ref}) = 2\,\text{Pa}$ one has $St_b < 0.4$. Non-linear effects impact both the inertance and the resistance of the slit. In particular, at the lowest frequency, the resistance for the highest amplitude ($\widehat{p}(x_{ref}) = 23\,\text{Pa}$) is 7 times higher than the resistance at the lowest amplitude ($\widehat{p}(x_{ref}) = 0.4\,\text{Pa}$). The inertance is reduced by almost a factor of 2, as expected from the model of Ingard and Ising [125]. In this study, sound generation as higher harmonics due to non-linearity is not considered. For long slits, the plots of ΔR_{NL} and ΔI_{NL} are provided as a function of the Strouhal number for several amplitudes of the acoustic waves. On the lower horizontal scale, the Strouhal number based on the slit width St_b is used. On the upper horizontal scale, the Strouhal number based

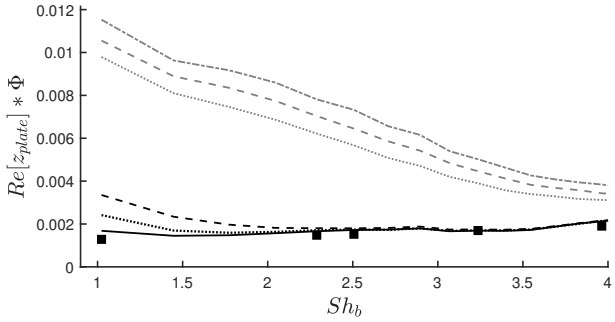

(a)

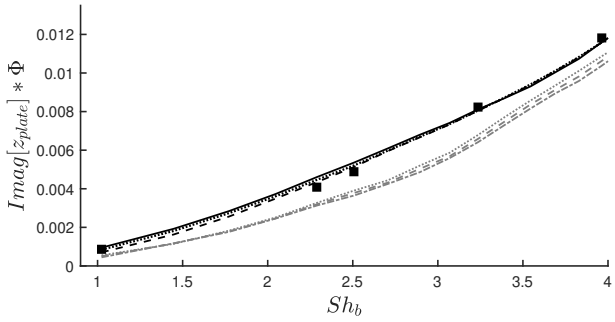

(b)

Figure 3.7. Comparison of the *a*) slit resistance and *b*) slit inertance for long slits compared to 2D model (■) as a function of Shear number for several amplitudes at the reference microphone. Low amplitudes: (——)0.4 Pa, (·····)1 Pa, (- - -)2 Pa. High amplitudes: (——)17 Pa, (·····)20 Pa, (- - -)23 Pa.

on the plate thickness at the slit St_t appears. In Figure 3.8, results are shown for high amplitudes of the acoustic waves ($\widehat{p}(x_{ref}) \geq 10\,\text{Pa}$). Both the change in resistance and inertance due to non-linearity increase (in absolute value), as expected, for decreasing Strouhal number ($St_b = \omega b/\widehat{u}_p$). For $1/St_b >> 1$ the change in resistance ΔR_{NL} is approaching the theoretical quasi-steady potential flow limit with correction for the viscous boundary layer for $St_b \to 0$. The change in inertance approaches $\Delta I_{NL} = -0.5$. The correction in the inertance due to non-linear effects is almost half the inertance in the linear case. Figure 3.9 compares the non-linear resistance and inertance for long slits to that of short slits for high amplitudes ($\widehat{p}(x_{ref}) \geq 10\,\text{Pa}$).

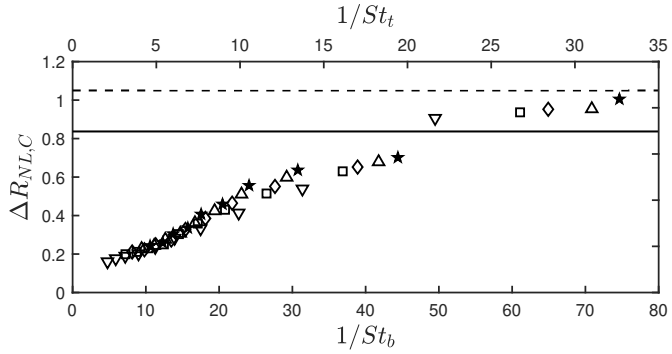

(a)

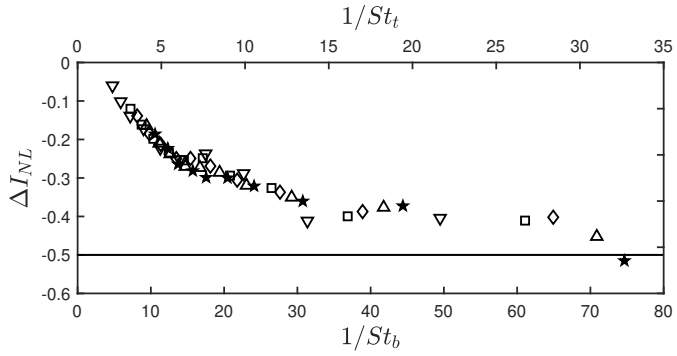

(b)

Figure 3.8. Change in a) slit resistance and b) slit inertance due to non-linearity for long slits as a function of St_b and St_t for several amplitudes at the reference microphone: 10 Pa (△), 15 Pa (□), 17 Pa (◇), 20 Pa (△), 23 Pa (★). In a) quasi-steady potential flow theory (——) and quasi-steady potential flow theory corrected for the effect of quasi-steady viscous boundary layer(- - -); in b) limit proposed by Ingard and Ising [125] (——).

In Figure 3.10, the results are shown for low and moderate amplitudes for short and long slits ($\widehat{p}(x_{ref}) \leq 6\,\text{Pa}$). These results display a Shear number dependency, less pronounced at higher amplitudes. It can be seen that the resistance changes due to non-linearity are almost identical for long and short slits, both for high and moderate amplitudes. Non-linear effects on the inertance of short slits are, in absolute value, smaller than for long slits.

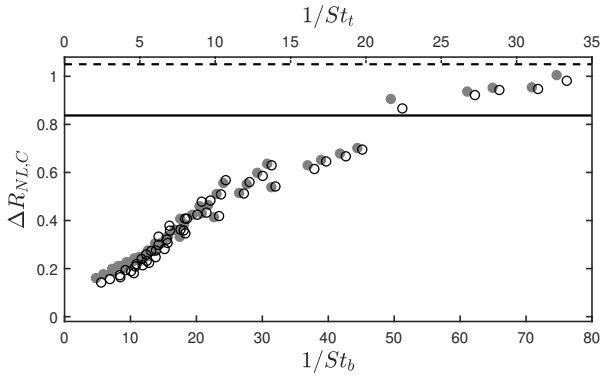

(a)

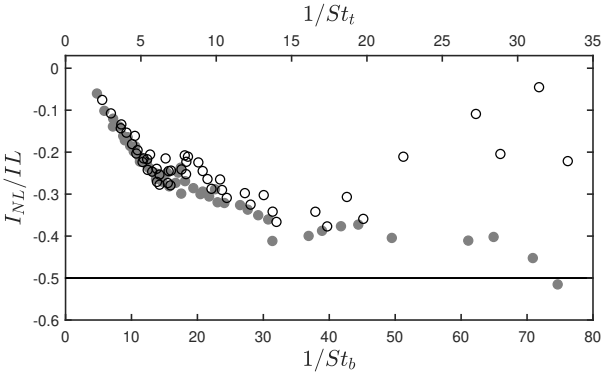

(b)

Figure 3.9. Change in *a*) slit resistance and *b*) slit inertance due to non-linearity for long (●) and short (○) slits as function of St_b and St_t for several amplitudes at the reference microphone ($\widehat{p}(x_{ref}) \geq 10\,\mathrm{Pa}$). In *a*) quasi-steady potential flow theory (——) and quasi-steady potential flow theory corrected for the effect of quasi-steady viscous boundary layer(- - -); in *b*) limit proposed by Ingard and Ising [125] (——).

At moderate amplitudes ($1/St_b < 20$) one observes a weak non-linear behavior reported by Ingard and Labate [123]. The vortices are formed at the edges, but they remain close to the slit. For $1/St_b > 20$ and higher amplitudes, the vortices start moving away from the slits. One observes in this region differences between long and short slits.

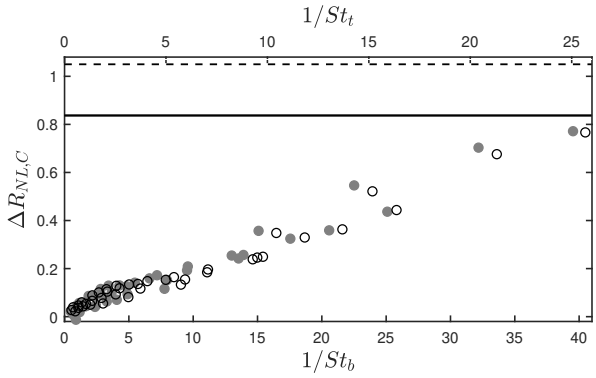

(a)

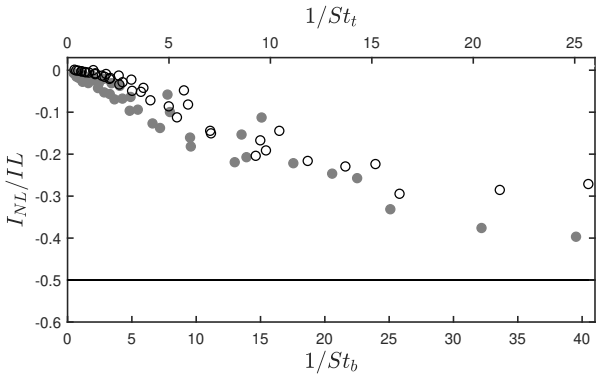

(b)

Figure 3.10. Change in *a*) slit resistance and *b*) slit inertance due to non-linearity for long (●) and short (○) slits as function of St_b and St_t for several amplitudes at the reference microphone ($\widehat{p}(x_{ref}) \leq 6\,\mathrm{Pa}$). In *a*) quasi-steady potential flow theory (——) and quasi-steady potential flow theory corrected for the effect of quasi-steady viscous boundary layer(- - -); in *b*) limit proposed by Ingard and Ising [125] (——).

For very high amplitudes $1/St_b > 50$ the behavior of the inertia of short and long slits is completely different. The flow for the short slits becomes essentially three-dimensional while it remains approximately two-dimensional for the long slits because of the confinement in the impedance pipe and hydro-dynamical interactions between slits. Differences for high amplitudes are most probably due to different

behavior of the synthetic jet (zero net mass flow) in 3D depending on the length of the aperture [132]. The difference in the slits (such as small surface perturbations in the edges) can generate different behavior of the jet and different spatial evolution of three-dimensional vortices. Examples of complex three-dimensional behavior of jets formed by a slit are the axis switching and forking [133, 134]. The behavior of short and long slits for low St_b is different. In axis switching, the lateral ends of the jet will curve towards the symmetry axis, so that, within a distance comparable to the jet width, an almost plane jet will be formed in a direction normal to the original jet. In forking, the planar jet breaks down into separate jets. These observations confirm that while the resistance is determined locally, the inertance is a more global flow effect.

3.6 Discussion and conclusions

In this Chapter, the effect of slit length on the linear and the non-linear acoustic transfer impedance of two accurately manufactured micro-slit plates has been investigated. The study is limited to sharp edges. Experimental data are obtained by impedance tube measurements. The frequency range of interest is $20\,\mathrm{Hz} < f < 700\,\mathrm{Hz}$ corresponding to Shear numbers in the range $1 < Sh_b < 6$. As for circular micro-perforations, the dissipation of sound occurs mainly at the edges of the micro-slits [23, 124]. Both in the linear and non-linear regimes, the resistance of a single slit is independent of the porosity of the plate and the slit length. Therefore, by dividing the transfer impedance of a slit by the porosity of the plate, one obtains an accurate prediction of the plate resistance for micro-slit plates. In the linear regime, an accurate prediction of the resistance of the plate is obtained using a two-dimensional numerical solution of the linearized Navier-Stokes equations in a single slit. In the non-linear regime, the plate resistance is strongly dependent on the amplitude of the acoustic waves. A simple quasi-steady model provides an order of magnitude for the asymptotic value of the non-linear resistance. Combining the results obtained in the present work for a specific geometry with the earlier studies on linear acoustical properties of micro-slits (see Aulitto *et al.* [124] and Temiz *et al.* [23]) one can conclude that the independence of resistance on the slit length is because the resistance is mainly determined by the local acoustic flow around the edges. Therefore, this observation is independent of the exact slit geometry. The inertance of slits is sensitive to the acoustic flow outside the perforations. This explains the strong difference between the behavior of slits and circular micro-perforations [124]. Also, one observes a small yet significant reduction of the inertance of short slits with respect to long slits. The linear inertance of long slits is accurately predicted by the locally two-dimensional incompressible numerical model. For moderate amplitudes, the non-linear inertance is not strongly affected by the slit length. For high amplitudes, one observes a strong deviation between the inertance of short and long slits.

For long slits, the inertance at very high amplitudes is reduced by a factor of 2 with respect to the linear case, as predicted by the intuitive model of Ingard and Ising [125]. For short slits, the amplitude dependency of the inertance is more complex due to three-dimensional effects. The weak dependency of the inertia on the slit length is also expected to be independent of the exact geometry of the slits. The non-linear behavior depends on the *vena contracta* factor, which is dependent on the details of the slit geometry [80, 115]. However, the fact that the slit length influences more the non-linear effects on the inertia than the resistance is expected to be independent of the details of the slit geometry. Hence, most conclusions drawn from the present study are expected to be quite general.

4

Onset of non-linear behavior in a micro-slit plate: analysis of experimental results and comparison with a two-dimensional model

Abstract - This Chapter focuses on the non-linear acoustic behavior of a micro-slit plate. The present work complements the findings of Chapter 3. The concept of an effective and amplitude-dependent acoustic transfer impedance is considered. A fit of the experimental results based on a quasi-steady model is proposed. The impedance tube measurements are compared with the results of a two-dimensional laminar incompressible viscous model. The two-dimensional numerical model provides a fair prediction of the changes in impedance due to non-linearities. The model is used to gain insight into the impact of the complex evolution of the vortex shedding as a function of the amplitude and frequency.

This chapter is based on:
A. Aulitto, A. Hirschberg, and I. Lopez Arteaga. Onset of non-linear behavior in a micro-slit plate: analysis of experimental results and comparison with a two-dimensional model. Submitted to Acta Acustica, January 2023.

4.1 Introduction

Micro-slit plates (MSPs) backed by a shallow cavity provide a lightweight solution for sound absorption in the low-frequency range [51]. MSPs are plates with slit widths in the sub-millimeter range and low porosity (order of 1%). Several studies describe the potential of slits in MSPs compared to that of circular perforations [52, 96, 99, 124, 135]. In Chapter 3, a geometry obtained by cutting the plate and bending the two portions close to the cut has been considered. This process is cheaper and more convenient than manufacturing circular perforations or slits in conventional ways (removing material), to obtain sub-millimeter slit widths. Impedance tube measurements on two accurately manufactured plates have been compared (in Chapter 3) to the numerical solution of the Linearized Navier-Stokes equations (LNSE) and analytical limits, for two-dimensional flows. In the linear regime, the two-dimensional model of a single slit provides a good prediction of the resistance and inertance of the plate. One finds a strong amplitude dependency and complex behavior in the non-linear regime. As suggested in several works, the presence of non-linear effects can deteriorate the performance of the absorbers [52, 58, 114, 115]. For micro-slit plates, the onset of such non-linear effects due to high acoustic amplitudes can occur in commonly encountered operating conditions.

In the present work, the authors complement the findings of Chapter 3 focusing on the effect of non-linearities on the acoustic behavior of the plate.

To our knowledge, there is little known about the generation of higher harmonics in the low-frequency range. The works of Cummings and Eversman [122] and Temiz *et al.* [115] focus on the time-domain signal generated at an orifice, while Richter investigates the time-domain impedance modeling of an acoustic liner [136].

To study the change in resistance and inertance of the plate as a function of the acoustic-excitation amplitude, an effective, amplitude-dependent, acoustic-transfer impedance is used. A fit of the experimental results is used to connect the change of resistance and inertance to dimensionless parameters connected to the frequency (Shear number) and the acoustic velocity. Experimental results are compared to a two-dimensional numerical model. The software used is Comsol Multiphysics v. 6 [94]. A model of the full plate with multiple slits is considered to capture interactions between slits at high acoustic-excitation amplitudes. The numerical model is further used to gain insight into the behavior of the plate due to vortex shedding and the formation of jets.

Sections 4.2 and 4.3 discuss the relevant parameters and the experimental setup. In Section 4.4.1, the two-dimensional numerical domain is presented. Section 4.5.1 proves the validity of the assumption of quasi-harmonic behavior in the range of amplitudes of interest for this study, considering the power spectral density of the acoustic pressure and justifying the use of the concept of acoustic impedance. Section 4.5.2 proposes a fit of the experimental results as a function of dimensionless parameters assuming the prior knowledge of the acoustic transfer impedance of

the plate in the linear case. This linear response was discussed in Chapter 3.
In Section 4.5.3, the results of the numerical model are compared to the experiments. Sections 4.5.4 and 4.5.5 show evolution in time of the vortex shedding as a function of the driving frequency and the acoustic-excitation amplitude.

4.2 Definitions

In the linear regime, the concept of transfer impedance is introduced in the frequency domain (for purely harmonic oscillations) of frequency f. The transfer impedance of the plate is defined as the ratio between the complex acoustic pressure difference $\Delta\widehat{p}$ and the amplitude of the acoustical velocity $\widehat{u}$ in a cross-section upstream of the plate. The pressure difference is found by the extrapolation of the plane-wave solutions (on both sides) to the sample surface. The dimensionless transfer impedance of the plate is

$$z_{plate} = \frac{\Delta\widehat{p}}{\rho c\widehat{u}} = Re[z_{plate}] + \mathrm{i}Im[z_{plate}], \tag{4.1}$$

with $\mathrm{i}^2 = -1$, $Re[z_{plate}]$ the resistive part of the transfer impedance of the plate (or resistance of the plate) and $Im[z_{plate}]$ the reactive part of the transfer impedance of the plate (or inertance of the plate). where ρ is the density of air and c is the speed of sound in air.
In the non-linear regime, the resistance due to vortex shedding at the edges of orifices dominates the absorption mechanism, as shown already by Ingard and Ising [125]. Aulitto *et al.* [137] presents an extensive description of the phenomena for the micro-slit geometry considered in this study. For low and moderate acoustic-excitation amplitudes, an effective, amplitude-dependent, impedance of the plate can be used to characterize the behavior of the plate. In the scope of this work, the changes in the resistance $\Delta\mathrm{Re}[z_{plate}]$ and inertance $\Delta\mathrm{Im}[z_{plate}]$ due to non-linear behavior with respect to the linear case are considered. In formulas, the relative changes are defined by

$$\frac{\Delta\mathrm{Re}[z_{plate}]}{\mathrm{Re}[z_{plate,linear}]} = \frac{\mathrm{Re}[z_{plate}] - \mathrm{Re}[z_{plate,linear}]}{\mathrm{Re}[z_{plate,linear}]} \tag{4.2}$$

and

$$\frac{\Delta\mathrm{Im}[z_{plate}]}{\mathrm{Im}[z_{plate,linear}]} = \frac{\mathrm{Im}[z_{plate}] - \mathrm{Im}[z_{plate,linear}]}{\mathrm{Im}[z_{plate,linear}]}. \tag{4.3}$$

The concept of an effective impedance is meaningful if the amplitude of the higher-order harmonics generated in the response signal is much lower than the amplitude at the fundamental, or driving, frequency. This signal is referred to as quasi-harmonic. In Section 4.5.1 the validity of this assumption is discussed for the experiments presented in Chapter 3. Two dimensionless parameters are considered, the Shear number (frequency) and the acoustic Strouhal number (amplitude).

The Shear number is the ratio between the slit width b and the thickness of the acoustic-viscous-boundary layer δ_v,

$$Sh = \frac{b}{\delta_v}, \tag{4.4}$$

with $\delta_v = \sqrt{2\mu/\omega\rho}$ [100], where $\omega = 2\pi f$ is the angular frequency, ρ is the air density ($\rho = 1.18\,kg/m^3$ at 25°C and atmospheric pressure) and μ is the dynamic viscosity of air ($\mu = 1.85 \times 10^{-5}\,kg/ms$ at 25°C). In a micro-slit plate, typical Shear numbers, in the frequency range of interest, are of order unity. The Strouhal number (St_b) is the ratio between the slit width b and the amplitude of the oscillating particle displacement at the slits. In formulas,

$$St_b = \frac{\omega b}{\widehat{u}_s}, \tag{4.5}$$

where $\widehat{u}_s$ is the cross-sectional surface averaged acoustic velocity amplitude at the slit ($\widehat{u}_s = \widehat{u}/\Phi$, with $\widehat{u}$ the uniform approaching velocity in the pipe). For $St_b >> 1$ (linear regime) the particle displacement is smaller than the slit width and vortices are not formed. For $St_b << 1$ (strongly non-linear), vortices are formed and move away from the slit forming a free jet. For $St_b \approx 1$ (moderately non-linear) vortices form at the edges of the slits and remain local [123]. The acoustic Reynolds number Re_{ac} is introduced as

$$Re_{ac} = \frac{2Sh^2}{St_b} = \frac{b^4 \frac{(\omega\rho)^2}{4\mu^2}}{\frac{(\omega b)^2}{\widehat{u}_s^2}} = \frac{\rho b \widehat{u}_s}{\mu}. \tag{4.6}$$

The relation between the acoustical velocity amplitude and the acoustical pressure amplitude is

$$|\widehat{u}_s| = \frac{|\widehat{p}|}{\Phi\rho c|z_{plate}|}, \tag{4.7}$$

with $|\widehat{p}|$ the acoustic pressure at the incident wave side of the plate and $\rho c z_{plate}$ the acoustic transfer impedance of the plate.

4.3 Experiments

For a description of the experimental setup and details of the sample geometry, the reader is directed to Chapter 3. In Figure 4.1, a picture of the sample is shown with next to it a sketch of the cross-section of a single slit. The plate thickness is $t_p = 5\,\text{mm}$ and the slit width is $b = 0.5\,\text{mm}$, with a porosity $\Phi = 2.7\%$. Note that the slit is parallel with the xz-plane and b is the width in the x-direction. The experimental setup used in this study is an impedance tube with 6 pre-polarized 1/4 in microphones (type BWSA, sensitivity 50 mV/Pa).

Figure 4.1. Sketches of the plate and the cross-section of a single slit.

The sensitivity of the microphones is known within 5% accuracy and the dynamic range is between 29 dB to 127 dB. The range of acoustic-excitation amplitudes is limited to 118 dB to avoid non-linearities in the response of the microphones. A script built-in *NILabView* software controls data acquisition and signal processing during the measurements. The amplitude of the excitation signal is provided in volts and it is adjusted automatically until it agrees within 2% with the predetermined value of the amplitude of the pressure fluctuation at the reference microphone (distant 45 mm from the plate). Here, the pressure is dominated by plane waves and uniform across the pipe cross-section. The quantities $\widehat{u}$ and $\widehat{p}$ are obtained from the acoustic-pressure signal $p(t)$ and velocity $u(t)$ using the Fourier transform. For this study, the sampling rate is 20 kHz for the excitation signal and 10 kHz for recording the input signal. An FFT of the time signal is considered. A Tukey window with cosine fraction 0.05 is used. For the velocity, the Fourier transform $\widehat{u}$ is related to $\widehat{p}$ measured at various positions of the pipe by assuming a plane waves propagation and deducing $\widehat{u}$ after correction for thermal/viscous attenuation [137].

4.4 Numerical model

In this section, the numerical model is presented. A two-dimensional numerical model of the plate containing three slits is considered. The software used is Comsol Multiphysics v. 6 [94].

4.4.1 Numerical domain

In Figure 4.2, the numerical domain is shown with the relevant parameters. The dimensions of the domain are chosen such that the porosity Φ_{2D} in the 2D-planar model (plate with three perforations each of width b placed in a channel of with a), is the same as the porosity of the actual sample when placed in the impedance tube ($\Phi = 2.7\%$).

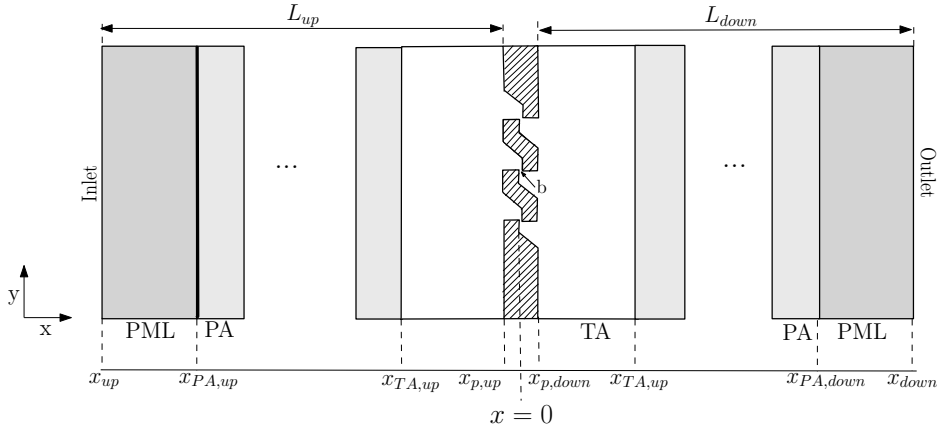

Figure 4.2. Schematic representation of the numerical domain. The slit entrance is placed at $x = 0$. The central slit is located at $y = 0$ and the other slits at $y = \pm 9\,\text{mm}$.

Table 4.1. Locations in the numerical domain represented in Figure 4.2

x	x_{in}	x_{out}	$x_{PA,up}$	$x_{PA,down}$	$x_{TA,up}$	$x_{TA,down}$
mm	−662.25	662.75	−612.25	612.75	−120.25	120.75

The porosity $\Phi_{2D} = 3b/a$ is obtained as the ratio between the width of the three slits $3 \times b$ and the channel height a. The slit width is $b = 0.5\,\text{mm}$, the confinement is $a = 56\,\text{mm}$. The distance between two slits is the same as for the sample, $d_s = 9\,\text{mm}$. The center ($x = 0$) is positioned at the slit inlet and the plate has a thickness of $t_p = 5\,\text{mm}$. Relevant positions are summarized in Table 4.1. The upstream and downstream duct lengths are $L_{up} = 660\,\text{mm}$ and $L_{down} = 660\,\text{mm}$. The numerical domain extends between x_{in} and x_{out}, where a perfectly matched layer of thickness $L_{PML} = 50\,\text{mm}$ is present on both sides (in gray in Figure 4.2). The PML layer is added to the acoustic model to mimic a non-reflecting pipe termination.
At $x_{PA,up}$, a downstream travelling pressure wave

$$p_+ = p_0 e^{(-ik_0 x)} \tag{4.8}$$

and an associated particle velocity

$$u_+ = -\frac{1}{\mathrm{i}\rho\omega}\frac{\partial p_+}{\partial x} \tag{4.9}$$

are generated, with $k_0 = \omega/c$ and x the direction of the flow propagation. Because $a/\delta_v >> 1$, viscous effects in the duct are neglected.

The amplitude p_0 is chosen to simulate different acoustic-excitation amplitudes. Between $x_{PA,up}$ and $x_{TA,up}$ and between $x_{PA,down}$ and $x_{TA,down}$, the scalar wave equation in the time domain is solved (Pressure acoustic interface [138]). Between $x_{TA,up}$ and $x_{TA,down}$, the perturbation formulation of the Navier-Stokes equations, including the non-linear contributions, in quiescent background conditions are considered. The continuity, momentum, and energy equations are solved to model the transient propagation of acoustic compressible waves (Thermoviscous Acoustic Model [139, 140]). Furthermore, the walls of the domain are modeled with no-slip boundary conditions, and isothermal conditions are applied.

4.4.2 Acoustic transfer impedance

The simulations run for $15T_0$ with $T_0 = 1/f$, and f the driving frequency ($f = f_f$). Considering the portion of domain between $x_{up} = -30\,\text{mm}$ and $x_{down} = 30\,\text{mm}$, in the frequency range of interest ($f \leq 220\text{Hz}$ and $\lambda = 1400\,\text{mm}$), the domain length is much smaller than the acoustic wavelength. Therefore, one can assume a locally incompressible flow, within the plate. This is confirmed by density variations being of order 10^{-4}. At the positions x_{up} and x_{down}, the cross-sectional acoustic velocity and pressure are calculated to obtain the acoustic transfer impedance of the plate. The cross-sectional averaged time signals for the pressure $p(t)$ and for the velocity $u(t)$ are extracted at x_{up} and x_{down}. A fast Fourier transform is applied on the last 5 periods of oscillations in the signal. Comparison with previous 5 periods does not show a significant difference in the range of amplitudes considered. The response in terms of pressure p_{up}, p_{down} and velocity u_{up}, u_{down} at the fundamental frequency f_f is extracted. The pressure difference $\Delta p = \Delta\widehat{p}\exp i\omega t$ used to calculate the plate transfer impedance z_{plate} (Equation 4.1) is determined using the linear extrapolation of the acoustic pressure in the plane-wave regions to both sides of the plate ($x_{p,up} = 2.25\,\text{mm}$ and $x_{p,down} = 2.75\,\text{mm}$).
The pressures extrapolated at the two sides of the plate are

$$p_{p,up} = p_{up} + 2\pi f_f \mathrm{i} u_{up}(x_{up} - x_{p,up}), \tag{4.10}$$

$$p_{p,down} = p_{down} + 2\pi f_f \mathrm{i} u_{down}(x_{down} - x_{p,down}). \tag{4.11}$$

The dimensionless acoustic transfer impedance of the plate is obtained as

$$z_{plate} = \frac{p_{p,up} - p_{p,down}}{\rho c u_{up}}. \tag{4.12}$$

4.5 Results

4.5.1 Validity of the quasi-harmonic assumption

To demonstrate the validity of the assumption of quasi-harmonic oscillations, the experimental results, in absence of bias flow, corresponding to the highest acoustic

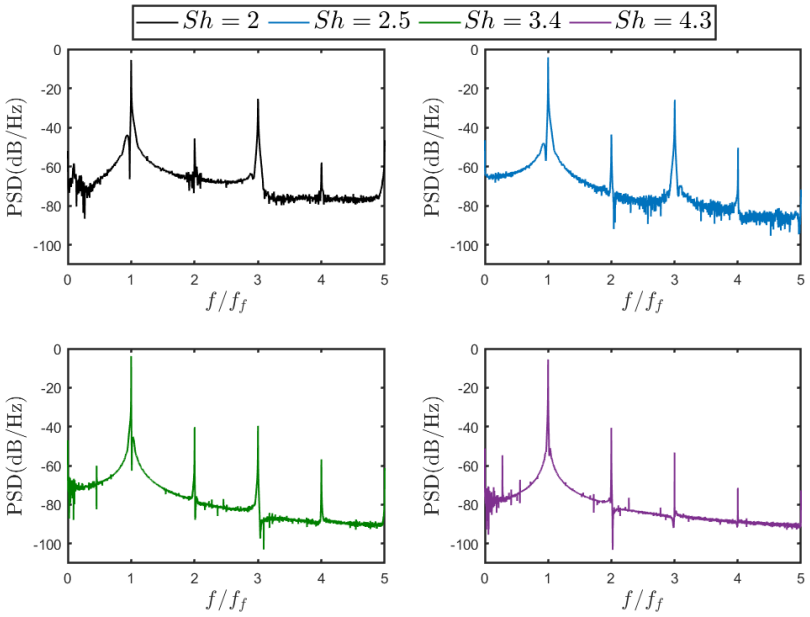

Figure 4.3. Power spectral density of the acoustic pressure PSD (dB/Hz) as a function of the dimensionless frequency f/f_f for different Shear numbers Sh at the same incident amplitude $\widehat{p}/\widehat{p}_{linear} = 57.5$.

amplitude ($\widehat{p}_{ref} = 23\,\text{Pa}$, $\widehat{p}/\widehat{p}_{linear} = 57.5$) are considered for four Shear numbers $Sh = 2, 2.5, 3.4$ and 4.3. Table 4.2 shows the values of the corresponding excitation frequencies. In Figure 4.3, the power spectral density of the acoustic pressure is presented as a function of the frequency, normalized with the fundamental frequency. The range shown in the figure is limited to the first four harmonics. For all the Shear numbers shown, the highest peak (corresponding to the fundamental frequency) is at least 20 dB higher than the second (or third) peak. This corresponds to an order of magnitude difference in the amplitudes. The power spectral density is then integrated over a narrow frequency range df around the peaks. The frequency range is chosen considering the 3dB decay. The results are fairly independent of the exact value of df (within 1%). The integrals correspond to the square of the amplitude of a pure sine. Hence, the square root of the power ratio (SPR) between the first and the second peak in Figure 4.3 provides the amplitude ratio between the second-order harmonic and the fundamental frequency. Results are summarized in Table 4.2. One finds at least an order of magnitude difference in amplitude between the fundamental frequency and higher harmonics. Hence, the assumption of the quasi-harmonic oscillations and the definition of an effective impedance is meaningful.

Table 4.2. Square roots of the power ratios (SPR) of the second ($2f_f$), third ($3f_f$), and fourth ($4f_f$) with respect to the fundamental frequency for several Shear numbers.

Sh	Fundamental frequency	SPR $2f_f$	SPR $3f_f$	SPR $4f_f$
2	80 Hz	1.2×10^{-2}	1.3×10^{-1}	3.2×10^{-3}
2.5	120 Hz	1.3×10^{-2}	9.2×10^{-2}	4.7×10^{-3}
3.4	220 Hz	1.6×10^{-2}	1.8×10^{-2}	2.9×10^{-3}
4.3	360 Hz	1.6×10^{-2}	3.4×10^{-3}	5.2×10^{-4}

For $Sh < 3.4$, the amplitude of the second harmonic is smaller than the third harmonic. This effect is amplitude-independent. The disappearance of the second harmonic of the response is also found in the case of the organ pipe. In those cases, the reduced amplitude of the second harmonic is connected to symmetries in the position of the labium relative to the impinging jet axis [141–143]. For the geometry considered in the study, this suggests a more symmetric pattern between the upstream and downstream sides of the plate for lower Strouhal numbers. This could be due to a dependency on the history of the vortex shedding on a reduction by large displacement amplitudes of the influence of residual vorticity near the slits. This is discussed more in detail using flow visualization obtained using the 2-D flow model (see Figure 4.11).
Another interesting point of discussion is the behavior around the fundamental frequency with a dip just before the first peak in the spectrum. Such dip moves from the left of the high peak ($Sh = 2, 2.5$), to the right ($Sh = 3.4, 4.3$) as the Shear number is increased and it is smaller for higher Shear numbers. Due to the presence of the dip at one side of the peak, this effect does not seem to be due to amplitude modulation but a frequency modulation due to transient effects could be possible. However, the effect seems to be independent of the windowing and clipping of the time signal. Finally, dips are also observed around the peaks of higher harmonics.

4.5.2 Fit of the experimental results

In this Section, a fit of the experimental results is proposed for the change in resistance and inertance due to non-linearities.
The linear resistance and inertance of the plate can be obtained as in Chapter 3 with numerical simulations or, in the case of the resistance, using the expression for a plate with sharp square edges [124]. In Chapter 3, the change of resistance due to non-linear effects is a function of the quasi-steady limit $\rho\widehat{u}_s/2Cv^2\Phi$ [137].

Following the proposed quasi-steady theory,

$$\Delta\mathrm{Re}[z_{plate}] = \frac{4}{3}\frac{\mu}{\rho b c}\frac{1}{C_v^2}\Phi^2\frac{Re_{ac}}{\left(1-\sqrt{\frac{9}{2}\frac{0.45}{Re_{ac}}}\right)^2}. \tag{4.13}$$

A fit of the results as a function of the Reynolds number is considered. The change in resistance can be expressed as

$$\frac{\Delta\mathrm{Re}[z_{plate}]}{\mathrm{Re}[z_{plate,linear}]} = \frac{-2.8\times10^{-3}}{1+3.55\times10^{1}Sh-1.98\times10^{3}St_b-2.38\times10^{4}\frac{1}{Re_{ac}}}. \tag{4.14}$$

The coefficient of determination R^2 for $\Delta\mathrm{Re}[z_{plate}]/\mathrm{Re}[z_{plate,linear}]$ is 0.96 [112]. In Figure 4.4, the experimental results, the results of the fit, and the quasi-steady model are shown as functions of the acoustical Reynolds number, with each curve corresponding to a different Shear number.

It can be seen that in the range considered, the quasi-steady behavior is only approached at the highest Reynolds number values. Furthermore, whereas the fit does give a global description of the change of non-linear resistance, details in the low amplitudes range are not accurately captured. The change of resistance seems to have, in the low Reynolds numbers range, a quadratic dependence on the velocity. Therefore, a fit of the results containing a dependency on the square of the amplitude is considered.

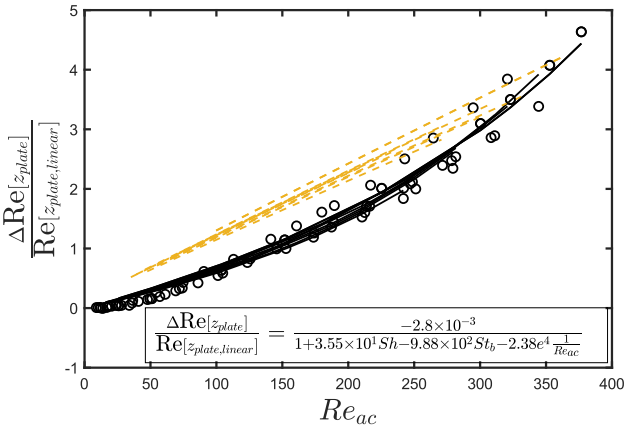

Figure 4.4. Change of the real part of the acoustic transfer impedance of the plate as a function of $Re_{ac} = \frac{\rho b\widehat{u}_s}{2\mu}$ [137]. Different curves correspond to different Shear numbers, $Sh = [2.05, 3.39]$. (○) Experimental results, (- - -) Quasi-steady model, (——) Fit lines.

The change in resistance can be expressed as

$$\frac{\Delta \mathrm{Re}[z_{plate}]}{\mathrm{Re}[z_{plate,linear}]} = \frac{-4.6}{1 - 0.63Sh + 61.3St_b^2 - 9.28 \times 10^4 \frac{1}{Re_{ac}^2}}. \tag{4.15}$$

The coefficient of determination $1-R^2$ for $\Delta \mathrm{Re}[z_{plate}]/\mathrm{Re}[z_{plate,linear}]$ is 0.98 [112], which is significantly better than the previous fit. A drawback of this fit is that it cannot be extrapolated to very high Reynolds numbers, at which a quasi-steady behavior is expected to prevail. In Figure 4.5, the fit with the square of the amplitude provides a better approximation for low Reynolds numbers since, at low amplitudes, the main contribution at the denominator of Equation 4.15 is the term containing $1/Re_{ac}^2$, with only this term shown in Figure 4.6. It appears that this simple fit well captures the behavior for low Reynolds numbers. Deviations for higher Reynolds numbers are mostly due to frequency effects. The contribution of the terms containing the shear number and the Strouhal number becomes important only for high acoustic amplitudes.

A fit for the change of inertance is also proposed with

$$\frac{\Delta \mathrm{Im}[z_{plate}]}{\mathrm{Im}[z_{plate,linear}]} = \frac{-0.29Sh^2(1 - 0.075Sh^2)}{Sh^2 - 0.077Sh^4 + 2.07e2St_b^2}. \tag{4.16}$$

The coefficient of determination for $\Delta \mathrm{Im}[z_{plate}]/\mathrm{Im}[z_{plate,linear}]$ is 0.96 [112]. The change in inertance is strongly dependent on the Strouhal number, hence, on the combination of frequency and acoustic amplitude.

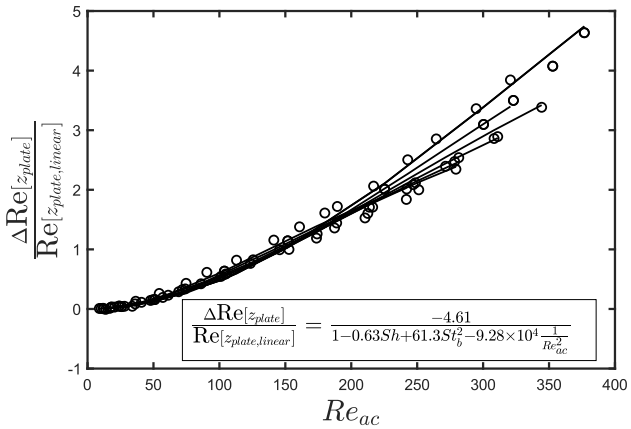

Figure 4.5. Change of the real part of the acoustic transfer impedance of the plate as a function of $Re_{ac} = \frac{\rho b \widehat{u}_s}{2\mu}$ [137]. Different curves correspond to different Shear numbers, $Sh = [2.05, 3.39]$. (○) Experimental results, (——) Fit lines.

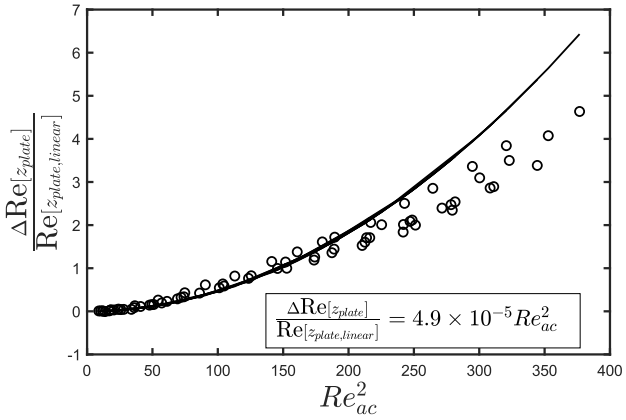

Figure 4.6. Fit of the experimental results as a function of $4.9 \times 10^{-5} Re_{ac}^2$ for the change in the real part of the acoustic transfer impedance of the plate as a function of $Re_{ac} = \frac{\rho b \widehat{u}_s}{2\mu}$ [137]. Different curves correspond to different Shear numbers, $Sh = [2.05, 3.39]$. (○) Experimental results, (——) Fit lines.

In Figure 4.7, the results of the fits are compared with the experimental results both for the resistance and for the inertance as a function of the inverse of the Strouhal number. This representation is chosen to observe the collapse at high Strouhal numbers, with a convergence of all lines.

4.5.3 Comparison of experiments and numerical results

In this section, the changes in the real and imaginary parts of the impedance due to non-linearities are discussed. Experimental results are compared to the results of two-dimensional numerical simulations.
In Figure 4.8, $\Delta\mathrm{Re}[z_{plate}]/\mathrm{Re}[z_{plate,linear}]$ and $\Delta\mathrm{Im}[z_{plate}]/\mathrm{Im}[z_{plate,linear}]$ are shown as a function of the inverse of the Strouhal number $1/St_b$ for four Shear numbers ($Sh = 2, 2.5, 2.9, 3.4$), where numerical results are represented as full lines and experiments with symbols. Higher values of $1/St_b$ correspond to higher acoustic-excitation amplitudes. This figure focuses on the onset of non-linearities ($1/St_b < 10$). The changes in resistance and inertance due to non-linearities appear to be both amplitude (Strouhal number) and frequency(Shear number) dependent. While the resistance increases with amplitude and frequency with respect to the linear case, the inertance decreases with the amplitude, and the decrease is steeper for higher frequencies. One observes that, globally, the two-dimensional numerical model provides a fair prediction of the results for low and moderate acoustic amplitude for both resistance and inertance, where the largest differ-

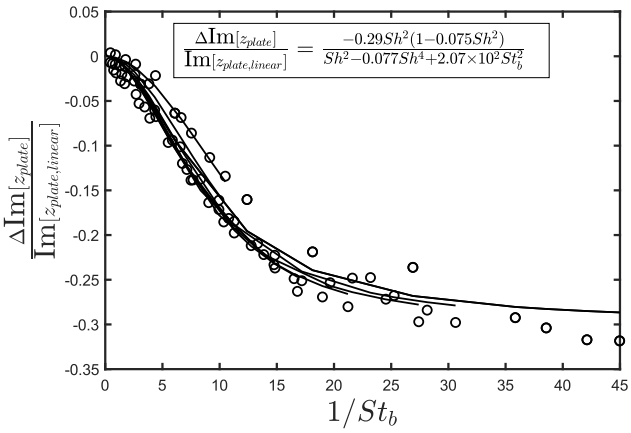

Figure 4.7. Fit of the experimental results for the change in the imaginary part of the acoustic transfer impedance of the plate as a function of the inverse of the Strouhal number $St_b = \omega b/\widehat{u}_s$. Different curves correspond to different Shear numbers, $Sh = [2.05, 3.39]$. (○) Experimental results, (——) Fit lines.

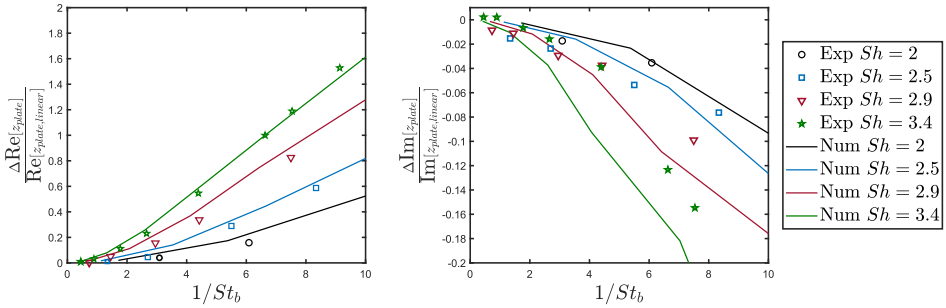

Figure 4.8. Comparison of numerical predictions and experimental results of the changes in the real and imaginary parts of the acoustic transfer impedance of the plate as a function of the inverse of the Strouhal number $St_b = \omega b/\widehat{u}_s$ for several Shear numbers. Results are limited to $1/St_b < 10$.

ences are found in the inertance. Figure 4.9 presents the same results on a larger range of Strouhal numbers that extends the experimental range ($1/St_b < 50$). For higher amplitudes, deviations between the numerical and the experimental results increase with the numerical model underestimating the resistance and overestimating the inertance. Such deviations could be explained by considering intrinsic differences between two-dimensional numerical simulations and experiments. Firstly, in the two-dimensional simulations, turbulence and three-dimensional ef-

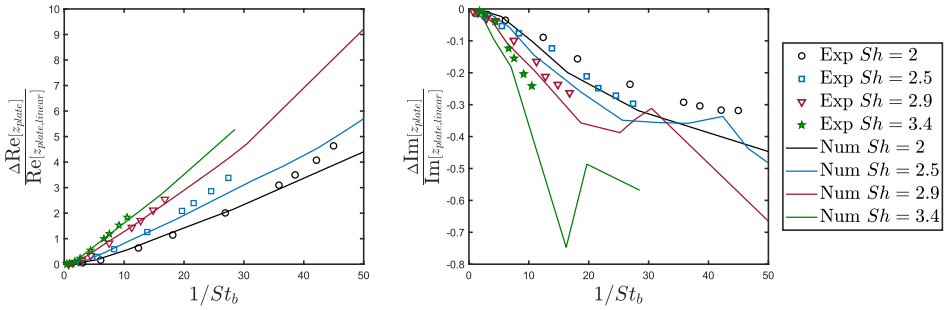

Figure 4.9. Comparison of numerical and experimental prediction of the changes in the real and imaginary parts of the acoustic transfer impedance of the plate as a function of the inverse of the Strouhal number $St_b = \omega b/\widehat{u}_s$ for several Shear numbers.

fects are absent. Secondly, in 2D, dissipation is lower and one expects vortices to persist longer, inducing significant (spurious) perturbations on the predicted flow during following oscillation periods and in neighboring slits. For high amplitudes, the inertance shows a complex behavior. One observes a minimum of inertance as the Strouhal number is decreased. The asymptotic value is of the order of $\Delta Im[z_{plate}]/Im[z_{plate-linear}] = -0.5$ as found when the inertance vanishes at the jet side of the slit (reference Chapter 3). This requires further study in terms of mesh convergence and longer numerical simulations to draw definitive conclusions. Note that Burgmayer *et al.* [144] also found a more complex nonlinear behavior for the inertance than for the resistance in circular perforations. In particular, they found a very similar minimum in the non-linear contribution to the inertance as a function of the Strouhal number, as the one predicted by the proposed 2D model. Overall, the two-dimensional numerical results provide a fair prediction of the experiments with deviations in the order 6% in resistance for low $1/St_b$. These deviations increase to a maximum of 13% for higher $1/St_b$, while deviations on the inertance are around 15%.

4.5.4 Evolution of the vortex shedding with amplitude

In this section, for a fixed Shear number $Sh = 2.5$, the two-dimensional numerical model is used to gain insight into the change in the vortex shedding with the acoustic excitation amplitude. Note that the domain (shown in Figure 4.2) is not symmetric, since the first (top) slit is closer to the wall than the third (bottom) slit. Figure 4.10, shows a portion of the numerical domain. The evolution of the vortex for increasing acoustic-excitation amplitude (p_0) is presented for increasing values of $1/St_b$. The spatial distribution of the amplitude of the velocity is shown by using a grayscale, which is presented next to each picture for reference.

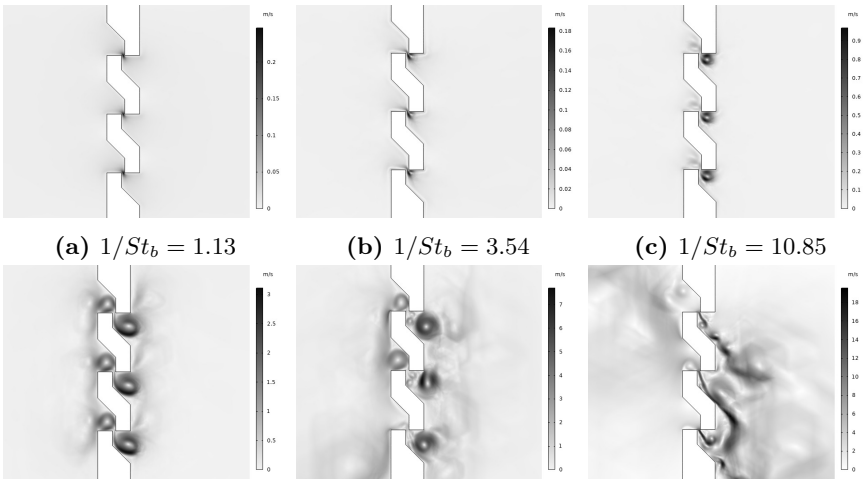

(a) $1/St_b = 1.13$ **(b)** $1/St_b = 3.54$ **(c)** $1/St_b = 10.85$

(d) $1/St_b = 25.6$ **(e)** $1/St_b = 51.08$ **(f)** $1/St_b = 118.25$

Figure 4.10. Jet evolution for increasing amplitudes (inverse of the Strouhal number $1/St_b$) at Shear number $Sh = 2.5$. Zoom of Figure 4.2.

The first picture (Figure 4.10a) shows the flow for $1/St_b = 1.13$ at which the orifice response is almost linear and no vortices are visible. For $1/St_b = 3.54$ (Figure 4.10b), small vortices appear near the edges of the slits and remain local and Figure 4.10c shows for $1/St_b = 10.85$ a larger vortex that remains within the cavity downstream of the slit. For increasing amplitudes (Figure 4.10d) at $1/St_b = 25.6$ one sees the vortex growing in size and the presence of residual vorticity remaining in the cavities after inversion of the flow direction, while the formation of a small secondary vortex is also observed within the downstream cavity. At higher amplitudes ($1/St_b = 51.08$), Figure 4.10e shows that the vortex moves from the edges of the slit to the exit of the cavity downstream and smaller secondary vortices are formed within the cavity. One sees differences in the vortex shedding between different slits. In particular, there are large differences in the residual vortices observed upstream of the slits. Finally, for $1/St_b = 118.25$ (Figure 4.10f), one observes a vortex sheet and jets that attach to the walls of the cavities. The behavior is quite chaotic and significant interactions between slits are observed. The flow is not symmetric between the two sides and significant differences between slits are observed.

4.5.5 Evolution of the vortex shedding with frequency

In this section, results for the highest amplitude $\widehat{p}/\widehat{p}_{linear}$ are shown for different Shear numbers. Figures 4.11-4.13 (at the end of the Chapter) show the evolution in time of the vortex shedding for $Sh = 1$, $Sh = 2$ and $Sh = 3.4$.

For $Sh = 1$ (Figure 4.11), the inverse of the Strouhal number is $1/St_b = 200$. One observes that for each slit, the vortices rapidly evolve into a jet that attaches to the lower wall of the downstream cavity. Outside the cavity (downstream of the plate), the jets are merging, and complex behavior is found. There is no significant asymmetry between the vortex shedding upstream and downstream. For $Sh = 2$ (Figure 4.12), one finds $1/St_b = 75.5$ and the single vortices are still visible as they move towards the outside of the cavity. One sees some difference between the shedding on the two sides of the plate. For example, in Figure 4.12, small vortices are formed and the jet is not perfectly attached to the walls. Downstream, the jet is fully attached to the wall and the vortices are mainly formed outside of the cavity. For $Sh = 3.4$ (Figure 4.13), differences between the two sides are also visible, resulting in large differences in the flows between slits. The Strouhal number in this case is lower $1/St_b = 19.5$. One sees interactions between slits on the downstream side. Note that the transfer impedance is mainly determined by the behavior within the cavities. The flow outside the cavities is only important when it results in a strong interaction between slits. This analysis seems to confirm the suggestion of Section 4.5.1, that for lower Strouhal numbers the behavior of the flows on both sides of the plate is symmetric. This symmetry explains the reduction of the even-order harmonics of the pressure signal compared to higher Strouhal number cases. Indeed, for perfectly symmetric flows, the even harmonics would disappear.

4.6 Discussion and conclusions

In this work, we focus on the effect of the onset of non-linearities on the acoustic behavior of a micro-slit plate, corresponding to amplitudes at which the concept of impedance can be used because the signal is almost harmonic. This study follows the research of Chapter 3 on a plate with geometry inspired by cutting and bending the plate [137]. For the amplitude range considered in this study, the amplitude of higher-order harmonics is at least one order of magnitude lower than the amplitude of the response at the fundamental frequency. Therefore, an effective and amplitude-dependent acoustic transfer impedance of the plate is defined. One does observe the significant presence of higher-order harmonics, often ignored in the literature. A quasi-steady model is used to propose a fit of the experimental results to study the effect of frequency and amplitude of the acoustic waves on the change in resistance and inertance due to non-linear behavior.
Two-dimensional numerical simulations are compared to impedance tube experiments. The two-dimensional numerical model provides a fair prediction of the change in resistance and inertance due to non-linear behavior and insight into the behavior of the acoustic field. One finds complex behavior of the inertance similar to the behavior for circular perforations [144] and significant interactions between neighboring slits for high amplitudes.

Three-dimensional effects, turbulence, residual effects, and low dissipation can potentially explain the differences found at high amplitudes between experiments and numerical simulations.
The numerical model is further used to study the evolution of the vortex shedding for increasing amplitudes. At low amplitudes, one finds local vortex shedding around the edges of the plate. For increasing amplitudes, the vortices move further away from the slit and disappear downstream of the plate for high amplitudes. Symmetries in the vortex shedding appear to be Strouhal number dependent and correspond to the reduction of even-order harmonics of the pressure signal for low Strouhal numbers (low frequencies).

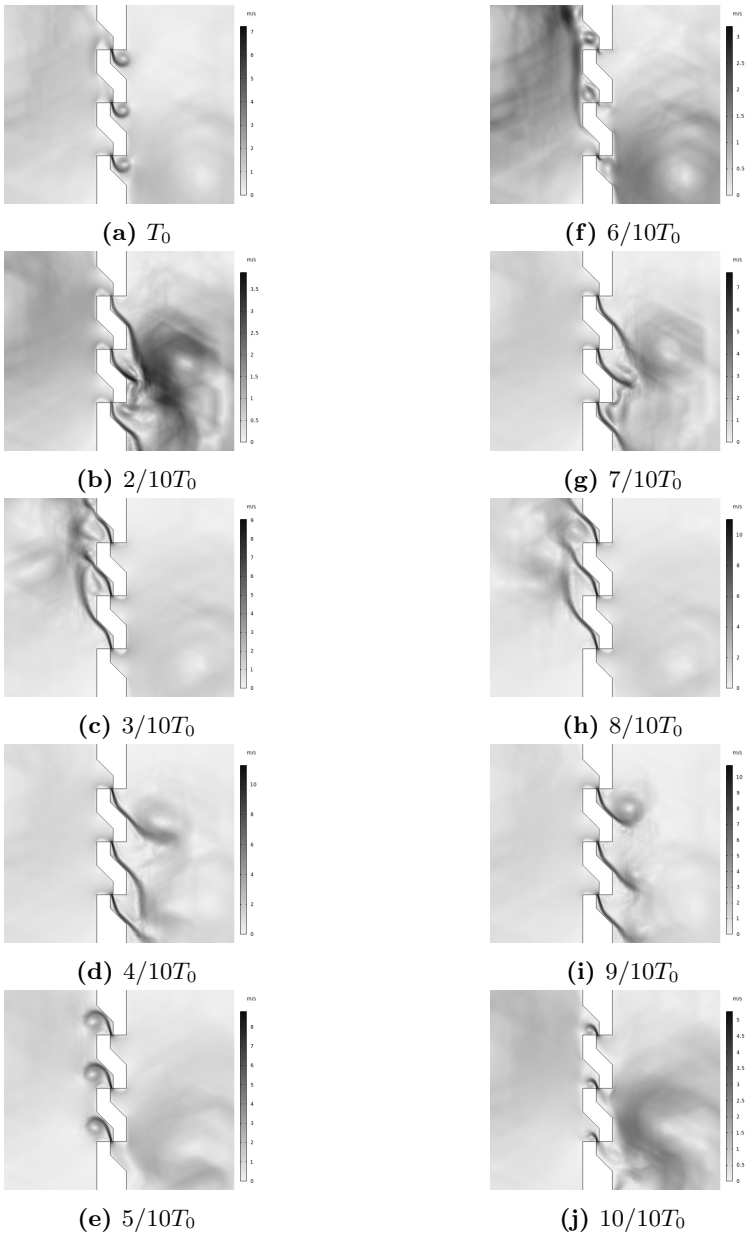

(a) T_0 **(f)** $6/10T_0$

(b) $2/10T_0$ **(g)** $7/10T_0$

(c) $3/10T_0$ **(h)** $8/10T_0$

(d) $4/10T_0$ **(i)** $9/10T_0$

(e) $5/10T_0$ **(j)** $10/10T_0$

Figure 4.11. Jet formation and oscillations for one period corresponding to $Sh = 1$ at incident amplitude $p_0/p_{0,linear} = 280$. The corresponding inverse of the Strouhal number is $1/St_b = 200$.

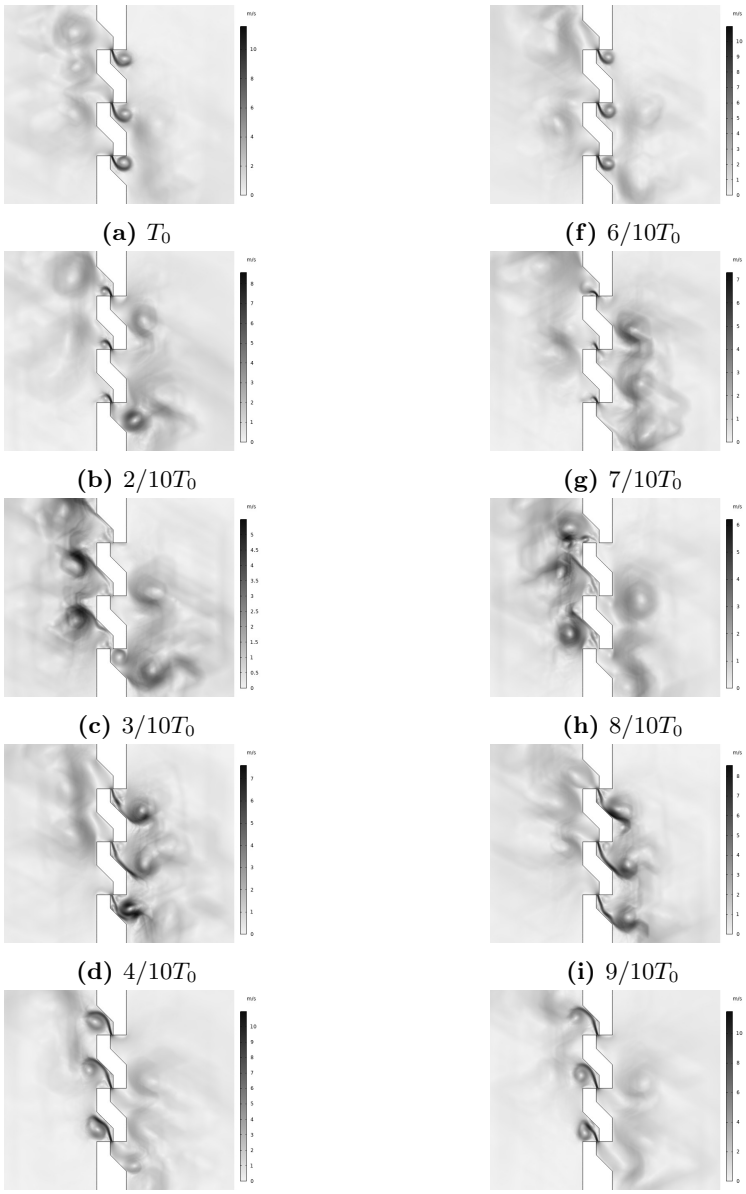

(a) T_0 **(f)** $6/10T_0$

(b) $2/10T_0$ **(g)** $7/10T_0$

(c) $3/10T_0$ **(h)** $8/10T_0$

(d) $4/10T_0$ **(i)** $9/10T_0$

(e) $5/10T_0$ **(j)** $10/10T_0$

Figure 4.12. Local vortices evolving into jets corresponding to $Sh = 2$ at incident amplitude $p_0/p_{0,linear} = 280$. The corresponding inverse of the Strouhal number is $1/St_b = 75.5$.

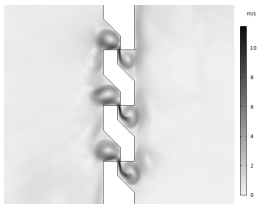

(a) T_0

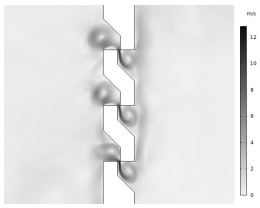

(f) $6/10T_0$

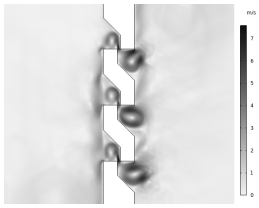

(b) $2/10T_0$

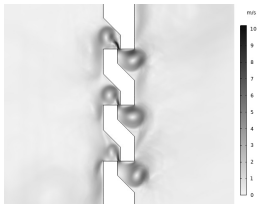

(g) $7/10T_0$

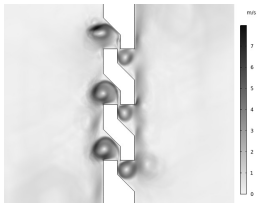

(c) $3/10T_0$

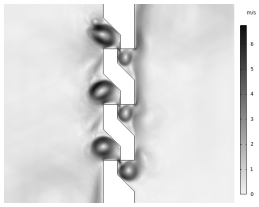

(h) $8/10T_0$

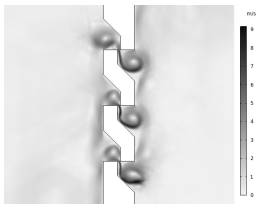

(d) $4/10T_0$

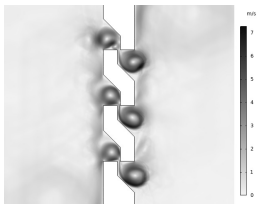

(i) $9/10T_0$

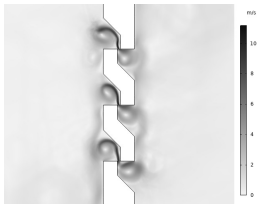

(e) $5/10T_0$

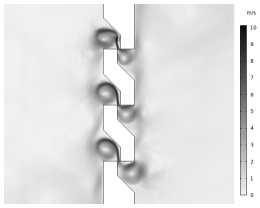

(j) $10/10T_0$

Figure 4.13. Vortices inside the cavities and residual effects corresponding to $Sh = 3.4$ at incident amplitude $p_0/p_{0,linear} = 280$. The corresponding inverse of the Strouhal number is $1/St_b = 19.5$.

5

Effect of a bias flow on the acoustic transfer impedance of a micro-slit plate in the linear regime

Abstract - Micro-Slit plates (MSPs) are plates with arrays of slit-shaped perforations, with the width of the order of the viscous-boundary-layer thickness. In this Chapter, the effect of a bias flow on the acoustic transfer impedance of a micro-slit plate is investigated in the linear regime for a specific slit geometry. This geometry is inspired by slits obtained by cutting and bending the plate and proposes an alternative to slanted perforations. In the presence of a bias flow, a wall jet is formed by the coalescence of the jets emerging downstream of the plate. This can provide film cooling to the wall. The behavior of the plate in the presence of a steady bias flow is characterized in the terms of the discharge coefficient. The discharge coefficient is qualitatively well predicted by a two-dimensional viscous-incompressible-flow model, except for deviations associated with whistling that is ignored in the model. Numerical solutions of the two-dimensional Linearized Navier-Stokes equations in the presence of a steady flow are compared to the acoustic transfer impedance measured using an impedance tube. The geometry of the slits is found to have a significant impact on their acoustic behavior. The interaction between neighboring slits generates complex Reynolds number dependency of the results with oscillations as a function of the Strouhal number based on the bias flow velocity. This effect does not occur for a single slit and is drastically reduced by increasing the distance between neighboring slits. A quasi-steady model based on the average velocity in the slit predicts the order of magnitude of the resistance. The inertance shows complex behavior, which is qualitatively predicted by the two-dimensional model.

This Chapter is based on:
A. Aulitto, V. Saxena, A. Hirschberg, and I. Lopez Arteaga. Effect of a bias flow on the acoustic transfer impedance of a micro-slit plate in the linear regime. Submitted to Journal of Sound and Vibration in February 2023

5.1 Introduction

In aero-engines and combustion chambers of gas turbines, multi-perforated liners are used to provide film cooling of the walls. These liners can also mitigate the rising of thermo-acoustic instabilities by damping acoustic energy. The presence of a bias flow through the orifices impacts the absorption characteristics of the liner and several models can be found in the literature to account for the effect of flow. Extensive research has been performed on the so-called *bias flow liners* and a recent review of such publications is presented by Lahiri and Bake [6]. Focus is given to studies with inclined perforations (tilted downstream), so-called *slanted perforations* or *grazing effusion holes*. For these geometries, the micro-jets coalesce downstream of the plate and form a cooling film along the wall that protects the wall surface from hot gasses [84]. Some works focus on inclined holes [87–91]. Other works study the effect of the geometry on the properties of these liners [34, 145–148]. Most of the models in the literature focus on single holes, applying periodic boundary conditions for the modeling of arrays of perforations. Multiple co-flowing jets can display strong hydrodynamic interactions leading to collective oscillations [149, 150]. Such effects are usually ignored when focusing on a single perforation and applying periodic boundary conditions suppresses jet interactions involving opposite movements of neighboring jets. However, studies report global flow instabilities occurring in a row of cavities due to a vorticity mode amplification [151–153] and similar effects are observed for sequences of Helmholtz resonators in the presence of a grazing flow [154, 155]. Whistling and sound amplifications are also found in corrugated pipes [156–158] and some cases involve hydrodynamic interaction between successive cavities [157]. While Hirschberg *et al.* [159] focus on a whistler nozzle as an aero-acoustic sound source, Testud *et al.* [78] and Lacombe *et al.* [79] focus on whistling of orifices. and several works of Anderson analyze the whistling of orifices in a pipe [160–163]. Instead of circular holes, Moers *et al.* [92] and Tonon *et al.* [93] consider oblique slits showing improved sound absorption compared to orthogonal perforations (with flow direction normal to the plate).

Micro-slit absorbers and plates (MSAs, MSPs) have been proposed as sound absorbers at low frequencies, providing lightweight and compact solutions to substitute conventional materials such as acoustic foams and porous materials [51]. MSPs are plates with slit widths in the sub-millimeter range and low porosity (order of 1%). In conventional designs, micro-slit plates are backed by a cavity, forming micro-slit absorbers (MSAs). Each micro-slit can replace a large number of circular perforations, keeping the same porosity. Several studies describe the potential of slits in MSAs, as sound absorbers, compared to that of circular perforations [52, 96, 99, 135] and a slit can also be used to delimit flexible structures [55–57, 72, 73]. Slanted holes and slits are expensive to manufacture in conventional ways. In Aulitto *et al.* [137], the geometry presented in Figure 5.1 is obtained by cutting the plate (without removing material) and bending the two

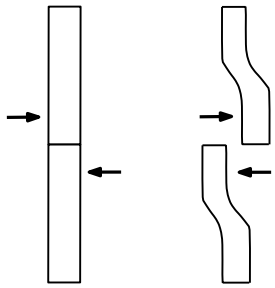

Figure 5.1. Schematic representation of a slit in a plate obtained by punching the two sides of the plate, in opposite directions.

portions close to the cut. This manufacturing process is cheaper and easier than the production of circular perforations or slits in conventional ways, obtaining sub-millimeter slit widths. An example of this manufacturing technique can be found in the Acustimet plates of Sontech [54, 113]. In this Chapter, the potential of the plate geometry shown in Figure 5.1 as a bias flow liner is investigated. This geometry could present a cheaper alternative to slanted perforations, keeping equivalent characteristics. Due to the particular manufacturing process, cavities are formed in the plate upstream and downstream of each slit. Because of the multiple-slits configuration, in the presence of a bias flow, the individual jets tend to attach to the wall of the cavity downstream of each slit. Figure 5.2 shows that downstream of the plate, the jets are coalescing and the combination of multiple slits creates the same effect of film cooling as grazing effusion holes.
This work is a first step toward optimizing the geometry of the slits to obtain an affordable and easy solution for a bias flow liner with film cooling. Firstly, the behavior of the plate in the presence of a bias flow is characterized in terms of the discharge coefficient. Secondly, the acoustic response of the plate is investigated in terms of the acoustic transfer impedance in the presence of a bias flow. Impedance tube measurements and steady flow measurements are considered. The study is limited to micro-slits with a ratio between the slit width and the viscous boundary layer thickness of order unity. Thirdly, a numerical solution of the two-dimensional Linearized Navier-Stokes equations with a steady flow is compared to the experimental results. After validation, this model is used to gain insight into the presence of interactions between slits upon varying the distance between successive slits. In Section 5.2, the geometry of the sample and experimental setups are presented. Two measurements setup are introduced: the first one is used for steady flow measurements and the second is used for acoustic transfer impedance measurements. Section 5.3 provides definitions of the acoustic transfer impedance and of dimensionless parameters used to present the results. In Section 5.4, the two-dimensional model is discussed. Firstly, the steady flow is solved. Secondly, an acoustic domain is added and incompressible acoustic simulations in the presence

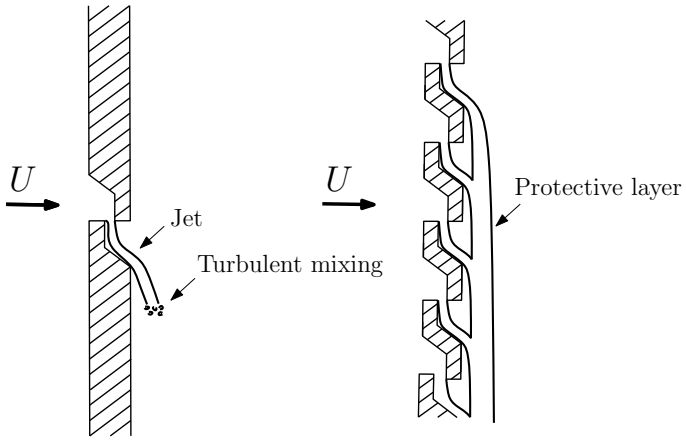

Figure 5.2. Schematic representation of the geometry with coalescence of the micro-jets used for film cooling.

of a viscous flow are performed. In Appendix D.1, the extrapolation of the pressure and the calculation of the impedance are discussed. In Section 5.5, the results of this Chapter are shown. Firstly, the results of the steady flow experiments are compared with the results of the two-dimensional numerical model for a steady flow. Secondly, the findings of the experiments for the acoustic transfer impedance in the presence of flow are presented. Thirdly, a comparison with the solution of the Linearized Navier-Stokes is shown and the numerical model is further used to investigate the effect of the distance between successive slits. Finally, the Chapter concludes with a discussion and conclusions in Section 5.6.

5.2 Experiments

5.2.1 Sample description

In Figure 5.3, a sketch of the plate geometry is shown together with a picture of the sample, with the relevant parameters summarized in Table 5.1. The porosity (of the portion of the plate in the impedance tube) is defined as the ratio between the total open area $A_{open} = 3bl_s$ and the total area of the plate $A_{tot} = \pi(D_i/2)^2$. The edges in contact with the slits are kept as sharp as possible to avoid effects due to the rounding of the edges. Measurements repeated with an inverted plate direction give the same results as for the original plate direction indicating that the plate geometry is effectively symmetric. Therefore, there is no significant difference between the upstream and downstream geometry, which confirms that the edges are indeed sharp.

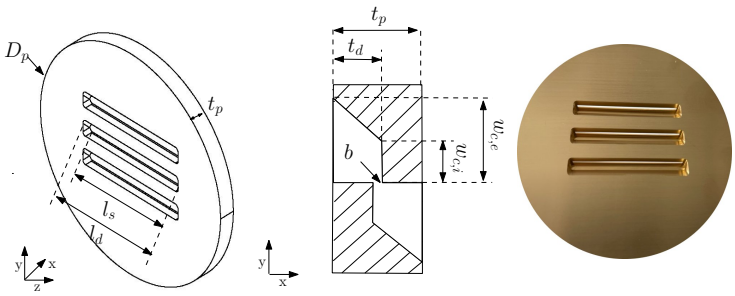

Figure 5.3. Sketches of the plate and the cross-section of a single slit with the definition of parameters and picture of the sample.

Table 5.1. Relevant parameters in Figure 5.3.

External diameter	$D_p = 70\,\text{mm}$
Internal diameter	$D_i = 50\,\text{mm}$
Plate thickness	$t_p = 5\,\text{mm}$
Slit width	$b = 0.5\,\text{mm}$
External width of the cavities	$w_{c,e} = 5\,\text{mm}$
Internal width of the cavities	$w_{c,i} = 2.25\,\text{mm}$
Depth of the cavities	$t_d = 2.75\,\text{mm}$
Thickness of the plate at the slit	$t = t_p - t_d = 2.25\,\text{mm}$
Slit length	$l_s = 35\,\text{mm}$
Total slit length	$l_{s,tot} = 3 \times l_s \approx 105\,\text{mm}$
Distance between slits	$d_s = 9\,\text{mm}$
Angle	$45°$
Porosity	$\Phi = 2.7\%$

5.2.2 Experimental setups

In this section, the experimental setup used for the study of the discharge coefficient and to estimate the transfer impedance are described.
Figure 5.4a shows a schematic representation of the setup used for the steady flow measurements, which consists of a Plexiglas tube, with one side connected to an aluminum air-tight junction for compressed air supply (6 Bar). The tube has an inner diameter $D_i = 50\,\text{mm}$ and a length of $l_t = 1000\,\text{mm}$. The sample is installed at the other end of the tube, in a plastic sample holder with length $L_h = 50\,\text{mm}$. The volume flux of air is controlled by Bronkhorst F-202AV mass flow controllers:

two mass flow controllers are available, for different flow ranges. The first has a maximum volume flux of 80 ln/min = 1.33×10^{-3}m s^{-1}, and it is used to control the flow during the low Reynolds numbers ($Re < 400$) measurements of the acoustic transfer impedance and the discharge coefficient. A second mass flow controller with a maximum volume flow of 250 ln/min = 4.17×10^{-2}m s^{-1} is used to complement the measurements of the discharge coefficient at higher Reynolds numbers. A manometer (TA400 Pitobuis, 1 Pa accuracy) is mounted on the side (using a side wall perforation) to measure the static pressure as a function of the flow speed, in absence of acoustic excitation. The room temperature is measured next to the set-up (accuracy 1 K) for each experiment and corrected in post-processing. The pressure drop Δp across the plate is used to determine the discharge coefficient α, defined as

$$\alpha = \frac{Q}{b l_{s,tot} \sqrt{\frac{2\Delta P}{\rho}}}, \tag{5.1}$$

where Q is the volume flux in cubic meters per second as measured by the flow meter, $l_{s,tot}$ is the total length of the slits, $l_{s,tot} = 3 \times l_s$, ΔP is the static pressure drop measured with the manometer (TA400 Pitobuis) and ρ is the density of dry air at ambient pressure and temperature. A schematic representation of the impedance tube is shown in Figure 5.4b. The impedance tube is made of an aluminum pipe with an inner diameter $D_i = 50$ mm, a wall thickness $t_w = 10$ mm and length $l_t = 1000$ mm. The sample is mounted at the flanged end of the tube in a sample holder of length $L_h = 50$ mm. A loudspeaker (25 W) is used as a source of harmonic excitation and an airflow is injected at the top wall of the setup (see Figure 5.4b). Six pre-polarized 1/4 in microphones (type BWSA, sensitivity 50 mV/Pa) are flush mounted in the tube wall with a spacing of 175 mm. The microphone closest to the sample (at position $x = x_{ref} = -47$ mm, where $x = 0$ corresponds to the first edge of the slit) is used as a reference for the measurements, and the calibration of the other microphones. A script built-in *NILabView* software controls the data acquisition and signal processing during the measurements. The amplitude of the excitation signal is provided in volts and is adjusted automatically until it agrees within 2% with the pre-determined acoustic-pressure amplitude measured at the reference microphone. This amplitude is used

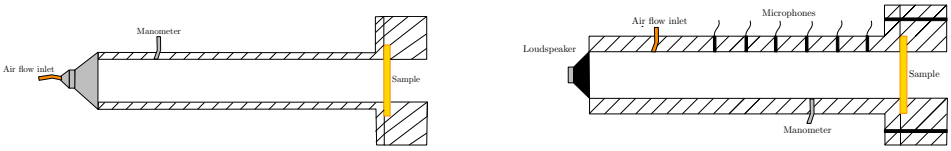

(a) **(b)**

Figure 5.4. Schematic representation of the experimental setups used in this Chapter: a) Steady-flow setup, b) Impedance tube setup

to estimate the acoustic velocity amplitude at the sample and retrieve the relative acoustic velocity defined in Section 5.3.2.

5.2.3 Measuring reflection coefficient and impedance

To measure the transfer impedance of the plate the procedure explained in Chapter 3 is followed. The transfer impedance of the sample is obtained by measurements of the reflection coefficient with and without the sample. For the evaluation of the reflection coefficient, the method from Jang and Ih is used [129]. For each frequency, every microphone records the complex pressure amplitude $\widehat{p}(x)$ at position x,

$$\widehat{p}(x) = \widehat{p}_+(x)e^{(-\mathrm{i}kx)} + \widehat{p}_-(x)e^{(\mathrm{i}kx)}, \tag{5.2}$$

with p^+ and p^- respectively the amplitudes of the wave traveling in the positive and in the negative directions, $x = 0$ correspond to the end of the impedance tube (sample side on the incoming wave side), k is the complex wavenumber and the $e^{(+i\omega t)}$ convention is used. Taking visco-thermal effects into account as proposed in Peters *et al.* [130], the complex wavenumber is

$$k = \frac{\omega}{c}\left[1 + \frac{1-\mathrm{i}}{\sqrt{2}Sh_D}\left(1 + \frac{\gamma-1}{Pr^{0.5}}\right)\right] - \frac{\omega}{c}\left[\frac{\mathrm{i}}{Sh_D^2}\left(1 + \frac{\gamma-1}{Pr^{0.5}} - \frac{1}{2}\gamma\frac{\gamma-1}{Pr}\right)\right], \tag{5.3}$$

where i is the imaginary unit, $\omega = 2\pi f$ is the angular frequency, Pr is the Prandtl number ($Pr = 0.72$), γ is the heat capacity ratio ($\gamma = 1.4$),

$$Sh_D = \frac{D_i}{\delta_v} = D_i\sqrt{\frac{\omega\rho}{2\mu}} \tag{5.4}$$

is the Shear number based on the impedance-tube inner-diameter D_i, ρ is the air density ($\rho = 1.18\,kg/m^3$ at 25°C and atmospheric pressure) and μ is the dynamic viscosity of air ($\mu = 1.85 \times 10^{-5}\,kg/ms$ at 25°C).
The speed of sound c is obtained by the measurement of the ambient temperature as

$$c = c_{ref}\sqrt{\frac{T}{T_{ref}}}, \tag{5.5}$$

with $c_{ref} = 343\,\mathrm{m/s}$ and $T_{ref} = 298.15\,\mathrm{K}$. The reflection coefficient at the end of the tube ($x = 0$) is

$$R = \frac{\widehat{p}_-}{\widehat{p}_+} \text{ [129].} \tag{5.6}$$

Before each set of measurements, the open pipe reflection coefficient R_o is measured. In this open pipe radiation impedance measurement, the sample is replaced by a ring in the sample holder so that the geometry (pipe length, position in the room) is the same as when measuring with a sample.
A microphone RMS-amplitude of 50 mV is chosen for the reference microphone,

corresponding to an acoustic pressure RMS amplitude $\widehat{p}_{ref} = 1\text{Pa}$. The dimensionless radiation impedance is obtained as

$$Z_{rad} = \frac{1 + R_o}{1 - R_o}. \tag{5.7}$$

Further, the impedance of the sample-loaded termination is obtained by measuring the sample-loaded reflection coefficient R_s as

$$Z_s = \frac{1 + R_s}{1 - R_s}. \tag{5.8}$$

Consequently, the dimensionless transfer impedance of the plate is

$$Z_{plate} = Z_s - Z_{rad}. \tag{5.9}$$

Since the samples have relatively low porosity, the radiation impedance is much lower than the impedance of the plate. The radiation impedance used to define the transfer impedance of the sample is obtained in the no-flow case. Tests in the presence of flow show a deviation smaller than 1% on the impedance of the sample, compared to no-flow tests.

5.3 Definitions

5.3.1 Definition of the acoustic transfer impedance

In the linear regime, the concept of transfer impedance is introduced in the frequency domain (for purely harmonic oscillations) of frequency f. At a distance large compared to the slit width b but small compared to the acoustic wavelength $\lambda = c/f$, the flow can be described in terms of plane acoustic waves. The complex transfer impedance of the plate is defined as the ratio between the complex acoustic pressure difference $\Delta\widehat{p}$ and the amplitude of the acoustical velocity $\widehat{u}$ in a cross-section upstream of the plate where the acoustic field can be described in terms of plane acoustic waves as

$$z_{plate} = \frac{\Delta\widehat{p}}{\widehat{u}} = Z_{plate}\rho c = \text{Re}[z_{plate}] + \text{iIm}[z_{plate}], \tag{5.10}$$

where $\text{Re}[z_{plate}]$ is the real part of the acoustic transfer impedance of the plate (or resistance of the plate) and $\text{Im}[z_{plate}]$ is the imaginary part of the acoustic transfer impedance of the plate (or inertance of the plate), Z_{plate} is the dimensionless acoustic transfer impedance. The quantities $\widehat{u}$ and $\widehat{p}$ are obtained from the acoustic pressure signal $p(t)$ and velocity $u(t)$ using Fourier transform, where the sampling rate is 20 kHz for the excitation signal and 10 kHz for recording the input signal. An FFT of the time signal, prefiltered with a Tukey window with

cosine fraction 0.05 is considered. For the velocity, the Fourier transform $\widehat{u}$ is related to $\widehat{p}$ measured at various positions of the pipe by assuming a plane wave propagation and deducing $\widehat{u}$ after correction for thermal/viscous attenuation for the wave number (Equation 5.6). In the presence of a bias flow, a dimensionless form of the impedance is used in Section 5.5.2. The resistance is divided by the quasi-steady approximation for the resistance $\rho U_s/\alpha^2$, with α the discharge coefficient and U_s the flow velocity in the slit. In this Chapter, the approximation with $\alpha = 1$ is considered for the quasi-steady model. In particular the quantities $\mathrm{Re}[z_{plate}]\Phi/(\rho U_s)$ and $\mathrm{Im}[z_{plate}]\Phi/(\rho b\omega)$ are considered, where U_s is the average flow velocity in the slit. As for the acoustic perturbation, $U_s = U_d/\Phi$, with Φ the porosity of the plate and U_d the average velocity in the duct. In the experiments, the velocity U_s is defined as

$$U_s = \frac{Q}{\Phi A_{tot}} = \frac{Q}{A_{open}}, \tag{5.11}$$

with Q the mass flow measured by the mass flow meter and $A_{open} = 3bl_s$ the total open area.

5.3.2 Definition of the dimensionless numbers

In this Chapter, several dimensionless numbers are used to describe the results. In the linear regime, dissipation of acoustic energy takes place in the oscillating boundary layer of thickness $\delta_v = \sqrt{2\mu/\omega\rho}$ [100]. The ratio between the slit width b and the thickness of the viscous boundary layer δ_v is the Shear number

$$Sh = \frac{b}{\delta_v}. \tag{5.12}$$

In a micro-slit plate, typical Shear numbers are of order unity. In the experiments, the amplitude of the excitation signal in terms of pressure is measured at the reference microphone, as explained in Section 5.2.2. The relation between the acoustical-velocity amplitude $|\widehat{u}_s|$ in the slit and the acoustical-pressure amplitude $|\widehat{p}|$ at the upstream side of the plate $x = 0$ (obtained by extrapolation of the acoustic far field) is

$$|\widehat{u}_s| = \frac{|\widehat{p}|}{\Phi|z_{plate}|}, \tag{5.13}$$

with z_{plate} the acoustic transfer impedance of the plate defined in Section 5.3.1. Note that $|z_{plate}|$ is a frequency-dependent quantity. At low frequencies, using Bernoulli's frictionless quasi-steady-flow equation

$$P \approx \frac{1}{2}\rho U_s^2, \tag{5.14}$$

one retrieves the limit for $Sh \to 0$ ($f \to 0$),

$$|\widehat{u}_s| = |\widehat{p}|/\rho U_s. \tag{5.15}$$

Hence, the dimensionless number $\bar{P}$ is introduced to define the ratio $U_s/|\widehat{u}_s|$ between the flow and the acoustic velocity in the experiments as

$$\bar{P} = \frac{\rho {U_s}^2}{2|\widehat{p}|} \approx \frac{P}{|\widehat{p}|}. \tag{5.16}$$

This representation of the dimensionless number is chosen (and not the inverse) to include the no-flow case for $U_s = 0$ with $\bar{P} = 0$. The behavior of the plate can be studied as a function of the Strouhal number St_b based on the slit width b or St_c based on the cavity width w_c. In formulas,

$$St_b = \frac{fb}{U_s} \qquad \text{or} \qquad St_c = \frac{fw_c}{U_s}. \tag{5.17}$$

The Reynolds number based on the slit width Re is defined as

$$Re = \frac{\rho U_s b}{\mu} = \frac{\rho Q}{\mu l_{s,tot}}, \tag{5.18}$$

with $l_{s,tot}$ the total length of the slits ($l_{s,tot} = 3 \times l_s$).

5.4 Numerical model

The flow within the slit is considered to be locally incompressible up to the first resonance frequency of the resonator, since for the frequencies considered in the present study $f < 1$ kHz, the square of the Helmholtz number is small, *i.e.*

$$He^2 = \left(\frac{\omega b}{c}\right)^2 < 2 \times 10^{-3}. \tag{5.19}$$

In this Chapter, a two-dimensional numerical model of the plate containing three slits is built in Comsol Multiphysics v. 6. In Figure 5.5, the numerical domain is shown with the relevant parameters. The dimensions of the domain are chosen so that the porosity Φ_{2D} in the 2D-planar model, is the same as the porosity of the actual sample when placed in the impedance tube ($\Phi = 2.7\%$). The porosity $\Phi_{2D} = 3b/a$ is obtained as the ratio between the width of the three slits $3\times b$ and the channel height a. The slit width is $b = 0.5$ mm, the confinement is $a = \pi D_i^2/(4l_s) = 56$ mm. The distance between two slits is the same as for the sample, $d_s = 9$ mm. The central slit is positioned at $y = 0$, the other two slits at $Y = \pm 9$ mm, and the slit entrance is located at $x = 0$.

5.4.1 Steady flow simulations

For the steady flow simulations, the upstream and downstream duct lengths are $L_{up} = 324$ mm and $L_{down} = 610$ mm.

Considering Figure 5.5, the domain where the flow is solved extends from the inlet at $x = -326.25\,\text{mm}$ to the outlet at $x = 612.75\,\text{mm}$. The slit inlet is at $x = 0$ and the plate has a thickness of $t_p = 5\,\text{mm}$. Tests with longer ducts were performed and the results do not show a significant dependence on the duct length. The Navier-Stokes equations for the conservation of momentum and the continuity equation for the conservation of mass are resolved for a steady laminar flow:

$$\rho\mathbf{U}\cdot\nabla\mathbf{U} = -\nabla\cdot[P\mathbf{I}+\mathbf{K}]+F \qquad \nabla\cdot\mathbf{U}=0, \tag{5.20}$$

with

$$\mathbf{K} = \mu(\nabla\mathbf{U}+(\nabla\mathbf{U})^T) \tag{5.21}$$

and μ is the dynamic viscosity of air, $\mathbf{U}$ is the fluid velocity, P is the fluid pressure, ρ is the density. The reference pressure level and the reference temperature are set at $P_{ref} = 1\,\text{atm} = 1.013\,\text{Bar}$ and $T_{ref} = 296.15\,\text{K}$ to match the typical experimental conditions.
At the inlet of the domain ($x = x_{in}$), the velocity is imposed as

$$U_d = -\frac{1}{A}\int_{\delta\Omega}(\mathbf{U}\cdot\mathbf{n})\,dS, \tag{5.22}$$

with

$$A = \int_{\delta\Omega} dS, \tag{5.23}$$

with Ω the computational domain. This boundary condition allows a parabolic flow to be imposed at the inlet of the duct with an average velocity equal to the selected one. At the outlet ($x = x_{out}$) a static pressure p equal to zero is imposed. No-slip boundary conditions are applied in all the models at the walls ($\mathbf{U} = 0$).

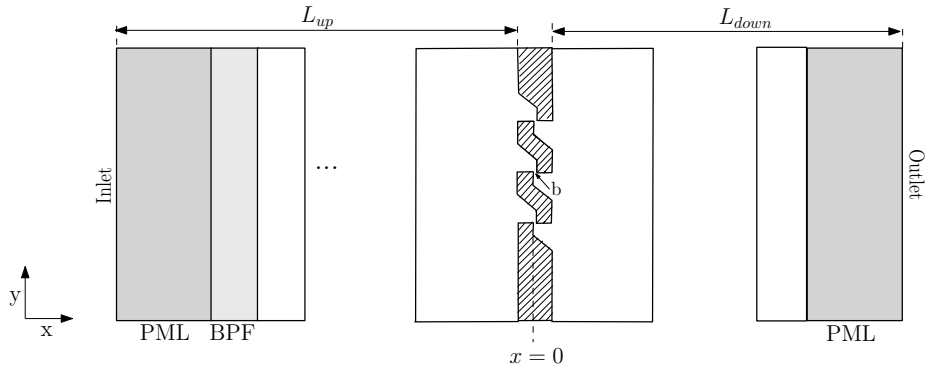

Figure 5.5. Schematic representation of the numerical domain, where PML is a Perfectly Matched layer with $L_{PML} = 50\,\text{mm}$ and BPF is a Background Pressure Field $L_{BPF} = 30\,\text{mm}$.

The mesh used for this study consists of 103110 elements, of which 3812 edge elements. This mesh is chosen for the full range of Reynolds numbers considered for the study. For higher Reynolds numbers the turbulent and complex behavior of the merging jets on the downstream wall of the plate required additional numerical dissipation (coarser mesh) or implementation of a model with local turbulence. To compare with the experiments, the 2D Reynolds number is defined as

$$Re = \frac{Q_{2D}}{3\nu}, \tag{5.24}$$

with $Q_{2D} = aU_d$ and U_d determined as the average velocity in the duct at a location $x = -56\,\text{mm}$ (upstream from the slit entrance). The discharge coefficient from the numerical simulations is calculated considering the average pressure and velocity at $x = -56\,\text{mm}$ as

$$\alpha = \frac{Q_{2D}}{b\sqrt{2\Delta P/\rho}}. \tag{5.25}$$

5.4.2 Acoustic simulations

For the acoustic simulations, the numerical domain is the same as discussed in the previous section. A perfectly matched layer of thickness $L_{PML} = 50\,\text{mm}$ is present on both sides. The PML layer is added to an acoustic model to mimic a non-reflecting pipe termination. The pressure p_0 and velocity $\mathbf{U}$ of the steady flow are mapped in the acoustic domain. A mapping between the mesh used for the resolution of the flow and the mesh for the acoustic is performed. The mesh used for the acoustic simulations contains 142129 elements, of which 93360 are used in the plate region (to resolve the acoustical viscous boundary layer). A mesh convergence test is performed. The Linearized Navier-Stokes equations in the frequency domain are solved:

$$\nabla \cdot (\mathbf{U} + \mathbf{u}) = 0, \tag{5.26}$$

$$\rho_0 \left(\mathrm{i}\omega\mathbf{u} + (\mathbf{u}\cdot\nabla)\mathbf{U} + (\mathbf{U}\cdot\nabla)\mathbf{u}\right) + \rho(\mathbf{U}\nabla)\mathbf{U} = \nabla\sigma, \tag{5.27}$$

where the stress tensor σ is

$$\sigma = -p\mathbf{I} + \mu(\nabla\mathbf{u} + (\nabla\mathbf{u})^T), \tag{5.28}$$

with μ the dynamic viscosity. On the walls, no-slip boundary conditions are implemented $\mathbf{u} = (0, 0)$. In a second section of L_{BPF}, an incident acoustic wave is generated. In this domain (see in Figure 5.5), a downstream traveling pressure wave and associated particle velocity are generated,

$$p_+ = p_0 e^{(-ik_0 x)} \quad \text{and} \quad u_+ = \frac{-1}{(\mathrm{i}\rho\omega)\partial p_+/\partial x}, \tag{5.29}$$

with $p_0 = 1\,\mathrm{Pa}$, $k_0 = \omega/c$ and x the direction of the flow propagation. In the numerical simulations, the effect of friction in the pipe is neglected due to the high Shear number based on the pipe diameter. This is also because a short propagation distance is considered. The pressure difference $\Delta p = \Delta\widehat{p}e^{i\omega t}$ used to calculate the plate impedance z_{plate} (Equation 5.10) is determined using the linear extrapolation of the acoustic pressure in the plane wave regions to both the sides of the plate, as described in Appendix D.1. The quantity $\widehat{u}$ in Equation 5.10 is obtained, from the results of the numerical simulation, as the cross-sectional average acoustic velocity at $x_{up} = -a$, as described in Appendix D.1.

5.5 Results

5.5.1 Steady flow results

In Figure 5.6 the discharge coefficient α obtained from steady flow numerical simulations by using Equation 5.1, is compared with the experimental results as a function of the Reynolds number. Experimental results below $Re = 64$ are not shown, because of the large uncertainties due to the limited sensitivity of the manometer ($1Pa$). Considering the numerical results, one sees a first region where the discharge coefficient increases monotonously with an increasing Reynolds number and it reaches a maximum of around $Re \approx 80$. At higher Reynolds numbers it decreases towards an asymptote around $\alpha \approx 0.8$ and above $Re = 500$, numerical simulations assuming a laminar flow behavior fail to converge.

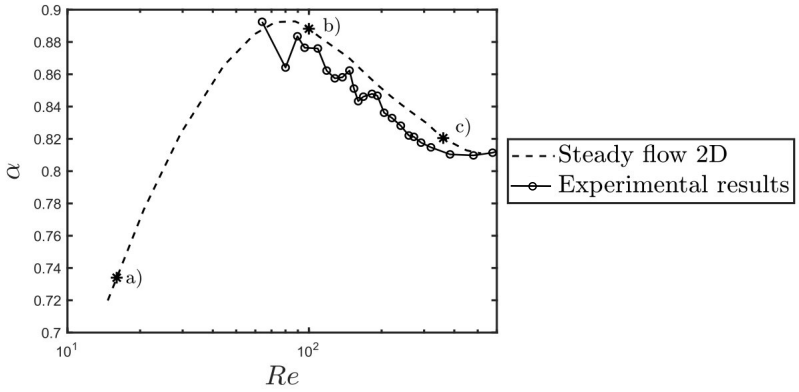

Figure 5.6. Discharge coefficient α as a function of the Reynolds number Re. Results obtained by steady flow simulations (dotted line) are compared with experimental data (circles). The stars on the numerical results indicate flow conditions for which the flow field is displayed in Figure 5.7.

One expects that this is related to the turbulent behavior of the flow downstream of the slits. Simulations using a turbulence model (RANS) do converge and give results higher than the laminar flow results by about 1%. Considering the experimental results, one observes globally a similar behaviour as the numerical simulation with the discharge coefficient reaching an asymptote close to the potential flow limit found in Chapter 3 of $\alpha = 0.82$. Fabre *et al.* [164] find, for a sharp-edged-thick circular orifice, a similar global Reynolds number dependency. Unlike the numerical results, the measured discharge coefficient is not a smooth function of the Reynolds number. This seems not to be due to errors in the measurements, as it appears reproducible. The difference between numerical simulations and experiments could be related to the definition of the velocity (and of the Reynolds number).

The behavior of the discharge coefficient observed in Figure 5.6 can be associated with the complex behavior of the flow in the cavity downstream of the slits. In Figure 5.7, the numerically predicted velocity field is visualized for three different Reynolds numbers indicated with stars, on the line of numerical results in Figure 5.6. In all cases, one observes the formation of a non-symmetric jet in the downstream cavity of the slit. Due to the Coanda effect [165, 166], the jet formed (by flow separation at the slit edges) downstream of the slit tends to attach to the cavity bottom in the downstream cavity. Further downstream, outside the cavity, one observes the merging of the individual jets from the different slits, resulting in the formation of a wall jet along the downstream side of the plate. One observes the evolution of the flow with varying Reynolds numbers. For low Reynolds numbers, the jet that exits the cavity just downstream of the slit is almost symmetric with respect to the slit, moving initially away from the cavity bottom wall. The position where the jet re-attaches to the cavity wall depends on the Reynolds number. For increasing Reynolds number, the re-attachment point moves downstream. The numerical results provide an estimation for the extension of the transition range and the discharge coefficient. Part of the differences between the numerical (2D) results and the experiments could be due to the exaggeration of the Coanda effect

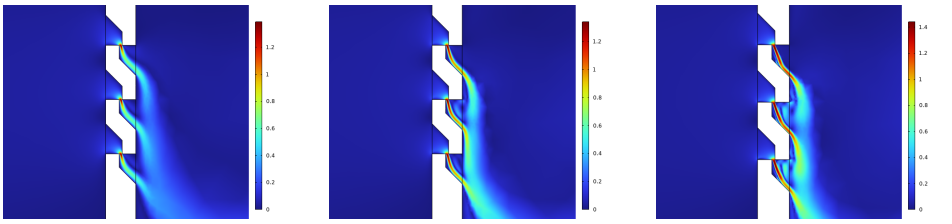

(a) $Re = 16.8$ **(b)** $Re = 100$ **(c)** $Re = 360$

Figure 5.7. Magnitude of the flow velocity U/U_s from numerical simulations for $Re = 16.8$, $Re = 100$ and $Re = 360$.

in the two-dimensional model. In reality, the airflow from the jets' sides mitigates the Coanda effect. Hence, the jet re-attaches later to the wall. In Figure 5.8, the profile of $\mathbf{U} \cdot \mathbf{n}$, where $\mathbf{n}$ is the unit normal to the slit plane in the middle slit is shown, normalized with the velocity $U_s = U_d/\Phi$, with U_d calculated considering the average velocity in the duct at location $x = -56\,\text{mm}$. This component corresponds to the flow through the slit. One can see that for low Reynolds numbers the flow within the slit approaches a parabolic profile with maximum velocity reached close to the middle of the slit. Increasing the Reynolds number, the flow velocity profile becomes flatter. As the Reynolds number is further increased, the maximum of the velocity is reached close to the upper slit edge $x/b = 1$, displaying an asymmetric behavior.

Measurements with a steady flow are also performed for single slits, by plugging the other slits, and results are shown in Figure 5.9. These measurements display hysteresis, at high Reynolds numbers, that is not observed for multiple slits. At these high Reynolds numbers the jet becomes turbulent, which strongly enhances the Coanda effect. In those experiments, the volume flow is either increased monotonously or decreased monotonously. The measured value of α is larger for decreasing volume flow than for increasing volume flow. Apparently, at high Reynolds numbers, the turbulent jet can potentially flap between two configurations outside the cavity: attached to the downstream wall of the plate or detached from it. At lower Reynolds numbers for a single slit, the jet does not attach to the downstream plate wall, as shown by numerical simulations. The enhancement of the Coanda effect due to turbulence does promote attachment. However, the flow configuration depends on the history of the flow [167, 168]. This is common in the presence of the Coanda effect and used in technologies to produce memory devices, such as fluidics [169, 170].

In the case of single slits, the detached configuration is unstable, while the interaction between the slits in the multiple-slits configuration forces the jet to one of the two configurations (downwards). This indicates that the behavior of three slits is

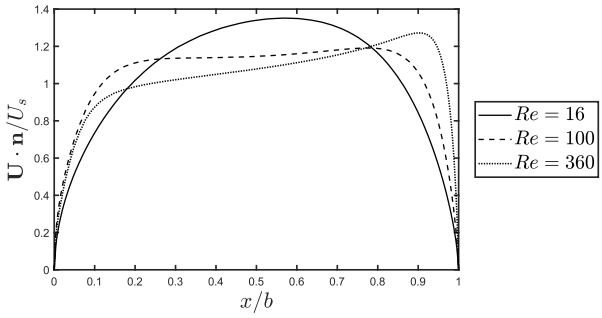

Figure 5.8. Profile of the $\mathbf{U} \cdot \mathbf{n}$ at the middle slit normalized with U_s.

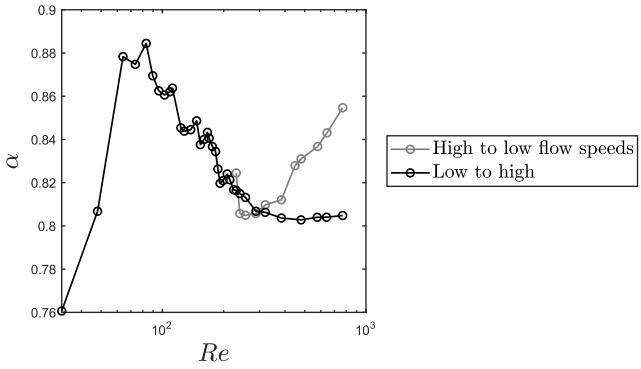

Figure 5.9. Discharge coefficient α of a single slit as a function of the Reynolds number Re. Effect of hysteresis.

less complex that the one of a single slit, in the presence of a steady bias flow. Whistling is observed at the first transversal pipe resonance frequency, $f \approx 4\,\text{kHz}$, for Reynolds numbers around $Re = 200$. The direct correlation of this whistling with the discharge coefficient dependency on the Reynolds number has yet to be investigated. Some of the non-monotonous behavior (small dips or peaks) observed in the experimental data might be related to whistling.

5.5.2 Acoustic transfer impedance

In this section, experimental results for the acoustic transfer impedance (Equation 5.10) of the micro-slit plate are presented, in the linear regime for an acoustic amplitude measured at the reference microphone $|\widehat{p}_{ac}| = 1\,\text{Pa}$. Tests show that the difference between the results obtained for $|\widehat{p}_{ac}| = 0.4\,\text{Pa}$ and the ones used in this section lies within 1% for both resistance and inertance. Results for $|\widehat{p}_{ac}| = 1\,\text{Pa}$ are chosen due to the presence of noise at higher frequencies for lower acoustic amplitudes. The quantity $\bar{P} = \rho U_s^2/(2|\widehat{p}|)$ (measure for $U_s/|\widehat{u}_s|$) ranges between $\bar{P} = 0$ (no-flow case) and $\bar{P} = 347$ (highest flow velocity is $17\,\text{m/s}$ in the slit). In Figure 5.10, the behavior of the real and imaginary parts of the impedance as a function of the Shear number is shown. Both the real and the imaginary parts of the acoustic transfer impedance are normalized by dividing by the value for the no-flow case ($Re = 0$). The resistance shows a global increase with increasing flow speeds (and Reynolds numbers) with respect to the no-flow case. For the highest Reynolds number considered ($Re = 581$), the resistance is 50 times higher than the no-flow case. One observes complex behavior in the range $164 < Re < 272$. Globally the inertance is lower, for all Reynolds numbers, than in the no-flow case. The behavior of the inertance for $Re > 164$ is also quite complex. The inertance shows a peak that moves slightly to the right with increasing flow velocities. This

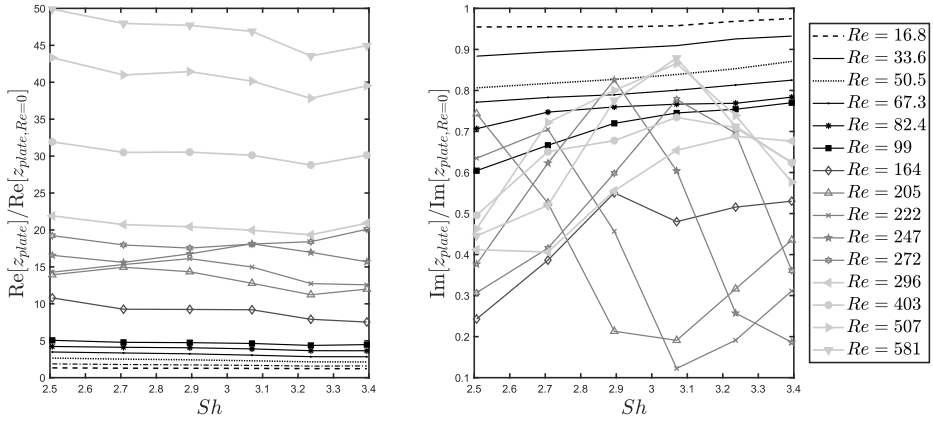

Figure 5.10. Real and imaginary part of the acoustic transfer impedance in dimensionless form with the no-flow case as a function of the Shear number $Sh = b/\delta_v$ for several flow speeds.

hints at the presence of a tonal, velocity-dependent forced phenomenon. As the behavior at low Reynolds numbers ($Re < 100$) is quite different from that at higher Reynolds numbers ($Re > 100$), these results are discussed separately in the next subsections.

Low Reynolds numbers $Re < 100$

Results are shown for $Re < 100$, corresponding to $\bar{P} = [0, 5.4]$. In Figure 5.11 the real and imaginary parts of the acoustic transfer impedance normalized by dividing with the no-flow case value ($Re = 0$), are presented as a function of the Shear number for several flow speeds. Next to the increase of the resistance $Re[z_{plate}]$ with increasing flow speed, one observes a decrease with increasing Shear number (Sh). The inertance ($Im[z_{plate}]$) of the plate decreases with increasing flow speeds.
In Figure 5.12, the transfer impedance of the plate is normalized using as reference the value obtained with the quasi-steady Bernoulli approximation assuming $\alpha = 1$, *i.e.* $\mathrm{Re}[z_{plate}\Phi]/(\rho U_s)$. The dimensionless slit resistance $\mathrm{Re}[z_{plate}\Phi]/(\rho U_s)$, with U_s the cross-sectionally averaged velocity within the slits, is shown as a function of the Shear number for several flow speeds. The figure shows that the quasi-steady approximation $\rho U_s/\Phi$ is of the order of the resistance, indicating that sound absorption by vortex shedding is dominant.
An excellent collapse is found in this dimensionless presentation except for the lowest Reynolds number. The increase in $Re[z_{plate}]/(\rho U_s)$ at the lowest Reynolds number, either due to the effect of viscous dissipation or the change in velocity

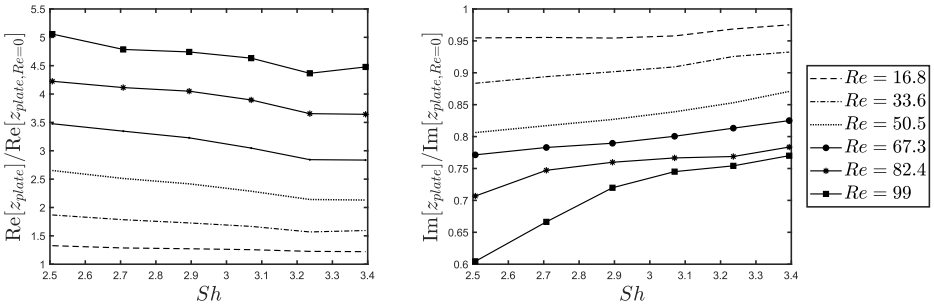

Figure 5.11. Real and imaginary part of the acoustic transfer impedance of the plate dimensionless with the no-flow case ($Re = 0$) as a function of the Shear number $Sh = b/\delta_v$ for several flow speeds ($Re < 100$).

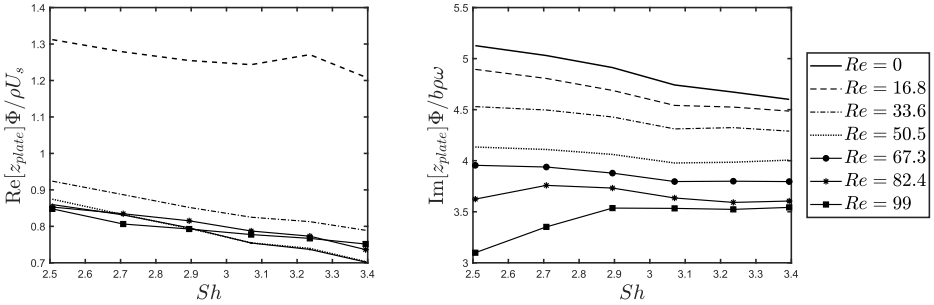

Figure 5.12. Real and imaginary part of the acoustic transfer impedance of the plate dimensionless with the quasi-steady approximation ρU_s, as a function of the Shear number $Sh = b/\delta_v$ for several flow speeds ($Re < 100$).

profile (in the jet formed downstream), should be further investigated.
In Figure 5.12. the imaginary part of the acoustic transfer impedance is shown as a function of the Shear number Sh normalized by dividing by $\rho b\omega$, with b the slit width. In this case, one observes that the quantity $\mathrm{Im}[z_{plate}]\Phi/\rho b\omega$ is of order unity, but there is no convergence of the data in this presentation. The Strouhal number dependency is further investigated in Section 5.5.2.

Higher Reynolds numbers

In this section, the transfer impedance of the plate for higher Reynolds numbers is described. In Figure 5.13, the dimensionless real and imaginary parts of the acoustic transfer impedance (respectively $Re[z_{plate}]\Phi/(\rho U_s)$ and $Im[z_{plate}]\Phi/(\rho\omega b)$) are shown for the full range of Reynolds numbers considered for the study ($16.8 <$

$Re < 576$). The behavior, for higher Reynolds, is complex. For $Re > 272$, one observes again a fair convergence of the resistance around the value found for low Reynolds numbers, while the behavior of the inertance remains chaotic and complex. In Figure 5.14, the dimensionless resistance and inertance are shown as a function of the Reynolds number for several Shear numbers. Considering the resistance, in the first region, one observes a Stokes behavior, *i.e.* the resistance is roughly decreasing with increasing Reynolds number as $1/Re$. For increasing Reynolds numbers, the behavior changes and we move towards a plateau when the resistance reaches a minimum with a more uniform flow profile in the slit (transition regime). The resistance further increases again for increasing Reynolds numbers, whereas complex behavior of the flow is observed between $167 < Re < 270$. Considering the inertance, one observes the first part in which the inertance decreases monotonously with increasing Reynolds number. In the transition regime, a complex non-monotonous behavior is observed. Globally, the same conclusions drawn in 5.5.2 hold: the quasi-steady approximation provides an order of magnitude of the real part of the impedance. However, the convergence of the dimensionless data as a function of Sh, observed for $Re < 100$, is not found for higher flow speeds and in particular for $167 < Re < 270$. For $Re > 270$, the dimensionless resistance shows again a smoother behaviour and partially collapses. The non-monotonous behavior in the transition range of resistance and inertance suggests a Strouhal number dependency. The transition zone $167 < Re < 270$ corresponds to $0.8/2\pi < St_c < 1.6/2\pi$. A transition in a similar Strouhal number range is found in Nakıboğlu *et al.* [157] for vortex shedding when considering the whistling of a compact axisymmetric cavity.
In Figure 5.15, the change of the real and imaginary parts of the acoustic transfer impedance due to flow is shown as a function of the Strouhal number.

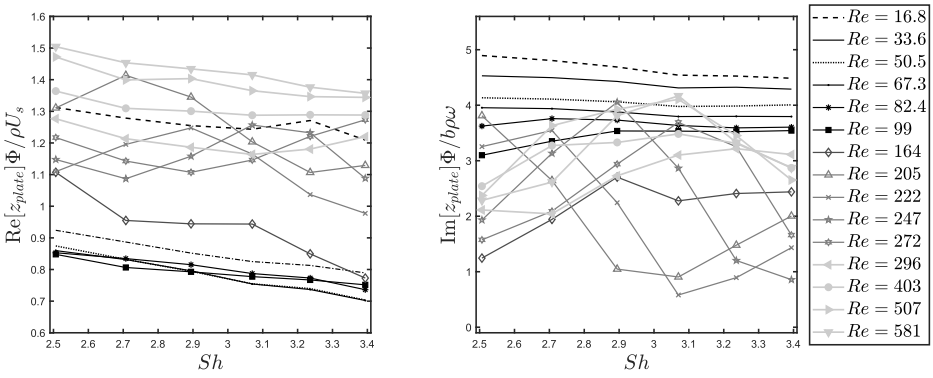

Figure 5.13. Real and imaginary part of the acoustic transfer impedance dimensionless with the quasi-steady approximation ρU_s as a function of the Shear number $Sh = b/\delta_v$ for several flow speeds.

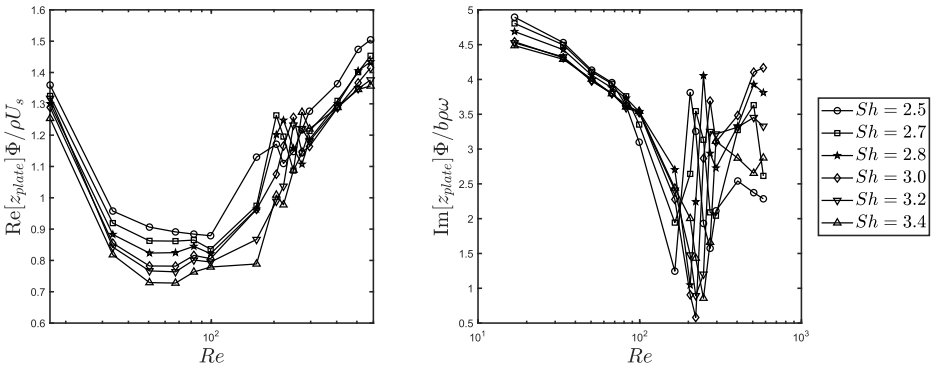

Figure 5.14. Real and imaginary part of the acoustic transfer impedance of the plate dimensionless with the quasi-steady approximation $\rho U_s/\alpha^2$ (with $\alpha = 1$) as a function of the Reynolds number $Re = bU_s/\nu$.

In particular, the quantities

$$\Delta\mathrm{Re}[z_{plate}] = \mathrm{Re}[z_{plate,flow}] - \mathrm{Re}[z_{plate,Re=0}] \tag{5.30}$$

$$\Delta\mathrm{Im}[z_{plate}] = \mathrm{Im}[z_{plate,flow}] - \mathrm{Im}[z_{plate,Re=0}] \tag{5.31}$$

are considered. One observes a fair collapse of the resistive correction proportional to $1/St_c$, while the inertial correction reaches negative values. This correction is the sum of two contributions: the first contribution is due to the upstream cavity (before the slit) and the second is due to the downstream cavity. The contribution given by the upstream cavity is expected to be similar to the behavior of the no-flow case. A negative inertial correction suggests that the downstream cavity has a reduced inertance due to the formation of a jet. Similar results are found in Tonon and Moers *et al.* [80, 171] and have been predicted by Rienstra for an open pipe termination [172]. For $St_c \approx 1/2\pi$ one observes a negative contribution to the real part of the impedance, which is associated with whistling [82, 164]. For $St_c > 1/2\pi$, the behavior of the inertial correction is smooth and is proportional to St_c and approaches the no-flow case. A similar dependency of $\Delta\mathrm{Im}[z_{plate}]$ on the Strouhal number is observed in Peters *et al.* [130] for an open pipe termination.

5.5.3 Comparison of numerical and experimental results

In this section, the results of the two-dimensional model for three slits solving the Linearized Navier-Stokes equations in the frequency domain in the presence of flow are compared with the results of the experiments. The numerical simulations are performed over a broader range of Shear numbers ($1 < Sh < 6$) than the experiments to observe the global behavior of the acoustic transfer impedance.

In Figure 5.15, the relative change of the real and imaginary parts of the acoustic transfer impedance due to the presence of flow is shown as a function of the Strouhal number based on the cavity width. It can be seen that, globally, the numerical simulations provide a fair prediction of the real and imaginary parts of the acoustic transfer impedance. In particular, the non-monotonous dependency of the inertance as a function of St_c is predicted for low St_c. In Figure 5.16, results are compared for three Reynolds numbers ($Re = 16.8, 164, 510$), showing the full range of Strouhal numbers for the numerical simulations. One observes a fair agreement between the numerical simulations and the experiments. The large oscillations as a function of St_c are associated with hydrodynamic interaction between successive slits. Minima in the real part of the impedance corresponds to flow conditions in which vortices shed at a slit interfere positively with vortices shed in the following slit. Such conditions are referred to as hydrodynamic modes. For $Re = 550$ at $St_c = 0.6/2\pi$ and $St_c = 1.2/2\pi$, the first and second hydrodynamic modes are observed, corresponding to respectively one and two vortices in each cavity. The oscillating behavior of the inertance around $St_c = 1/2\pi$ observed for $Re = 170$ are captured by the numerical model.

Numerical study of the influence of the distance between slits.

In Figure 5.17, five geometries are presented for the study of the interaction between neighboring slits. The duct dimensions are kept the same. The first shows the geometry with one slit. Then the geometries where the slits are equi-spaced ($d_1 = d_2$) are presented: $d_1 = d_2 = d_s = 9$ mm (the original geometry),

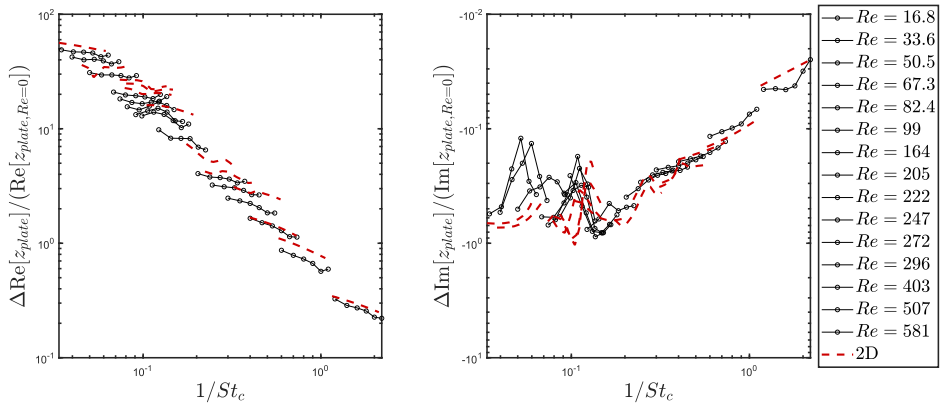

Figure 5.15. Comparison of numerical and experimental changes of the real and imaginary parts of the acoustic transfer impedance of the plate as a function of the inverse of the Strouhal number $St_c = fw_{c,e}/U_s$ for several flow speeds. The dotted lines are numerical results.

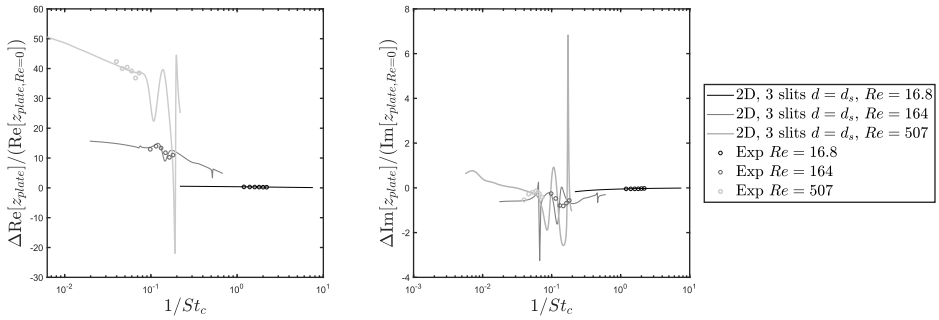

Figure 5.16. Comparison of numerical and experimental changes of the real and imaginary parts of the acoustic transfer impedance of the plate as a function of the inverse of the Strouhal number $St_c = fw_{c,e}/U_s$ for $Re = 16.8$, $Re = 164$ and $Re = 510$. Full lines are numerical results for three slits with $d = d_s$.

$d_1 = d_2 = 1.5d_s = 13.5$ mm, $d_1 = d_2 = 2d_s = 18$ mm. In the last geometry, the slits are not equispaced and $d_2 = d_s$ and $d_1 = 1.5d_s$. In Figure 5.18, the predicted spatial distribution of the amplitude of the linear perturbation of the velocity divided by U_s is displayed for $Re = 550$ at $St_c = 0.6/2\pi$ and $St_c = 1.2/2\pi$, for the geometry with three slits (Figure 5.17-b) and with a single slit (Figure 5.17-a). It can be seen that for three slits at $St_c = 0.6/2\pi$ and at $St_c = 1.2/2\pi$ the behavior of the vortices behind the plate is quite different. For a single slit at $St_c = 1.2/2\pi$, one observes a complex behavior of the jet inside the cavity. This is possibly related to the oscillation of the imaginary part as a function of the Strouhal number (see Figure 5.16 around $St_c = 1.2/2\pi$). In Figure 5.19, the numerical results for 3 slits at distance $d = d_s$ are compared with the results for other geometries shown in Figure 5.17. The complex behavior at $St_c < 1$ observed in the experiments and the numerical simulations is not present in the simulations with one slit or for

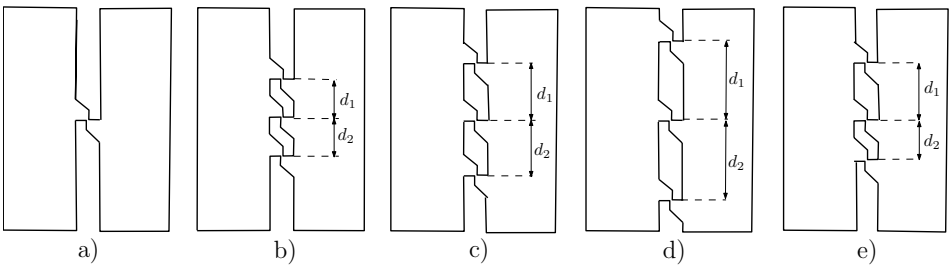

Figure 5.17. Schematic representation of the geometries used for the study of the interaction between slits: a) 1 slit, b) 3 slits with $d_1 = d_2 = d_s$, c) 3 slits with $d_1 = d_2 = 1.5d_s$, d) 3 slits with $d_1 = d_2 = 2d_s$, e) 3 slits with $d_2 = d_s$, $d_1 = 1.5d_2$.

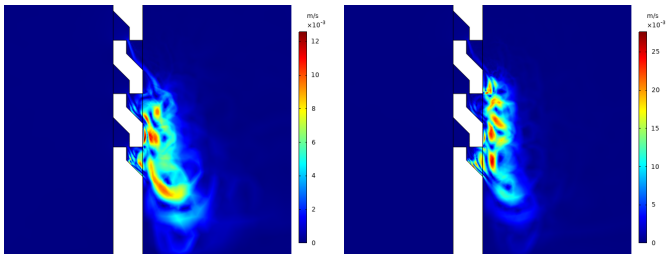

(a) 3 slits, $St_c = 0.6/2\pi$ **(b)** 3 slits, $St_c = 1.2/2\pi$

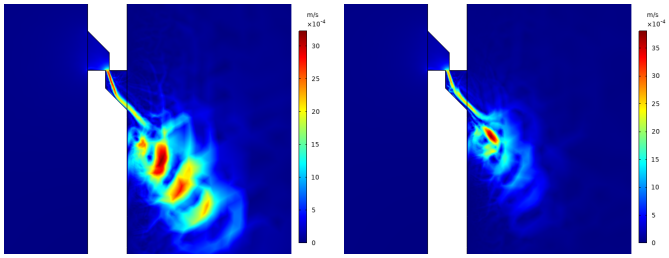

(c) 1 slit, $St_c = 0.6/2\pi$ **(d)** 1 slit, $St_c = 1.2/2\pi$

Figure 5.18. Spatial distribution of the dimensionless velocity perturbation $|\widehat{u}|/U_s$: (a) and (b), 3 slits at $St_b = 0.6/2\pi$ and $St_b = 1/2\pi$. Subfigures (c) and (d), 1 slit at $St_b = 0.6/2\pi$ and $St_b = 1/2\pi$.

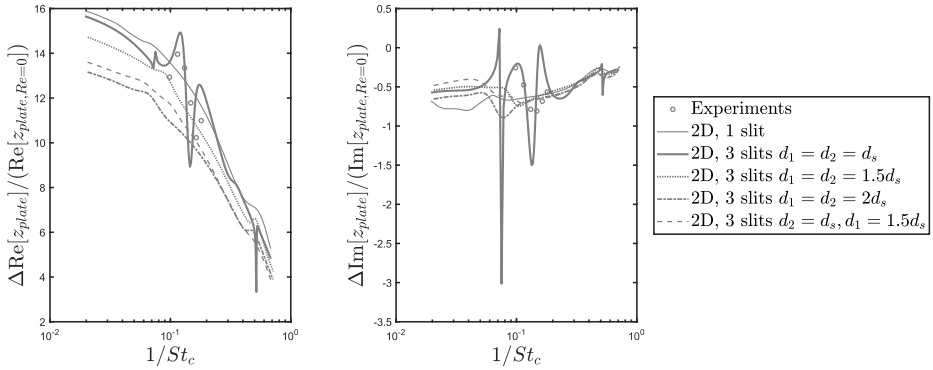

Figure 5.19. Effect of the distance between slits. Comparison of numerical and experimental changes of the real and imaginary parts of the acoustic transfer impedance of the plate as a function of the inverse of the Strouhal number $St_c = fw_{c,e}/U_s$ for $Re = 164$ of the geometries shown in Figure 5.17.

increased distances between the slits. Minor oscillation as a function of Strouhal

is observed around $St_c \approx 1/2\pi$ for the case with $d_1 = d_2 = 1.5d_s$. In this case, also the waviness at higher Strouhal numbers is captured. The distance between the slits seems to have a significant impact on the transfer impedance and the acoustic behavior of the plate with multiple slits. The effect of the interaction between slits decreases with increasing distance. The plate with three slits not equispaced also does not show the oscillating behavior. This hints that increasing the distance between the slits or using non-equispaced slit configurations reduces the oscillations as a function of the Strouhal number and the risk of whistling.

5.6 Discussion and conclusions

In applications such as combustion chambers, liners with slanted perforations are used to obtain a wall jet that provides protective film cooling to the walls. Inspired by this concept, in the present work, a micro-slit plate with a particular slit geometry is studied. This slit geometry is cheaper and easier to manufacture than slanted perforations, maintaining a similar wall jet downstream of the plate. A study of the acoustic response in terms of the acoustic transfer impedance in the presence of a bias flow is performed and focuses on the interaction between slits in a perforated plate with multiple slits. The study is limited to micro-slits defined as slits with Shear numbers based on the slit width of order unity. The discharge coefficient of a single slit displays hysteresis at high Reynolds numbers when the jet is expected to be turbulent. This is expected to be due to the Coanda effect allowing two metastable flow conditions (a jet leaving the plate and a jet along the downstream side of the plate). For multiple slits, the jets merge downstream of the plate to form a jet along the plate surface. This suppresses the existence of two meta-stable flow configurations. The Reynolds number is chosen for the acoustic transfer impedance measurements in the range $16.8 < Re < 581$ to limit the effects of turbulence, allowing a simplified (laminar) model. The transfer impedance of the plate is measured using an impedance tube. These acoustic measurements are complemented by steady flow discharge coefficient measurements. The steady flow is predicted using an incompressible two-dimensional viscous flow model. The corresponding acoustic impedance is predicted by a solution of two-dimensional Linearized Navier-Stokes equations.

The hydrodynamic interaction between slits is found to have a significant impact on the acoustic response of the plate and a model for the three slits provides a fair prediction of the experimental results, both for the discharge coefficient and the acoustic transfer impedance of the plate. Insight into the complex Reynolds number dependency found for the plate with multiple slits is gained. A strong impact of the interaction between neighboring slits is found for short distances between the slits. A quasi-steady Bernoulli approximation $\rho U_s/\alpha^2$, with U_s the cross-sectional averaged flow velocity provides an order of magnitude for the real part of the acoustic transfer impedance of the plate that increases for increasing

flow speeds (and Reynolds numbers). This shows that, in first-order approximation, the real part of the acoustic transfer impedance is dominated by convective effects within the slits. For the imaginary part of the acoustic transfer impedance (inertance), complex behavior is found around $St_c = fw_{c,e}/U_s = 1/2\pi$ and oscillations are observed, as a function of the Strouhal number. These are related to the hydrodynamic interaction between successive slits. Globally, a bias flow increases the resistance of the plate and decreases the inertance. A higher resistance means a larger bandwidth of absorption. A lower inertance at low frequencies $St_b = fb/U_s << 1$ is reducing the reflection of the waves for an infinitely large cavity. This study represents a first step toward optimization of the geometry of the slits to exploit the coalescence of the jets downstream of the plate to obtain film cooling.

6

Experimental study of non-linear effects in the presence of a bias flow

Abstract - In applications such as combustion chambers, a micro-slit plate used as a liner encounters moderate to high-amplitude acoustic excitation. In this chapter, impedance tube experiments in the presence of a bias flow for moderate and high acoustic amplitudes are discussed for the geometry inspired by bending and cutting the plate. In the range considered for this study, a bias flow appears to have two main effects. The presence of a bias flow enhances the absorption properties of the plate. A maximum of the enhancement factor is found at a specific ratio between the acoustic velocity and the mean flow velocity. Two simple asymptotic behaviors are found, either dominated by the flow or by the acoustic excitation, respectively. The behavior of the inertance is complex. Globally the inertance decreases with decreasing flow Strouhal number. Its dependency on the amplitude of the acoustic velocity is less obvious.

This Chapter is based on:
A. Aulitto, A. Hirschberg, V. Saxena, and I. Lopez Arteaga. Experimental study of a slit in the presence of a bias flow under medium and high level acoustic excitations. Submitted to the International Journal of Spray and Combustion Dynamics in February 2023.

6.1 Introduction

Perforated plates appear in many applications, such as combustion chambers or aircraft liners, where they encounter medium to high-acoustic excitation amplitudes and high temperatures. These are amplitudes at which a non-linear response appears.
In the previous chapter, the potential of a micro-slit plate with geometry obtained by punching and cutting the plate as a bias-flow liner is discussed. In Chapter 4, it is found that the onset of non-linear effects such as vortex shedding appears at fairly low acoustic excitation amplitudes and heavily impacts the acoustic behavior of the plate. In Chapter 5, the presence of a bias flow is found to increase the resistance and enhance the sound absorption properties of the plate for low acoustic amplitudes. In this Chapter, the study of the effect of a bias flow is extended to conditions where the plate encounters medium and high acoustic excitation amplitudes, *i.e.* in the presence of non-linear effects.
In the literature, most of the works focus on circular perforations in the presence of a mean flow [144, 173–176]. Salikuddin *et al.* [173] find that the effect of acoustic excitation amplitude is similar to that of a bias flow. Jing and Sun [175] compare a discrete vortex model and a quasi-steady method to study high-intensity sound absorption at an orifice with a bias flow. Eldredge and Dowling [87] prove the effectiveness of a perforated liner system with a mean bias flow in the absorption of planar acoustic waves in a circular duct. The combination of a bias flow and high acoustic amplitudes is also studied by Luong *et al.* [177] to extend the linear theory of Howe [178, 179] to predict the attenuation of sound by vorticity production in a bias flow aperture. Furthermore, several works focus on experimental results for the interaction between an acoustic field with a bias flow [144, 147, 180–182]. Zhou and Bodén [87, 176] find that a bias flow makes the acoustic properties more complex compared to the no bias-flow case, especially when the velocity ratio between acoustic velocity and mean flow velocity is close to unity. In recent works, Hirschberg *et al.* [82] and Burgmayer *et al.* [144, 183] discuss the effect of the geometry of the perforations on the acoustic response in the presence of flow. Interesting results are obtained with so-called zero mass flow liners (ZML) where a single-degree-of-freedom liner is attached to an acoustic actuator emitting a secondary high-amplitude sound field, inducing a periodic bias flow in the orifices [32–34, 48].
The scope of this Chapter is to discuss the effect of a bias flow in the presence of medium to high-acoustic-excitation amplitudes at which non-linear response is observed. However, we restrict our analysis to conditions of moderately high acoustic excitation amplitudes, for which the response is dominated by a single frequency so that the concept of impedance remains meaningful.
The acoustic transfer impedance of the micro-slit plate is experimentally studied, using impedance tube measurements. Special attention is given to the search for relevant dimensionless parameters and asymptotic behavior for low or high values

of these parameters, which are defined in Section 6.2.
Section 6.3 discusses the enhancing effect of a bias flow on the resistance of the plate. Following, Section 6.4 provides a study of the change of resistance due to non-linearities. Section 6.5 focuses on the behavior of the inertance. Finally, the conclusions are summarized in Section 6.6.

6.2 Definitions

In the previous chapters, the concept of transfer impedance is introduced in the frequency domain of frequency f. In Chapter 4, the validity of assuming an amplitude-dependent effective impedance is proven. The study is limited to moderately high amplitudes. In this chapter, the concept of impedance is extended in the presence of a bias flow. The dimensionless numbers used in this Chapter are presented here.
The Shear number is the ratio between the slit width b and the thickness of the viscous boundary layer δ_v

$$Sh = \frac{b}{\delta_v}, \tag{6.1}$$

with $\delta_v = \sqrt{2\mu/\omega\rho}$, where $\omega = 2\pi f$ is the angular frequency, ρ is the air density ($\rho = 1.18\,kg/m^3$ at 25°C and atmospheric pressure) and μ is the dynamic viscosity of air ($\mu = 1.85 \times 10^{-5}\,kg/ms$ at 25°C). The Shear number is used as a dimensionless presentation of the frequency.
The acoustical Strouhal number (St_{ac}) is the ratio between the slit width b and the amplitude of the oscillating particle displacement at the slits

$$St_{ac} = \frac{\omega b}{|\widehat{u}_{ac}|}, \tag{6.2}$$

where $\widehat{u}_{ac}$ is the cross-sectional surface averaged acoustic velocity amplitude defined as $\widehat{u}_{ac} = \widehat{u}/\Phi$, with Φ the plate porosity and

$$\widehat{u} = \frac{|\widehat{p}|}{\Phi|z_{plate}|} \tag{6.3}$$

the approaching acoustic-flow velocity, $|\widehat{p}_{ref}|$ the acoustic pressure at the reference microphone and z_{plate} the acoustic transfer impedance of the plate. The acoustic pressure is obtained assuming a sensitivity of the reference microphone of 50 mV. There is an uncertainty of the order of 5% in the absolute calibration of this microphone. The acoustic Strouhal number contains both the frequency and the acoustic amplitude.
The behavior of the plate can be studied as a function of the Strouhal number of the flow St_{flow} based on the cavity width w_c, expressed as

$$St_{flow} = \frac{\omega w_c}{U_s}, \tag{6.4}$$

with U_s the average flow velocity in the slit, $U_s = U_d/\Phi$, with Φ the porosity of the plate and U_d the average velocity in the duct. In the experiments, the velocity U_s is defined as

$$U_s = \frac{Q}{\Phi A_{tot}} = \frac{Q}{A_{open}}, \tag{6.5}$$

with Q the mass flow measured by the mass flow meter and $A_{open} = 3bl_s$ the total open area.
At low frequencies, using Bernoulli's frictionless quasi-steady-flow equation

$$p_{flow} \approx \frac{1}{2}\rho U_s^2 \tag{6.6}$$

one retrieves the limit for $Sh \to 0$ ($f \to 0$),

$$|\widehat{u}_{ac}| = |\widehat{p}|/\rho U_s. \tag{6.7}$$

The quantity $St_{flow}/2\pi$ is an estimation of the ratio of travel time over the cavity of fluid particles in the jet formed by flow separation downstream of the perforation and the oscillation period $1/f$.
The Reynolds number based on the slit width Re is defined, for a given volume flux Q through the perforated plate, as

$$Re = \frac{\rho U_s b}{\mu} = \frac{\rho Q}{\mu l_{s,tot}}, \tag{6.8}$$

with $l_{s,tot}$ the total length of the slits ($l_{s,tot} = 3 \times l_s$). This definition is used because in the experiments the steady mass-flow rate is measured. From this, the mass-flow rate Q can easily be estimated.
An acoustic Reynolds number

$$Re_{ac} = \frac{|\widehat{p}_{ac}|b}{\Phi c \mu}, \tag{6.9}$$

is defined as if the plate behaves as an anechoic termination. This representation shows a $Re_{ac} \approx 1$ in the linear case (corresponding to a sound pressure level SPL 86 dB, with $SPL = 20log_{10}(\widehat{p}_{ac,rms}/p_{ref})$ with $p_{ref} = 2 \times 10^{-5}$ Pa.
The dimensionless number $\bar{P}$ is introduced to define the ratio between the flow and the acoustic pressure in the experiments as

$$\bar{P} = \frac{\rho {U_s}^2}{2|\widehat{p}|} \approx \frac{p_{flow}}{|\widehat{p}|}. \tag{6.10}$$

This representation of the dimensionless number is chosen (and not the inverse) to include the no-flow case for $U_s = 0$ with $\bar{P} = 0$. The parameter $\bar{P}$ is the ratio between the dynamic pressure of the steady flow and the acoustic pressure.
For this study, the impedance tube discussed in the previous chapters is used,

according to the detailed description of experiments provided in Chapter 5. In this study, Reynolds numbers $Re < 100$ are considered to avoid the complex effects found in the previous chapter. The acoustic excitation amplitudes are chosen between 86 dB, corresponding to the linear limit, to 120 dB, within the range of linearity of the microphones. The range of Shear numbers is kept the same as in the previous Chapter ($1.8 \leq Sh \leq 3.5$). This range is chosen to obtain a good signal-to-noise ratio for the linear case.

6.3 Enhancement of the resistance

Maa [51] suggested that maximum absorption for a micro-slit plate can be obtained when $Z/\rho c$ is approximately unity. Hence, for optimal absorption, the impedance of the plate should approach the characteristic impedance of air. In this section, the potential of adding a bias flow to enhance the absorption properties is investigated. In Figure 6.1, the real part of the impedance is shown normalized with the characteristic impedance of air for several flow speeds (Reynolds numbers) as a function of the ratio between the amplitude of the acoustic velocity and the flow velocity. The relevant parameter is the mean flow Reynolds number Re (in legend the line corresponding to the highest acoustic amplitude is used for representation).
Globally, in the presence of flow, one achieves a higher resistance for low and high acoustic excitations. This shows that even for high acoustic excitations, the presence of a flow does produce a significant effect on the resistance.

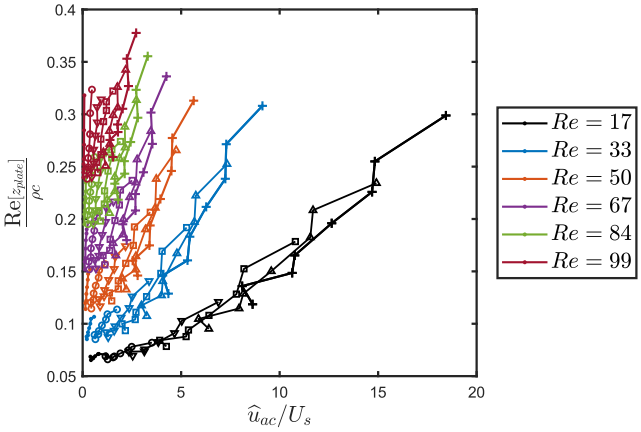

Figure 6.1. Real part of the acoustic transfer impedance of the plate normalized with the characteristic impedance as a function of the velocity ratio $\widehat{u}_{ac}/U_s$. The different symbols represent different frequencies.

In Chapter 5, the quasi-steady limit $\rho\widehat{u}_{ac}/2\alpha^2\Phi$ provides an order of magnitude for the resistance in the linear regime. The same normalized representation is used in Figure 6.2, where the real part of the acoustic transfer impedance is shown, normalized with the quasi-steady limit as a function of the ratio between the acoustic velocity $\widehat{u}_{ac}$ and the mean flow velocity U_s. The dimensionless number Re_{ac} is used in the legend to discuss the effect of the amplitude. It can be seen that for $\widehat{u}_{ac}/U_s < 2$, the behavior of the resistance is dominated by the mean flow. The dimensionless resistance follows the linear quasi-steady asymptote $U_s/\widehat{u}_{ac}$. For $2 < \widehat{u}_{ac}/U_s < 4$, one observes a clear transition. For $\widehat{u}_{ac}/U_s > 4$, the resistance is dominated by the non-linear behavior due to high acoustic excitation amplitude and tends to a horizontal asymptote. This asymptote corresponds to the high amplitude limit for the no-flow case. One observes that the effect of a bias flow is similar to the effect of acoustic excitation amplitude.

A third dimensionless representation for the real part of the acoustic transfer impedance is used in Figure 6.3. The linear quasi-steady limit ρU_s allows quantifying the contribution of convection on the resistance. It can be seen that for $\widehat{u}_{ac}/U_s < 4$, around 80% of the resistance is due to the linear contribution.

At a given acoustic excitation amplitude (defined in decibels, dB), the ratio between the resistance and the resistance in the no-flow case can be defined as the enhancement factor EF. This factor quantifies the increase in the absorption that can be obtained by introducing a bias flow and can be expressed as

$$rEF = \frac{\mathrm{Re}[z_{plate}]}{\mathrm{Re}[z_{plate,no-flow}]}, \tag{6.11}$$

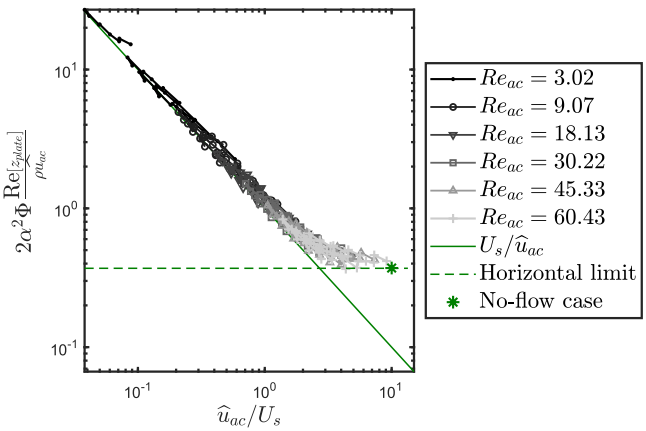

Figure 6.2. Real part of the acoustic transfer impedance of the plate normalized with quasi-steady limit for high acoustic excitations as a function of the velocity ratio $\widehat{u}_{ac}/U_s$.

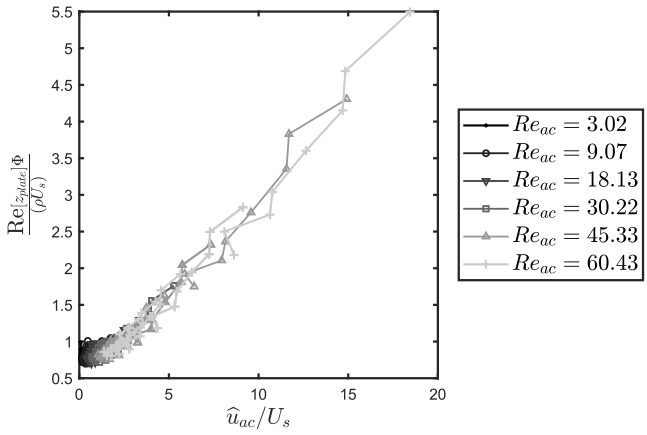

Figure 6.3. Real part of the acoustic transfer impedance of the plate normalized with linear quasi-steady limit as a function of the ratio $\widehat{u}_{ac}/U_s$.

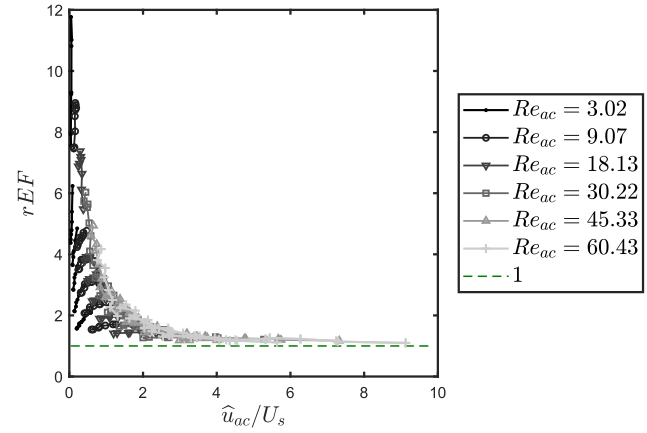

Figure 6.4. Enhancement factor as a function of the ratio $\widehat{u}_{ac}/U_s$ for several acoustic excitation amplitudes.

where rEF stands for the resistance enhancement factor. An enhancement of the resistance corresponds to an increase in the bandwidth of the absorption. In Figure 6.4, the enhancement factor is shown as a function of the velocity ratio for several acoustic excitation amplitudes. One sees that, overall, the presence of a bias flow increases the resistance with respect to the no-flow case. Hence, the enhancement factor is larger than one.

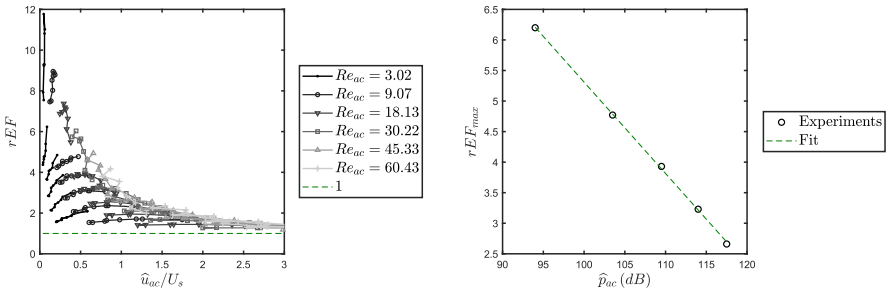

(a) **(b)**

Figure 6.5. a) A zoom of the enhancement factor for velocity ratio $\widehat{u}_{ac}/U_s < 3$. b) Maximum of the enhancement factor rEF_{max} shown as a function of the acoustic excitation amplitude in decibels.

For low velocity ratios $\widehat{u}_{ac}/U_s < 0.4$, which corresponds to the region dominated by the mean flow, one observes an increase of the resistance with the velocity ratio. The curves show a maximum around $\widehat{u}_{ac}/U_s \approx 1$, where, after the maximum, one finds a transition zone where the enhancement factor decreases with increasing velocity ratios. Jing and Sun [175] and Zhou and Bodén [176] found a similar transition range for an orifice in the presence of a bias flow ($0.3 < \widehat{u}_{ac}/U_s < 4$). In this range, they observe a dip in the resistance. For $\widehat{u}_{ac}/U_s > 4$, the resistance tends to the no-flow case, as shown in Figure 6.3. A horizontal asymptote close to $rEF = 1$ is found. From the engineering point of view, this means that, given an acoustic pressure excitation, a bias flow velocity can be tuned to achieve the largest resistance, *i.e.* the maximum of sound absorption. In Figure 6.5a, a zoom of Figure 6.4 for $\widehat{u}_{ac}/U_s < 3$ is shown. The maximum enhancement factor is shown in Figure 6.5b as a function of the acoustic excitation amplitude in decibels. This shows that the maximum enhancement decreases with increasing acoustic excitation amplitudes. A linear fit of the experimental results with $rEF_{max} = 20.26 - 0.15\,\mathrm{dB}^{-1}\widehat{p}_{ac}$, with $\widehat{p}_{ac}$ in decibels is proposed. The parameters of this fit are specific to this geometry.

6.4 Change of resistance due to non-linearities

In this section, the change of resistance due to the presence of non-linearities at moderate and high acoustic amplitudes is discussed. In the linear case, for the full range of frequencies, the resistance is constant. Figure 6.6 shows the change of resistance $\Delta\mathrm{Re}[z_{plate}] = \mathrm{Re}[z_{plate}] - \mathrm{Re}[z_{plate,linear}]$ normalized with the resistance in the linear case ($\mathrm{Re}[z_{plate,linear}]$) and presented as a function of the Shear number.

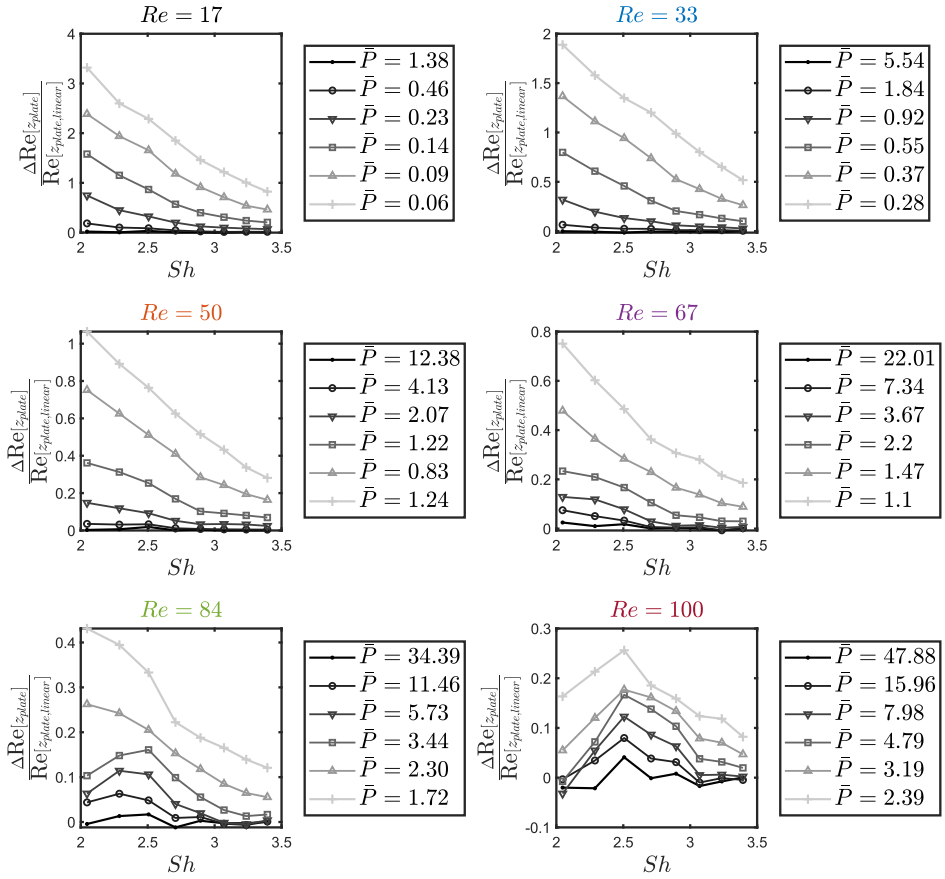

Figure 6.6. Change of the real part of the acoustic transfer impedance of the plate normalized with the linear case as a function of the Shear number $Sh = b/\delta_v$ for several Reynolds numbers.

The linear contribution $\mathrm{Re}[z_{plate,linear}]$ is obtained at the lowest experimental amplitude (86 dB).
Each of the figures corresponds to a fixed flow speed (Reynolds number).
Each curve corresponds to a different value of the parameter $\bar{P} = p_{flow}/|\widehat{p}_{ac}| = \rho U_s^2/(2|\widehat{p}_{ac}|)$.
It can be seen that, globally, one observes an amplitude-dependent resistance that increases with increasing amplitude (and decreasing $\bar{P}$) for all mean flow speeds. For $Re < 67$, the resistance decreases with the Shear number.
Increasing the flow speed, the effect of the non-linearities decreases and for $Re = 100$ one observes a non-monotonous behavior of the resistance.

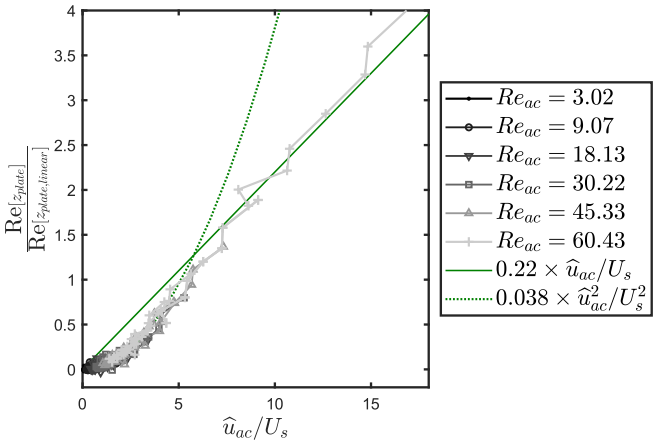

Figure 6.7. Change of the real part of the acoustic transfer impedance of the plate normalized with the linear case as a function of the velocity ratio $\widehat{u}_{ac}/U_s$.

For low values of $\bar{P}$ ($\bar{P} < 10$), the behavior of the resistance is heavily affected by the presence of a bias flow.
In Figure 6.7, the change of resistance is shown as a function of the velocity ratio $\widehat{u}_{ac}/U_s$ for several acoustic excitation amplitudes.
The change in resistance increases with increasing velocity ratios. In the first region, $\widehat{u}_{ac}/U_s < 4$, the dependence on the velocity ratio is quadratic, transitioning to a linear dependence and approaching the quasi-steady behavior for higher velocity ratios. The change in resistance is seen to be proportional to the ratio $\widehat{u}_{ac}/U_s$ for high acoustic amplitudes and to the ratio $(\widehat{u}_{ac}/U_s)^2$ for low and moderate amplitudes.
Considering the parameter $\bar{P} = p_{flow}/|\widehat{p}_{ac}| = \rho U_s^2/(2|\widehat{p}_{ac}|)$, in the quasi-steady limit, when $\bar{P} << 1$, the acoustic velocity is

$$\widehat{u}_{ac} \simeq \sqrt{\frac{2\widehat{p}_{ac}}{\rho}}. \tag{6.12}$$

One obtains

$$\frac{\widehat{u}_{ac}}{U_s} = \sqrt{\frac{1}{\bar{P}}}. \tag{6.13}$$

Therefore, the change in resistance is expected to be proportional to $\sqrt{\bar{P}}$ for high acoustic amplitudes and to $\bar{P}$ for low and moderate amplitudes.
In Figure 6.8, the change of resistance due to non-linear effects is shown for similar $\bar{P}$ as a function of the inverse of the acoustic Strouhal number. For each Reynolds number considered in Figure 6.6, the lines corresponding to $\bar{P} < 10$ are considered.

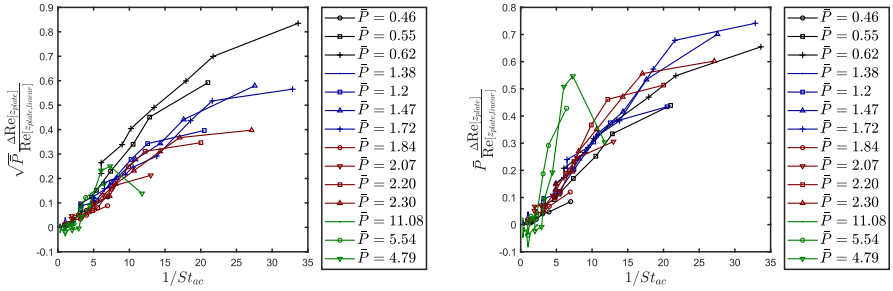

(a) **(b)**

Figure 6.8. Change of the real part of the acoustic transfer impedance of the plate normalized with the linear case as a function of the inverse of the acoustic Strouhal number ($St_{ac} = \omega b/u_{ac}$) for similar pressure ratios $\bar{P}$. a) Scaling with $\sqrt{\bar{P}}$, b) Scaling with $\bar{P}$.

This representation offers a better collapse of the results than a representation with the flow Strouhal number. The change of resistance is scaled (multiplied) with the parameter $\sqrt{\bar{P}}$ (Figure 6.8a) and with the parameter $\bar{P}$ (Figure 6.8b).
One sees a good collapse of the results for both representations with the dimensionless change of resistance approaching order unity for increasing acoustic Strouhal numbers. Although, a better global collapse is observed for a change in resistance scaled with $\bar{P}$ (Figure 6.8b), some discrepancies are found with the highest $\bar{P}$, corresponding to the flow-dominated results.

6.5 Change of inertance due to non linearities

In this section, the behavior of the imaginary part of the acoustic transfer impedance (inertance) is discussed. The inertance is responsible for a shift in the frequency of the peak of absorption.
In Figure 6.9, the change of inertance due to the presence of a bias flow is shown as a function of the velocity ratio. One sees that, for low and moderate acoustic amplitudes, the inertance is lower in the presence of flow, whereas for high amplitudes, it is slightly higher. A deep in the inertance can be seen around the same $\widehat{u}_{ac}/U_s$ as the peak of resistance. Overall, the change in inertance is not as high as the change of resistance observed in Figure 6.4. There appears to be a dependence on the flow Strouhal number, with the mean flow dominating the inertance.

In Figure 6.10, the change of inertance with respect to the linear case is shown as a function of the inverse of the flow Strouhal number. One observes a fair collapse of the results for $1/St_{flow} < 0.4$ with a fairly constant correction. Above $1/St_{flow} \approx 0.6$, the change of inertance increases linearly with increasing $1/St_{flow}$.

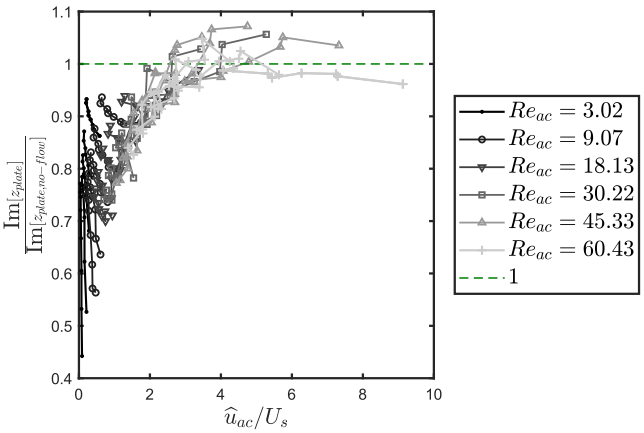

Figure 6.9. Imaginary part of the acoustic transfer impedance of the plate normalized with the no-flow case as a function of $\widehat{u}_{ac}/U_s$.

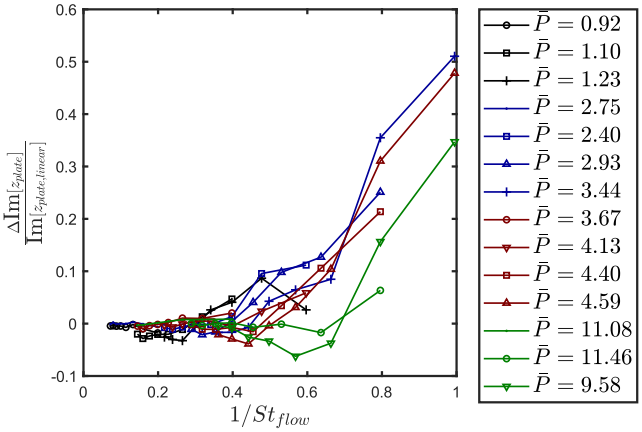

Figure 6.10. Change of the imaginary part of the acoustic transfer impedance of the plate normalized with the linear case as a function of the inverse of the flow Strouhal number ($St_{flow} = \omega w_{c,e}/U_s$) for similar pressure ratio $\bar{P}$.

6.6 Conclusions

Experimental results for the non-linear acoustic transfer impedance in the presence of a bias flow are discussed. Maa [51] suggested that optimal absorption can be obtained with a micro-slit plate backed by a cavity when the resistance of the plate

matches the characteristic impedance of air. Introducing a bias flow produces a significant change in the resistance of the plate, which can potentially enhance the absorption properties of the plate. The presence of the flow shows a double effect. On one side it increases the resistance, increasing the bandwidth of absorption. On the other, the inertance decreases, shifting the peak of absorption toward higher frequencies. For low acoustic excitations, the behavior is dominated by the flow, and a simple linear quasi-steady model ρU_s captures around 80% of the resistance of the plate. For high acoustic excitation, the behavior is fully non-linear, with the resistance approaching the resistance in the no-flow case. A transition range is found for a ratio of the amplitude acoustic velocity and the mean flow velocity between 0.3 and 4. Such a transition range is also observed in literature for circular perforations, where a minimum of the resistance is seen in this transition zone [175, 176]. For this particular geometry, a maximum of the resistance is seen, when the mean flow velocity is in the same order as the amplitude of the acoustic velocity. It is found that the resistance depends on the square of the velocity ratio for low and moderate amplitudes, while for high amplitudes, a linear dependency is found. The same behavior is found when considering the change of resistance due to non-linearities, which appears to be a function of the ratio between the dynamic pressure and the acoustic pressure. The inertance shows a more complex behavior with a strong dependence on the flow Strouhal number.

7

Sound absorption properties of a single-degree-of-freedom liner based on micro-slit plates

Abstract - In this Chapter, a simple and directly applicable lumped-element model is used to analyze the sound absorption properties of a single-degree-of-freedom liner where the plate is backed by a cavity, for plane waves at normal incidence. The effect of the heat transfer at the walls of the cavity is included. In the linear regime, the sound absorption of the micro-slits is similar to the one of circular perforations. Differences are found only for low Shear numbers. Such differences disappear in the presence of a cavity. However, the sound absorption of the absorber is strongly influenced by the acoustic transfer impedance of the plate. Therefore, the focus is given to the influence of geometric parameters (thickness and porosity of the plate and edge geometry) on the sound absorption of the plate, when backed by a semi-infinite cavity. Vortex shedding associated with non-linear effects or the presence of a bias flow increases the sound absorption properties of the plate. A bias flow is essential for the absorption at high Shear numbers.

This Chapter is based on:
A. Aulitto, A. Hirschberg, and I. Lopez Arteaga. Sound absorption properties of a single-degree-of-freedom liner based on micro-slit plates. In preparation for submission to Applied Acoustics in March 2023.

7.1 Introduction

Since the second half of the 20th (twentieth) century, perforated plates appeared as means to suppress instabilities in combustion [7–9]. High efficiency and low emission combustion systems are more sensitive to combustion instabilities [10, 11]. In recent years, hydrogen combustion has appeared as an emerging technology to replace fossil fuels and provide carbon-neutral energy. When dealing with hydrogen, thermo-acoustic instabilities provide a serious limitation to safe combustion, in combination with the presence of flashbacks. Thermo-acoustic instabilities are generated by a complex feedback mechanism between heat release fluctuations, flow, and acoustic oscillations. The coupling can generate large-amplitude self-sustained pressure oscillations that can lead to catastrophic damages to the hardware [12]. Perforated plates, backed by shallow cavities, offer an excellent sound absorption ability and provide means to manipulate and re-distribute the acoustic energy loss at the walls of the chamber, making the system stable [13–17]. When considering a micro-perforated plate or a micro-slit plate, the main focus has been given, in this thesis, to the acoustic transfer impedance of an isolated plate (with an infinitely large back cavity) and not to the actual sound absorption properties of the plates, as commonly used with a back cavity. The system formed by the plate, a back cavity, and a solid back plate is commonly referred to in the literature as a single-degree-of-freedom (SDOF) liner [19, 20]. In this Chapter, the concept of acoustic transfer impedance is translated into the sound absorption of the plate. The aim is to use the most simple model to discuss the influence of basic parameters on the sound absorption properties of perforated plates. The first goal is to gain insight into the combination of effects discussed in the previous chapters. This could provide a design and optimization tool, useful for several practical applications. The study ranges from room acoustics (linear regime, low or negligible mean flow speeds) to combustion chamber applications (high acoustic excitation amplitudes and higher mean flow speeds). When considering a slit or a circular perforation, several parameters come into play. From the geometric point of view, an optimization process should consider the thickness of the plate, the slit width, the length of the slits, and the porosity of the plate. The viscosity effects, connected to the frequency, add another parameter. A schematic representation of the slit width b, the slit length l_s, and the plate thickness t_p is shown in Figure 7.1. In this Chapter, we focus on a given porosity ($\Phi = 2.7\%$) and a ratio between the slit width and the plate thickness equal to one ($b/t_p = 1$). The findings of this work can be extended to perform a parametric study and applied to several different geometries. A lumped-element model for the absorption of a micro-perforated plate is proposed in Section 7.2. Some of the aspects not taken into account by the adiabatic-wall model are discussed in Section 7.2.1. A correction for the heat transfer by the cavity walls is proposed in the isothermal-wall model in Section 7.2.2. Sections 7.2.3 and 7.2.4 focus on the acoustic transfer impedance of micro-slit plates and micro-perforated plates with sharp and rounded edges.

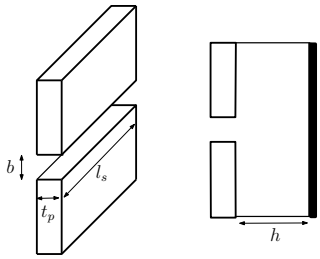

Figure 7.1. Schematic representation of a rectangular slit in a plate, backed by a cavity.

Section 7.3 focuses on the plate backed by a back cavity and Section 7.4 investigates the acoustic properties of MPPs and MSPs in several conditions with an infinitely deep back cavity. In the linear case, the effect of the change of thickness and porosity of the plate is discussed (Section 7.4.1) together with the effect of not-sharp edges of the slit (Section 7.4.2). Section 7.4.3 focuses on the contribution of non-linear effects on the sound absorption of the plate. In Section 7.4.4, the enhancing effect of a bias flow is discussed. A discussion of the findings and conclusive remarks follows in Section 7.5.

7.2 A lumped-element model for the sound absorption

Consider a micro-perforated plate or micro-slit plate with a back cavity of depth h in the case of plane waves at normal incidence. The lumped-element impedance of the wall is the sum of the inertance and resistance of the orifice and the compliance of the back cavity. In this work, the discussion is limited to a simple empty cavity. The lumped-element impedance is here defined as $\Delta\widehat{p}/\widehat{q}$ where $\widehat{q}$ is the amplitude of volume-flux oscillation. Hence, the impedance is $Z = \Delta\widehat{p}/\widehat{u}$ divided by the surface of the duct S_d. The lumped neck inertance is given by:

$$\left(\frac{\Delta\widehat{p}}{S_n\widehat{u}_s}\right)_{\text{In}} = -\frac{i\omega\rho_0 t_{\text{eff}}}{S_n}, \tag{7.1}$$

where S_n is the area of the duct, normal to the wave propagation direction, and t_{eff} is the effective length of the plate with $t_{eff} = t_p + 2\delta_{in}$. The lumped neck resistance is given by:

$$\left(\frac{\Delta\widehat{p}}{S_n\widehat{u}_s}\right)_{\text{Res}} = R_v + \frac{\rho_0(U_s + \widehat{u}_s)}{S_n\alpha^2}, \tag{7.2}$$

where R_v is the viscous contribution and the second term is the quasi-steady convective lumped resistance, including a non-linear term $\widehat{u}_s$, with U_s the cross-

sectional averaged steady bias-flow speed in the perforation and α the *vena-contracta* factor [122, 125]. The viscous contribution is given by $R_v = \int \mu \nabla^2 u \cdot \mathrm{d}s$ [184]. The lumped compliance of the back cavity can be deduced when assuming an iso-entropic variation of the density in the cavity:

$$\frac{\Delta \widehat{V}}{V} = \frac{S_n \widehat{u}_s}{i\omega S_d h} = -\frac{\widehat{\rho_0}}{\rho_0} = -\frac{\widehat{p}}{\rho_0 c_0^2}, \tag{7.3}$$

where the volume of the cavity is $V = hS_n/\Phi$ with S_n/Φ the surface area and h the depth of the cavity. The quantity

$$\frac{\Delta \widehat{V}}{V} = \frac{\widehat{q}}{V} = \frac{\widehat{q}\Phi}{S_n h}. \tag{7.4}$$

Combining the last parts of Equation 7.3 and Equation 7.4, one has

$$\left(\frac{\Delta \widehat{p}}{\widehat{q}}\right)_{Comp} = \frac{i\rho_0 c_0^2 \Phi}{\omega S_n h}, \tag{7.5}$$

with $\nabla \widehat{p} = \mathrm{i}\omega \widehat{p}$. The total lumped impedance is given by:

$$Z_{tot}/S_d = \left(\frac{\Delta \widehat{p}}{S_n \widehat{u}_s}\right)_{\mathrm{In}} + \left(\frac{\Delta \widehat{p}}{S_n \widehat{u}_s}\right)_{\mathrm{Res}} + \left(\frac{\Delta \widehat{p}}{\widehat{q}}\right)_{\mathrm{Comp}}, \tag{7.6}$$

where the influence of heat transfer to the walls of the cavity is neglected (adiabatic-wall model). The reflection coefficient R is

$$R = \frac{Z_{tot} - \rho_0 c_0}{Z_{tot} + \rho_0 c_0}, \tag{7.7}$$

and the sound absorption of the plate is obtained as

$$A = 1 - |R|^2. \tag{7.8}$$

This absorption represents the amount of energy that is not reflected and contains both the contribution of the dissipated energy and the transmitted acoustic waves. For a single-degree-of-freedom system, when the plate is backed by a cavity, there is no transmission and this absorption corresponds to the energy dissipated by the plate. For a perforated plate without a back wall, the actual dissipation of the plate, neglecting convective effects, can be defined as

$$D = 1 - |R|^2 - |T|^2, \tag{7.9}$$

where T is the transmitted wave amplitude. For an incoming wave of amplitude I and a reflected wave of amplitude RI, with R the reflection coefficient, the particle velocity at the front of the plate is $\widehat{u} = I(1-R)/Z_0$ with $Z_0 = \rho_0 c_0$. The

transmitted wave amplitude is $Z_0\widehat{u} = I(1-R)$ and $T = 1-R$. Therefore, the dissipation can be calculated as

$$D = 1 - |R|^2 - |1-R|^2. \tag{7.10}$$

When R_v is negligible and $St_b = fb/U_s << 1$ we have in the linear case:

$$z_{plate} = \frac{Z_{tot}}{\rho_0 c_0} = \frac{U_s}{c\Phi\alpha^2} + \frac{i\omega t_{\text{eff}}}{\Phi c_0}\left[\frac{1}{khkt_{\text{eff}}} - 1\right]. \tag{7.11}$$

For a semi-infinite space behind the plate $k^2 h t_{\text{eff}} >> 1$ we see that a lower inertance kt_{eff} results in a reduced reflection. Furthermore, for each value of U_s there is a critical porosity $\Phi = \frac{U_s}{c\alpha^2}$ such that reflections are minimized (if kt_{eff} is negligible). This corresponds to the idea of Bechert [185] of an anechoic termination (see also Hofmans*et al.* [186] and Durrieu *et al.* [187]). At the Hemholtz-resonance frequency $k^2 h t_{\text{eff}} = 1$ and the impedance becomes purely real.

7.2.1 Limitations of the adiabatic-wall model

The model proposed in the previous section represents the most simple model and several phenomena are, therefore, not included. The first limitation is that visco-thermal dissipation within the cavity is not considered. These effects become important when $h/b = O(1)$, *i.e* when $h/\delta_v \approx 1$. In this case, an additional impedance in series with the plate and the cavity capacity should be added, as discussed in Landau and Lifchitz [188] and Rienstra and Hirshberg [106]. Furthermore, for shallow cavities the model for the end-corrections proposed in Aulitto *et al.* [124] is not accurate because it assumes $h >> \delta_v$. Therefore the model cannot be applied to very shallow cavities.
When considering large cavities, for $h >> b$, the standing wave pattern within the cavity should be considered. The first longitudinal frequency is, for low porosity, $f_r = c/2h$, where for $b = 0.5\,\text{mm}$ and $h = 50\,\text{mm}$, $f_r = 7\,\text{kHz}$. Hence, the model fails when the frequency approaches cavity resonances.
Finally, when $h/b \approx 1$, between the plate and the cavity wall a thin air-gap, is created and, therefore, wall vibrations due to the flexibility of the plates can become a significant dissipation mechanism for shallow cavities, even without perforations [189, 190, 190, 191].

7.2.2 Isothermal-wall model

When including the contribution of the heat transfer to the top and bottom walls of the cavity, the acoustic impedance of the system changes. The compliance impedance Z_{Comp} and the thermal contribution $Z_{Thermal}$ share the same pressure fluctuation, whereas the mass flow through the neck of the resonator is the sum of a mass flow associated with the heat transfer and a mass flow associated to

the acoustic wave. Hence, the combined impedance of the cavity Z_{cavity} in the presence of thermal effects is

$$Z_{cavity} = \frac{1}{\frac{1}{\left(\frac{\Delta\widehat{p}}{\widehat{q}}\right)_{\text{Comp}}} + \frac{1}{\left(\frac{\Delta\widehat{p}}{\widehat{q}}\right)_{\text{Thermal}}}}, \tag{7.12}$$

with the compliance of the cavity and the thermal effect acting in parallel. The thermal contribution, according to Landau and Lifchitz [188] and Rienstra and Hirshberg [106] is

$$\left(\frac{\Delta\widehat{p}}{\widehat{q}}\right)_{\text{Thermal}} = \frac{(1-i)\rho_0 c_0^2 \Phi}{2(\gamma-1)\omega\delta_T S_n}, \tag{7.13}$$

where $\delta_T = \delta_v\sqrt{Pr}$ and $Pr = 0.72$ is the Prandtl number of air (ratio of kinematic viscosity and heat diffusivity). The factor of 2 takes into account that both the bottom and top walls of the cavity are involved. It is assumed that they have the same surface because $\Phi << 1$. One can also take into account the effect of heat transfer at the front of the plate by considering the cavity impedance Z_{tot} placed in parallel to the plate surface impedance $Z_{Thermal}$:

$$Z_{Thermal} = \frac{(1-i)\rho_0 c_0^2}{(\gamma-1)\omega\delta_T}. \tag{7.14}$$

This effect is however negligible in most of the cases considered here. The total impedance becomes

$$\frac{Z_{tot}}{S_d} = \left(\frac{\Delta\widehat{p}}{S_n\widehat{u}_s}\right)_{\text{In}} + \left(\frac{\Delta\widehat{p}}{S_n\widehat{u}_s}\right)_{\text{Res}} + \frac{1}{\frac{1}{\left(\frac{\Delta\widehat{p}}{\widehat{q}}\right)_{\text{Comp}}} + \frac{1}{\left(\frac{\Delta\widehat{p}}{\widehat{q}}\right)_{\text{Thermal}}}}. \tag{7.15}$$

7.2.3 Impedance of MPPs and MSPs

In the linear case, for a micro-perforated plate with sharp squared edges, Temiz *et al.* [23] propose a semi-empirical expression for the acoustic transfer impedance of the plate with sharp edges

$$Z_{tot} = \mathrm{i}\omega t_p \rho_0 \left[1 - \frac{2}{\frac{Sh}{\sqrt{2}\sqrt{-\mathrm{i}}}} \frac{J_1\left(\frac{Sh}{\sqrt{2}}\sqrt{-\mathrm{i}}\right)}{J_0(\frac{Sh}{\sqrt{2}}\sqrt{-\mathrm{i}})}\right] + 2\beta_r R_s + \frac{\mathrm{i}}{2}\delta_i\omega\rho_0, \tag{7.16}$$

with

$$\beta_r = 5.08\left(\frac{Sh}{\sqrt{2}}\right)^{-1.45} + 1.70, \tag{7.17}$$

and

$$\delta_i/d_p = 0.97e^{\left(-0.20\frac{Sh}{\sqrt{2}}\right)} + 1.54, \tag{7.18}$$

where R_s is the surface resistance on one side of the plate

$$R_s = 0.5\sqrt{2\mu\rho_0\omega} = \frac{1}{2}\rho_0\omega\delta_v. \tag{7.19}$$

The impedance of the micro-slit plate with infinitely long slits is proposed in Aulitto *et al.* [124] for sharp edges, for $Sh << 1$

$$Z_{tot,l} = \rho_0 c_0 12\frac{\nu(t_p + 2\delta_{res,l})}{c_0 b^2 \Phi} + \mathrm{i}\rho_0 c_0 \frac{6}{5}\frac{\omega(t_p + 2\delta_{in,l})}{c_0\Phi}, \tag{7.20}$$

with the end-corrections

$$\delta_{res,l} = 0.425b \quad \text{and} \quad \delta_{in,l} = b\left(-2.17 + 2.18\frac{1}{\Phi^{0.13}}\right). \tag{7.21}$$

In the high Shear number range ($Sh >> 1$)

$$Z_{tot,h} = \rho_0 c_0 \omega\frac{(t_p + 2\delta_{res,h})}{c_0\Phi} + \mathrm{i}\rho_0 c_0\frac{\omega(t_p + 2\delta_{in,h})}{c_0\Phi}\left(1 + \frac{1}{Sh}\right), \tag{7.22}$$

with the end-corrections

$$\delta_{res,h} = 0.82b\left(1 + \frac{5.19 + 28.74\Phi}{Sh(1.69 + 3.97\Phi + Sh)}\right), \tag{7.23}$$

and

$$\delta_{in,h} = 0.98b\frac{0.52 + 9.34\Phi}{1.27 + 7.45\Phi + Sh}, \tag{7.24}$$

where the index h indicates the high Shear number limit and l is the low Shear number limit. In Figure 7.2, the inertial end-corrections of slits and circular perforations are compared from the literature [97, 100, 108]. A similar plot is proposed

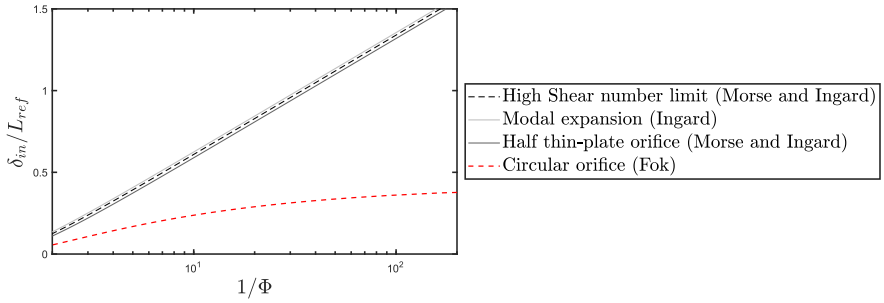

Figure 7.2. Inertial end-corrections (δ_{in} for slits and δ_i for circular perforations) from literature for slits and circular perforation [124]. $L_{ref} = b$, for slits. $L_{ref} = d_p$, for circular perforations.

in Aulitto *et al.* [124]. The reference length L_{ref} is the slit width b for slits and the perforation diameter d_p for circular perforations. For slits, the inertial end-correction becomes infinitely large for vanishing porosity.
This divergence can be avoided by taking into account the effects of compressibility. For circular perforations, a finite limit is reached. In Figure 7.3, the behavior of the inertial and resistive end-corrections as a function of the Shear number is shown for a rectangular slit for several porosities.

7.2.4 Effect of rounded edges on the impedance

For micro-perforated plates with circular perforations, Temiz *et al.* [23] proposes a modification of the coefficient β_r and δ_i in case of perforations with chamfered edges from both sides. The formulas provided in Temiz *et al.* [23] refer to a plate with a core thickness $t_{p,core} = t_p - 2c_p$, with t_p the total plate thickness, and c_p the length of one chamfer. Please note that this definition is in contradiction with the figures in the paper of Temiz *et al.* [23]. The parameters for respectively the chamfered-perforations, the smoothed-edges perforations, and the rounded-edges perforations are defined in each subfigure of Figure 7.4: the length of the chamfer c_p, the transition length d, and the rounding of the edge r. The core thickness of the plate $t_{p,core}$ represents the straight (horizontal) portion of the perforation in the plate, and this thickness is used in Equation 7.16 to obtain the impedance of the micro-perforated plate in the presence of a chamfer. Temiz *et al.* [23] propose empirical expression for the end-corrections in case of rounded edges with

$$\beta_r = 5.08\left(\frac{Sh}{\sqrt{2}}\right)^{-1.45} + 1.70 + 1.18\left(\frac{c_p}{d_p}\right)^{1.74}\left(\frac{Sh}{\sqrt{2}}\right)^{-0.26}, \tag{7.25}$$

$$\delta_i/d_p = 0.97e^{\left(-0.20\frac{Sh}{\sqrt{2}}\right)} + 1.54 + 0.97\left(\frac{c_p}{d_p}\right)^{0.56} e^{\left(-0.01\frac{Sh}{\sqrt{2}}\right)}. \tag{7.26}$$

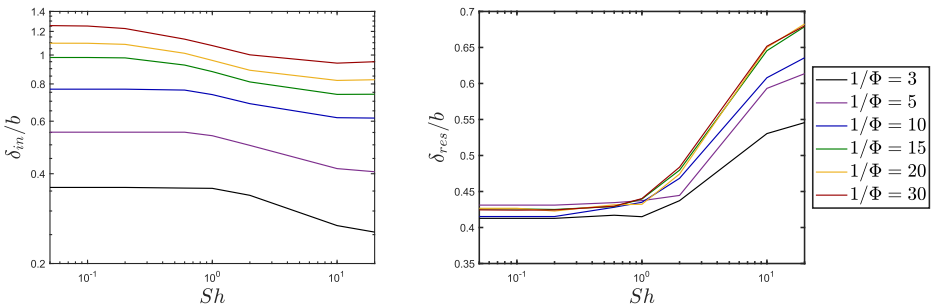

Figure 7.3. Inertial and resistive end-corrections as a function of the Shear number for a rectangular slit for several porosities.

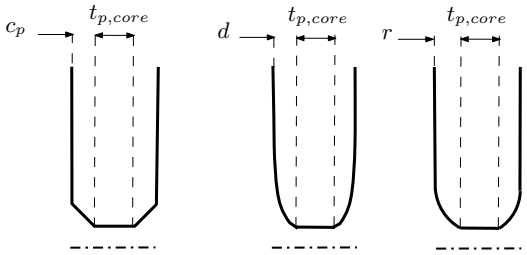

Figure 7.4. Schematic representation of the perforation with chamfered, smoothed, and rounded edges.

Table 7.1. Values of the end-corrections for slits with rounded edges [124].

Correction	$d/b = 0.1$	$d/b = 0.5$	$c_p/b = 0.5$	$r/b = 0.5$
$\frac{\delta_{res,round}}{\delta_{res,sharp}}$	0.89	0.59	0.27	0.47
$\frac{\delta_{in,round}}{\delta_{in,sharp}}$	0.96	0.80	0.56	0.73

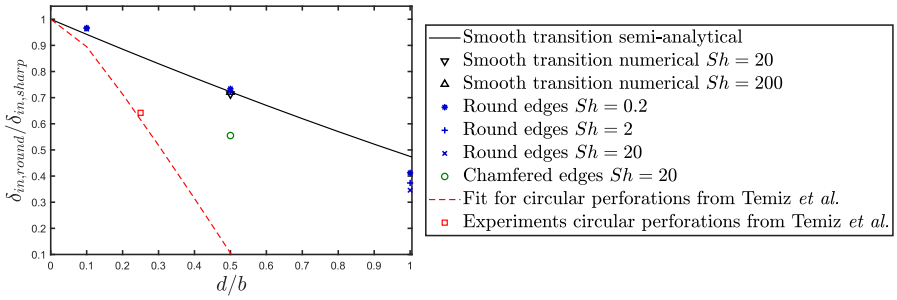

Figure 7.5. Inertial end-correction as function of the ratio d/b for slits and circular perforations.

For a micro-slit plate, the effect of rounded and chamfered edges is discussed in Aulitto *et al.* [124] as a function of the ratio d/b, for high Shear numbers. Analytical formulas for the end-corrections $\delta_{res,round}$ and $\delta_{in,round}$ are provided for a smooth (Henrici) transition. Numerical results for rounded edges with $r = 0.5b$ and chamfered edges with $c_p = 0.5b$ are also provided in Aulitto *et al.* [124] in the high Shear numbers limit. Hence, the end-corrections for the sharp edge configuration refer to $\delta_{res,h}$ and $\delta_{in,h}$. In Table 7.1, values of the end-corrections are summarized. Figures 7.5-7.6 show the effect of rounded edges on the resistive and inertance end-corrections for slits and circular perforations [124].

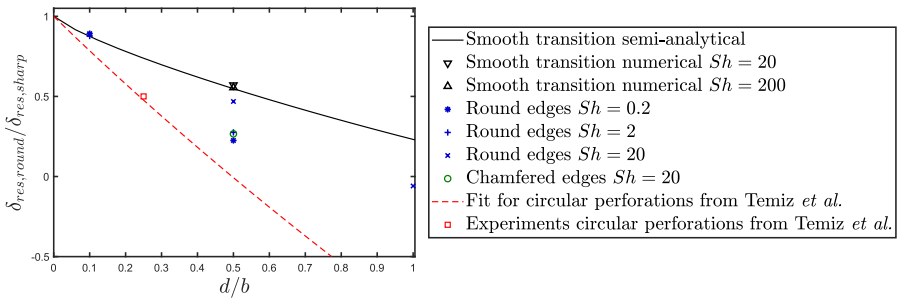

Figure 7.6. Resistive end-correction as function of the ratio d/b for slits and circular perforations.

7.3 Sound absorption in the presence of a cavity

7.3.1 Sound absorption of MPPs and MSPs

The impedance of a micro-perforated plate with circular perforations and of a micro-slit plate are compared in the audible frequency range using the equations coming from Section 7.2.3. The diameter of the perforation d_p is chosen to be the same as the slit width $b = 0.5\,\text{mm}$, as is the porosity $\Phi = 2.7\%$ and the thickness of the plate is $t_p = b$. In Figure 7.7, the sound absorption in terms of $1 - |R|^2$ is shown as a function of the Shear number Sh, for circular perforations and slits. Results for the slit liners proposed in Aulitto *et al.* [137] are also shown.

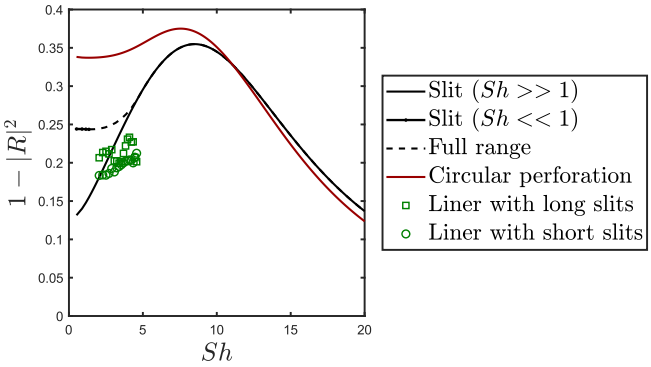

Figure 7.7. Comparison of the sound absorption of a micro-slit and a micro-perforated plate as a function of the Shear number Sh. The dots correspond to a manual junction between the low and high Shear number approximations.

The dots correspond to a manual junction between the low and high Shear number approximations proposed in Aulitto *et al.* [124]. The range of interest extends from $f = 5\,\text{Hz}$ to $f = 8\,\text{kHz}$, corresponding to $Sh \approx 0.5$ and $Sh \approx 20$, with $Sh = b/\delta_v = b/\sqrt{2\mu/\omega\rho_0}$, with μ the dynamic viscosity of air and ρ_0 the density of air. Both circular perforations and slits show a maximum of sound absorption around $Sh \approx 10$ and for $Sh < 10$ the absorption of circular perforations is slightly higher than the absorption of slits. Differences between circular perforations and slits are mainly due to geometry. This is because, at fixed porosity and the same diameter/slit width, a circular perforation has a higher surface, hence, the viscous effects act on a larger area and the absorption is higher. In the limit for $Sh \to 0$, the ratio between the sound absorption of circular perforations should be close to the surface ratio between circular perforations and slits for equal porosity. Assuming that the slit width b and the perforation diameter d_p are the same, the number of perforations N is given by $N\pi d_p^2 = bL_{tot}$ or $N = 4L_{tot}/(\pi b)$, where L_{tot} is the total slit length (neglecting the edges). The total surface of the sides of the perforations and slits are

$$S_{side,circular} = N\pi d_p t_p = 4t_p L_{tot}, \tag{7.27}$$

$$S_{side,slits} = 2t_p L_{tot}. \tag{7.28}$$

At equal thickness, one has $S_{side,circular}/S_{side,slit} \approx 2$. This limit is valid when the Stoke layer is thin compared to the slit width.
Furthermore, the difference in peak location is due to the different volumes of air effectively affected by the viscosity. For $Sh > 10$, the difference between circular perforations and slits is negligible. For higher Shear numbers, slits exhibit a slightly higher absorption than circular perforations. Furthermore, the response of the slit liner with long and short slits is in the range of transition from low to high Shear number limits. The plate with short slits has a slightly lower absorption than the plate with long slits (10%). However, both the plates show similar absorption properties as a rectangular slit with sharp edges for a high Shear number. This could be because, as shown in numerical simulations, at low Shear numbers, the velocity profile in the slits significantly differs from a fully developed Poiseuille (parabolic) profile due to the geometry of the slit. The peak of absorption is located around $Sh \approx 10$.

The limiting effect for the maximum sound absorption of circular perforations and slits is the inertance of the perforations. This effect is evident when observing the actual dissipation of the plate, shown in Figure 7.8. The dissipation for an ideal plate with purely real acoustic transfer impedance is displayed. For low Shear numbers, the effect of the inertance is small. For higher Shear numbers, the dissipation for a plate with zero inertance is much higher. The dissipation D follows the behavior of $2|R| - 2|R|^2$ and tends to zero for high Shear numbers when the plate becomes transparent to acoustic waves.

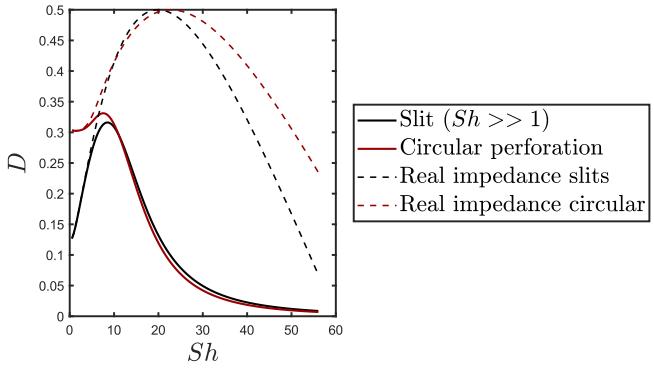

Figure 7.8. Comparison of the acoustic dissipation $D = 1 - |R|^2 - |1 - R|^2$ of a micro-slit and a micro-perforated plate as a function of the Shear number Sh in the case of a purely real acoustic transfer impedance.

7.3.2 Sound absorption using the adiabatic-wall model

In this Section, a finite cavity behind the micro-slit plate is considered. In Figure 7.9, the sound absorption of a micro-slit plate (with the impedance obtained in Equation 7.22) is compared to the sound absorption of a micro-slit plate. Results are shown for several cavity depths. Whereas for an infinitely deep cavity, a strong difference can be seen between circular perforations and slits in the low Shear number range, such difference disappear in the presence of a cavity. The results for slits and circular perforations at the peak of absorption are similar. The maximum deviations of the order of 5% are found for a semi-infinite cavity. Deviations reduce with decreasing the cavity depth, becoming negligible for $h = 3b$

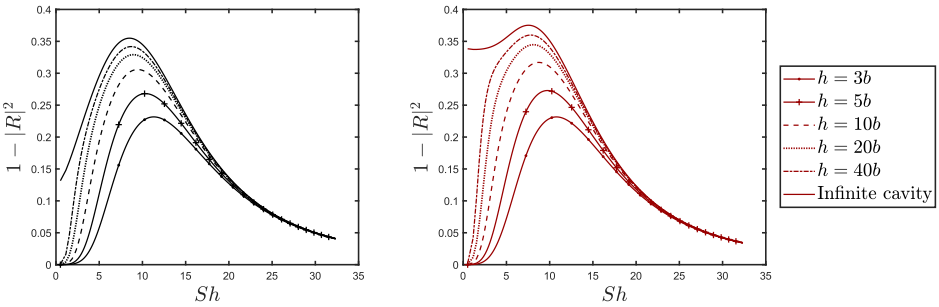

Figure 7.9. Sound absorption as a function of the Shear number Sh for a micro-slit plate (a) and a micro-perforated plate (b) for several cavity depths.

($10^{-2}\%$). For $h = 3b$, as mentioned in Section 7.2.1, the end-correction calculated with a semi-infinite cavity is not expected to be accurate.

7.3.3 Implementation of the isothermal-wall model

In this Section, the effect of the heat transfer at the walls of the cavity on the sound absorption is shown in Figure 7.10. The effect of the heat transfer becomes important in the low Shear number range. While for $h = 5b$, the cavity dominates the absorption in this region, for $h = 3b$, the effect becomes visible also around the peak of absorption. The result is similar for slits and circular perforations.
In the low Shear number range, the presence of a cavity and thermal effects dominates the absorption for low Shear numbers, where the presence of the cavity drastically reduces the absorption. Hence, in practical applications where a cavity is present, the low Shear number approximation of the impedance becomes irrelevant.
Figure 7.11 shows the sound absorption for several cavity depths as a function of the ratio f/f_H where f_H is the Helmholtz-resonance frequency of the system obtained as

$$f_H = \frac{c_0}{2\pi}\sqrt{\frac{\Phi}{h(t_p + 2\delta_{in})}}, \tag{7.29}$$

for the micro-slit plate and

$$f_H = \frac{c_0}{2\pi}\sqrt{\frac{\Phi}{h(t_p + 2\delta_{i})}}, \tag{7.30}$$

for the micro-perforated plate, with δ_{in} and δ_i provided in Section 7.2.3. It can be seen that the maximum of the sound absorption is not at $f/f_H = 1$ and it shifts

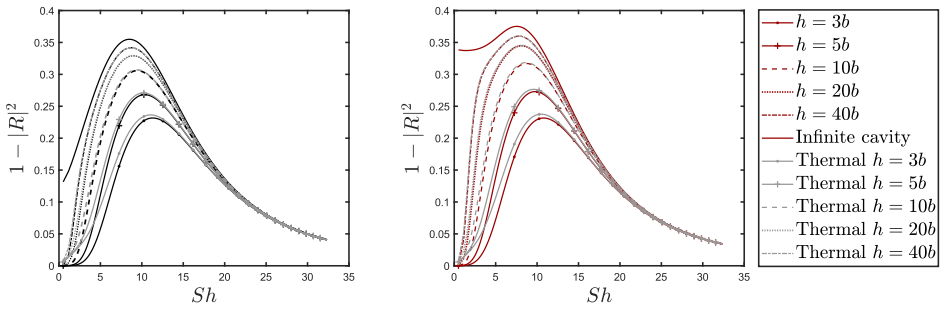

Figure 7.10. Sound absorption as a function of the Shear number Sh for a micro-slit plate (a) and a micro-perforated plate (b) for several cavity depths including heat transfer at the walls.

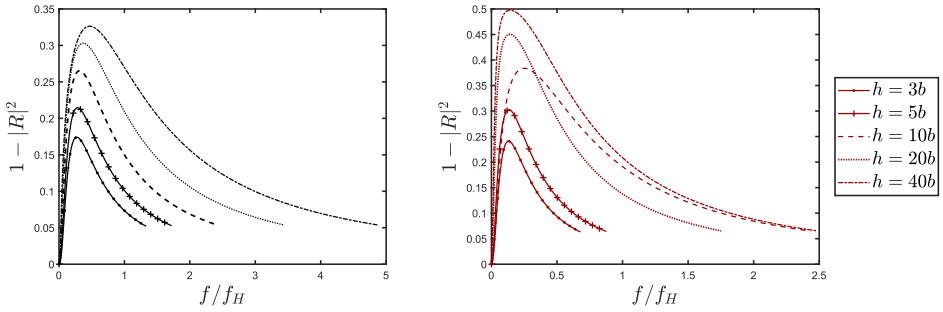

Figure 7.11. Sound absorption as a function of the ratio f/f_H with f_H the Helmholtz resonance for a micro-slit plate (a) and a micro-perforated plate (b) for several cavity depths including heat transfer at the walls.

towards lower f/f_H with decreasing cavity depths. This suggests that sound absorption is strongly affected by the acoustic transfer impedance of the plate. For slits, δ_{res} increases with the frequency and δ_{in} decreases. The magnitude of the acoustic transfer impedance increases with increasing frequencies. Therefore, in the next Section, the acoustic properties of the plate are considered in detail.

7.4 Sound absorption of MPPs and MSPs

In this section, the lumped-element model is used to derive the sound absorption properties of the plate, assuming an infinitely deep cavity, to focus on the influence of geometric parameters of the plate in the linear and non-linear case. The study is limited to the high Shear number limit described in Section 7.2.3 and Equation 7.22 for slits. Firstly, the effect of the plate thickness and porosity is investigated using the model for the impedance of circular perforations and rectangular slits presented in Section 7.2.3. Secondly, experimental results on the particular geometry studied in Chapters 3-5 and 6 are used to investigate the effect of non-linearities and a bias flow on the sound absorption of the plate.

7.4.1 Effect of thickness and porosity

Figure 7.12 shows the sound absorption of the plate as a function of the Shear number for several thicknesses of the plate, ranging from $t_p = b$ to $t_p = 5b$. With a thicker plate, one sees a shift of the peak of absorption towards lower Shear numbers (lower frequencies) with a decreasing quality factor, and the maximum absorption increases with increasing thickness. For higher Shear numbers, the sound absorption decreases with the increase in the thickness of the plate. The effect of the porosity on the sound absorption is investigated in Figure 7.13. Con-

sidering the high shear number limit one sees that, increasing the porosity, the curve becomes flatter, and the peak moves towards higher porosity, while the maximum absorption is lower. Vice-versa, by decreasing the porosity the peak of absorption moves to lower frequencies and increases, and the quality factor is reduced and one observes a narrower bandwidth of absorption.
At higher Shear numbers, one sees that with increasing porosity the sound absorption of the plate is higher, as for circular perforations. The dots correspond to a manual junction between the low and high Shear number approximations.

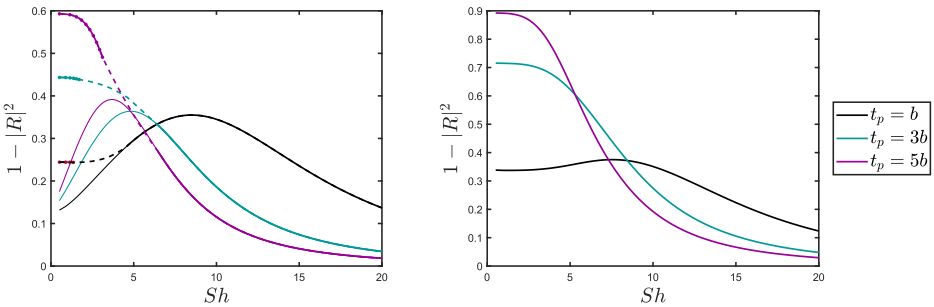

Figure 7.12. Sound absorption as a function of the Shear number Sh for a micro-slit plate (a) and a micro-perforated plate (b) for several thicknesses of the plate (porosity $\Phi = 2.78\%$). The dots correspond to a manual junction between the low and high Shear number approximations.

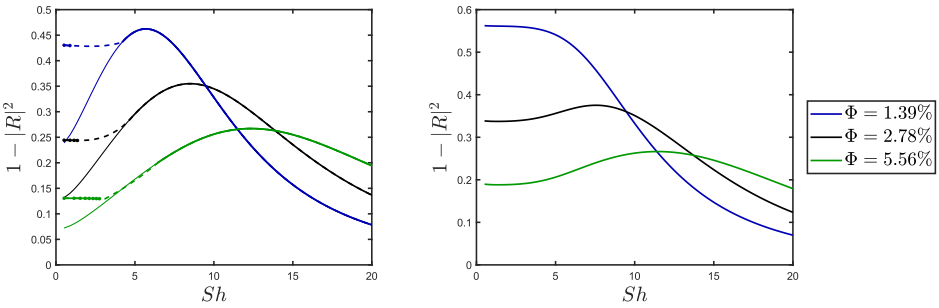

Figure 7.13. Sound absorption as a function of the Shear number Sh for a micro-slit plate (a) and a micro-perforated plate (b) for several porosities of the plate (thickness $b = t_p$). The dots correspond to a manual junction between the low and high Shear number approximations.

7.4.2 Effect of edge shape

In this Section, the effect of not sharp edges of the slits and of circular perforations is discussed. A plate with total thickness $t_p = 2b = 2d_p$ is considered for this study. The study is limited to the high Shear number limit described in Section 7.2.3 and Equation 7.22 for slits to focus on the effect of the edge geometry on the maximum sound absorption of the plate.

A thickness $t_p = b$ with $t_{p,core} = 0.5b$ corresponds to the geometry of the slit liner discusses in Chapter 3. Figure 7.14 shows the influence of the edge geometry on the sound absorption of the plate for a micro-slit plate and a micro-perforated plate. For the micro-slit plate, only the high Shear number limit is considered and it can be seen that the peak of absorption reduces in the presence of not-sharp edges. A smooth transition with transition length $d = 0.1b$ reduces the maximum absorption by approximately 5% and for $d = 0.5b$ the absorption is reduced by 16%. The effect of rounded and chamfered edges leads to an ever stronger reduction of the absorption with a 20% reduction for rounded edges with $r = 0.5b$, and 30% for a chamfered edge with $c_p = 0.5$.

No significant shift of the resonance is observed for slits, indicating a stronger impact of the presence of edges on the resistance rather than the inertance.

For circular perforations, the effect of chamfered edges reduces drastically the sound absorption, with a reduction of 35% for a chamfered edge with $c_p = 0.5d_p$ and a significant shift of the maximum towards higher frequencies. For circular perforations, Kottapalli *et al.* [192] find that an orifice with $t_p = 0.5b$ and $c_p = 0.165b$ corresponds to a minimum of broadband noise production equivalent with very thin orifices with $t_p = 0.125b$. Such orifices are 20dB less noisy than a thick plate with $t_p = 0.5b$ with sharp edges.

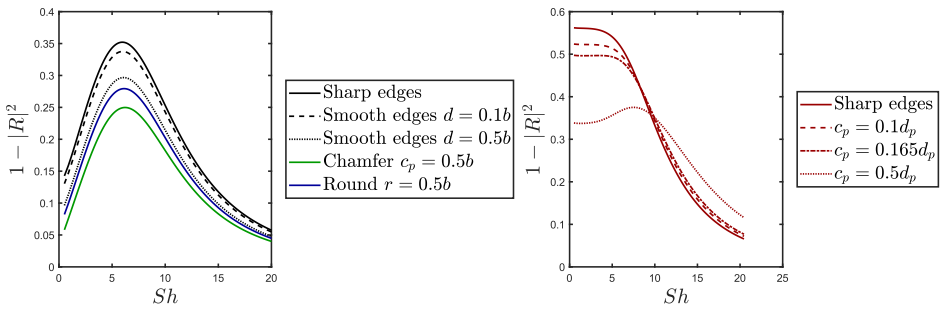

Figure 7.14. Sound absorption obtained using the high Shear number approximation as a function of the Shear number Sh for (a) a micro-slit plate and (b) a micro-slit plate in the presence of not sharp edges such as chamfered or rounded edges.

7.4.3 Effect of onset of non-linear behavior

Several publications refer to the deteriorating effect of non-linear effects on the absorption properties of a micro-perforated plate [52, 58, 114, 115]. In this Section, results for the slit liner in the linear regime are compared to the sound absorption in the presence of moderate and high acoustic excitations amplitudes.
In Figure 7.15, the sound absorption $(1-|R|^2)$ is shown as a function of the Shear number for several excitation amplitudes, defined in terms of an acoustic Reynolds number

$$Re_{ac} = \frac{b\widehat{p}_{ac}|}{\Phi c_0 \mu}, \tag{7.31}$$

with $\widehat{p}_{ac}$ the acoustic excitation amplitude and μ is the dynamic viscosity of air. It can be seen that the sound absorption increases for increasing Reynolds numbers, reaching a maximum of 0.9 for the range of amplitude considered in this study.
In the linear case, the absorption is almost independent of the Shear number, while in the non-linear cases, the absorption decreases for increasing Shear numbers, indicating a strong Strouhal number dependence. In Figure 7.16, this Strouhal number dependency is more evident and it is clear that the sound absorption increases, independently of the frequency, for increasing acoustic excitation amplitudes. However, the enhancement of sound absorption due to the presence of non-linear effects is limited to the fundamental frequency. In fact, in Chapter 4, it is shown that the presence of non-linear effects generates high-order harmonics in the signal. Symmetries in the geometry of the slits can be exploited to disrupt the generation of even-order harmonics. However, the effect of such symmetries

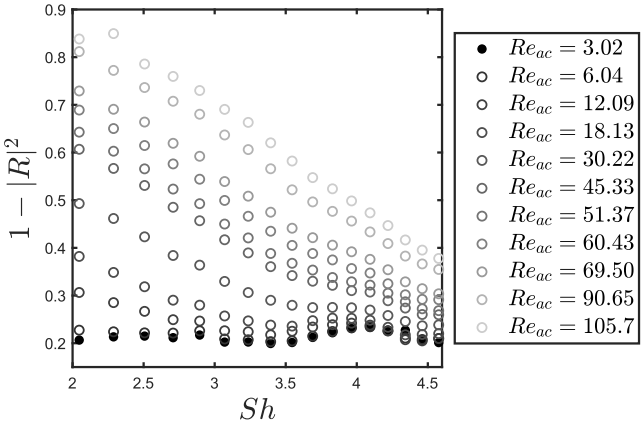

Figure 7.15. Sound absorption of the micro-slit plate as a function of the Shear number Sh for several acoustic excitation amplitudes. The symbols correspond to experimental data.

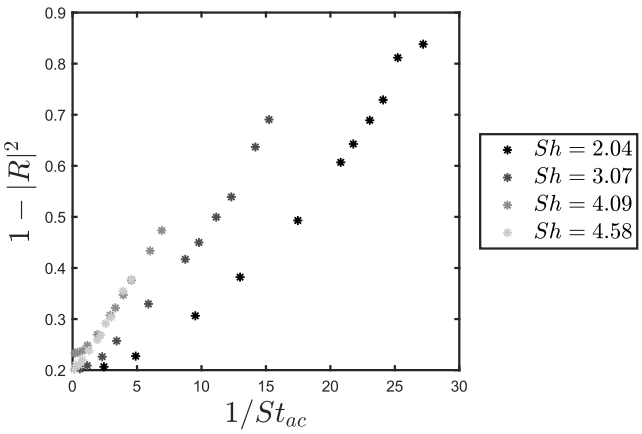

Figure 7.16. Sound absorption of the micro-slit plate as a function of the inverse of the acoustical Strouhal number $1/St_{ac} = \widehat{u}_s/(\omega b)$ for several Shear numbers. Symbols correspond to experimental results.

disappears in the presence of a bias flow.

7.4.4 Effect of a bias flow

In this section, the effect of introducing a bias flow on the sound absorption of the plate is discussed. In Figure 7.17, the sound absorption is shown as a function of the Mach number for several acoustic amplitudes. Focusing on the linear case, the experimental sound absorption shows a maximum with nearly perfect absorption at $Ma = 0.022$. Two theoretical lines are shown corresponding to the absorption of acoustic energy by the flow, in the presence of purely convective effects, with

$$1 - |R|^2 = 1 - \left|\frac{1 + \Phi Ma}{1 - \Phi Ma}\right|^2 \left|\frac{\alpha^2\Phi - Ma}{\alpha^2\Phi + Ma}\right|^2 , \tag{7.32}$$

where α is the *vena contracta* factor and Ma the Mach number $Ma = U_s/c$. with $U_s = U/\Phi$ and U the mean flow velocity in the duct. This theoretical limit is discussed in Rienstra and Hirschberg [106] concerning the influence of a steady flow on the response of a Helmholtz resonator, which adds a damping effect to the resonator. The optimal theoretical absorption occurs at $Ma = \alpha^2\Phi$. Considering the theoretical limit of the *vena contracta* factor $\alpha = 0.82$ found in Aulitto *et al.* [124] using potential flow theory and a porosity $\Phi = 2.7\%$, the maximum absorption is predicted at a $Ma \approx 0.018$, smaller than the experimental one. In reality, as observed in Chapter 5 in Figure 5.6, the discharge coefficient depends on the mean flow velocity, showing a maximum $\alpha_{max} = 0.89$ around

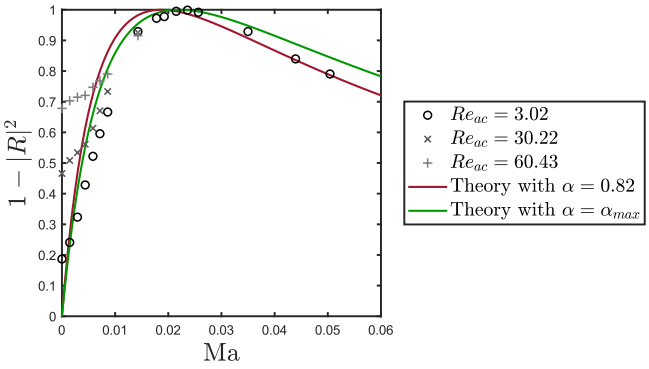

Figure 7.17. Sound absorption of the micro-slit plate as a function of the Mach number Ma based on the mean flow velocity for several acoustic excitation amplitudes. The lines correspond to the linear theory with $\alpha = 0.82$ and $\alpha = \alpha_{max} = 0.89$. The symbols correspond to experimental results for various acoustical Reynolds numbers $Re_{ac} = \rho_0 b\widehat{u}_s/\mu$.

$Re = U_s b/\nu = 10^2$ corresponding here to $Ma \approx 0.01$ and reaching the theoretical limit $\alpha = 0.82$ at high Reynolds numbers. Therefore, we consider the maximum value of the discharge coefficient $\alpha_{max} = 0.89$ found numerically in Chapter 5, predicting a maximum of the absorption around $Ma \approx 0.022$ in line with the experimental absorption maximum (Figure 7.17). However, in the linear regime, the presence of viscous effects in the slits reduces the absorption with respect to the ideal case ($< 10\%$), with the effect being most visible for $Ma \approx 0$ and low Mach numbers. In the presence of non-linear effects (higher acoustic excitation amplitudes), the absorption in the low Mach number range is higher, with the results converging to the linear case for $Ma \approx 0.015$. Both in the linear and non-linear regime, a bias flow shows a significant increase in the sound absorption properties of the plate for small mean flow velocities.

7.5 Conclusions and discussion

In this Chapter, a lumped-element model is used to predict sound absorption for plane waves under normal incidence. The sound absorption of a micro-slit plate is compared to that of a micro-perforated plate, with circular perforations for the same porosity and plate thickness to perforation width ratio. Differences due to the different geometries are observed in the low Shear number range, below the peak of absorption which occurs for $Sh = O(10)$. Such differences disappear in the presence of a back cavity because for low Helmholtz numbers $hf/c_0 << 1$ the compressibility of the air in the cavity becomes negligible. In that case, the

plate with the back cavity behaves as a hard wall. The effect of the heat transfer at the walls of the cavity becomes important only for very shallow cavity depths $h/\delta_v \leq 3$. The peak of sound absorption depends on the cavity depth h but its location in the frequency range is strongly affected by the impedance of the plate. In most of the examples shown in this Chapter, the maximum absorption occurs in the range $5 < Sh < 10$, where the high Shear number model is valid. Therefore, the impedance obtained in the high Shear numbers limit, based on a thin boundary layer approximation [25, 100, 124], appears to be the most relevant approximation for practical applications. The effect of geometric parameters such as the thickness and the porosity of the plate has been investigated. The maximum absorption was found to increase for increasing thicknesses and decreasing porosities. Smoothing or chamfering the edges of the perforations significantly reduced the sound absorption both for slits and circular perforations. In the presence of moderate and high acoustic excitation amplitudes, non-linear effects are generated. In that case, the sound absorption of the plate increases with the acoustic amplitude. The addition of a bias flow can drastically enhance the sound absorption of the plate reaching perfect absorption at a Mach number within the perforations of magnitude $Ma = \alpha\Phi$. However, a bias flow can induce noise production, both broadband noise and tonal sound (whistling), as discussed in Chapter 1.

8
Conclusions and recommendations

8.1 Conclusions

Circular perforations are perfect candidates for sound absorption in several industrial applications, such as combustion chambers or aircraft liners. However, manufacturing and fatigue issues limit in practice the applicability of micro-perforations. This work discusses the alternative offered by micro-slits, that have the same advantages as circular perforations. Slits provide a lightweight, compact, and robust solution for sound absorption in the low-frequency range. Firstly, they can be produced in several ways, overcoming the high costs of manufacturing circular micro-perforations. Secondly, slits can delimit flexible structures embedded in the plate, allowing a combination of viscous and structural effects to obtain a broader absorption range. Thirdly, the slits can be designed as bias flow liners, using the enhancing effects of flow to absorb sound, redistribute acoustic energy and implement film cooling.
In a single-degree-of-freedom liner based on a micro-slit absorber, the plate is backed by a cavity. A lumped-element impedance model of the system is proposed. The model describes the acoustic behavior of the plate in terms of the total plate impedance, which is the sum of the resistance and inertance of the plate plus the compliance of the back cavity. This simple model, described in Chapter 7, is a first step towards design tools allowing the optimization of micro-slit absorbers connecting all aspects discussed in this thesis.

The main conclusions from the present work are listed below.

- **Micro-slit plates with back cavities are efficient and potentially cost-effective sound absorbers in the low-frequency range**. Micro-slits and circular perforations have similar acoustical absorption properties but micro-slits can be cheaper to manufacture.

  (Chapter 7)

- **Slits appear naturally as the delimitation of locally-flexible elements.** Therefore, an accurate prediction of the acoustical properties of slit-shaped perforations is needed to optimize the sound absorption properties of flexible micro-slit plates

  (Chapter 1 and Appendix A)

- **Simplified models provide useful and fairly accurate design tools.** The acoustic properties of the plates are intrinsically connected to complex interactions and three-dimensional effects. However, two-dimensional models and lumped-element analytical models based on locally incompressible flow models are efficient tools in the first stages of design to obtain a reasonably accurate prediction of the acoustic properties of perforated plates.

  (Chapters 2 to 7)

- **For a single-degree-of-freedom liner with a micro-perforated plate, the maximum of sound absorption does not necessarily occur at the Helmholtz-resonance frequency (Equation 7.29).**

  (Chapter 7)

- **For shallow back cavities, the Helmholtz resonance peak corresponds to high Shear numbers, at which viscous sound absorption by the neck flow is negligible.** At frequencies much lower than the Helmholtz-resonance frequency (Equation 7.29), the perforated plate with a shallow back cavity reflects acoustic waves as a hard wall. This limits the design of thin micro-perforated absorbers based on single-degree-of-freedom absorbers.

  (Chapter 7)

- **The sound absorption of a micro-slit plate backed by a cavity is strongly affected by the impedance of the plate**. Therefore, the acoustic transfer impedance of the plate has to be investigated in detail.

  (Chapter 7)

- **In the linear regime, a locally-incompressible two-dimensional model of a single slit is sufficient to obtain a fair prediction of the impedance of a micro-slit plate**. In fact, due to the hydrodynamic interactions between neighboring slits, single slits in an array behave as confined in a channel.

  (Chapter 2)

- **A model based on a thin boundary layer approximation provides a reasonable prediction of the sound absorption of micro-perforated and micro-slit plates.**

  (Chapters 2 and 7)

- **The resistance is a local effect.** In the linear regime, the acoustic resistance of perforated plates. is governed by local viscous effects within the slits and at

the edges of the perforations.

(Chapter 2)

- **Rounded or chamfered edges due to manufacturing limitations reduce the absorption properties of perforated plates.** The presence of rounded edges reduces the effective thickness of the plate, drastically reducing the resistance of the plate. A significant impact is also found on the inertance. The edges should be kept as sharp as possible to ensure high sound absorption properties.

  (Chapters 2 and 7)

- **At high amplitudes and in the presence of a bias flow the sound dissipation of perforated plates is controlled by vortex shedding.** In the presence of moderate and high acoustic amplitudes, the resistance is governed by the local vortex shedding at the edges of the plate. Bias flow results in the formation of a jet by flow separation. Modulation of the vorticity in the shear layers of the jet is, in that case, the sound absorption mechanism. It can, in first-order approximation, be described using a quasi-steady model.

  (Chapters 3 to 6)

- **A micro-perforated or micro-slit plate should have a low inertance to achieve maximum sound absorption.**

  (Chapter 7)

- **The inertance of perforated plates is a global effect**. It is strongly dependent on the geometry of the plate and three-dimensional properties, such as the porosity, asymmetries in the perforation pattern, and the length of the slits. With moderate and high acoustic amplitudes, the inertance is affected by the evolution of the vortex shedding. Globally it decreases with increasing amplitude, but it displays complex behaviors, which are not easy to predict.

  (Chapters 2 to 4)

- **The presence of non-linear effects increases the sound absorption of perforated plates at the fundamental frequency but also generates noise at higher harmonics. Symmetries in the design of the slits can be exploited to suppress even harmonics.**. This constitutes a problem because higher-order harmonics are generated in frequency ranges where the human ear is most sensitive. The effect of the symmetry vanishes in the presence of a mean flow with a velocity of the same order as the acoustic velocity amplitude or higher.

  (Chapters 3,4 and 7)

- **The presence of convective effects due to a bias flow through perforated plates is significant, even for low mean flow velocities relevant for air-conditioning applications**. A nearly-perfect absorption can be obtained at a critical Mach number of the order of the plate porosity, within the perforations. This holds both in the linear regime and in the presence of moderately high acoustic excitations. The presence of a bias flow acts in two ways. On the one hand, due to an increase in the resistance the peak-absorption level and the bandwidth of sound absorption are increased. On the other hand, the inertance of the plate decreases, and the peak of high absorption is shifted towards higher frequencies. Reducing the inertance, one approaches an ideal absorber with a purely real transfer impedance.

  (Chapters 5 to 7)

- **Collective behavior of slanted slits leads to the formation of a protective wall jet downstream of a perforated plate**. The jet formed downstream of the plate can be used to obtain film cooling for the wall of a combustion chamber. Interactions between slits stabilize the jet flow along the wall, reducing the hysteresis observed at high Reynolds numbers for single perforations upon changing the magnitude of the steady bias flow. For short distances, interactions between neighboring slits can induce an oscillatory behavior of the impedance as a function of the Strouhal number based on the bias-flow velocity. This disappears for large distances.

  (Chapter 5)

- **Slits obtained by punching and cutting a plate combine an efficient manufacturing process with good acoustic performances for a bias flow liner with film cooling.**

  (Chapter 5)

8.2 Discussion and recommendations

In the following discussion, the conclusions are combined with the results of the literature survey presented in Chapter 1, to clarify the limits of the present results and propose some extensions to the research project.
In the preliminary stages of the design of liners, analytical and simplified models provide alternatives to complex, time-consuming and detailed flow simulations or expensive experimental campaigns. Only if accurate predictions are needed, do three-dimensional models become necessary. However, simplified models cannot replace experimental validation.
The combination of a micro-slit or a micro-perforated plate combined with a shal-

low cavity referred to as a single-degree-of-freedom SDF resonator, is not the most efficient configuration. For shallow cavities, the Helmholtz resonance peak corresponds to Shear number ranges at which viscous sound absorption by the neck flow is negligible. Therefore, the applicability of single-degree-of-freedom liner models to the design of thin micro-perforated absorbers is limited. Furthermore, sound absorption is directly dependent on the geometry of the perforations. However, the basic understanding of the sound absorption mechanisms by micro-slit plates obtained in this study remains essential to develop complex sound absorbers, such as multi-degree-of-freedom liners or zero-mass-flow liners. The complexity of such sound absorbers represents a drawback in several applications.

Bias flow drastically enhances the sound absorption properties of the plate, but presents dangers to broad-band and tonal sound production. Bias flow for optimal sound absorption corresponds to low-subsonic Mach numbers of the order of the plate porosity. Hence, the combination of MPPs or MSPs with air conditioning is realistic. In combustion chambers, a bias flow is commonly used for the protection of walls. The presence of a bias flow reduces the non-linear generation of higher harmonics, as long as the acoustic velocity amplitudes remain smaller than the steady flow velocities. The whistling of the plate only occurs when the Strouhal number based on the bias flow reaches values of order unity, as discussed in Chapter 4.

For a simple sound absorber (MSPs or MPP backed by a cavity), it is worth exploring the possible contribution of viscous-thermal dissipation driven by flexible structures. In thin-double walls, the flexibility of the wall can be used to obtain significant sound absorption. Locally limited flexible structures delimited by slits allow the combination of acoustic absorption with mechanical stop-band vibrational damping.

In this work, a particular slit geometry is studied, where interesting effects due to the symmetry of the slits and the distance between slits are found. In the numerical simulations, differences between the behavior of an array of slits and a single slit are found with high acoustic excitations and a bias flow. Extended experimental studies on different plates with single and multiple slit configurations could provide interesting insight into the whistling potentiality and hysteresis effects of such plates.

The experimental part of the present study focuses on a particular plate geometry manufactured with micron accuracy. Further study with different samples could provide direct insight into the properties of the plate. Interesting phenomena are expected in the case of rounded or chamfered edges.

The plate is assumed to be infinitely rigid and remain motionless, even in the

presence of high acoustic amplitudes. A combination of acoustic measurements and vibrational measurements with a Doppler laser vibrometer could provide insight into the contribution of plate vibrations to the observed acoustic response.

In the present study, only the effect of a bias flow is studied, while in many applications a grazing flow is present. Investigating differences in the behavior of the plate in the presence of a combined bias-grazing flow is relevant for applications such as combustion chambers and aircraft engine inlets.

A
Appendix to Chapter 1

A.1 Frequency-stop-band optimization in a micro-slit plate

A.1.1 Introduction

Acoustic noise reduction has been a topic of interest in the scientific community for years. As technology evolves, novel solutions are emerging to deal with problems such as soundproofing of recording studios, aero-engine noise reduction, or preventing the propagation of structure-borne sound to protect high-tech machinery. For the past decades, heavy materials such as absorptive foams or porous materials have been the most common choice. These materials are proven effective for wavelengths up to a quarter of the thickness of the material [193]. For this reason, foams require a large thickness to achieve low-frequency noise reduction. In the architectural sector, the impact of the weight and thickness of the absorptive materials is not a primary concern. However, for high-speed trains or aircraft, designs are required to be compact and lightweight. Acoustic metamaterials offer a lightweight and compact solution for noise reduction in harsh environments with high heating and ventilation such as launcher fairings [194] or mufflers [113]. Metamaterials are plates with periodic structures consisting of small repeated unit cells, with dimensions in the order of centimeters [195].

In recent years, acoustic metamaterials have gained a lot of interest [196–200]. One particular property of interest is the use of resonators to create frequency stop-bands to achieve low-frequency sound reduction. A frequency stop-band is a range of frequencies where the free propagation of incoming acoustic waves is prohibited because a fano-type-like interference occurs between the incoming and re-radiated waves [67]. In Claeys *et al.* [198], the potential of applying stop-bands to decrease the vibrational response of panels is discussed. Another property of interest is the inclusion of micro-slits to improve acoustic absorption. When the width of the slits is in the sub-millimeter range (micro-slits), viscous and thermal losses occur in the perforations and improve acoustic absorption. Because of the dimensions of the slits, the accuracy of the manufacturing process is of key importance. Firstly, the sharpness of the edges in contact with the slits can not be guaranteed. Rounded edges heavily affect the impedance of the micro-

Appendix A.2 is based on: De Priester, J., Aulitto, A., and Arteaga, I. L. (2022). Frequency stop-band optimization in micro-slit resonant metamaterials. Applied Acoustics, 188, 108552.

slits and the absorption. Secondly, the periodicity of the perforation pattern can be not perfect. Both these effects are discussed in Aulitto *et al.* [124]. Several manufacturing techniques can be employed to realize accurate slits such as laser cutting or milling. Plates with micro-perforations (MPPs) and micro-slit plates (MSPs) backed by a shallow cavity have been introduced by Maa[201]. As shown in recent works, MPPs and MSPs are efficient sound absorbers in the low-frequency range [137, 202–204]. Metamaterials can achieve similar effects by embedding micro-slits in the design of the unit cell. In each unit cell, the micro-slits and resonator are created by cutting out a resonant shape instead of positioning a mass-spring resonator on top [195, 197]. Another advantage of micro-slit metamaterials is that they are easier to manufacture than the original structure with resonators added on top. In the works of Ruiz *et al.* [197] and Zieliński *et al.* [195], a numerical and experimental study is performed on the normal absorption of the unit cell shown in Figure A.1. The design can be optimized to improve the size of the stop-bands. The stop-bands can be improved by changing the shape of the resonator and by increasing the ratio between the resonant area and the total area of the unit cell. In these works, the presence of the stop-bands is assumed, based on the presence of previous findings on the original metamaterials.

In this paper, an optimized unit cell design based on the work of Ruiz *et al.* [197] and Zieliński *et al.* [195] of a micro-slit resonant metamaterial is proposed with larger frequency stop-bands and enhanced sound absorption at normal incidence. Furthermore, an elastic numerical model is described to derive the absorption curves for micro-slit resonant metamaterials. The software used for the numerical simulations is COMSOL Multiphysics V5.5 [94]. In Section A.1.2, the methodology and proposed data processing technique is discussed to derive the dispersion curves of the unit cells. In this novel algorithm, the stiffness and mass matrices are not used, and the procedure can be applied even when the bending waves are non-smooth, unlike the branch-tracking algorithm discussed in Magliacano *et al.* [205]. In Section A.1.3, the unit cell design is optimized with the use of genetic algorithms to maximize the size of the first frequency stop-band. In Section A.1.4, the absorption curves of the proposed unit cell design are compared to the design currently used in the literature using a combination of rigid and elastic numerical models and the semi-phenomenological JCAPL model [193, 206–211].

A.1.2 Dispersion curves

Methodology

The structure of resonant metamaterials is given by the repetition of the same unit cell. In Figure A.1, an example of such a unit cell is shown: a double-legged resonator (DLR) design with corresponding design variables and slit size as used in the work of Ruiz *et al.* [197] and Zieliński *et al.* [195].

Floquet-Bloch theory is applied to reduce the computational cost for analysis of these materials [212]. The theorem states that the response of a two-dimensional

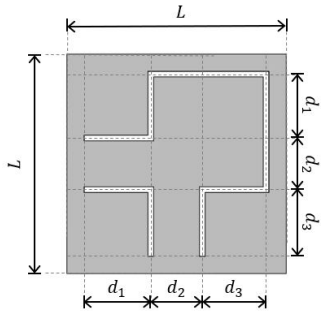

Figure A.1. Geometry overview of the DLR unit cell design as used in the work of Ruiz *et al.* [197] and Zieliński *et al.* [195]. The unscaled design variables are $L = 11.5$ mm, $d_1 = 3.6$ mm, $d_2 = 2.7$ mm, and $d_3 = 3.5$ mm [195, 197]. The plate thickness $t_p = 4.0$ mm is in the out-of-plane direction. The slit size is given by $s = 0.3$ mm.

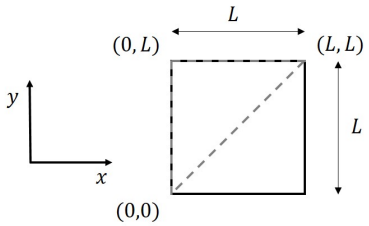

Figure A.2. The dashes gray line represents the IBC for a 2D periodic square unit cell.

periodic system can be expressed in terms of the response of a reference unit cell and an exponential term describing the amplitude and phase change as the wave travels from one cell to the adjacent cell [213]. As stated in Fok *et al.* [196], the unit cells are very small and have minimal crosstalk, leaving the individual resonator eigenfrequencies insensitive to lattice parameters and direction. As a result, to describe the behavior of the entire structure, only a single unit cell has to be analyzed. In this work, the dispersive behaviors of various unit cell designs are analyzed along the irreducible Brillioun contour (IBC) $0, 1, 2, 3 \mapsto (0, 0), (0, L), (L, L), (0, 0)$, where L is the length of the square unit cell [214–216]. The IBC is the smallest contour in the wave space that captures all information, that is, the minimum and maximum eigenvalues, required to compute the frequency stop-bands for the unit cell. For a 2D periodic square unit cell, the IBC is shown in Figure A.2. The Floquet wavenumber $k_F = [k_x \; k_y]^\top$ is spanned along this contour by imposing wavenumbers in x-direction k_x, and y-direction k_y. Floquet boundary conditions

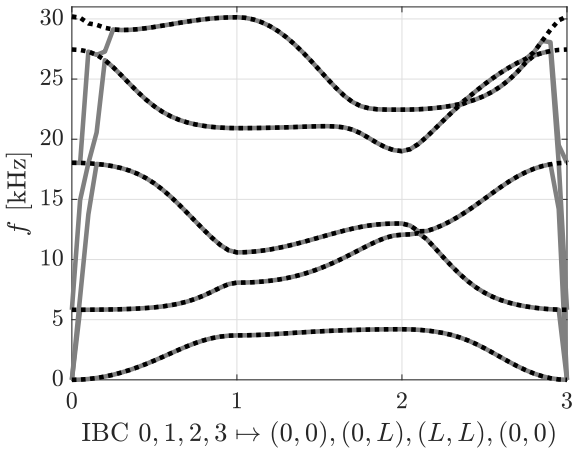

Figure A.3. Dispersion curves of the DLR unit cell design. In gray, the dispersion curves are plotted from the raw model output data. In black, the dispersion curves after the decoupling algorithm.

are applied at the edges of the unit cell using the Floquet wavenumber. The Floquet wavenumber is represented by 60 discretizations and the eigenvalue problem is solved with the use of COMSOL Multiphysics [94]. The output of the model is a matrix containing the eigenvalues along the IBC used to produce the dispersion curves. The Finite Element Method (FEM) model and the validation used to derive the dispersion curves are discussed.

Decoupling waves algorithm

The raw data retrieved from the FEM model contains in-plane waves (longitudinal and transverse waves) and bending waves. The curves are intertwined since the sorting order of the eigenvalues is mixed in the matrix representation. In Figure A.3, this issue is visualized. In Magliacano *et al.* [205], a branch-tracking algorithm is discussed for periodic porous materials. The algorithm only considers the gradient between points and does not consider the euclidean distance between them, hence failing when the curves become non-smooth. For the unit cell discussed in the present work, the resonant element introduces additional dispersion curves above its resonance frequencies, that are non-smooth. This phenomenon is similar to the result shown for a two-dimensional infinite structure with a mass-spring system, as discussed in Claeys *et al.* [198]. Consequently, the algorithm cannot be applied. As a solution, a new algorithm is designed. The proposed algorithm does not utilize the stiffness and mass matrices, allowing for fast computations. The proposed algorithm considers the gradient between points on the dispersion curves and the euclidean distance between points. Furthermore, the new

algorithm removes in-plane waves from the dispersion curves as they are inefficient as acoustic radiators compared to bending waves [200]. The ratio $Ra = t_p/L$ is defined as the ratio between the plate thickness t_p and the side length of a unit cell L, as shown in Figure A.1. In this work, only square unit cells are considered. The dispersion curves corresponding to the bending modes are not influenced by variations in the ratio Ra, whereas the transverse and longitudinal waves are. The ratio Ra is chosen small (i.e. $Ra < 0.02$), such that the in-plane waves have a significantly higher gradient than the bending waves and waves are decoupled along the contour $1, 2 \mapsto (0, L), (L, L)$. A threshold check is implemented on the gradient between points to remove the in-plane waves from the data. Estimates of the bending waves are created with the use of 4^{th} order polynomial fits. The eigenvalue branches are tracked based on the difference between the estimates and available points. Furthermore, the fits are iteratively updated to improve accuracy. A description of the algorithm is provided in [57]. The algorithm is able to remove the in-plane waves from the dispersion curves and sort the remaining eigenvalues of the raw data to obtain the dispersion curves even when the bending waves are non-smooth.

A.1.3 Optimization of the unit cell

For the simulations, the same structural properties as used in the work of Ruiz *et al.* [197] are considered, namely, density $\rho = 950$ kg/m^3, Young's modulus $E = 1750$ MPa, and Poisson's ratio $\nu = 0.3$. Furthermore, the unscaled unit cells have the same slit size s, plate thickness t_p, and plate length L, as the DLR design shown in Figure A.1. A ratio $Ra = 0.02$ is used for scaling the unit cells. Scaling is performed by multiplying the length of the unit cell L, the slit size s, and the design parameters with a scaling factor. The plate thickness t_p is unaffected by scaling.

Genetic algorithms methodology

A genetic algorithm is a search heuristic inspired by the principle of natural selection [217]. In this work, genetic algorithms are used to optimize the design of a unit cell design to maximize the size of the first frequency stop-band. The metric for optimization is the stop-band factor (SBF), which is defined as the ratio between the lower bound of a stop-band and its upper bound. Furthermore, two SBFs are considered: the first SBF (SBF1), and the second SBF (SBF2). The index refers to the appearance of the stop-band ranked from low to higher frequencies. In Figure A.4, the dispersion curves and frequency stop-bands are shown for the DLR design as shown in Figure A.1. The frequency range of the first stop-band is around 5 kHz. Note that this range is obtained by using the same design, design parameters, and structural properties as used in the work of Ruiz *et al.* [197] and Zieliński *et al.* [195]. A lower range can be realized by choosing a different material with, for instance, a lower Young's modulus. In Figure A.4, it can be seen that

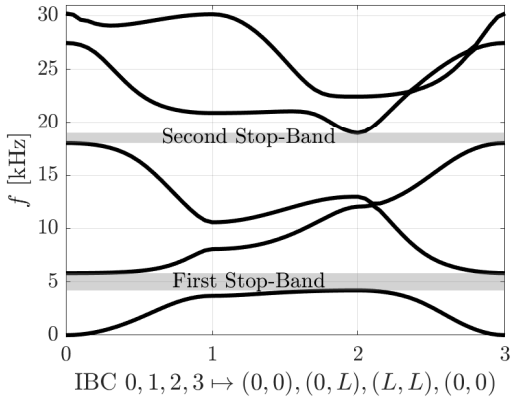

Figure A.4. Dispersion curves and frequency stop-bands of the DLR unit cell design.

the first stop-band is located between the first and second curve, as is also found in the work of Claeys *et al.* [200], and the second stop-band between the third and fourth curve. SBF1 is then defined as the ratio between the minimum of the second curve and the maximum of the first curve. Likewise, SBF2 is then defined as the ratio between the minimum of the fourth curve and the maximum of the third curve. SBF1 is chosen as the metric for optimization because it is located in the frequency range of application of micro-slit resonant metamaterials.

Influence unit cell design characteristics

In this subsection, the influence of the unit cell design characteristics on the stop-bands is discussed. The design considered, is the DLR design shown in Figure A.1. By linearly increasing the variables d_1, d_2, and d_3, the relative size of the resonator with respect to the surface of the unit cell increases. An increase in the relative size of the resonator increases both SBF1 and SBF2. By increasing the relative size of the resonant structure, the maximum kinetic energy of the structure increases as well. This leads to a greater fano-type-like interference, and to larger stop-bands. By choosing d_1 and d_2 constant, and varying d_3, the influence of the resonator mass is investigated. An increase in resonator mass increases SBF1, albeit smaller than the increase observed in SBF1 by increasing the resonator size. By choosing d_1 constant, d_2+d_3 constant, and varying d_2, the influence of the resonator stiffness is investigated. An increase in resonator stiffness increases SBF1 however decreases SBF2. Lastly, an increase in slit size has a small negative effect on SBF1 and SBF2. Note that due to manufacturability and accuracy constraints, a slit size of 0.3 mm is considered.

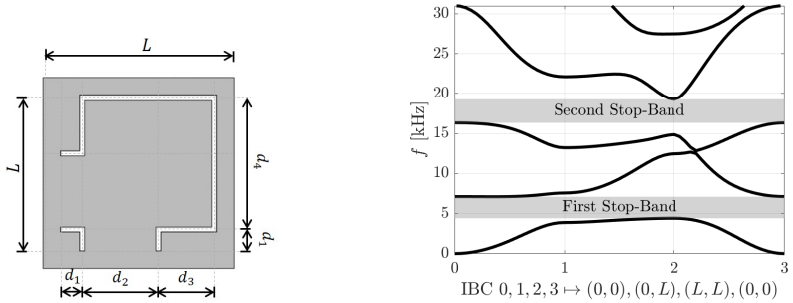

(a) Optimized geometry overview with respect to SBF1 of the DLR unit cell design. The unscaled design variables are $d_1 =$ 1.0 mm, $d_2 = 4.5$ mm, and $d_3 = 4.0$ mm.

(b) Dispersion curves and frequency stop-bands of the optimized DLR unit cell design with respect to SBF1.

Figure A.5. Geometry and dispersion curves of the optimized DLR unit cell design with respect to SBF1.

Designs considered during optimization

The DLR design as shown in Figure A.1, is optimized to increase SBF1. The accompanying dispersion curves are shown in Figure A.4, in which it can be seen that SBF1 = 1.38 and SBF2 = 1.05. For manufacturability, constraints are applied to the design variables to ensure a minimum length of 1 mm for each variable and a minimum distance of 1 mm between the slit and the edges of the plate. The optimized geometry and dispersion curves are shown in Figure A.5. In Figure A.5b, the dispersion curves of the optimized DLR unit cell design are plotted over the IBC. It can be seen that SBF1 = 1.61 and SBF2 = 1.18, an increase of 16.7% and 12.3%, respectively. It can be seen that the resulting resonant structure is maximized within the given constraints. Other notable designs considered during optimization are shown in Figure A.6. A single-legged resonator design is considered to compare its performance to the DLR design. Double resonator designs are explored to see if the interaction between two resonators at different frequencies can lead to greater stop-bands. Lastly, the implementation of internal slits in the resonant structure is investigated to see how small changes in the mode shapes can alter the stop-band behavior. Again, for manufacturability, constraints are applied to the design variables to ensure a minimum length of 1 mm for each variable and a minimum distance of 1 mm between the slit and the edges of the plate. The resulting SBFs are shown in Table A.1.

In Figure A.6 and Table A.1, it can be seen that the geometries converge to a configuration where the size of the resonator is maximized within the design constraints. The single-leg design, as shown in Figure A.6a, significantly underperforms the optimized DLR design, as shown in Figure A.5a. The addition of

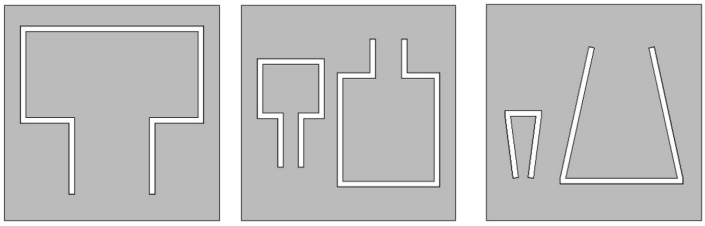

(a) Single-leg design. **(b)** Double resonator design, single-leg. **(c)** Double resonator design, triangular.

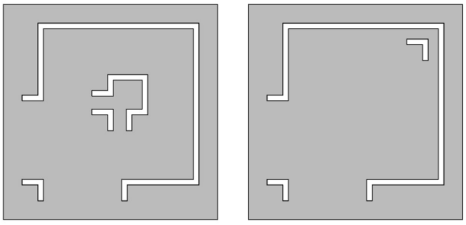

(d) Internal DLR design **(e)** DLR internal slit design.

Figure A.6. Optimized geometries of notable designs considered during optimization.

Design	A.6a	A.6b	A.6c	A.6d	A.6e
SBF1	1.34	1.17	1.23	1.60	1.65
SBF2	1.13	1.14	–	1.31	1.32

Table A.1. SBF1 and SBF2 of the optimized geometries of notable designs considered during optimization.

the second leg increases the maximum displacement of the resonant shape, and thereby the maximum kinetic energy of the resonant structure. In Figure A.6, it can be seen that the addition of internal slits, Figures A.6d and A.6e, significantly improves SBF2. The stop-bands of these designs are located around the same frequencies as the DLR designs considered earlier, see Figures A.4 and A.5b. The best-performing design is the one with the internal slit in the top right corner of the cell, as shown in Figure A.6e. The motivation for this design is further elucidated in Section A.1.3. To improve the manufacturability of the design, a slanted trim (ST) design is proposed. In Figure A.7, the unit cell design is depicted and the corresponding dispersion curves are shown. In Figure A.7, it can be seen that SBF1 = 1.65 and SBF2 = 1.31. All the designs considered during optimization converge to a configuration where the size of the resonator is maximized within each unit cell.

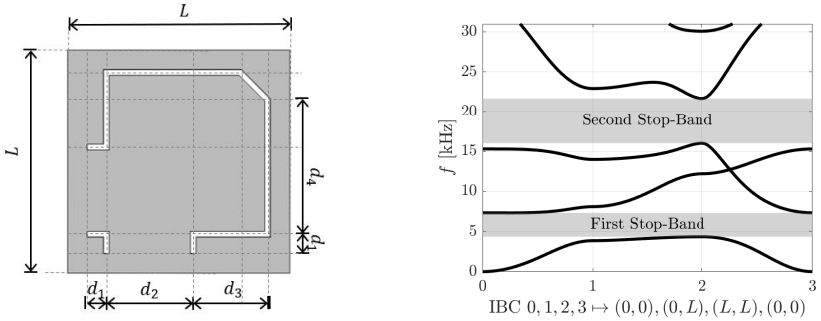

(a) Overview of the ST unit cell design. The unscaled design variables are $d_1 = 1.0$ mm, $d_2 = 4.5$ mm, $d_3 = 4.0$ mm, and $d_4 = 6.85$ mm.

(b) Dispersion curves and frequency stop-bands of the ST unit cell design.

Figure A.7. Geometry and dispersion curves of the ST unit cell design.

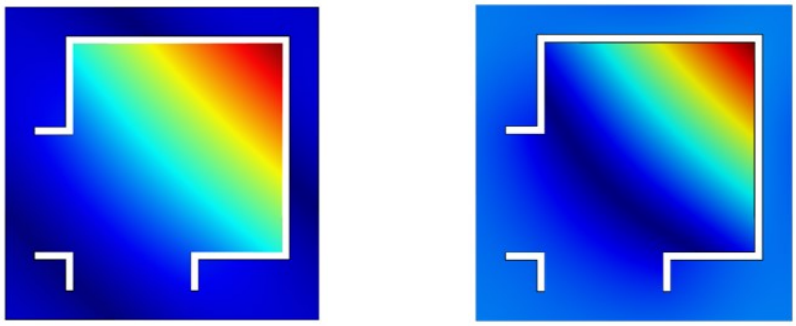

(a) Mode shape lower bound first stop-band.

(b) Mode shape upper bound first stop-band.

Figure A.8. Modes shapes displaying the out-of-plane real displacement of the first stop-band of the optimized DLR unit cell design.

ST design results

The implementation of the ST design is motivated by comparing the mode shapes of the optimized DLR unit cell design (Figure A.5a) to the ST design (Figure A.7a). In Figures A.8 and A.9 the real displacements of the unit cell at the bounds of the first stop-band is shown for the optimized DLR and for the trimmed DLR, respectively. In Figures A.8 and A.9, it can be seen that there is a difference between the lower and upper bound mode shapes of the first stop-band. The deflection for the lower bound gradually increases along the diagonal of the cell. For

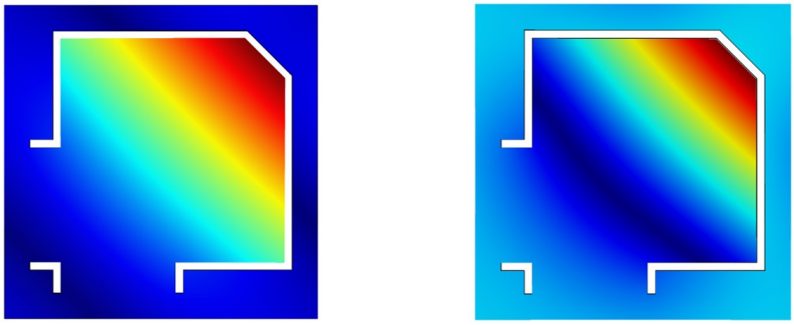

(a) Mode shape lower bound first stop-band. **(b)** Mode shape upper bound first stop-band.

Figure A.9. Modes shapes displaying the out-of-plane real displacement of the first stop-band of the ST unit cell design.

the upper bound, this increase is much steeper. For the design in Figure A.8 and the material properties as shown in Section A.1.3, the resonance frequencies are 4.4 kHz and 7.1 kHz for the lower and upper bounds, respectively. For the design in Figure A.9 and the material properties as shown in Section A.1.3, the resonance frequencies are 4.4 kHz and 7.3 kHz for the lower and upper bounds, respectively. By reducing the mass of the resonant cell at the maximum deflection (the top right corner), the mode shape of the lower bound is not significantly affected. However, the mode shape of the upper bound becomes stiffer and therefore an increase in resonance frequency and SBF1 is realized. The ST design has an increase in SBF1 of 20% and SBF2 of 25% with respect to the DLR design currently used in literature, see Figures A.1 and A.4. A small increase ($< 1\%$) in SBF1 can be realized by the implementation of an additional internal and external slit. However, the small increase does not justify the increase in manufacturing complexity.

A.1.4 Absorption

In this section, the absorption curves are compared for the DLR and the ST design. Furthermore, the absorption curves are also compared to the numerical and experimental results obtained in the work of Zieliński *et al.* [195]. For the simulations, the same properties for the plate are considered as described in Section A.1.3. The following properties of air are considered: density $\rho_f = 1.225$ kg/m^3, speed of sound $c_f = 343$ m/s, ambient pressure $P = 100.5$ kPa, ambient temperature $T_a = 22$ °C, kinematic viscosity $\nu_f = 1.55{\times}10^{-5}$ m^2/s, Prandtl number $N_f = 0.71$, bulk modulus $K_f = 0.141$ MPa, and ratio of specific heats $\gamma_f = 1.40$.

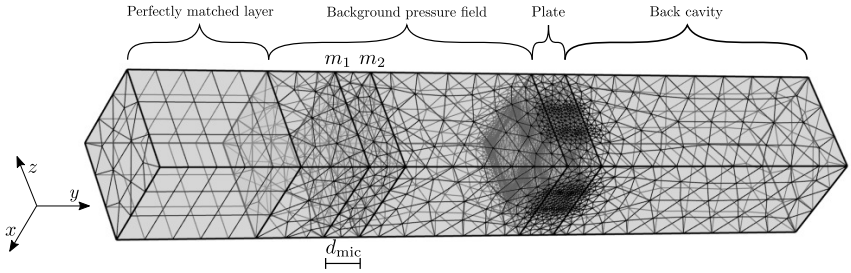

Figure A.10. Overview of the numerical model. The curly brackets denote the layers of the model, namely, the perfectly matched layer, the background pressure field, the plate with slits, and the back cavity. The planes corresponding to microphones 1 and 2 are denoted by m_1 and m_2, respectively. The distance between the two microphones is denoted by d_{mic}. Frequency of imposed wave $f = 800$ Hz. Mesh: 208219 domain elements, 23011 boundary elements, and 2009 edge elements.

Methodology

The two-microphones method, as discussed by Bodén *et al.* [218], Jang *et al.* [219], and Labašová *et al.* [220], is implemented in a numerical model to compute the absorption coefficient at normal incidence for the micro-slitted metamaterial. In Figure A.10, an overview of the numerical model is shown. The linearized Navier-Stokes module is used to consider the viscous and thermal effects caused by the slits [221]. The model is composed of four layers, as shown in Figure A.10; a perfectly matched layer (PML), a background pressure field (BPF), the plate with the slits, and a back cavity layer. The PML acts as a perfect absorber, which ensures that no waves are reflected into the BPF. The BPF is used to impose an incident pressure wave with a certain frequency. The structural mechanics module is used to model the plate with the slits as an elastic body [222]. The height of the BPF is empirically chosen at 30 mm. This height allows the mesh to transition from small elements at the slits of the plate to larger elements at the microphones. Furthermore, taller heights increase the number of total elements in the model but do not significantly improve the accuracy. Similarly, the height of the PML is chosen at 10 mm. Tetrahedral elements are used in the background pressure field, the plate, and the back cavity layer. A swept mesh is used for the perfectly matched layer and the slits in the plate. To model an infinite plate, symmetric boundary conditions are applied in the x and z directions as displayed in A.10. Furthermore, a rigid wall boundary condition is applied at the rightmost plane in Figure A.10. At the microphones, the average gross pressure is computed. The

Table A.2. Derived JCAPL parameters for the DLR design and ST design.

Parameter	Symbol	DLR	ST	Unit
Porosity	ϕ	7.670	6.080	%
Permeabilities	$k_0 = k_0'$	5.552	4.360	$10^{-10}\mathrm{m}^2$
Inertial tortuosity	α_∞	1.105	1.115	-
Static viscous tortuosity	α_0	1.308	1.322	-
Static thermal tortuosity	α_0'	1.167	1.167	-
Characteristic lengths	$\Delta = \Delta'$	0.295	0.293	mm

absorption coefficient is then given by

$$\mathcal{A} = 1 - \left| \frac{H_{12} - e^{-ikd_{\mathrm{mic}}}}{e^{ikd_{\mathrm{mic}}} - H_{12}} \right|, \tag{A.1}$$

where H_{12} is the ratio between the average gross pressure at microphone 2 and the average gross pressure at microphone 1 [218]. The model configuration, as shown in Figure A.10, is 2.5 GB in size, takes around 3 minutes to solve on an AMD Ryzen 9 3900X 12-Core 3.97 GHz CPU, and requires around 16 GB of RAM for fast computation.

The numerical results are compared to an analytical estimation of the absorption curves based on the Johnson-Champoux-Allard-Pride-Lafarge (JCAPL) model [193, 206–211].

Results

The JCAPL model is used to derive an analytical solution for the absorption curves. The parameters used for the JCAPL model are shown in Table A.2.

Absorption curves are computed with the rigid numerical model for two cavity depths: 30 mm and 53 mm. In the rigid numerical model, the plate itself is not modeled; only the slits are. Therefore, the structural effects of the plate, such as the resonance of the resonator, are not considered. Given the configurations, the first stop-band is located between 4.2 and 5.8 kHz for the DLR design, and between 4.4 and 7.3 kHz for the ST design. Since both stop-bands are outside the frequency range of interest, a rigid numerical model is used. The absorption curves for the DLR design and the ST design for a cavity depth of 30 mm and 53 mm are shown in Figures A.11 and A.12, respectively.

In Figures A.11 and A.12, it can be seen that for both cavity depths, the rigid numerical model closely resembles the analytical solution. Furthermore, it can be seen that the results from the rigid model and the analytical solution for the DLR design are in agreement with the numerical results and impedance tube measurements done in the work of Zieliński *et al.*[195]. It can be seen that the ST design produces a higher sound absorption peak at a lower frequency with respect to the DLR design. The ST design shows a 9% increase in the first peak of

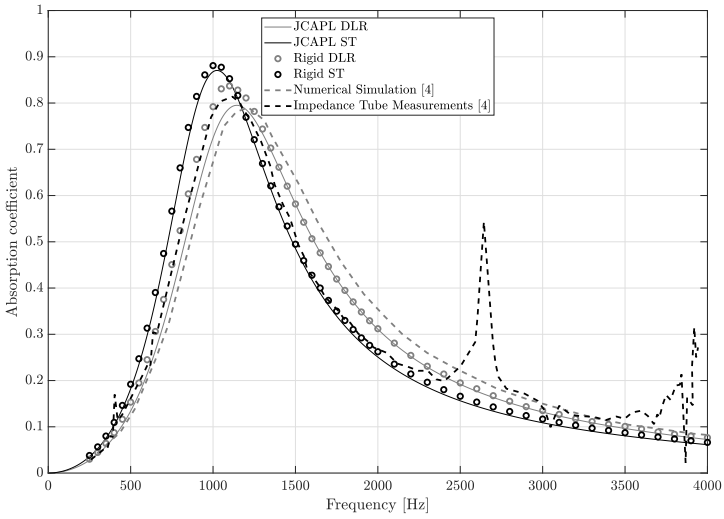

Figure A.11. Absorption curves for the DLR design and the ST design. A cavity depth of 30 mm is used. The JCAPL solutions are represented by the solid lines and the rigid numerical solutions by the circles. The results obtained for the DLR design in the work of Zieliński *et al.* [195] are displayed by the dashed lines.

absorption coefficient compared to the DLR design at a cavity depth of 30 mm, and an increase of 10% at a cavity of size 53 mm. The lower porosity of the ST design decreases the resonance frequency of the Helmholtz resonator, see Table A.2. The smaller characteristic lengths of the ST design lead to a higher sound absorption peak due to the smaller losses in the slits.

To inspect the influence of a stop-band on the resulting absorption curves of the ST design, an elastic numerical model is used. To artificially reduce the frequency bounds of the first stop-band, the Young's modulus is reduced from $E = 1750$ MPa to $E_{red} = 26.25$ MPa. This brings the first stop-band to lie between 545 and 900 Hz. In Figure A.13, the absorption curves are shown for the ST design for a cavity depth of 30 mm using the elastic numerical model.

In Figure A.13, it can be seen that there is a negligible difference between the absorption curves for the two different Young's moduli. Also, the difference between the rigid and elastic numerical models is negligible. For the elastic model, it appears that the stop-band behavior and structural properties of the plate have a negligible influence on the resulting absorption curves. From the perspective of the JCAPL model, this is an expected result since there is no dependency on the structural parameters of the plate in this model. For both numerical models, the wall at the back of the cavity is considered to be perfectly rigid, meaning that

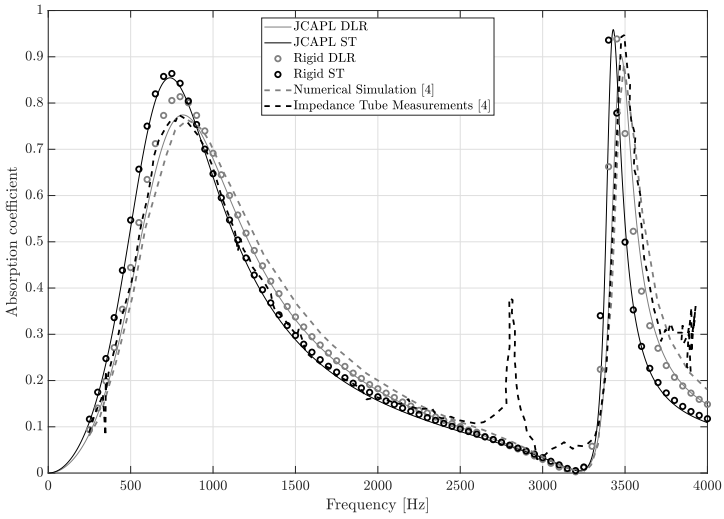

Figure A.12. Absorption curves for the DLR design and the ST design. A cavity depth of 53 mm is used. The JCAPL solutions are represented by the solid lines and the rigid numerical solutions by the circles. The results obtained for the DLR design in the work of Zieliński *et al.* [195] are displayed by the dashed lines.

the transmitted particle velocity is zero. The only losses occur due to the viscous and thermal effects of the slits. When there exists a transmitted pressure wave through the back cavity, for instance, due to an absence of a perfectly rigid back cavity wall, the structural properties of the plate will affect the reflected pressure wave and therefore also the absorption coefficient. The elastic numerical model would have to be extended with an elastic back cavity wall to capture these effects. Similarly, the JCAPL model would have to be extended to include a dependency on the effective density and bulk modulus of the plate to capture its structural effects.

A.1.5 Conclusion

An optimized unit cell design of a micro-slit resonant metamaterial is proposed to increase the size of the frequency stop-bands and to enhance sound absorption at normal incidence. The design is referred to as the ST design. A FEM model is used to derive the dispersion curves of various unit cell designs. To post-process the output of the FEM model, an algorithm is proposed. The algorithm removes the in-plane waves from the dispersion curves and sorts the remaining eigenvalues of the raw data to obtain the dispersion curves even when the bending waves are non-

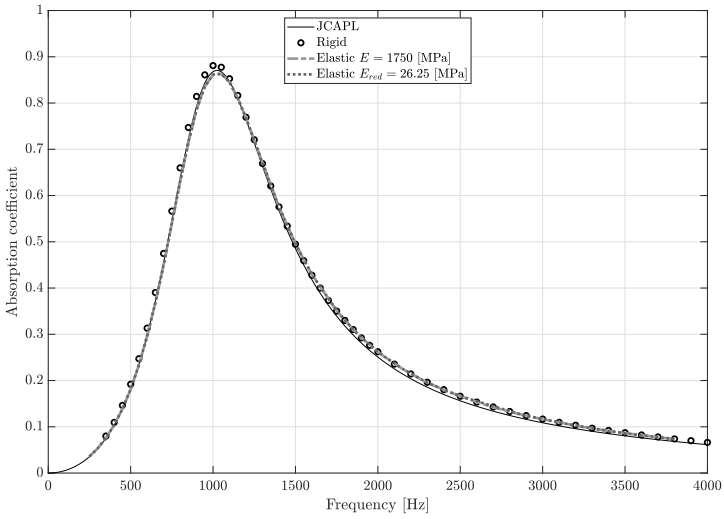

Figure A.13. Absorption curves the ST design. A cavity depth of 30 mm is used. The JCAPL solution is represented by the solid line, the rigid numerical solutions by the circles, and the elastic numerical solutions by the dotted lines.

smooth. The proposed algorithm does not utilize the stiffness and mass matrices, allowing for fast computations. Unit cell designs are optimized to maximize the size of the frequency stop-bands. The first stop-band factor is chosen as the metric for optimization since it is located in the frequency range of the application of micro-slit resonant metamaterials. Optimized designs converge to a configuration where the relative size of the resonant structure with respect to the surface of the unit cell is maximal. By increasing the relative size of the resonant structure, the maximum kinetic energy of the structure increases as well. In turn, this leads to a greater fano-type-like interference, and to larger stop-bands. The ST design reduces the mass of the resonant cell at the maximum deflection. The resonance frequencies of both the lower and upper bound of the mode shapes increase; however, the ratio between the resonance frequencies increases as well. The ST design has an increase in SBF1 of 20% and SBF2 of 25% with respect to the DLR design currently used in literature. A small increase ($< 1\%$) in SBF1 can be realized by the implementation of an additional internal and external slit. However, the small increase does not justify the increase in manufacturing complexity. The ST design shows a 9% increase in the first peak of absorption coefficient compared to the DLR design at a cavity depth of 30 mm, and an increase of 10% at a cavity of size 53 mm. The smaller characteristic lengths of the ST design lead to a higher sound absorption peak due to the smaller losses in the slits. Furthermore, the

lower porosity of the ST design reduces the frequency of the first peak. Stop-band behavior does not influence sound absorption at normal incidence of acoustic waves in the frequency range of interest. To capture the structural effects of the unit cell, the elastic numerical model would have to be extended with an elastic back cavity wall. Similarly, the JCAPL model would have to be extended to include a dependency on the effective density and bulk modulus of the plate to capture its structural effects.

B
Appendix to Chapter 2

B.1 Transformation of Henrici

In this appendix, the high Sh_b limit theory is described for the smooth and asymmetric transitions presented in Sec. II E. The duct can be associated with a region in the complex $z-$plane by $z = x + iy$, with $i^2 = -1$ where (x, y) are the coordinates in the physical plane. Using conformal mapping, the flow region in the duct in the complex $z-$plane is mapped into the upper half-plane in the complex $\zeta-$plane The transformation of [110] is used to derive the results for a smooth transition from a slit of height b to a channel of height a. The geometry is presented in Figure 2.4. The integral form of the transformation proposed by [110] is:

$$z = \alpha \left[\ln \frac{1+\tau}{1-\tau} - \frac{1}{G} \ln \left(\frac{G+\tau}{G-\tau} \right) \right] + \beta \ln \left[\frac{\zeta}{G^2} \right] \text{ [111]}, \tag{B.1}$$

where τ is:

$$\tau = \sqrt{\frac{\zeta - G^2}{\zeta - 1}}. \tag{B.2}$$

The point far downstream of the transition A$((-\infty, a)$ can be mapped into point A'$(\zeta = 0)$, the start of the transition B$(-d, a - b/2)$ corresponds to B'$(\zeta = 1)$, the end of the transition C$(0, 0)$ corresponds to C'$(\zeta = G^2)$. The coefficients are related to parameter G by:

$$\alpha = \frac{a-b}{\pi} \left[\frac{G}{G-1} \right] \tag{B.3}$$

and

$$\beta = \frac{G\ b - a}{\pi (G-1)}. \tag{B.4}$$

The parameter G is found by solving the non-linear equation:

$$G = \frac{a}{b} \left[1 + \frac{\pi\ d}{2\ a \ln G} (G-1) \right]. \tag{B.5}$$

This equation can be solved by successive substitution for $\pi d\,(2b) < 2$ using $G_0 = a/b$ as an initial guess. For $\pi d\,(2b) > 2$ the successive substitutions should

be applied to:

$$G = \exp\left[\frac{\pi d}{2b}\left(\frac{G-1}{G-\frac{a}{b}}\right)\right], \tag{B.6}$$

using $G_0 = \exp\left(\frac{\pi d}{2b}\right)$. For sharp edges $d = 0$ and $G = a/b$. For an asymmetric slit positioned at the wall, it is necessary to identify the point ζ_0 on the ζ-axes that corresponds to $z_0 = ia$ on the flat wall in the z-plane. ζ_0 is found by solving numerically the equation $z_0 = z(\zeta_0) = ia$. This can be done for any value of the transition length d. Here, only the sharp edge ($d = 0$) is considered for the fully asymmetric slit position ($a_2 = 0$).

B.2 Thin boundary layer approximation

The thin boundary layer method of Morse and Ingard [100] for the transition from a slit of height b to a channel a with sharp edges are extended to a smooth transition and to a fully asymmetric slit positioned at the wall ($a_2 = 0$). The inertial and resistive end-corrections can be found by comparing the actual configuration with an ideal configuration. The ideal reference flow, used to define the end-corrections, has for $x > 0$ a uniform velocity u_a in the channel of height a and for $x < 0$ a uniform velocity $u_b = (a/b)u_a$. The potential flow far upstream is obtained by placing a volume source at the origin $\zeta = 0$ (far downstream the transition) with potential $\varphi = (au_a/\pi)\, ln(\zeta)$. The local flow velocity is the vector field $\boldsymbol{v}_{wall} = (u, v) = \nabla\varphi$. The linearized form of the frictionless equation of motion is

$$-\nabla p = \rho\frac{\partial \boldsymbol{v}}{\partial t}. \tag{B.7}$$

To compare the actual and the reference configurations two points in the transformed $\zeta-$plane are necessary. Choosing $\zeta_1 \to \infty$ and $\zeta_2 = 0$ corresponds to z_1 and z_2 respectively far upstream and far downstream of the transition. Integrating Equation B.7 between $z_1 = (x_1; y_1)$ and $z_2 = (x_2; y_2)$ with $x_1 > 0$ and $x_2 < 0$, one has for a harmonic oscillating acoustic field:

$$\mathrm{i}\rho\omega(\varphi_2 - \varphi_1) = p_1 - p_2, \tag{B.8}$$

with $\varphi = \int \boldsymbol{v} \cdot d\boldsymbol{z}$. If the flow velocity would remain uniform $(u_a, 0)$ for $x > 0$ and jump to $(u_b, 0)$ with $u_b = u_a a/b$ for $x < 0$, we would have:

$$(\varphi_2 - \varphi_1)_{ideal} = u_a\frac{a}{b}x_2 - u_a x_1. \tag{B.9}$$

The inertia $Im[Z_t]$ is given by:

$$Im[Z_t] = \frac{\rho\omega\Delta\varphi}{awu_a}, \tag{B.10}$$

Where $\Delta\varphi$ is defined as the difference $(\varphi_2 - \varphi_1)_{actual} - (\varphi_2 - \varphi_1)_{ideal}$. Choosing real values ζ_1 and ζ_2, so that the values of z_1 and z_2 are far from the origin of the axis, one has:

$$Im[Z_t] = \frac{\rho\omega}{wb}\left[\frac{b}{\pi}\ln\left(\frac{\zeta_2}{\zeta_1}\right) - Re(z_2) + \frac{b}{a}Re(z_1)\right]. \tag{B.11}$$

For $\zeta_1 \to \infty$ and $\zeta_2 \to 0$ in Equation B.1 and Equation B.2 we can expand at the first order τ and obtain an expression for z_1 and z_2 to substitute in Equation B.11. One arrives at Equation B.12. For $d = 0$ this expression recovers the result of Morse and Ingard [100].

$$Im[Z_t] = \frac{\rho\omega}{\pi w}\left\{\frac{(a-b)^2}{2ab}\ln\left(\frac{G+1}{G-1}\right) + \frac{a-b}{b(G-1)} \cdot \left[\frac{Gb+a}{2a}\ln\left(\frac{(1+G)^2}{4G^2}\right)\right] + \ln G\right\}. \tag{B.12}$$

Using Equation 2.14 one can find the inertial end-correction. The additional dissipation due to the transition can be derived by integrating along the wall the dissipation per unit surface presented in Sec. II B for the actual and the reference configuration. It should be noted that the actual configuration and the ideal configuration should be combined to obtain converging integrals. In terms of potential, the velocity at the wall is:

$$|\widehat{u}_{tan}|^2 = \left|\frac{d\varphi}{dz}\right|^2 = \left|\frac{d\varphi}{d\zeta}\right|^2 \left|\frac{d\zeta}{dz}\right|^2. \tag{B.13}$$

The power dissipated at the junction compared to an ideal configuration is:

$$\bar{P}_W = \frac{1}{2\delta_v}\eta w\left[\int_{\zeta_2}^{\zeta_0}\left(\left|\frac{d\varphi}{d\zeta}\right|^2\frac{d\zeta}{dz} - u_a^2 * \left(\frac{a}{b}\right)^2 Re\left[\frac{dz}{d\zeta}\right]\right)d\zeta + \int_{\zeta_0}^{\zeta_1}\left(\left|\frac{d\varphi}{d\zeta}\right|^2\frac{d\zeta}{dz} - u_a^2 Re\left[\frac{dz}{d\zeta}\right]\right)d\zeta\right], \tag{B.14}$$

where for a symmetric slit $\zeta_1 \to \infty$, $\zeta_2 \to 0$ and ζ_0 corresponds to $z = 0$ and it is found from $\zeta_0 = G^2$. The second integral in Equation B.14 contains the effect of the dissipation in the channel. For a slip boundary condition prevailing in a confinement channel resulting from hydrodynamic interactions, one can take $\zeta_1 \to \zeta_0$ and calculate the dissipation using only the first integral. These integrals can be solved by numerical integration with standard numerical solvers. The resistance of the discontinuity can be defined as Morse and Ingard [100]:

$$Re[Z_t] = \frac{2\bar{P}_W}{(aw|u_a|)^2}. \tag{B.15}$$

Solving analytically the integrals for the symmetric smooth-edged configuration with friction at the channel walls leads to an approximated expression for $Re[Z_t]$,

$$Re[Z_t] = \frac{\rho\omega}{2Sh_b w}\frac{(G-1)}{G(a-b)}\left\{(G-1)\left[\frac{(G+1)}{\pi(G-1)}\left(\frac{G^2(a-b)^2}{b^2(G+1)(G-1)^2}-1\right)\right.\right.$$
$$\left.\left.\cdot\ln\left(\frac{G+1}{G-1}\right)+1\right]-\frac{2DG^2}{\pi}\ln(G)\right\}, \quad \text{(B.16)}$$

with $D = \frac{Gb-a}{G(a-b)}$. This formula is valid for $\Phi > 1/2$. For $d = 0$ one recovers $D = 0$ and $G = 1/\Phi$ and one obtains an approximation of the result of Morse and Ingard [100], with an error of the order of 10^{-4} for a porosity $\Phi = 1/10$. This error decreases for decreasing porosities. Using Equation 2.15 one can find the resistive end-correction.

For an asymmetric slit, the dissipation of the transition, in this case, is the sum of the dissipation of the wall with an edge and the dissipation at the opposite flat wall. The same integrals can be solved by changing the integration to $\zeta_1 \to \infty$, $\zeta_2 \to -\infty$, and ζ_0 can be found solving numerically the equation $z_0 = z(\zeta_0) = ia$, using Henrici's transformation formula (Equation B.1).

C
Appendix to Chapter 3

C.1 *Vena contracta* factor for potential flow

At high amplitudes, the flow detaches at the edges and then forms a free jet that contracts. The computation of jet flow is difficult, but in plane potential flow the problem of the free jet can be solved by conformal mapping. The contraction factor of the jet (*vena contracta* factor) can be calculated for several geometries following approaches found in literature [126, 127]. In Figure C.1 the geometry of a single slit is compared with a simplified model that will be used to calculate the *vena contracta* factor using the method of Spurk [126]. As defined in Section 3, the porosity of the two-dimensional model is $\Phi_{2D} = b/a$. The simplified geometry is connected to the idea that for low b/a, the main parameter is the $\pi/2$ angle between the two sides of the slit because the interaction of the jet with the walls can be neglected. The emerging jet contracts from the cross-section $B - B'$ of width b to the cross-section $C - C'$ of width αb, with α the *vena contracta* factor. At section $C - C'$ the pressure inside the jet is equal to the ambient pressure since the curvature of the streamlines vanishes. From Bernoulli's equation, the velocity on the boundary of the jet is

$$u_0 = \sqrt{\frac{2}{\rho}(p_1 - p_0)}, \tag{C.1}$$

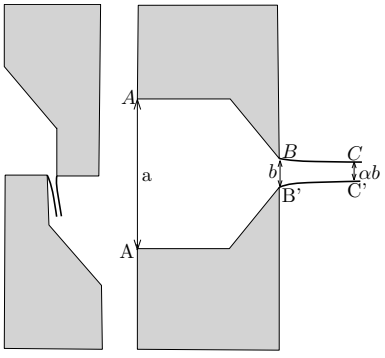

Figure C.1. Schematic representation of the slit and zoomed simplified model for the contraction of the free jet after the plate.

where p_1 and p_0 are the pressure before the slit and after the slit, respectively. The duct can be associated with a region in the complex $z-$plane by $z = x + iy$, with $i^2 = -1$ and spatial coordinates (x, y). In order to determine the shape of the free jet, a mapping resulting from the definition of the complex conjugate velocity can be used

$$\zeta = f(z) = \frac{\mathrm{d}F}{dz} = u - \mathrm{i}v = w. \tag{C.2}$$

Using conformal mapping, the flow region in the duct can be mapped into a velocity plane, the so-called *hodograph plate*. For small porosity ($b/a << 1$) the flow can be generated from the superposition of a source of strength $4\alpha b u_0$ at $w = (u - iv) = 0$ and sinks of $2\alpha b u_0$ at $w = -1, +1, -\mathrm{i}, +\mathrm{i}$, with u_0 the velocity at the edge of the jet. The complex potential is

$$F = \frac{\alpha b u_0}{\pi}\left[2ln\,(w) - \ln(w + u_0) - \ln(w - u_0) - \ln(w + \mathrm{i}u_0) - \ln(w - \mathrm{i}u_0)\right]. \tag{C.3}$$

In the present work the limit for $b/a << 1$ is considered. The mapping function $z = z(\zeta)$ has to be calculated to determine the free surface in the z-plane. From Equation C.2 follows that

$$z = \int \frac{\mathrm{d}F}{\zeta} = \int \frac{\mathrm{d}F}{\mathrm{d}\zeta}\frac{\mathrm{d}\zeta}{\zeta}. \tag{C.4}$$

The solution to this integral is

$$z = \frac{\alpha b u_0}{\pi}\left[-\frac{2}{w} + \frac{1}{u_0}\ln\left(\frac{w + u_0}{w - u_0}\right) - \frac{i}{u_0}\ln\left(\frac{w + \mathrm{i}u_0}{w - \mathrm{i}u_0}\right)\right] + \text{costant}. \tag{C.5}$$

The integration constant can be found assuming $w = (1 + i)u_0/\sqrt{2}$ at $z = 0 + \mathrm{i}b/2$ and $w = u_0$ at $z = \infty + i\alpha b/2$. It follows that the *vena contracta* factor in the limit $b/a << 1$ is $\alpha = 0.82$.

C.2 Quasi-steady incompressible flow

Assuming a quasi-steady incompressible flow with a free jet of *vena contracta* factor α, the pressure difference $\Delta p(t)$ across the plate resulting from the oscillating flow velocity $u_p(t) = U_p \cos(\omega t)$ is

$$u_p(t) = \frac{1}{2}\rho u_j |u_j| \tag{C.6}$$

where ρ is the air density and u_j is the free jet velocity. For the continuity of the velocity, one has that $u_j = u_p/\alpha$ and $u_p = u/\Phi$ where $u_p(t) = U_p \cos(\omega t)$ is the cross-sectional averaged acoustical velocity in the perforation, $u(t) = U \cos(\omega t)$ is

the cross-sectional averaged acoustical velocity in the pipe upstream the plate and Φ is the porosity. Hence, the pressure difference across the plate is

$$\Delta p = \frac{1}{2}\rho u_j|u_j| = \frac{1}{2}\rho\frac{u_p|u_p|}{\alpha^2} = \frac{1}{2}\rho\frac{u|u|}{\alpha^2\Phi^2} \tag{C.7}$$

The instantaneous power dissipated P_w is given by

$$P_w = \Delta p\, u A_i, \tag{C.8}$$

where $A_i = \pi\left(\frac{D_i}{2}\right)^2$ is the pipe cross-section. Assuming a harmonically oscillating velocity in the pipe u_p, one finds for the time-averaged dissipated power

$$\bar{P}_w = A_i\frac{4}{T}\int_0^{T/4}\Delta p\, u\,\mathrm{d}t = A_i\frac{\rho\Phi U_p^3}{2\alpha^2}\frac{4}{T}\int_0^{T/4}\cos^3(\omega t)\,\mathrm{d}t, \tag{C.9}$$

where T is the period of the harmonic oscillation. Substituting Equation C.6-C.7, this becomes

$$\bar{P}_w = A_i\rho\frac{U^3}{\pi\alpha^2\Phi^2}\int_0^1(1-y^2)\,\mathrm{d}y = A_i\rho\frac{2U^3}{3\pi\alpha^2\Phi^2}. \tag{C.10}$$

One can define the time-averaged non-linear plate resistance as $R_{plate,NL,t}$ using the expression

$$\bar{P}_w = \frac{1}{2}A_i R_{plate,NL,t}U^2. \tag{C.11}$$

This implies that

$$R_{plate,NL,t} = \frac{4\rho U}{3\pi\alpha^2\Phi^2}. \tag{C.12}$$

Using as reference the expression in Temiz *et al.* [115] ($R_{ref} = (\rho U)/(2\alpha^2\Phi^2)$) one finds the theoretical asymptote:

$$\frac{R_{plate,NL,t}}{R_{ref}} = \frac{8}{3\pi} = 0.849. \tag{C.13}$$

The value of $R_{plate,NL,t}$ is used to derive the analytical asymptote in Figure 3.8-3.10. This value is fairly close to the asymptote $0.7 < R_{plate,NL,t}/R_{ref} < 0.8$ found in Temiz *et al.* and Auriemma [52, 115]. Temiz *et al.* [115] is considering circular perforations with sharp square edges. Auriemma is considering slit-shaped perforations with right-angled edges. In the geometry proposed in this work, the channel length is zero.

C.3 Correction for boundary layer thickness.

For $\widehat{p}(x_{ref}) = 40Pa$ (really high amplitude) and $\alpha = 0.82$, we have $|\widehat{u}_p| = \alpha\sqrt{\frac{2\Delta\widehat{p}}{\rho}} = 6.7\,m/s$. For $b = 0.5\,mm$, the Reynolds number $Re_b = \rho U_p b/\mu = 223$.

The steady viscous boundary layer has a thickness of the order of $\delta_v/b \approx \sqrt{\frac{1}{Re_b}} \approx 0.1$. Therefore, one can expect the frictionless theory to have an accuracy of the order of 10%. For very high amplitudes, using the Twaites solution [223] of the integral boundary layer equation of Von Karman one can obtain an estimation of the viscous boundary layer thickness. One has

$$\theta^2\, U_p^6 \approx 0.45\nu \int_{-t}^{0} [U(x)]^5\, \mathrm{d}x, \tag{C.14}$$

with $\theta = \int_0^{\delta_v} \frac{y}{\delta_v}\left(1 - \frac{y}{\delta_v}\right) \mathrm{d}y$ is the momentum thickness of the viscous boundary layer of thickness δ_v and $x = 0$ is at the slit neck. Neglecting the boundary layer thickness and assuming a uniform velocity $U(x)$ the mass conservation law becomes

$$U(x)(b - 2x) \approx U_p b \tag{C.15}$$

because the slit angle is $\pi/2$ (see Figure C.1) and for $t >> b$

$$\frac{\theta^2}{b^2} \approx \frac{0.45\nu}{U_p b^2} \int_{-t}^{0} \frac{1}{(1 - 2\frac{x}{b})^5}\, \mathrm{d}x \approx \frac{1}{8}\frac{0.45\nu}{U_p b}. \tag{C.16}$$

Assuming a linear velocity profile in the boundary layer of thickness δ_v, one has a displacement thickness $\delta_v^* = \delta_v/2$ and a momentum thickness $\theta = \delta_v/6$. This implies:

$$\frac{\delta_v^*}{b} \approx \frac{3\theta}{b} \approx \sqrt{\frac{9}{8}\frac{0.45\nu}{U_p b}}. \tag{C.17}$$

Given $Re_b = \rho b U_p/\mu \approx 223$ one has $\delta_v^* \approx 0.05b$. This implies a reduction of the power because of the reduction of the porosity $\Phi_{eff} = \Phi(1 - 2\delta_v^*/b)$ so that

$$\frac{R_{plate,NL,t}}{R_{ref}} = \frac{\Phi^2}{\Phi_{eff}^2}\frac{8}{3\pi} \approx 1.05. \tag{C.18}$$

D
Appendix to Chapter 5

D.1 Extrapolation of pressure from numerical simulations

Consider the numerical model discussed in Section 3.4 and the numerical domain presented in Figure 5.5. In this appendix, the linear extrapolation used to extract the pressure at the plate surface (as for the experiments) is explained. The inlet of the slit is at $x = 0$. The plate upstream surface is located at $x_{p,up} = -2.25\,\text{mm}$. The plate downstream surface is at $x_{p,down} = 2.275\,\text{mm}$. The plate thickness is $t_p = 5\,\text{mm}$. Two sections of the duct on the two sides of the plate at $x_{up} = -a = -56\,\text{mm}$ and $x_{down} = -a = -56\,\text{mm}$ are considered. The distances of the cut-lines from the upstream side of the plate are $l_{up} = |x_{up} - x_{p,up}| = 53.8\,\text{mm}$ and $l_{down} = |x_{down} - x_{p,down}| = 53.8\,\text{mm}$. In the two mentioned sections, the average cross-section acoustic pressure and velocity and the flow velocity are calculated, $p_{up}, p_{down}, u_{up}, u_{down}, U_{up}, U_{down}$. The flow velocity is used to define $U_s = U_{up}/\Phi$. The acoustic pressure and velocity are used to extrapolate the pressure at the surface of the plate and estimate the plate impedance. Using the notation

$$p = p^+ e^{-\mathrm{i}k^+ x} + p^- e^{\mathrm{i}k^- x}, \tag{D.1}$$

where $k^+ = \omega/(c+U)$ and $k^- = \omega/(c-U)$, are the wave number for the wave traveling in the flow direction and against the flow direction, respectively. At $x = x_{up}$,

$$p^+_{up} = \frac{1}{2}\left(p_{up} + \rho c u_{up}\right) e^{\mathrm{i}k^+_{up} x_{up}} \qquad \text{and} \qquad p^-_{up} = \frac{1}{2}\left(p_{up} - \rho c u_{up}\right) e^{-\mathrm{i}k^+_{up} x_{up}}, \tag{D.2}$$

and at $x = x_{down}$

$$p^+_{down} = \frac{1}{2}\left(p_{down} + \rho c u_{down}\right) e^{\mathrm{i}k^+_{down} x_{down}} \text{ and } p^-_{down} = \tag{D.3}$$

$$= \frac{1}{2}\left(p_{down} - \rho c u_{down}\right) e^{-\mathrm{i}k^+_{down} x_{down}}, \tag{D.4}$$

with $k^+_{up} = \omega/(c+U_{up})$ and $k^-_{down} = \omega/(c+U_{down})$. At the surface of the plate, the pressure and velocity at the plate surface p_p and u_p are extrapolated as

$$p_{p,up} = p^+_{up} e^{-\mathrm{i}k^+ x_{p,up}} + p^-_{up} e^{\mathrm{i}k^- x_{p,up}} \tag{D.5}$$

and

$$u_{p,up} = \frac{1}{\rho c}\left(p^{+}_{up} e^{-\mathrm{i}k^{+}x_{p,up}} - p^{-}_{up} e^{\mathrm{i}k^{-}x_{p,up}}\right). \tag{D.6}$$

$$p_{p,down} = p^{+}_{down} e^{\mathrm{i}k^{+}x_{p,down}} + p^{-}_{down} e^{-\mathrm{i}k^{-}x_{p,down}} \tag{D.7}$$

$$u_{p,down} = \frac{1}{\rho c}\left(p^{+}_{down} e^{\mathrm{i}k^{+}x_{p,down}} - p^{-}_{down} e^{-\mathrm{i}k^{-}x_{p,down}}\right). \tag{D.8}$$

The dimensionless impedance of the plate is obtained as

$$z_{plate} = \frac{p_{p,up} - p_{p,down}}{\rho c u_{p,up}}, \tag{D.9}$$

with $\rho = 1.2\,\mathrm{kg}/m^3$ and $c = 343\,\mathrm{m/s}$. In principle as $He^2 << 1$ we should have $u_{p,up} = u_{p,down}$.

Bibliography

[1] E.-A. Müller and F. Obermeier, "Vortex sound," *Fluid Dynamics Research*, vol. 3, no. 1-4, pp. 43–51, 1988.

[2] A. A. Putnam, *Combustion-driven oscillations in industry*. Elsevier Publishing Company, 1971.

[3] J. Allard and N. Atalla, *Propagation of sound in porous media: modelling sound absorbing materials 2e*. John Wiley & Sons, 2009.

[4] H. V. Fuchs and X. Zha, "Micro-perforated structures as sound absorbers–a review and outlook," *Acta acustica united with acustica*, vol. 92, no. 1, pp. 139–146, 2006.

[5] S. Allam, Y. Guo, and M. Åbom, "Acoustical study of micro-perforated plates for vehicle applications," in *SAE Noise and Vibration Conference*, pp. 19–21, 2009.

[6] C. Lahiri and F. Bake, "A review of bias flow liners for acoustic damping in gas turbine combustors," *Journal of Sound and Vibration*, vol. 400, pp. 564–605, 2017.

[7] A. W. Blackman, "Variable pressure wave absorption for combustion chambers," June 21 1960. US Patent 2,941,356.

[8] D. Utvik, H. Ford, and A. Blackman, "Evaluation of absorption liners for suppression of combustion instability in rocket engines.," *Journal of Spacecraft and Rockets*, vol. 3, no. 7, pp. 1039–1045, 1966.

[9] B. Phillips, N. P. Hannum, and L. M. Russell, *On the design of acoustic liners for Rocket Engines: Helmholtz resonators evaluated with a rocket Combustor*. National Aeronautics and Space Administration, 1969.

[10] Y. Huang and V. Yang, "Dynamics and stability of lean-premixed swirl-stabilized combustion," *Progress in energy and combustion science*, vol. 35, no. 4, pp. 293–364, 2009.

[11] M. Heckl and B. Kosztin, "Analysis and control of an unstable mode in a combustor with tuneable end condition," *International journal of spray and combustion dynamics*, vol. 5, no. 3, pp. 243–271, 2013.

[12] T. García-Armingol and J. Ballester, "Operational issues in premixed combustion of hydrogen-enriched and syngas fuels," *International Journal of Hydrogen Energy*, vol. 40, no. 2, pp. 1229–1243, 2015.

[13] N. Tran, S. Ducruix, and T. Schuller, "Damping combustion instabilities with perforates at the premixer inlet of a swirled burner," *Proceedings of the Combustion Institute*, vol. 32, no. 2, pp. 2917–2924, 2009.

[14] L. Lei, G. Zhihui, Z. Chengyu, and S. Xiaofeng, "A passive method to control combustion instabilities with perforated liner," *Chinese Journal of Aeronautics*, vol. 23, no. 6, pp. 623–630, 2010.

[15] D. Zhao, A. S. Morgans, and A. P. Dowling, "Tuned passive control of acoustic damping of perforated liners," *AIAA journal*, vol. 49, no. 4, pp. 725–734, 2011.

[16] D. Zhao and X. Li, "A review of acoustic dampers applied to combustion chambers in aerospace industry," *Progress in Aerospace Sciences*, vol. 74, pp. 114–130, 2015.

[17] D. Zhao, E. Gutmark, and A. Reinecke, "Mitigating self-excited flame pulsating and thermoacoustic oscillations using perforated liners," *Science Bulletin*, vol. 64, no. 13, pp. 941–952, 2019.

[18] D.-Y. Maa, "Theory and design of microperforated panel sound-absorbing constructions," *Scientia Sinica*, vol. 18, no. 1, pp. 55–71, 1975.

[19] D. Casalino, F. Diozzi, R. Sannino, and A. Paonessa, "Aircraft noise reduction technologies: a bibliographic review," *Aerospace Science and Technology*, vol. 12, no. 1, pp. 1–17, 2008.

[20] P. Murray and M. Di Giulio, "Development and validation of a single degree of freedom perforate impedance model under high spl and grazing flow," in *28th AIAA/CEAS Aeroacoustics 2022 Conference*, p. 2929, 2022.

[21] D.-Y. Maa, "Potential of microperforated panel absorber," *the Journal of the Acoustical Society of America*, vol. 104, no. 5, pp. 2861–2866, 1998.

[22] J. S. Bolton and N. Kim, "Use of cfd to calculate the dynamic resistive end correction for microperforated materials," *Acoust. Aust*, vol. 38, no. 3, pp. 134–139, 2010.

[23] M. A. Temiz, I. Lopez Arteaga, G. Efraimsson, M. Åbom, and A. Hirschberg, "The influence of edge geometry on end-correction coefficients in micro perforated plates," *The Journal of the Acoustical Society of America*, vol. 138, no. 6, pp. 3668–3677, 2015.

[24] V. Naderyan, R. Raspet, C. J. Hickey, and M. Mohammadi, "Acoustic end corrections for micro-perforated plates," *The Journal of the Acoustical Society of America*, vol. 146, no. 4, pp. EL399–EL404, 2019.

[25] R. Billard, G. Tissot, G. Gabard, and M. Versaevel, "Numerical simulations of perforated plate liners: Analysis of the visco-thermal dissipation mechanisms," *The Journal of the Acoustical Society of America*, vol. 149, no. 1, pp. 16–27, 2021.

[26] R. Tayong, "On the holes interaction and heterogeneity distribution effects on the acoustic properties of air-cavity backed perforated plates," *Applied acoustics*, vol. 74, no. 12, pp. 1492–1498, 2013.

[27] J. Carbajo, J. Ramis, L. Godinho, P. Amado-Mendes, and J. Alba, "A finite element model of perforated panel absorbers including viscothermal effects," *Applied Acoustics*, vol. 90, pp. 1–8, 2015.

[28] J. Yu and E. Chien, "Folding cavity acoustic liner for combustion noise reduction," in *12th AIAA/CEAS Aeroacoustics Conference (27th AIAA Aeroacoustics Conference)*, p. 2681, 2006.

[29] M. G. Jones, W. R. Watson, D. M. Nark, and B. M. Howerton, "Evaluation of variable-depth liner configurations for increased broadband noise reduction," in *21st AIAA/CEAS Aeroacoustics Conference*, p. 2697, 2015.

[30] M. G. Jones, D. M. Nark, W. R. Watson, and B. M. Howerton, "Variable-depth liner evaluation using two nasa flow ducts," in *23rd AIAA/CEAS Aeroacoustics Conference*, p. 3022, 2017.

[31] L. Rego, F. Avallone, D. Ragni, D. Casalino, and H. Denayer, "Acoustic liners for jet-installation noise reduction," *Journal of Sound and Vibration*, vol. 537, p. 117189, 2022.

[32] C. Heuwinkel, L. Enghardt, and I. Röhle, "Concept and experimental investigation of a zero mass flow liner," in *14th AIAA/CEAS Aeroacoustics Conference (29th AIAA Aeroacoustics Conference)*, p. 2931, 2001.

[33] C. Lahiri, B. Pardowitz, F. Bake, and L. Enghardt, "The application of an aeroacoustic actuator in a zero mass flow liner for acoustic damping," in *17th AIAA/CEAS Aeroacoustics Conference (32nd AIAA Aeroacoustics Conference)*, p. 2725, 2011.

[34] R. Burgmayer, F. Bake, and L. Enghardt, "Design and evaluation of a zero mass flow liner," *AIAA Journal*, pp. 1–12, 2022.

[35] A. S. Hersh and J. Tso, "Extended frequency range helmholtz resonators," June 2 1992. US Patent 5,119,427.

[36] H. Matsuhisa, B. Ren, and S. Sato, "Semiactive control of duct noise by a volume-variable resonator," *JSME international journal. Ser. 3, Vibration, control engineering, engineering for industry*, vol. 35, no. 2, pp. 223–228, 1992.

[37] J. M. De Bedout, M. A. Franchek, R. J. Bernhard, and L. Mongeau, "Adaptive-passive noise control with self-tuning helmholtz resonators," *Journal of Sound and Vibration*, vol. 202, no. 1, pp. 109–123, 1997.

[38] S. J. Estève and M. E. Johnson, "Adaptive helmholtz resonators and passive vibration absorbers for cylinder interior noise control," *Journal of Sound and Vibration*, vol. 288, no. 4-5, pp. 1105–1130, 2005.

[39] A. Abbad, K. Rabenorosoa, M. Ouisse, and N. Atalla, "Adaptive helmholtz resonator based on electroactive polymers: modeling, characterization, and control," *Smart Materials and Structures*, vol. 27, no. 10, p. 105029, 2018.

[40] A. Benouhiba, P. Rougeot, N. Andreff, K. Rabenorosoa, and M. Ouisse, "Origami-based auxetic tunable helmholtz resonator for noise control," *Smart Materials and Structures*, vol. 30, no. 3, p. 035029, 2021.

[41] H. H. Hubbard, *Aeroacoustics of flight vehicles: theory and practice*, vol. 1258. NASA Office of Management, Scientific and Technical Information Program, 1991.

[42] S. Horowitz, T. Nishida, L. Cattafesta Iii, and M. Sheplak, "Characterization of a compliant-backplate helmholtz resonator for an electromechanical acoustic liner," *International Journal of Aeroacoustics*, vol. 1, no. 2, pp. 183–205, 2002.

[43] E. Drevon, "Measurement methods and devices applied to a380 nacelle double degree-of-freedom acoustic liner development," in *10th AIAA/CEAS aeroacoustics conference*, p. 2907, 2004.

[44] H. Lissek, E. Rivet, S. Karkar, and R. Boulandet, "Design of active multiple-degrees-of-freedom electroacoustic resonators for use as broadband sound absorbers," tech. rep., 2017.

[45] H. Lissek, E. Rivet, T. Laurence, and R. Fleury, "Toward wideband steerable acoustic metasurfaces with arrays of active electroacoustic resonators," *Journal of Applied Physics*, vol. 123, no. 9, p. 091714, 2018.

[46] D. L. Sutliff, D. M. Nark, and M. G. Jones, "Multi-degree-of-freedom liner development: Concept to flight test," *International Journal of Aeroacoustics*, vol. 20, no. 5-7, pp. 792–825, 2021.

[47] N. Jiménez, W. Huang, V. Romero-García, V. Pagneux, and J.-P. Groby, "Ultra-thin metamaterial for perfect and quasi-omnidirectional sound absorption," *Applied Physics Letters*, vol. 109, no. 12, p. 121902, 2016.

[48] C. Lahiri, B. Pardowitz, F. Bake, I. Röhle, and L. Enghardt, "Excitation of a zero mass flow liner for acoustic damping," *AIAA journal*, vol. 49, no. 3, pp. 513–519, 2011.

[49] A. Guess, "Calculation of perforated plate liner parameters from specified acoustic resistance and reactance," *Journal of Sound and Vibration*, vol. 40, no. 1, pp. 119–137, 1975.

[50] M. Jones, M. Tracy, W. Watson, and T. Parrott, "Effects of liner geometry on acoustic impedance," in *8th AIAA/CEAS Aeroacoustics Conference & Exhibit*, p. 2446, 2002.

[51] D.-Y. Maa, "Theory of microslit absorbers," *Acta Acustica*, vol. 25, no. 6, pp. 481–485, 2000.

[52] F. Auriemma, "Acoustic performance of micro-grooved elements," *Applied Acoustics*, vol. 122, pp. 128–137, 2017.

[53] P. Cobo, C. de la Colina, and F. Simón, "On the modelling of microslit panel absorbers," *Applied Acoustics*, vol. 159, p. 107118, 2020.

[54] S. AB, "Acustimet plates®," *Kungsängen Sweden. https://www.sontech.se/product-page/acustimet*.

[55] H. Ruiz, C. Claeys, E. Deckers, and W. Desmet, "Numerical and experimental study of the effect of microslits on the normal absorption of structural metamaterials," *Mechanical Systems and Signal Processing*, vol. 70, pp. 904–918, 2016.

[56] T. G. Zieliński, F. Chevillotte, and E. Deckers, "Sound absorption of plates with micro-slits backed with air cavities: Analytical estimations, numerical calculations and experimental validations," *Applied Acoustics*, vol. 146, pp. 261–279, 2019.

[57] J. De Priester, A. Aulitto, I. L. Arteaga, *et al.*, "Frequency stop-band optimization in micro-slit resonant metamaterials," *Applied Acoustics*, vol. 188, p. 108552, 2022.

[58] T. Abily, J. Regnard, G. Gabard, and S. Durand, "Non-linear effects in thin slits for low frequency sound absorption," *Journal of Sound and Vibration*, p. 117432, 2022.

[59] J. Lee and G. W. Swenson, "Compact sound absorbers for low frequencies," *Noise Control Engineering Journal*, vol. 38, p. 109, 1992.

[60] Y. Lee, E. Lee, and C. Ng, "Sound absorption of a finite flexible micro-perforated panel backed by an air cavity," *Journal of Sound and Vibration*, vol. 287, no. 1-2, pp. 227–243, 2005.

[61] M. Toyoda, R. L. Mu, and D. Takahashi, "Relationship between helmholtz-resonance absorption and panel-type absorption in finite flexible microperforated-panel absorbers," *Applied Acoustics*, vol. 71, no. 4, pp. 315–320, 2010.

[62] J. S. Bolton and K. Hou, "Finite element models of micro-perforated panels," 2009.

[63] T. Bravo, C. Maury, and C. Pinhède, "Sound absorption and transmission through flexible micro-perforated panels backed by an air layer and a thin plate," *The Journal of the Acoustical Society of America*, vol. 131, no. 5, pp. 3853–3863, 2012.

[64] T. Bravo, C. Maury, and C. Pinhède, "Enhancing sound absorption and transmission through flexible multi-layer micro-perforated structures," *The Journal of the Acoustical Society of America*, vol. 134, no. 5, pp. 3663–3673, 2013.

[65] M. A. Temiz, J. Tournadre, I. L. Arteaga, and A. Hirschberg, "Modelling vibro-acoustic coupling in flexible micro-perforated plates by a patch-impedance approach," *Applied Acoustics*, vol. 125, pp. 80–90, 2017.

[66] S. Ren, L. Van Belle, C. Claeys, F. Xin, T. Lu, E. Deckers, and W. Desmet, "Improvement of the sound absorption of flexible micro-perforated panels by local resonances," *Mechanical Systems and Signal Processing*, vol. 117, pp. 138–156, 2019.

[67] H. Ruiz, C. Claeys, E. Deckers, and W. Desmet, "On the acoustic absorption of micro slitted metamaterials: a numerical and experimental study," Crocker, MJ, INT INST ACOUSTICS & VIBRATION, 2015.

[68] R. Bossart, N. Joly, and M. Bruneau, "Hybrid numerical and analytical solutions for acoustic boundary problems in thermo-viscous fluids," *Journal of Sound and Vibration*, vol. 263, no. 1, pp. 69–84, 2003.

[69] N. Joly, M. Bruneau, and R. Bossart, "Coupled equations for particle velocity and temperature variation as the fundamental formulation of linear acoustics in thermo-viscous fluids at rest," *Acta Acustica united with Acustica*, vol. 92, no. 2, pp. 202–209, 2006.

[70] K. Šimonová, P. Honzík, M. Bruneau, and P. Gatignol, "Modelling approach for mems transducers with rectangular clamped plate loaded by a thin fluid layer," *Journal of Sound and Vibration*, vol. 473, p. 115246, 2020.

[71] M. E. D'elia, T. Humbert, and Y. Aurégan, "On articulated plates with micro-slits to tackle low-frequency noise," *Acta Acustica*, vol. 5, p. 31, 2021.

[72] M. Farooqui and Y. Aurégan, "Compact beam liners for low frequency noise," in *2018 AIAA/CEAS Aeroacoustics Conference*, p. 4101, 2018.

[73] Y. Aurégan and M. Farooqui, "In-parallel resonators to increase the absorption of subwavelength acoustic absorbers in the mid-frequency range," *Scientific reports*, vol. 9, no. 1, pp. 1–6, 2019.

[74] V. Prakash, P. Kumar, P. Singh, M. Hussain, A. Das, and S. Chattopadhyaya, "Micro-electrical discharge machining of difficult-to-machine materials: a review," *Proceedings of the Institution of Mechanical Engineers, Part B: Journal of Engineering Manufacture*, vol. 233, no. 2, pp. 339–370, 2019.

[75] S. Smith and J. Tlusty, "An overview of modeling and simulation of the milling process," 1991.

[76] J. Grzelak and R. Szwaba, "Influence of holes manufacture technology on perforated plate aerodynamics," *Materials*, vol. 14, no. 21, p. 6624, 2021.

[77] K. Opiela, T. Zieliński, and K. Attenborough, "Limitations on validating slitted sound absorber designs through budget additive manufacturing," *Materials & Design*, vol. 218, p. 110703, 2022.

[78] P. Testud, Y. Aurégan, P. Moussou, and A. Hirschberg, "The whistling potentiality of an orifice in a confined flow using an energetic criterion," *Journal of Sound and Vibration*, vol. 325, no. 4-5, pp. 769–780, 2009.

[79] R. Lacombe, P. Moussou, and Y. Aurégan, "Whistling of an orifice in a reverberating duct at low mach number," *The Journal of the Acoustical Society of America*, vol. 130, no. 5, pp. 2662–2672, 2011.

[80] E. Moers, D. Tonon, and A. Hirschberg, "Strouhal number dependency of the aeroacoustic response of wall perforations under combined grazing-bias flow," *Journal of Sound and Vibration*, vol. 389, pp. 292–308, 2017.

[81] F. Tao, P. Joseph, X. Zhang, O. Stalnov, M. Siercke, and H. Scheel, "Investigation of the sound generation mechanisms for in-duct orifice plates," *The Journal of the Acoustical Society of America*, vol. 142, no. 2, pp. 561–572, 2017.

[82] L. Hirschberg, J. G. Guzman Inigo, A. Aulitto, J. Sierra, D. Fabre, A. Morgans, and A. Hirschberg, "Linear theory and experiments for laminar bias flow impedance: Orifice shape effect," in *28th AIAA/CEAS Aeroacoustics 2022 Conference*, p. 2887, 2022.

[83] S. Kottapalli, A. Hirschberg, N. Waterson, D. M. Smeulders, and G. Nakiboglu, "Influence of chamfers on broadband orifice noise in a water-pipe flow," in *28th AIAA/CEAS Aeroacoustics 2022 Conference*, p. 2888, 2022.

[84] R. J. Goldstein, "Film cooling," in *Advances in heat transfer*, vol. 7, pp. 321–379, Elsevier, 1971.

[85] J. Eldredge, D. Bodony, and M. Shoeybi, "Numerical investigation of the acoustic behavior of a multi-perforated liner," in *13th AIAA/CEAS Aeroacoustics Conference (28th AIAA Aeroacoustics Conference)*, p. 3683, 2007.

[86] S. Mendez and F. Nicoud, "Large-eddy simulation of a bi-periodic turbulent flow with effusion," *Journal of Fluid Mechanics*, vol. 598, pp. 27–65, 2008.

[87] J. D. Eldredge and A. P. Dowling, "The absorption of axial acoustic waves by a perforated liner with bias flow," *Journal of Fluid Mechanics*, vol. 485, pp. 307–335, 2003.

[88] S. Mendez, J. Eldredge, F. Nicoud, T. Poinsot, M. Shoeybi, and G. Iaccarino, "Numerical investigation and preliminary modeling of a turbulent flow over a multi-perforated plate," in *Proceedings of the Summer Program*, p. 1, 2006.

[89] A. Andreini, C. Bianchini, B. Facchini, F. Simonetti, and A. Peschiulli, "Assessment of numerical tools for the evaluation of the acoustic impedance of multi-perforated plates," in *Turbo Expo: Power for Land, Sea, and Air*, vol. 54624, pp. 1065–1077, 2011.

[90] S. Agarwal, L. Gicquel, F. Duchaine, N. Odier, and J. Dombart, "Analysis of the unsteady flow field inside a fan-shaped cooling hole predicted by large eddy simulation," *Journal of Turbomachinery*, vol. 143, no. 3, 2021.

[91] C. Zong, C. Ji, J. Cheng, and T. Zhu, "Comparison of adiabatic and conjugate heat transfer models on near-wall region flows and thermal characteristics of angled effusion cooling holes," *Thermal Science and Engineering Progress*, vol. 30, p. 101269, 2022.

[92] E. Moers, D. Tonon, and A. Hirschberg, "Sound absorption by perforated walls with bias/grazing flow: experimental study of the influence of perforation angle," in *Acoustics 2012*, 2012.

[93] D. Tonon, E. Moers, and A. Hirschberg, "Quasi-steady acoustic response of wall perforations subject to a grazing-bias flow combination," *Journal of Sound and Vibration*, vol. 332, no. 7, pp. 1654–1673, 2013.

[94] Comsol, "Comsol multiphysics®," *COMSOL AB, Stockholm, Sweden. www.comsol.com*, v.5.5.

[95] U. R. Kristiansen and T. E. Vigran, "On the design of resonant absorbers using a slotted plate," *Applied Acoustics*, vol. 43, no. 1, pp. 39–48, 1994.

[96] R. Randeberg, "Adjustable slitted panel absorber," *Acta Acustica united with Acustica*, vol. 88, no. 4, pp. 507–512, 2002.

[97] U. Ingard, "On the theory and design of acoustic resonators," *The Journal of the acoustical society of America*, vol. 25, no. 6, pp. 1037–1061, 1953.

[98] L. Jaouen and F. Chevillotte, "Length correction of 2d discontinuities or perforations at large wavelengths and for linear acoustics," *Acta Acustica united with Acustica*, vol. 104, no. 2, pp. 243–250, 2018.

[99] T. Vigran, "The acoustic properties of panels with rectangular apertures," *The Journal of the Acoustical Society of America*, vol. 135, no. 5, pp. 2777–2784, 2014.

[100] P. M. Morse and K. U. Ingard, *Theoretical acoustics*. Princeton University press, 1986.

[101] P. R. Andersen, V. C. Henriquez, and N. Aage, "On the validity of numerical models for viscothermal losses in structural optimization for micro-acoustics," *Journal of Sound and Vibration*, 2022.

[102] H. Ruiz, P. Cobo, and F. Jacobsen, "Optimization of multiple-layer microperforated panels by simulated annealing," *Applied Acoustics*, vol. 72, no. 10, pp. 772–776, 2011.

[103] L. Landau and E. Lifshitz, "Course of theoretical physics, vol. 6: Fluid mechanics 2, nd, ed," 1987.

[104] M. J. Lighthill, *Waves in fluids*. Cambridge university press, 2001.

[105] M. Berggren, A. Bernland, and D. Noreland, "Acoustic boundary layers as boundary conditions," *Journal of Computational Physics*, vol. 371, pp. 633–650, 2018.

[106] S. W. Rienstra and A. Hirschberg, "An introduction to acoustics," *Eindhoven University of Technology*, vol. 18, p. 19, 2004.

[107] M. Lesser and J. Lewis, "Applications of matched asymptotic expansion methods to acoustics. ii. the open-ended duct," *The Journal of the Acoustical Society of America*, vol. 52, no. 5B, pp. 1406–1410, 1972.

[108] V. Fok, "Teoreticheskoe issledovanie provodimosti kruglogo otverstiya v peregorodke, postavlennoi poperek truby (theoretical study of the conductance of a circular hole in a partition across a tube)," *Doklady Akademii Nauk SSSR (Soviet Physics Doklady)*, vol. 31, no. 9, pp. 875–882, 1941.

[109] J. Kergomard and A. Garcia, "Simple discontinuities in acoustic waveguides at low frequencies: critical analysis and formulae," *Journal of Sound and Vibration*, vol. 114, no. 3, pp. 465–479, 1987.

[110] P. Henrici, *Applied and computational complex analysis, Volume I*. John Wiley & Sons, 1974.

[111] L. Hirschberg, T. Schuller, J. Collinet, C. Schram, and A. Hirschberg, "Analytical model for the prediction of pulsations in a cold-gas scale-model of a solid rocket motor," *Journal of Sound and Vibration*, vol. 419, pp. 452–468, 2018.

[112] S. Glantz and B. Slinker, *Primer of Applied Regression & Analysis of Variance, ed.* McGraw-Hill, Inc., New York, 2001.

[113] S. Allam and M. Åbom, "A new type of muffler based on microperforated tubes," *Journal of vibration and acoustics*, vol. 133, no. 3, 2011.

[114] M. Dah-You, "Microperforated panel at high sound intensity [j]," *Acta Acustica*, vol. 1, 1996.

[115] M. A. Temiz, J. Tournadre, I. L. Arteaga, and A. Hirschberg, "Non-linear acoustic transfer impedance of micro-perforated plates with circular orifices," *Journal of Sound and Vibration*, vol. 366, pp. 418–428, 2016.

[116] F. Auriemma, "Study of a new highly absorptive acoustic element," *Acoustics Australia*, vol. 45, no. 2, pp. 411–419, 2017.

[117] X. Dai, X. Jing, and X. Sun, "Vortex shedding and its nonlinear acoustic effect occurring at a slit," *AIAA journal*, vol. 49, no. 12, pp. 2684–2694, 2011.

[118] X. Jing and X. Sun, "Sound-excited flow and acoustic nonlinearity at an orifice," *Physics of Fluids*, vol. 14, no. 1, pp. 268–276, 2002.

[119] J. Su, J. Rupp, A. Garmory, and J. F. Carrotte, "Measurements and computational fluid dynamics predictions of the acoustic impedance of orifices," *Journal of Sound and Vibration*, vol. 352, pp. 174–191, 2015.

[120] Z. Chen, Z. Ji, and H. Huang, "Acoustic impedance of perforated plates in the presence of bias flow," *Journal of Sound and Vibration*, vol. 446, pp. 159–175, 2019.

[121] A. Komkin, A. Bykov, and M. Mironov, "Experimental study of nonlinear acoustic impedance of circular orifices," *The Journal of the Acoustical Society of America*, vol. 148, no. 3, pp. 1391–1403, 2020.

[122] A. Cummings and W. Eversman, "High amplitude acoustic transmission through duct terminations: Theory," *Journal of sound and vibration*, vol. 91, no. 4, pp. 503–518, 1983.

[123] U. Ingård and S. Labate, "Acoustic circulation effects and the nonlinear impedance of orifices," *The Journal of the Acoustical Society of America*, vol. 22, no. 2, pp. 211–218, 1950.

[124] A. Aulitto, A. Hirschberg, and I. Lopez Arteaga, "Influence of geometry on acoustic end-corrections of slits in microslit absorbers," *The Journal of the Acoustical Society of America*, vol. 149, no. 5, pp. 3073–3085, 2021.

[125] U. Ingard and H. Ising, "Acoustic nonlinearity of an orifice," *The journal of the Acoustical Society of America*, vol. 42, no. 1, pp. 6–17, 1967.

[126] J. H. Spurk and N. Aksel, *Fluid mechanics. Introduction into theory of flows. 8. rev. and enl. ed.; Stroemungslehre. Einfuehrung in die Theorie der Stroemungen.* 2010.

[127] D. Gilbarg, "Jets and cavities," in *Fluid Dynamics/Strömungsmechanik*, pp. 311–445, Springer, 1960.

[128] K. Mohammad, V. Kornilov, I. Lopez Arteaga, and P. de Goey, "Thermo-acoustic flame instability criteria based on upstream reflection coefficients," *Combustion and Flame*, vol. 225, pp. 435–443, 2021.

[129] S.-H. Jang and J.-G. Ih, "On the multiple microphone method for measuring in-duct acoustic properties in the presence of mean flow," *The journal of the acoustical society of America*, vol. 103, no. 3, pp. 1520–1526, 1998.

[130] M. Peters, A. Hirschberg, A. Reijnen, and A. Wijnands, "Damping and reflection coefficient measurements for an open pipe at low mach and low helmholtz numbers," *Journal of Fluid Mechanics*, vol. 256, pp. 499–534, 1993.

[131] C. Suryanarayana, "Mechanical alloying and milling," *Progress in materials science*, vol. 46, no. 1-2, pp. 1–184, 2001.

[132] M. Amitay and F. Cannelle, "Evolution of finite span synthetic jets," *Physics of Fluids*, vol. 18, no. 5, p. 054101, 2006.

[133] E. Gutmark and F. Grinstein, "Flow control with noncircular jets," *Annual review of fluid mechanics*, vol. 31, no. 1, pp. 239–272, 1999.

[134] W. Reynolds, D. Parekh, P. Juvet, and M. Lee, "Bifurcating and blooming jets," *Annual review of fluid mechanics*, vol. 35, no. 1, pp. 295–315, 2003.

[135] G. d. N. Almeida, E. F. Vergara, L. R. Barbosa, A. Lenzi, and R. S. Birch, "A low-frequency sound absorber based on micro-slit and coiled cavity," *Journal of the Brazilian Society of Mechanical Sciences and Engineering*, vol. 43, no. 3, pp. 1–9, 2021.

[136] C. Richter, *Liner impedance modeling in the time domain with flow*. Univerlagtuberlin, 2009.

[137] A. Aulitto, A. Hirschberg, I. L. Arteaga, and E. L. Buijssen, "Effect of slit length on linear and non-linear acoustic transfer impedance of a micro-slit plate," *Acta Acustica*, vol. 6, p. 6, 2022.

[138] "Acoustic module user's guide, pp. 124, comsol multiphysics® v. 6.0.." `https://doc.comsol.com/5.4/doc/com.comsol.help.aco/AcousticsModuleUsersGuide.pdf`. COMSOL AB, Stockholm, Sweden.

[139] "Thermoviscous acoustic model, comsol multiphysics® v. 6.0.." `https://doc.comsol.com/5.6/doc/com.comsol.help.aco/aco_ug_thermo.09.30.html#1065039,`, note = COMSOL AB, Stockholm, Sweden.

[140] "Non linear thermoviscous acoustic model, comsol multiphysics® v. 6.0.." `https://doc.comsol.com/5.6/doc/com.comsol.help.aco/aco_ug_thermo.09.31.html#1058860,`, note = COMSOL AB, Stockholm, Sweden.

[141] N. H. Fletcher and L. M. Douglas, "Harmonic generation in organ pipes, recorders, and flutes," *The Journal of the Acoustical Society of America*, vol. 68, no. 3, pp. 767–771, 1980.

[142] A. Nolle, "Flue organ pipes: Adjustments affecting steady waveform," *The Journal of the Acoustical Society of America*, vol. 73, no. 5, pp. 1821–1832, 1983.

[143] M.-P. Verge, B. Fabre, A. Hirschberg, and A. Wijnands, "Sound production in recorderlike instruments. i. dimensionless amplitude of the internal acoustic field," *The Journal of the Acoustical Society of America*, vol. 101, no. 5, pp. 2914–2924, 1997.

[144] R. Burgmayer, F. Bake, and L. Enghardt, "Effects of a secondary high amplitude stimulus on the impedance of perforated plates," *The Journal of the Acoustical Society of America*, vol. 149, no. 5, pp. 3406–3415, 2021.

[145] U. Bhayaraju, J. Schmidt, K. Kashinath, and S. Hochgreb, "Effect of cooling liner on acoustic energy absorption and flame response," in *Turbo Expo: Power for Land, Sea, and Air*, vol. 43970, pp. 511–522, 2010.

[146] S. Laurens, S. Tordeux, A. Bendali, M. Fares, and P. R. Kotiuga, "Lower and upper bounds for the rayleigh conductivity of a perforated plate," *ESAIM: Mathematical Modelling and Numerical Analysis*, vol. 47, no. 6, pp. 1691–1712, 2013.

[147] A. Andreini, B. Facchini, L. Ferrari, G. Lenzi, F. Simonetti, and A. Peschiulli, "Experimental investigation on effusion liner geometries for aero-engine combustors: evaluation of global acoustic parameters," in *Turbo Expo: Power for Land, Sea, and Air*, vol. 44687, pp. 1357–1368, American Society of Mechanical Engineers, 2012.

[148] D. Dupuy, A. Perrot, N. Odier, L. Y. Gicquel, and F. Duchaine, "Boundary-condition models of film-cooling holes for large-eddy simulation of turbine vanes," *International Journal of Heat and Mass Transfer*, vol. 166, p. 120763, 2021.

[149] E. Villermaux and E. Hopfinger, "Periodically arranged co-flowing jets," *Journal of Fluid Mechanics*, vol. 263, pp. 63–92, 1994.

[150] P. M. Moretti, "Flow-induced vibrations in arrays of cylinders," *Annual review of fluid mechanics*, vol. 25, no. 1, pp. 99–114, 1993.

[151] D. Marx, Y. Aurégan, H. Bailliet, and J.-C. Valière, "Piv and ldv evidence of hydrodynamic instability over a liner in a duct with flow," *Journal of Sound and Vibration*, vol. 329, no. 18, pp. 3798–3812, 2010.

[152] X. Dai and Y. Aurégan, "A cavity-by-cavity description of the aeroacoustic instability over a liner with a grazing flow," *Journal of Fluid Mechanics*, vol. 852, pp. 126–145, 2018.

[153] M. D'Elia, T. Humbert, and Y. Aurégan, "Effect of flow on an array of helmholtz resonators: Is kevlar a "magic layer"?," *The Journal of the Acoustical Society of America*, vol. 148, no. 6, pp. 3392–3396, 2020.

[154] M. Derks and A. Hirschberg, "Self-sustained oscillation of the flow along helmholtz resonators in a tandem configuration," in *8th International Conference on Flow Induced Vibration, FIV*, pp. 435–440, 2004.

[155] X. Dai, X. Jing, and X. Sun, "Flow-excited acoustic resonance of a helmholtz resonator: discrete vortex model compared to experiments," *Physics of Fluids*, vol. 27, no. 5, p. 057102, 2015.

[156] G. Nakiboğlu, S. Belfroid, J. Golliard, and A. Hirschberg, "On the whistling of corrugated pipes: effect of pipe length and flow profile," *Journal of Fluid Mechanics*, vol. 672, pp. 78–108, 2011.

[157] G. Nakiboğlu and A. Hirschberg, "Aeroacoustic power generated by multiple compact axisymmetric cavities: effect of hydrodynamic interference on the sound production," *Physics of fluids*, vol. 24, no. 6, p. 067101, 2012.

[158] J. Golliard, F. Sanna, Y. Auregan, and D. Violato, "Measured source term in corrugated pipes with flow. effect of diameter on pulsation source," in *22nd AIAA/CEAS Aeroacoustics Conference*, p. 2886, 2016.

[159] A. Hirschberg, J. Bruggeman, A. Wijnands, and N. Smits, "The "whistler nozzle" and horn as aero-acoustic sound sources in pipe systems," *Acta Acustica united with Acustica*, vol. 68, no. 2, pp. 157–160, 1989.

[160] A. Anderson, "Dependence of pfeifenton (pipe tone) frequency on pipe length, orifice diameter, and gas discharge pressure," *The Journal of the Acoustical Society of America*, vol. 24, no. 6, pp. 675–681, 1952.

[161] A. Anderson, "Dependence of the primary pfeifenton (pipe tone) frequency on pipe-orifice geometry," *The Journal of the Acoustical Society of America*, vol. 25, no. 3, pp. 541–545, 1953.

[162] A. Anderson, "A circular-orifice number describing dependency of primary pfeifenton frequency on differential pressure, gas density, and orifice geometry," *The Journal of the Acoustical Society of America*, vol. 25, no. 4, pp. 626–631, 1953.

[163] A. Anderson, "A jet-tone orifice number for orifices of small thickness-diameter ratio," *The Journal of the Acoustical Society of America*, vol. 26, no. 1, pp. 21–25, 1954.

[164] D. Fabre, R. Longobardi, V. Citro, and P. Luchini, "Acoustic impedance and hydrodynamic instability of the flow through a circular aperture in a thick plate," *Journal of Fluid Mechanics*, vol. 885, 2020.

[165] D. J. Tritton, *Physical fluid dynamics*. Springer Science & Business Media, 2012.

[166] N. A. Ahmed, *Coanda Effect: flow phenomenon and applications*. CRC Press, 2019.

[167] C. Henri, "Device for deflecting a stream of elastic fluid projected into an elastic fluid," Sept. 1 1936. US Patent 2,052,869.

[168] L. N. Cattafesta III and M. Sheplak, "Actuators for active flow control," *Annual Review of Fluid Mechanics*, vol. 43, pp. 247–272, 2011.

[169] S. SIMULTEC, "Fluidic elements based on coanda effect,"

[170] J. W. Joyce and R. N. Gottron, *Fluidics: basic components and applications*. US Army Electronics Research and Development Command, Harry Diamond Laboratories, 1979.

[171] D. Tonon, "Aeroacoustics of shear layers in internal flows: closed branches and wall perforations," 2011.

[172] S. Rienstra, "On the acoustical implications of vortex shedding from an exhaust pipe," 1981.

[173] M. Salikuddin, A. Syed, and P. Mungur, "Acoustic characteristics of perforated sheets with throughflow in a high intensity noise environment," *Journal of sound and vibration*, vol. 169, no. 2, pp. 145–177, 1994.

[174] C. K. Tam and K. A. Kurbatskii, "Microfluid dynamics and acoustics of resonant liners," *AIAA journal*, vol. 38, no. 8, pp. 1331–1339, 2000.

[175] X. Jing and X. Sun, "High-intensity sound absorption at an orifice with bias flow," *Journal of propulsion and power*, vol. 18, no. 3, pp. 718–720, 2002.

[176] L. Zhou and H. Bodén, "Experimental investigation of an in-duct orifice with bias flow under medium and high level acoustic excitation," *International Journal of Spray and Combustion Dynamics*, vol. 6, no. 3, pp. 267–292, 2014.

[177] T. Luong, M. S. Howe, and R. S. McGowan, "On the rayleigh conductivity of a bias-flow aperture," *Journal of Fluids and Structures*, vol. 21, no. 8, pp. 769–778, 2005.

[178] M. Howe, "On the theory of unsteady high reynolds number flow through a circular aperture," *Proceedings of the Royal Society of London. A. Mathematical and Physical Sciences*, vol. 366, no. 1725, pp. 205–223, 1979.

[179] M. S. Howe and M. S. Howe, *Acoustics of fluid-structure interactions*. Cambridge university press, 1998.

[180] J. Rupp, J. Carrotte, and A. Spencer, "Interaction between the acoustic pressure fluctuations and the unsteady flow field through circular holes," *Journal of Engineering for Gas Turbines and Power*, vol. 132, no. 6, 2010.

[181] D. Zhao, Y. Sun, S. Ni, C. Ji, and D. Sun, "Experimental and theoretical studies of aeroacoustics damping performance of a bias-flow perforated orifice," *Applied Acoustics*, vol. 145, pp. 328–338, 2019.

[182] M. Ikwubuo, J. Song, and J. G. Lee, "Experimental investigation of acoustic characteristic on orifice shaped with bias flow," in *Turbo Expo: Power for Land, Sea, and Air*, vol. 84959, p. V03BT04A033, American Society of Mechanical Engineers, 2021.

[183] R. Burgmayer, F. Bake, and L. Enghardt, "Reduction of inertial end correction of perforated plates due to secondary high amplitude stimuli," *JASA Express Letters*, vol. 2, no. 4, p. 042801, 2022.

[184] T. H. Melling, "The acoustic impendance of perforates at medium and high sound pressure levels," *Journal of Sound and Vibration*, vol. 29, no. 1, pp. 1–65, 1973.

[185] D. Bechert, "Sound absorption caused by vorticity shedding, demonstrated with a jet flow," *Journal of Sound and Vibration*, vol. 70, no. 3, pp. 389–405, 1980.

[186] G. Hofmans, R. Boot, P. Durrieu, Y. Aurégan, and A. Hirschberg, "Aeroacoustic response of a slit-shaped diaphragm in a pipe at low helmholtz number, 1: Quasi-steady results," *Journal of sound and vibration*, vol. 244, no. 1, pp. 35–56, 2001.

[187] P. Durrieu, G. Hofmans, G. Ajello, R. Boot, Y. Aurégan, A. Hirschberg, and M. Peters, "Quasisteady aero-acoustic response of orifices," *The Journal of the Acoustical Society of America*, vol. 110, no. 4, pp. 1859–1872, 2001.

[188] L. D. Landau and E. M. Lifshitz, *Fluid Mechanics: Landau and Lifshitz: Course of Theoretical Physics, Volume 6*, vol. 6. Elsevier, 2013.

[189] W. Beltman, P. Van der Hoogt, R. Spiering, and H. Tijdeman, "Implementation and experimental validation of a new viscothermal acoustic finite element for acousto-elastic problems," *Journal of sound and vibration*, vol. 216, no. 1, pp. 159–185, 1998.

[190] W. Beltman, "Viscothermal wave propagation including acousto-elastic interaction, part ii: applications," *Journal of Sound and Vibration*, vol. 227, no. 3, pp. 587–609, 1999.

[191] T. Basten, P. Van Der Hoogt, R. Spiering, and H. Tijdeman, "On the acousto-elastic behaviour of double-wall panels with a viscothermal air layer," *Journal of sound and vibration*, vol. 243, no. 4, pp. 699–719, 2001.

[192] S. Kottapalli, S. van Aken, A. Hirschberg, N. Waterson, D. M. Smeulders, and G. Nakiboglu, "Influence of orifice thickness and chamfer on broadband noise in a water circuit," *submitted to Acta Acustica*, 2022.

[193] J. Allard and N. Atalla, *Propagation of Sound in Porous Media: Modelling Sound Absorbing Materials, Second Edition*. 12 2009.

[194] P. Soon-Hong, "A design method of micro-perforated panel absorber at high sound pressure environment in launcher fairings," *Journal of Sound and Vibration*, vol. 332, no. 3, pp. 521–535, 2013.

[195] T. G. Zieliński, F. Chevillotte, and E. Deckers, "Sound absorption of plates with micro-slits backed with air cavities: Analytical estimations, numerical calculations and experimental validations," *Applied Acoustics*, vol. 146, pp. 261 – 279, 2019.

[196] L. Fok, M. Ambati, and X. Zhang, "Acoustic metamaterials," *MRS Bulletin*, vol. 33, no. 10, p. 931–934, 2008.

[197] H. Ruiz, C. Claeys, E. Deckers, and W. Desmet, "Numerical and experimental study of the effect of microslits on the normal absorption of structural metamaterials," *Mechanical Systems and Signal Processing*, vol. 70-71, pp. 904 – 918, 2016.

[198] C. C. Claeys, K. Vergote, P. Sas, and W. Desmet, "On the potential of tuned resonators to obtain low-frequency vibrational stop bands in periodic panels," *Journal of Sound and Vibration*, vol. 332, no. 6, pp. 1418 – 1436, 2013.

[199] M. Yang and P. Sheng, "Sound absorption structures: From porous media to acoustic metamaterials," *Annual Review of Materials Research*, vol. 47, pp. 83–114, 07 2017.

[200] C. Claeys, E. Deckers, B. Pluymers, and W. Desmet, "A lightweight vibro-acoustic metamaterial demonstrator: Numerical and experimental investigation," *Mechanical Systems and Signal Processing*, vol. 70-71, pp. 853 – 880, 2016.

[201] D. Maa, "Theory of microslit absorbers," *Shengxue Xuebao/Acta Acustica*, vol. 25, pp. 481–485, 11 2000.

[202] T. Vigran and T. Haugen, "Silencers for circular ducts-application of plates with micro-slits," *Acta Acustica united with Acustica*, vol. 102, pp. 566–577, 05 2016.

[203] C. Pedro and F. Simón, "Multiple-layer microperforated panels as sound absorbers in buildings: A review," *Buildings*, vol. 9, p. 53, 02 2019.

[204] P. Cobo, C. de la Colina, and F. Simón, "On the modelling of microslit panel absorbers," *Applied Acoustics*, vol. 159, p. 107118, 2020.

[205] D. Magliacano, M. Ouisse, A. Khelif, S. De Rosa, F. Franco, N. Atalla, and M. Collet, "Computation of dispersion diagrams for periodic porous materials modeled as equivalent fluids," *Mechanical Systems and Signal Processing*, vol. 142, p. 106749, 2020.

[206] D. L. Johnson, J. Koplik, and R. Dashen, "Theory of dynamic permeability and tortuosity in fluid-saturated porous media," *Journal of Fluid Mechanics*, vol. 176, p. 379–402, 1987.

[207] Y. Champoux and J. Allard, "Dynamic tortuosity and bulk modulus in air-saturated porous media," *Journal of Applied Physics*, vol. 70, no. 4, pp. 1975–1979, 1991.

[208] S. R. Pride, F. D. Morgan, and A. F. Gangi, "Drag forces of porous-medium acoustics," *Phys. Rev. B*, vol. 47, pp. 4964–4978, Mar 1993.

[209] D. Lafarge, *Propagation du son dans les matériaux poreux à structure rigide saturés par un fluide viscothermique: définition de paramètres géométriques, analogie électromagnétique, temps de relaxation.* 1993.

[210] D. Lafarge, P. Lemarinier, J. F. Allard, and V. Tarnow, "Dynamic compressibility of air in porous structures at audible frequencies," *The Journal of the Acoustical Society of America*, vol. 102, no. 4, pp. 1995–2006, 1997.

[211] D. Lafarge, *The Equivalent Fluid Model*, ch. 6, pp. 153–204. John Wiley & Sons, Ltd, 2010.

[212] G. Floquet, "Sur les équations différentielles linéaires à coefficients périodiques," *Annales scientifiques de l'École Normale Supérieure*, vol. 2e série, 12, pp. 47–88, 1883.

[213] L. Brillouin, *Wave propagation in periodic structures; electric filters and crystal lattices, by Leon Brillouin.* McGraw-Hill Book Company New York, London, 1st ed. ed., 1946.

[214] C. Kittel, *Introduction to Solid State Physics.* Wiley, 2004.

[215] A. Diaz, A. Haddow, and L. Ma, "Design of band-gap grid structures," *Structural and Multidisciplinary Optimization*, vol. 29, pp. 418–431, 2005.

[216] R. T. Bonnecaze, G. J. Rodin, O. Sigmund, and J. Søndergaard Jensen, "Systematic design of phononic band gap materials and structures by topology optimization," *Philosophical Transactions of the Royal Society of London. Series A: Mathematical, Physical and Engineering Sciences*, vol. 361, no. 1806, pp. 1001–1019, 2003.

[217] M. Mitchell, *An Introduction to Genetic Algorithms.* Cambridge, MA, USA: MIT Press, 1996.

[218] H. Bodén and M. Åbom, "Influence of errors on the two-microphone method for measuring acoustic properties in ducts," *The Journal of the Acoustical Society of America*, vol. 79, no. 2, pp. 541–549, 1986.

[219] S.-H. Jang and J.-G. Ih, "On the multiple microphone method for measuring in-duct acoustic properties in the presence of mean flow," *The Journal of the Acoustical Society of America*, vol. 103, no. 3, pp. 1520–1526, 1998.

[220] E. Labašová and R. Ďuriš, "Measurement of the acoustic absorption coefficient by impedance tube," *Research Papers Faculty of Materials Science and Technology Slovak University of Technology*, vol. 27, pp. 94–101, 09 2019.

[221] "Comsol multiphysics: Acoustics module user's guide," version 5.4.

[222] "Comsol multiphysics: Structural mechanics module user's guide," version 5.4.

[223] B. Thwaites, "On two solutions of the boundary-layer equations," in *50 Jahre Grenzschichtforschung*, pp. 210–215, Springer, 1955.

Acknowledgements

When doing a PhD, it does not matter what is on the other side of these 4 years, it is all about the journey itself, about the things you learn, mostly about yourself. A journey that I have been so lucky to share with some incredible people. First, an immense thank you to my supervisors, Ines and Mico. Ines, I have for you more words than this thesis can contain. You are for me someone to look up to, someone with a clear mission, someone to remind me of my values and my pitfalls when I forgot them. You have been, on more occasions than I can count, like a second mother to me. Thanks, for all the talks and the discussions, also the ones about binge-watching Bridgerton.
Mico, thank you for reding [cit.] right through me, for pushing me and stopping me, for the never-ending chain of ideas, comments, misunderstandings, chocolates, and discussions. You have thought me most of what I know about acoustics, academia, and quite a lot about life. Thanks also to your better half for enduring your 24/7 commitment.
Next, I would like to thank everyone in the POLKA Network for giving me more than a project but something close to a family. Thanks to Maria for setting everything up, for all the attention to each and one of us, for the little chats, and for the support in the last stages of this journey. Thanks to Jemma, you are simply extraordinary. Thanks for the help, the laughs, the games, and the serious things. Thanks to Alessandra for setting up the POLKA coffees. Thanks to all the supervisors for the organization for the comments and the questions that have helped my work. I want to thank each of the fellows that have shared this journey with me, for the laughs, the mafia, and word games, for the drinks in the evening, and for the quizzes. To Sadaf, Jiasen, Charita, and Vertika, being a girl in our research field (and not only) is not always easy, thanks for never making me feel alone. Special mention to Vertika, a friend more than a colleague. Thanks for the help in the lab and for the moments we shared outside, for your friendship, for your gentle words and attention. Ginger misses you. A thought for Charita, for sharing with me gossip and girly activities, and for Alex, for introducing me to the rudiments of Morse code (- .... .- -. -.- ...). Thanks to Shail, for the useful talks and discussions on aero-acoustics in a group of people working with flames and to Punithan for the long talks over dinner (I will see you soon).
I want to mention prof. De Rosa and prof. Petrone, i miei ringraziamenti vanno

anche a voi. Senza di voi non sarei qui.
A deep-felt thanks go to the members of this big family that is the D&C. First a big thanks to Geertje, you simply have all the answers. Thanks for being always there for me and for everyone else, from bureaucratic stuff to the bunny-bunny inside jokes. Thanks to Nathan, for being always interested in our well-being, for your thoughtful questions, and your support.
I have so many colleagues and friends to thank, here. A general thanks to the people in the Lunch group, thanks for the shared, sitting meals as opposed to the march, for the talks, the laughs, the just-dances, the parties, and the Friday drinks. Anahita, we started this journey together, in the middle of a pandemic and you have always been there, in and outside the university. Thanks. Krishna, thanks for the laughs and the plant talks, you have thought me so much about dedication. Haleh, for sharing the office with me and for our chit-chatting. Also, thanks to Viral, Brandon, and Rinus. Dario, you have been a constant presence in my life in the last years, *nonostante tutti i nonostante* (it does not look good in English, sorry reader). Thanks to the people in the PhD council of Mechanical Engineering for sharing this experience with me.
A thought for my master students, both going on the other side of the world, Jan and Esmée thanks for tolerating my comments and teaching me more than I thought you.
Experiments are always complex, especially when you are small objects. Thanks to Lucien, Peter, and Harrie for helping me through the experimental journey. Thanks to Bram, for following all my absurd requirements without complaining (too much). Thanks to Hamed, Mohammad, and Viktor for the help in the thermo-acoustics lab and the fruitful discussions that led to the leakage-proof-bag experience. Thanks to Lionel for the grammar tips and the enjoyable conversations and discussions.
I want to thank some people for their (in)-direct support. Cristina, Paola and Clelia you made the distance disappear, you supported me during these years in the Netherlands and during Covid. Cristina, grazie di dirmi sempre ció che pensi, anche se spesso non é quello che voglio sentirmi dire. Paola, grazie di non farmi sentire sola nelle sfide del dottorato. Clelia, grazie di essere qui, anche e soprattutto qui fisicamente per affrontare le sfide olandesi. Bensu and Tim, thanks for listening to my complains and offer solid advice on more than one occasion. Francesca, we met by chance on a tennis field, and we kept choosing to spend time in each other company, moving from tennis to brunch to Paris to Enschede with a yellow van. Il tuo supporto, fisico ed emotivo, le nostre chiaccherate, le nostre discussioni sul futuro dell'accademia sono state un'ancora di salvezza negli scorsi due anni e ancora di piú per superare i dubbi e le difficoltá di questo ultimo anno. Grazie. Let's go and hide in that small, cute library in Paris we talked about.
Mamma e papa, grazie. Grazie di avermi ascoltata, di aver accorciato le distanze, di aver reso questa esperienza un po' piú semplice. Andrea, senza i tuoi compiti di fisica alle 8 di mattina avrei iniziato a lavorare prima ma avrei riso molto meno.

Anche se oggi vi sono lontana, siete sempre a un millimetro dal mio cuore e nei miei pensieri. Grazie a zia Alba, nonostante tutto e tutti sempre fiera di me. Grazie a zia Mena, zio Baldo e Nonna Maria, sempre interessati a sapere su cosa stessi lavorando. Voglio lasciare qui un pensiero per nonna Patapata. Quanto vorrei che fossi qui per vivere questo momento con me. Ora sei lí insieme a nonno Generoso a vegliare su di me.
A heartfelt thank you to Hellen, who painted the beautiful illustration and to Niek that put the cover together. An amazing team, dank jullie wel.
The last year of my PhD has been a roller-coaster of emotions, doubts, disappointments, proud moments, happiness, and successes. In this last period, you have been my rock, you held my hand tight through it making sure I would keep my head on top of the water. You gave me the push I needed to finish this thesis in the best way I could, and the strength to say no when needed, you taught me how to Dutch-ify myself and gave me so much more love and support than I could have ever imagined. Thank you, Tino, I can't wait to see what the future brings us, I can't wait to make a million more first times together.
This a note to myself and my fellow and future PhD colleagues. Once your PhD journey is over, you won't even remember how you made it through and you will underestimate the work you have done and the knowledge you have acquired. You will probably second-guess all the choices you have made. One thing is certain when you finish your PhD, you are not the same person who walked in on the first day. I would say, that's what a PhD is really about.

List of publications

Journal articles

1. A. Aulitto, A. Hirschberg, and I. Lopez Arteaga. Influence of geometry on acoustic endcorrections of slits in microslit absorbers. The Journal of the Acoustical Society of America, vol. 149, no. 5, pp. 3073–3085, 2021.

2. A. Aulitto, A. Hirschberg, I. L. Arteaga, and E. L. Buijssen. Effect of slit length on linear and non-linear acoustic transfer impedance of a micro-slit plate. Acta Acustica, vol. 6, p. 6, 2022.

3. J. De Priester, A. Aulitto, and I. Lopez Arteaga. Frequency stop-band optimization in microslit resonant metamaterials. Applied Acoustics, vol. 188, p. 108552, 2022.

4. A. Aulitto, A. Hirschberg, and I. Lopez Arteaga. Onset of non-linear behavior in a micro-slit plate: analysis of experimental results and comparison with a two-dimensional model. Submitted to Acta Acustica in January 2023.

5. A. Aulitto, V. Saxena, A. Hirschberg, and I. Lopez Arteaga. Effect of bias flow on the acoustic transfer impedance of a micro-slit plate in the linear regime. Submitted to Journal of Sound and Vibration in February 2023.

6. A. Aulitto, V. Saxena, A. Hirschberg, and I. Lopez Arteaga.Experimental study of a slit in the presence of a bias flow under medium and high level acoustic excitations. Submitted to International Journal of Spray and Combustion Dynamics. February 2023.

7. A. Aulitto, V. Saxena, A. Hirschberg, and I. Lopez Arteaga. Sound absorption properties of a single-degree-of-freedom liner based on micro-slit plates. In preparation for submission to Applied Acoustics in March 2023.

Articles in conference proceedings

1. A. Aulitto, V. Saxena, A. Hirschberg, and I. Lopez Arteaga. Non-linear behavior of the transfer impedance of a Micro-Slit-Plate: effect of slit length in presence of a bias flow. Internoise 2022 Conference.

2. A. Aulitto, E. Cierco Molins, M. Abom, T. Kohrs, I. Lopez Arteaga, and D. Passato. Noise control in HVAC systems with ultra-thin low-frequency (UTLF) absorbers. ISMA – International Conference on Noise and Vibration 2022.

3. L. Hirschberg, J. G. Guzman Inigo, A. Aulitto, J. Sierra, D. Fabre, A. Morgans, and A. Hirschberg. Linear theory and experiments for laminar bias flow impedance: Orifice shape effect. 28th AIAA/CEAS Aeroacoustics 2022 Conference, p. 2887, 2022.

4. A. Aulitto, A. Hirschberg, and I. Lopez Arteaga. The influence of edge geometry on end-corrections in microslit absorbers. 27th International Congress on Sound and Vibration 2021.

5. A. Aulitto, I. Lopez Arteaga, S. De Rosa, and G. Petrone. Machine health diagnostics using acoustic imaging and algorithms for machine learning. Proceedings of MEDYNA2020, 3rd Euro-Mediterranean Conference on Structural Dynamics and Vibroacoustics 2022.

About the author

Alessia Aulitto was born on 11-06-1996 in Naples, Italy. She grew up in Pozzuoli, a small city near Naples.

She studied Aerospace Engineering in Naples at the University of the Studies of Naples, "Federico II". Her bachelor's end-project focused on vibration tests on stiffened cylinders. She finished her Master's degree *cum laude* in October 2019. Her Master's End-project was performed in collaboration with Eindhoven University of Technology and ASM-PT. The main focus was on the use of acoustic images for non-intrusive condition monitoring of a wire bonder machine. In November 2019, she started a Ph.D. project at Eindhoven University of Technology in the Mechanical Engineering department at the Dynamics and Control group. Her work was supervised by prof. Ines Lopez Arteaga and prof. Avraham Hirschberg. She was an Early Stage Researcher of the Marie Skłodowska-Curie Initial Training Network Pollution Know-How and Abatement (POLKA). Her task focused on linear and non-linear sound absorption mechanisms of perforated plates. The study was performed with attention to slits rather than circular perforations. The present dissertation provides the findings of her work in TU/e.